

Ductility and strain rate-dependency of adhesively-bonded timber joints

THÈSE N° 7838 (2017)

PRÉSENTÉE LE 14 JUILLET 2017

À LA FACULTÉ DE L'ENVIRONNEMENT NATUREL, ARCHITECTURAL ET CONSTRUIT
LABORATOIRE DE CONSTRUCTION EN COMPOSITES
PROGRAMME DOCTORAL EN GÉNIE CIVIL ET ENVIRONNEMENT

ÉCOLE POLYTECHNIQUE FÉDÉRALE DE LAUSANNE

POUR L'OBTENTION DU GRADE DE DOCTEUR ÈS SCIENCES

PAR

Myrsini ANGELIDI

acceptée sur proposition du jury:

Prof. M. Bierlaire, président du jury
Prof. T. Keller, Dr A. Vassilopoulos, directeurs de thèse
Prof. R. Adams, rapporteur
Dr S. Franke, rapporteur
Prof. Y. Weinand, rapporteur



ÉCOLE POLYTECHNIQUE
FÉDÉRALE DE LAUSANNE

Suisse
2017

To my parents and my brother

Preface

Timber is a widely used construction material that is characterized by its structural efficiency in terms of relatively high strength- and stiffness-to-weight ratios and high sustainability. Two major concerns exist on the material level however, i.e. the strong anisotropy and limited ductility, particularly if subjected to tension. The anisotropy complicates the joining of structural components, which in most cases is done using steel elements such as bolts or nails. The joint design thus often governs the overall design and results in an overdesigning of the components between the joints.

The approach adopted in this thesis was to overcome these two problems by developing ductile adhesively-bonded joints. The use of ductile adhesives improves the stress state in the joints, resulting in greater joint efficiency compared to bolted or nailed joints. The adhesive's ability to dissipate inelastic energy also allows system ductility to be incorporated into the timber structure. To develop such ductile adhesive joints, the adhesive's viscoelastic material behavior under large strains and variable strain rates and the inelastic energy dissipation capacity had first to be investigated and characterized. The joint concept was then validated by full-scale experiments and numerical modeling.

I would like to acknowledge the support for this research project provided by the Swiss National Science Foundation (Grant No. 406640-136680) and Sika AG, Switzerland.

Lausanne, June 2017

Prof. Dr. Thomas Keller

Acknowledgements

This doctoral thesis has been developed over the past 4.5 years at the École Polytechnique Fédérale de Lausanne (EPFL), in the Composite Constructions Laboratory (CCLab). Firstly, I would like to express my sincere gratitude to my thesis director, Professor Thomas Keller for the opportunity that he has given me to perform my PhD studies in EPFL and for his wise guidance throughout this project. I am thankful for all the regular meetings and fruitful discussions, which lead to the completion of this thesis.

Then, I would like to acknowledge the Swiss National Scientific Foundation (SNSF) for the funding and the National Research Program 66 (NRP 66) in particular, for funding this project in structural timber engineering and organizing frequent meetings for exchange of information and helpful feedback from the other members of the program. Special thanks go to Sika Zurich AG as well, for providing us with all the necessary material (structural adhesives) needed for the experimental part of this thesis.

I would like to express my acknowledgement to the thesis jury members for the time and effort they devoted into reading and evaluating the dissertation as well as their suggestions for improving the manuscript: Prof. Robert Adams (from Bristol University, UK), Prof. Weinand Yves (from Timber Laboratory, IBOIS in EPFL) and Dr. Franke Steffen (from the School of timber engineering and applied sciences in Biel), whose help was very significant for improving the final chapter of the thesis. Many thanks to Prof. Bierlaire Michel (from Transportation and Mobility Laboratory, TRANSP-OR in EPFL) as well, for managing a nice discussion during the private defense.

My deepest thanks also go to Dr Julia de Castro for her help and support at many occasions during these years. We have collaborated in teaching activities and activities related to the planning of this project. I appreciate a lot her assistance, comments and positive attitude, without which it would not have been the same.

All the experimental work performed during the first three years, would not have been possible without the assistance of the incredible group of technicians in the Structures

Laboratory in EPFL: Gilles and Sylvain for their patience teaching me how to install and use the monitoring equipment and machines, François for assisting me during the cutting of the timber specimens, Frédérique and Armin for helping me prepare my beloved adhesive specimens as well as other additional equipment, Patrice, Gerald and Serge for their availability and problem-solving ideas. I will cherish the funny dialogues and the nice Christmas coffees we shared.

The friendly and collaborative environment of CCLab group has been a great support during all these years: my favorite office-mates Moslem, Mario and Aida, my colleagues Maria, Haifeng, Vahid, Wei, Sonia, Michael, Xing and Zhengwen for all the scientific and non-discussions; thank you and I will always remember the funny moments we shared. I would also like to thank my friends and colleagues from other labs too: Francesco C, Francesco V, Angelica, Ioannis, Bastian, Dan, Fabio, Manuel, Martina, Alessandro and Albano for the time we spent together during the holidays, the Eurovision contests and the movie nights.

And regarding life outside EPFL, I thank all my Greek friends for making my life in Lausanne much more fun and pleasant: Ariadni, Loukia, Apostolis, Alexis, Vassilis, Stefanos, Anna-Maria, and Angeliki. And thank you Thodoris for your continuous support and encouragement through all hard times.

A very special thank goes to my Swiss “family” as well, the Mühlberg family, for letting me stay at their place for almost 5 years and making me always feel like “at home”. Thank you for all your support and advices and for helping me with the French and German translations of the abstract.

Last but not least, I would like to express a huge “thank you” («ευχαριστώ») to my beloved family: my parents, Grigoris and Maria, and my brother, Nikos. They selflessly encouraged me to explore new horizons in life and they raised me with the most valuable life principles and love for sciences. I would not be standing anywhere without their continuous love and support; I love you («Σας α γαπώ»).

From my heart,

Myrsini

Abstract

One of the most important characteristics of load-bearing structures is ductility, i.e. the ability of a material or a structure to sustain inelastic deformation prior to failure, without loss of resistance. The topic of this PhD Thesis was to develop ductile adhesively bonded timber joints, in order to compensate for the inherent lack of ductility of timber.

After the rate-dependent true tensile and compressive properties of the acrylic adhesive had been established (including Poisson ratio, ductility and recovery), two types of adhesively-bonded timber joints were experimentally studied in tension and compression: stiff epoxy and ductile acrylic joints. The latter ones exhibited lower stiffness but higher capacity and ductility, as explained by the extracted stresses and strains too.

Furthermore, finite element (FE) models, including these strain rate-dependent properties of the acrylics, were developed to validate all the experimental results obtained and study the parametric effect of the different applied displacement rates on the acrylic joints. Extensive simulation using the developed FE models has shown their capacity to accurately predict the rate effect on bonded joints' mechanical response: stiffness, yield, ductility, ultimate failure. Finally, the behavior of the developed bonded joints over mechanical joints was analytically compared, based on Eurocode and the results confirmed the promising potential of the developed joint concept.

To summarize, if ductile adhesives are used, it is possible to create ductile timber joints, which can perform better compared to other existing assembling techniques (i.e. mechanical fasteners or epoxy-adhesives) and their complex, rate-dependent behavior can be modeled with precision with the help of FE. This knowledge can lead to a broader and more efficient use of timber, contributing subsequently to achieving more sustainable modern structures.

Keywords: *timber, adhesive, bonded, joint, ductility, capacity, rate effect, mechanical joints*

Résumé

La ductilité, soit la capacité d'un matériau ou d'une structure à se déformer de manière inélastique avant sa rupture est une des plus importantes caractéristiques de structures porteuses. Le sujet de cette Thèse de Doctorat était de développer des joints en bois, collés et ductiles, afin de compenser le manque de ductilité inhérent au bois.

Une fois que le comportement de la colle à base d'acrylique sous traction et compression ainsi que sous des vitesses de chargement différentes avait été établi, deux types des joints collés ont été étudiés en traction et compression: joints avec époxy (rigides) et acrylique (ductiles). Ces derniers ont présenté une rigidité réduite mais une capacité et ductilité beaucoup plus importantes, comme montré par les contraintes et déformations mesurées.

En plus, un modèle aux éléments finis (FE), comprenant ces propriétés dépendantes de la vitesse de déformation imposée, a été développé pour valider tous les résultats expérimentaux obtenus et pour étudier l'effet paramétrique des différentes vitesses de chargement (mode déplacement) appliqué sur les joints. Le modèle FE développé a été capable d'estimer avec précision cet effet des vitesses sur le comportement mécanique des joints : rigidité, limite d'élasticité (fluage), ductilité et niveau de rupture finale. Enfin, ce comportement composé de joints collés a été comparé avec des joints par organes métalliques (clous ou boulons), sur la base de l'Eurocode.

En résumer, si des colles adhésives ductiles sont utilisées, il est possible de créer des assemblages en bois ductiles, qui peuvent se comporter mieux que d'autres méthodes d'assemblages existantes (i.e. assemblages mécaniques) et leur comportement, complexe et dépendent de la vitesses de déformation imposée, peut être modélisé à l'aide des éléments finis. Grâce à cette connaissance, une utilisation plus large et plus efficace du bois peut être atteinte, contribuant par la suite à la réalisation des structures modernes plus durables.

Mots-clés: bois, adhésif, collé, joint, assemblage, ductilité, capacité, vitesse de déformation, assemblages mécanique

Zusammenfassung

Eine der wichtigsten Eigenschaften von Tragwerken ist die Duktilität, das heisst, die Fähigkeit eines Material oder einer Struktur, sich vor einem Bruch – ohne Verringerung der Querschnittswiderstands - plastisch zu verformen. Das Thema dieser Doktorarbeit ist die Entwicklung von duktilen Klebefugen, mit dem Ziel die mangelhafte Duktilität des Baustoffs Holz zu kompensieren.

Nachdem das Verhalten von Klebefugen auf Acrylbasis unter Zug- und Druckbeanspruchung sowie unter verschiedenen Belastungsgeschwindigkeiten untersucht worden war, wurden zwei Typen von Klebefugen untersucht: solche auf Epoxid (spröde) sowie auf Acryl (duktil) basierende. Letztere weisen zwar ein geringere Festigkeit auf, sind aber duktiler, was durch die gemessenen Spannungen und Verformungen belegt wird.

Weiterhin wurde, um die Versuchsergebnisse rechnerisch zu bestätigen, ein Modell aus finiten Elementen entwickelt, deren Eigenschaften von der Geschwindigkeit der aufgetragenen Verformungen abhängen. Das FE-Modell ermöglicht den Einfluss der Belastungsgeschwindigkeit auf Steifigkeit, Elastizitätsgrenze, Kriechen, Duktilität und Bruchfestigkeit präzise einzuschätzen. Weiterhin wurde das vorteilhafte Verhalten von Klebefugen im Vergleich zu mechanischen Verbindungen durch Nägel oder Schrauben anhand des Eurocodes verglichen.

Zusammenfassend wird festgestellt: die Verwendung von duktilen Klebern ermöglicht die Schaffung von Holzbauverbindungen, die sich besser und duktiler verhalten können als mechanische Verbindungen. Ihr von der Belastungsgeschwindigkeit abhängiges Verhalten kann mit Hilfe von finiten Elementen modelliert werden. Dieses Wissen kann zu einer breiteren und effizienteren Nutzung von Holz führen und dazu beitragen, nachhaltigere moderne Strukturen zu erreichen.

Schlüsselwörter: Holz, geklebt, Fuge, Holzbaustoff, Duktilität, Verformungsgeschwindigkeit, metallische Holzbaustöße,

Σύνοψη

Ένα από τα πιο σημαντικά χαρακτηριστικά των φέρουσων κατασκευών είναι η πλαστιμότητα, η ικανότητα δηλαδή ενός υλικού ή μίας κατασκευής να φέρει ανελαστικές παραμορφώσεις προτού αστοχήσει. Το θέμα της παρούσας διδακτορικής διατριβής ήταν να αναπτύξει πλάστιμες, ξύλινες συνδέσεις, χρησιμοποιώντας ειδικές δομικές κόλλες, προκειμένου να αναπληρώσουν την εγγενή έλλειψη πλαστιμότητας που χαρακτηρίζει το ξύλο ως υλικό.

Για αυτόν το σκοπό χρησιμοποιήθηκε μια ακρυλική κόλλα (acrylic). Αφού προσδιορίστηκαν πειραματικά όλες οι πραγματικές (λαμβάνοντας δηλαδή υπόψιν τις όποιες γεωμετρικές αλλαγές) μηχανικές της ιδιότητες υπό διαφορετικές ταχύτητες επιβαλλόμενης φόρτισης, εν συνεχεία, αναπτύχθηκαν και μελετήθηκαν σε εφελκυσμό και θλίψη δύο διαφορετικά είδη συνδέσεων: άκαμπτες με εποξειδική ρητίνη (epoxy) και εύκαμπτες, πλάστιμες με το παραπάνω ακρυλικό. Οι τελευταίες παρουσίασαν μειωμένη δυσκαμψία, αλλά αρκετά μεγαλύτερη πλαστιμότητα και φέρουσα ικανότητα (φορτίο αστοχίας), όπως απεδείχθη και από τις μετρήσεις τάσεων και παραμορφώσεων, κατόπιν πειραμάτων.

Επιπλέον, αναπτύχθηκε ένα μοντέλο πεπερασμένων στοιχείων (finite element, FE), το οποίο, λαμβάνοντας υπόψιν την εξάρτηση των ιδιοτήτων του ακρυλικού από τις διαφορετικές επιβαλλόμενες ταχύτητες παραμόρφωσης, είχε στόχο να επικυρώσει τα πειραματικά συμπεράσματα αλλά και να διεξάγει μία παραμετρική μελέτη εκτίμησης της μηχανικής απόκρισης της σύνδεσης για διαφορετικές ταχύτητες φόρτισης. Το μοντέλο που αναπτύχθηκε ήταν ικανό να προσομοιώσει με ακρίβεια τη μηχανική συμπεριφορά των παραπάνω συνδέσεων που είχε παρατηρηθεί πειραματικά: δυσκαμψία, όριο διαρροής, πλαστιμότητα και τελικό φορτίο αστοχίας, κατανομή τάσεων και παραμορφώσεων. Επίσης, μπόρεσε να προσομοιώσει την επιρροή των διαφορετικών επιβαλλόμενων ρυθμών ως προς τα παραπάνω όπως επίσης και να προσδιορίσει με ποιά ταχύτητα (και άρα μηχανικές ιδιότητες) ανταποκρινόταν κάθε πεπερασμένο τμήμα της στρώσης του ακρυλικού. Τέλος, οι ανεπτυγμένες συγκολλητές συνδέσεις συγκρίθηκαν με

μηχανικές συνδέσεις αντίστοιχης γεωμετρίας με μεταλλικά μέσα σύνδεσης (π.χ. καρφια ή κοχλίες), οι οποίες σχεδιάστηκαν σύμφωνα με τον κατάλληλο Ευροκώδικα: η φέρουσα ικανότητα των ακρυλικών συνδέσεων απεδείχθη ανώτερη έναντι των μηχανικών για διάφορες προτεινόμενες γεωμετρίες που εξετάστηκαν.

Συνοψίζοντας, εάν χρησιμοποιηθούν πλαστικές ακρυλικές κόλλες, είναι δυνατόν να επιτευχθούν πλαστικές ξύλινες συνδέσεις, οι οποίες μπορούν να επιτύχουν καλύτερη μηχανική συμπεριφορά σε επιβαλλόμενη φόρτιση σε σχέση, για παράδειγμα, με τις πιο ευρέως χρησιμοποιούμενες μηχανικές συνδέσεις. Η μηχανική τους συμπεριφορά, σύνθετη και εξαρτώμενη από το ρυθμό επιβολής της φόρτισης, μπορεί να προσομοιωθεί με ακρίβεια, με τη βοήθεια των πεπερασμένων στοιχείων.

Λέξεις-κλειδιά: ξύλο, κόλλα, συσκολλητή σύνδεση, πλαστιμότητα, φέρουσα ικανότητα, ταχύτητα φόρτισης, μηχανικοί σύνδεσμοι

Table of contents

Preface	i
Acknowledgements	iii
Abstract	v
Résumé	vii
Zusammenfassung	ix
Σύνοψη	xi
1. Introduction	1
<hr/>	
1.1. Motivation	3
1.2. Objectives	6
1.3. Methodology	6
1.4. Thesis organization	7
1.5. List of publications	10
2. Acrylic Poisson ratio: Displacement and structural effects	13
<hr/>	
2.1. Introduction	15
2.2. Experimental set-up and instrumentation	16
2.2.1. Material and specimen fabrication	16
2.2.2. Experimental program and instrumentation	17
2.3. Experimental results	18
2.3.1. DMA experiments	18
2.3.2. Tension experiments	19
2.3.3. Compression experiments	22
2.4. Discussion	23
2.4.1. Engineering vs true strains	23
2.4.2. Poisson ratio based on engineering or true strains	26
2.4.3. True strain Poisson ratio in tension	29
2.4.4. True strain Poisson ratio in compression	31
2.4.5. Comparison between Poisson ratio in tension and compression	32
2.5. Conclusions	34

3.	Acrylic ductility, recovery and strain rate-dependency	37
<hr/>		
3.1.	Introduction	39
3.2.	Experimental set-up	41
	3.2.1. Material and specimen fabrication	41
	3.2.2. Experimental procedure and instrumentation	42
3.3.	Experimental results	43
	3.3.1. Differential scanning calorimetry	43
	3.3.2. Load-displacement responses	44
3.4.	Discussion	46
	3.4.1. True stress-strain relationships	46
	3.4.2. Strain-rate effects	51
	3.4.3. Ductility	53
	3.4.4. Time-dependent recovery	55
3.5.	Conclusions	59
4.	Ductile adhesively-bonded timber joints: experimental investigation	63
<hr/>		
4.1.	Introduction	65
4.2.	Experimental set-up	66
	4.2.1. Materials and specimens	66
	4.2.2. Experimental procedure and instrumentation	67
4.3.	Results and discussion	68
	4.3.1. Failure modes and load-displacement responses	68
	4.3.2. Displacement and strain fields	71
	4.3.3. Mechanical characterization	75
	4.3.4. Joint ductility	76
	4.3.5. Ultimate load prediction	80
4.4.	Conclusions	82
5	Ductile adhesively-bonded timber joints: strain rate effect	85
<hr/>		
5.1.	Introduction	87
5.2.	Summary of experimental set-up	88
5.3.	Numerical models	90

5.4.	Numerical model validation	92
5.4.1.	Load-displacement responses	92
5.4.2.	Stress and strain distributions	93
5.4.3.	Ultimate load prediction	97
5.4.4.	Ductility indexes	98
5.5.	Rate effect on acrylic joints – parametric study	99
5.5.1.	Rate effect on load-displacement responses and ultimate loads	99
5.5.2.	Rate effect on stress-strain responses and true strain rates	101
5.5.3.	Rate effect on ductility	104
5.6.	Conclusions	105

6	Comparison of adhesively-bonded and mechanical timber joints	109
----------	---	------------

6.1.	Introduction	111
6.2.	Adhesively-bonded joint design values of resistance	112
6.2.1.	Summary of experimental setup	112
6.2.2.	Characteristic and design values of joint resistance	113
6.3.	Design value of resistance of dowel-type joints using nails	114
6.4.	Design value of resistance of dowel-type joints using bolts	119
6.5.	Comparison between adhesively-bonded and mechanical joints	121
6.5.	Conclusions	127

7	Conclusions and future work	129
----------	------------------------------------	------------

7.1.	Main Conclusions	131
7.2.	Original Contribution	134
7.3.	Future research	135

Annexes

A	Tensile and compressive properties of the acrylic (Poisson ratio)	137
B	Tensile and compressive properties of the acrylic (Ductility and recovery)	149
C	Experiments on double-lap joints: Failure modes	157
D	Numerical modeling of double-lap joints: Compression	167
E	Geometrical and material parameters on the double-lap timber joint capacity	171
F	Preliminary numerical investigations (parametric study)	195

Curriculum vitae (CV)

Chapter 1

Introduction

1.1. Motivation

The global construction industry consumes vast quantities of energy, materials and other resources. Buildings represent a huge share of the global and European market size, with a predicted industry value of up to €9.7 trillion [1] and €2.6 trillion by 2020 [2] respectively. They also represent 35% of the total consumed energy (see Figure 1.1), making it the largest end-use sector worldwide [3]; this energy is required for space heating and cooling, water heating, lighting, cooking and electrical appliances in general. Thus, modern civil engineering research is oriented towards finding sustainable materials and building techniques.

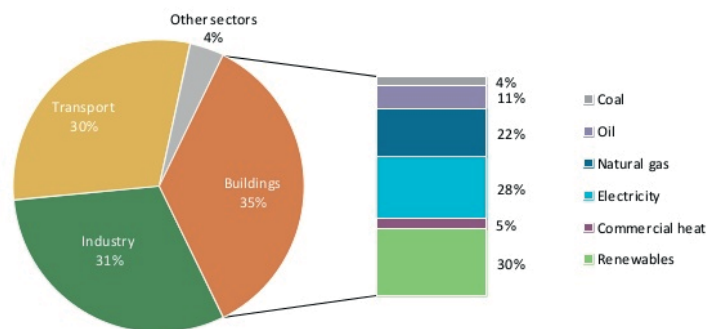


Figure 1.1: Final energy consumption by sector, 2010 (worldwide) [3]

Among the most popular choices of architects and civil engineers is timber, a natural material that combines several advantages. Timber is particularly abundant in central Europe and is naturally recyclable; as long as people continue to plant new trees to replace those harvested, timber will continue to exist. Furthermore, it is a natural material, with no toxic emissions, which makes it easy and safe to work with but also means that it will not decompose into environmentally harmful ingredients [4]. Moreover, timber has the lowest embodied energy of many other building materials used in construction, such as concrete, steel, aluminum or bricks (see Figures 1.2 and 1.3) [5]. Embodied energy is the energy related to the life cycle of a product or material from resource extraction to end-of-life [8]; from harvest or mine, manufacture and transportation to use and final removal. Timber requires the minimum amounts of energy for processing during all these stages, assuming that it does not have to be transported from a great distance. For example, sun provides the energy to grow the trees, unlike fossil fuels, which are the principal source for aluminum or concrete production [9]. Another important aspect of timber is that it helps to diminish the greenhouse effect, as it stores carbon; trees capture carbon throughout their lives and when they are logged, all of this carbon is trapped within for as long as the timber continues to exist in any form [10]. Finally, timber is a good insulator due to air pockets within its cellular structure; it is 15 times better than masonry, 400 times better than steel and 1770 times better than aluminum [11]. Consequently, timber results in reduced energy consumption for heating [4], which is one of the main energy requirements during

the life of a building. For all the aforementioned reasons, timber is in many respects related to sustainability (i.e. energy needed for its production and use, implication of other natural resources, pollution) and remains the most ecological option when compared to other traditional materials, as also shown in Figure 1.4.

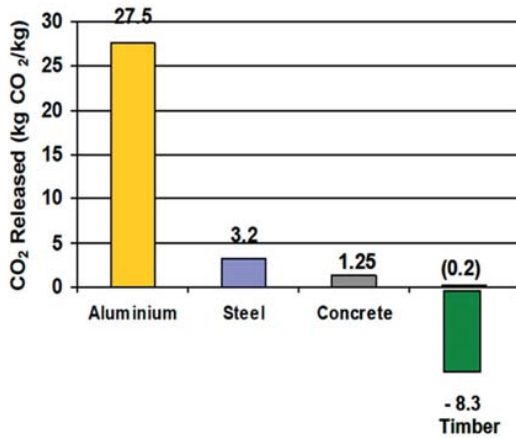


Figure 1.2: Carbon dioxide released and stored during manufacture [6]

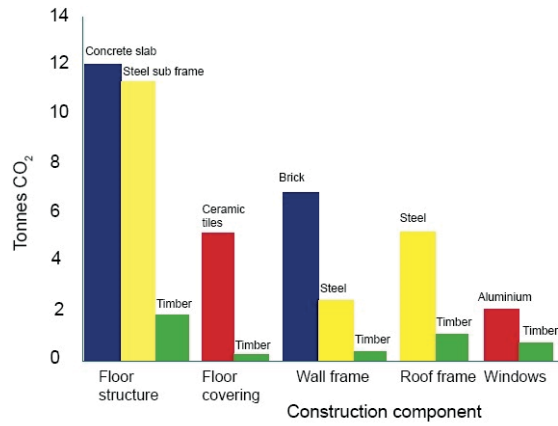


Figure 1.3: Carbon dioxide released for each structural component [7]

Sustainability of Building Materials	Wood (including Western Red Cedar)	Steel	Concrete
Total Energy Use	Lowest	140% more	70% more
Greenhouse Gases	Lowest	45% more	81% more
Air Pollution	Lowest	42% more	67% more
Water Pollution	Lowest	1900% more	90% more
Solid Waste	Lowest	36% more	96% more
Ecological Resource Use	Lowest	16% more	97% more

Figure 1.4: Sustainability of building materials [12]

Despite the numerous benefits of timber, it comprises certain shortcomings that restrict its use as a structural material; as a natural fibrous and brittle material, timber lacks ductility, which is an essential characteristic for all modern structures. Ductility is the ability of a material or structure to sustain large deformations without significant loss of its resistance, by dissipating inelastic energy. As a result, it is crucial in cases of impact or overloading, i.e. earthquakes, and engineers should consider this property in the structural concept and material selection. One solution to compensate for the lacking ductility is to develop ductile timber joints.

The main assembling techniques are mechanical fasteners (nails, bolts or rivets) and adhesive bonding, while others like interlocking [13] and friction welding[14] are currently being developed as well, but still rarely applied in practice. Among the two main aforementioned techniques, the doweled joints can only

exhibit limited ductility, because steel cannot be sufficiently deformed before wood fails, as steel is much more rigid (with a modulus of elasticity 20 times bigger on average). On the other hand, adhesive bonding can prove advantageous, if suitable, ductile adhesives are used. These adhesives can compensate for the lack of timber ductility and increase ultimate joint capacity, due to local stress redistribution, with lower edge stress peaks close to the bond line [15]. However, there are three main limitations concerning adhesive bonding that limit its application:

- The current standards fail to include all the necessary information related to timber adhesive bonding and this is one of the main reasons for its relatively limited use nowadays compared to concrete or steel for instance, despite it being one of the oldest and most traditional building materials.
- Ductile adhesives, like acrylics, are flexible, highly deformable materials [16], susceptible to any changes in the applied loading rate [17, 18], unlike stiff adhesives, like epoxies, which are rate-independent. Thus, their mechanical behavior at different rates should be established, related to those that may occur in real applications; for example, the fast loading of a bridge or a building by a vehicular crossing or wind respectively, or the slower loading of any structure in the case of people or snow load. Nevertheless, the existing literature and manufacturers' guidelines do not provide sufficient information related to the mechanical properties of these adhesives (i.e. elastic modulus, yield, ductility, recovery, Poisson ratio, true and engineering stress-strain curves) and as a result, extensive research on these adhesives should be conducted, before modeling or using them in a timber joint.
- Finally, even in cases where the non-linearity and rate-dependency of the adhesive employed are expected, few finite element (FE) models have been developed that accommodate such behaviors and can accurately simulate the rate-dependent mechanical behavior of ductile joints. The majority of investigations assume an average stress-strain curve for the adhesive properties as input, ignoring the rate-dependency. Therefore, part of this research should also be oriented towards developing a validated numerical model, which can predict the mechanical response to any loading rate of such ductile adhesively-bonded joints and serve as a basis for any future investigations in the field of ductile adhesive joints; this model would allow the parametric study of the rate effect on such joints and lead to a better understanding of joint behavior.

Thus, the main objective was to develop ductile adhesively-bonded timber joints that could dissipate more energy during loading compared to the existing assembling techniques, leading to higher ultimate loads. For this purpose, a ductile acrylic adhesive (SikaFast 5221NT in this study [19]) and one of the most commonly used structural soft woods (spruce) were selected for the formation of the joints. First, the ductility of the adhesive needed to be quantified and compared with that of other ductile and widely used materials, such as steel or concrete. Then, acrylic-bonded joints were experimentally investigated in terms of capacity and ductility in order to prove the desired concept. Finally, the developed joint had to be

modeled using finite elements providing engineers with an experimentally validated numerical tool that could predict joint behavior under different loading conditions when such ductile, rate-dependent adhesives are used.

Having addressed the main issue of absence of ductility associated with the use of timber, this study is of great importance in a structural, architectural and environmental framework, as it aims to increase the applicability of timber and knowledge related to its assembly. It can form the basis for further research in the field of timber joints and structures, eventually leading to more sustainable solutions.

1.2. Objectives

The aim of this research was to develop ductile adhesively-bonded timber joints and evaluate their structural performance under the various rates of displacements that may occur in real applications. In order to achieve this, the following main objectives were defined:

- a) Evaluate the true rate-dependent mechanical properties of acrylic, including the Poisson's ratio, elastic modulus, yield and strength, ductility and recovery, in tension and compression, as a potential adhesive for ductile timber joints.
- b) Develop ductile adhesively-bonded timber joints, using this ductile, acrylic adhesive and quantify the acrylic effect on the mechanical behavior of the joint compared to another, stiffer adhesive epoxy in terms of: stiffness, failure mode, capacity, ductility and strain distribution and angle.
- c) Model and predict the mechanical response of the developed joints and assess the rate effect on the acrylic joint's mechanical properties, i.e. ductility, stiffness and capacity.
- d) Compare the developed bonded joints with mechanical joints, using traditional mechanical fasteners (nails and bolts), for the same geometry and type of wood.

1.3. Methodology

To achieve these objectives, the following methodology was adopted:

For objective (a):

- Experimental investigation of the acrylic adhesive (SikaFast 5221 NT) to obtain its complete set of properties under different displacement rates, including reloading cycles to evaluate its ductility and potential for recovery.
- Validation of the observed rate-dependent mechanical properties and recovery, using established analytical models.

For objective (b):

- Experimental investigation and comparison of two timber joint types; stiff epoxy- and ductile acrylic-bonded double-lap joints.
- Digital Image Correlation (DIC) as additional experimental technique, which provides the complete monitoring of the strains and thus an understanding of the deformation mechanisms in both joint types.
- Establishment of an analytical model that predicts ductility, based on the joint's ultimate displacement and the damage incurred during loading.

For objective (c):

- Numerical models (FE) that simulated both joints' behavior.
- Parametric study of the rate effect on acrylic joints, with the help of the FE model.

For objective (d):

- Analytical design of mechanical joints and comparison with the developed bonded joints, using Eurocodes 0 and 5 [20, 21].

1.4. Thesis organization

The main core of the current research is organized in five **chapters** (Chapters 2-6), which address the aforementioned objectives. As can also be seen from the schematic chart presented in Figure 1.5, the first four chapters (Chapters 2-5) correspond to the four journal papers that were developed in parallel and are either submitted for publication or already published. More precisely, the main content of each chapter is summarized as follows:

- Chapter 2: The effect of the displacement rate on the Poisson ratio of an acrylic adhesive (SikaFast 5221NT) has been assessed under tension and compression, for true and engineering strains, with the help of the digital image correlation (DIC) technique. The results obtained are also linked to the changes that occur in the molecular structure (i.e. necking) and serve to convert engineering to true stresses.
- Chapter 3: The ductility and time-dependent recovery of this acrylic adhesive were evaluated, after the true stress-strain curves have been established in tension and compression. The effect of the displacement rate on the different mechanical properties (such as yield and failure) as well as the time-dependent recovery of the adhesive are then analytically modeled. For this part, reloading cycles were performed on the adhesive for both loading types.

- Chapter 4: Acrylic-bonded timber joints were studied experimentally in tension and compression. Their mechanical behavior was compared with that of epoxy joints, in terms of failure mode, displacement and strain distribution, stiffness, yield, capacity and ductility. The detailed monitoring of the surface strains was achieved using the DIC technique and the plotted strains were used for comparing the two joint types and predicting failure, based on the Norris failure criterion (strain-based version). Reloading cycles were then performed once more and the ductility close to failure was estimated based on the degradation of the unloading stiffness. The calculated ductility indexes were also compared with those in the standards and those of other existing structural systems.
- Chapter 5: Finite element models for both joint types were developed to simulate joint behavior (rate-dependent for the case of the acrylic joints). The models were validated by the previously obtained experimental results. In the second part of this chapter, the acrylic joint model has been extended for different applied displacement rates, in order to assess its effect on the main joint's mechanical properties.
- Chapter 6: Mechanical double-lap joints using the same timber and geometry were designed. The characteristic capacity of the developed bonded joints were compared with the latter, after all design values had already been converted into characteristic values, using the material and safety factors proposed by the standards.

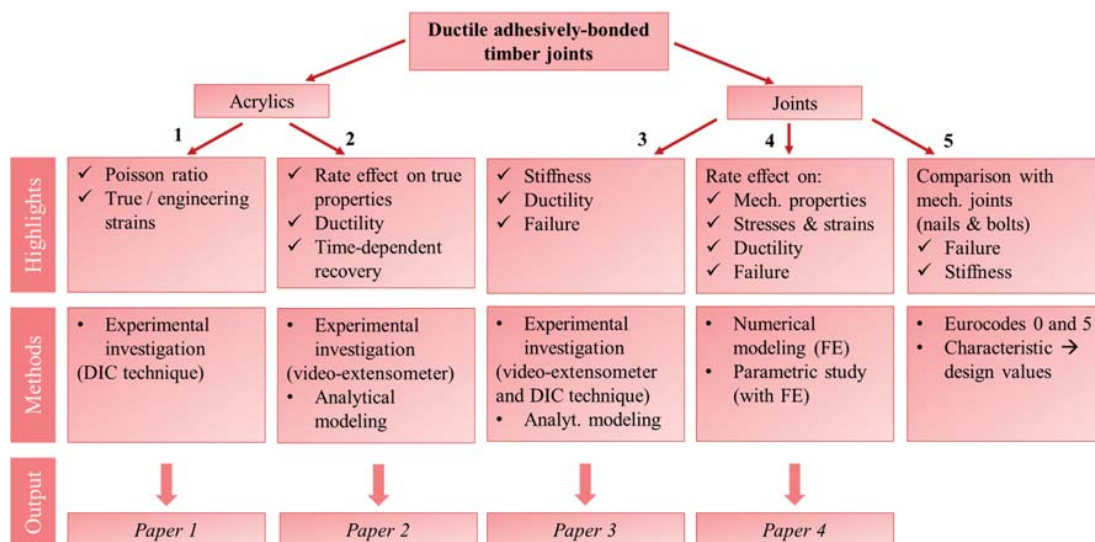


Figure 1.5: Thesis' structure

Supplementary experimental and analytical results are then included in the **Annexes**, which are intended to complement the chapters of the thesis. More precisely, the content of the Annexes can be summarized as follows:

- Annex A: This annex contains all the experimental results related to Chapter 2, which focuses on the acrylic's Poisson ratio; all the stress-strain curves from 15 specimens in tension and 15 in compression (as derived from the machine's measurements) and all the Poisson ratios calculated for the different rates in tension (extracted from the DIC measurements). All the mechanical properties presented earlier in the tables of this chapter as well as one of the main conclusions linked to the rate-sensitivity of the Poisson ratio to the rate applied in tension can be linked to the figures presented in this annex.
- Annex B: Similarly to the previous annex, here all the experimental results related to the rate-dependent mechanical properties of the investigated acrylic adhesive (Chapter 3) are presented for reference; 20 specimens in tension and 20 in compression. The results include the eight specimens for which reloading cycles were performed. These specimens were used for the calculation of ductility and time-dependent recovery.
- Annex C: This annex includes all the experimental results from the study on the acrylic and epoxy joints (Chapter 4); load-displacement curves, photos of failure and DIC results for the displacement at specific reference loads close to 40 kN.
- Annex D: The finite element model for the two joint types was also developed for the case of compression and compared with the experimental curves, obtained in Chapter 4.
- Annex E: The effect of two geometrical (overlap length and bond line thickness) and two material (type of wood and adhesive) parameters on the adhesively-bonded timber joint's capacity was assessed with the help of two statistical methods: the full and fractional factorial designs. All the results concerning the joint's capacity are derived from the finite element simulations, which were performed in Ansys 15.0 but some were also experimentally validated from the first, preliminary series of joints.
- Annex F: A further numerical study on the effect of different material and geometry parameters on the joint's capacity and stress distribution was conducted considering the optimum overlap length, adhesive thickness and type to achieve ductility without compromising the joint's load resistance. Finally, certain stress-reduction methods, mainly originating from the existing literature on composite materials, were examined in order to increase the joint capacity; tapered ends, bi-adhesive bond line and application of pre-stress were among those that were most influential, for which the results are presented.

1.5. List of publications

The results of this thesis have been included in one conference and four journal papers, two of which have been accepted, two are under review and one is still in progress. These four papers correspond to each chapter of this thesis, as shown in Figure 1.5, and they are listed below:

Journal papers

1. M. Angelidi, A.P. Vassilopoulos, T. Keller. Displacement rate and structural effects on Poisson ratio of a ductile structural adhesive under tension and compression, *International Journal of Adhesion and Adhesives* (accepted)
2. M. Angelidi, A.P. Vassilopoulos, T. Keller. Ductility, recovery and strain rate dependency of an acrylic structural adhesive, *Construction and Building materials* (available online)
3. M. Angelidi, A.P. Vassilopoulos, T. Keller. Ductile adhesively-bonded timber joints: experimental investigation (submitted in March 2017, under review)
4. M. Angelidi, T. Keller. Ductile adhesively bonded timber joints: rate effect (submitted in April 2017)

Conference papers

1. M. Angelidi, A. Vassilopoulos, J. de Castro San Roman and T. Keller. Time-dependent mechanical behavior of acrylic adhesives, 3rd International Conference of Structural Adhesives Bonding, Porto, Portugal, 2015.
2. M. Angelidi, A. Vassilopoulos and T. Keller. Ductility of adhesively-bonded timber joints, 1st International Conference on Timber Structures and Engineering, New Forest, UK, 2017.

References

- [1] Construction Global. 2020: A global forecast for the construction industry over the next decade to 2020, (2010).
- [2] <https://buildingradar.com/construction-blog/european-construction-market-forecast/>
- [3] <https://www.slideshare.net/internationalenergyagency/webinar-27-june-2013-launch-event-final>, International Energy Agency
- [4] http://www.tastimber.tas.gov.au/SusArticle_View.aspx?articleid=71
- [5] Hammond G. P., Jones C. I. Embodied energy and carbon in construction materials. *Proceedings of the Institution of Civil Engineers-Energy*, 161(2), 87-98 (2008).
- [6] <http://www.habitechsystems.com.au/low-enviro-impact/>
- [7] <http://www.treehugger.com/green-architecture/guardian-covers-tall-wood-construction-we-cover-comment-section.html>
- [8] Puettmann, M. E., Wilson, J. B. Life-cycle analysis of wood products: Cradle-to-gate LCI of residential wood building materials. *Wood and Fiber Science*, 37, 18-29 (2007).
- [9] Kretschmann D. E, Ross R. J. Wood handbook: wood as an engineering material, USDA Forest Service General Technical Report FPL-GTR-113, (5): 29, Madison (2010).
- [10] <https://www.softwoods.com.au/timber/benefits-of-timber/>
- [11] <http://makeitwood.org/benefits-of-wood/>
- [12] <http://www.linwoodhomes.com/the-green-facts-on-western-red-cedar/>
- [13] Weinand Y. (Ed.). *Advanced timber structures: Architectural designs and digital dimensioning*. Birkhäuser, p: 200-201 (2017).
- [14] Hahn B., Weinand Y., Stamm B. & Vallée T. Experimental investigations on welded double lap joints composed of timber. *Procedia Engineering*, 10, p: 2526-2531 (2011).
- [15] De Castro J.: “System ductility and redundancy of FRP structures with ductile adhesively-bonded joints”, EPFL PhD Thesis no 3214, Lausanne (2005).
- [16] Banea M. D., da Silva L. F. M. “Mechanical characterization of flexible adhesives”, *Journal of Adhesion*, Vol.85 (Issue: 4-5) p: 261-285 (2009).
- [17] Angelidi M., Vassilopoulos A. P., Keller T. Ductility, recovery and strain rate dependency of an acrylic structural adhesive. *Construction and Building Materials*, 140, p: 184-193 (2017).
- [18] Zgoul M., Crocombe A. D. Numerical modelling of lap joints bonded with a rate-dependent adhesive. *International journal of adhesion and adhesives*, 24(4), p: 355-366 (2004).
- [19] Sika AG. SikaFast5221 NT: Fast-curing 2-component structural adhesive. Zurich (2013).
- [20] BSi. Eurocode 0: Basis of structural design. BS EN 1990:2002 + A1:2005. Brussels: British Standards Institute (2002).
- [21] EN, B. 1-1: 2004, Eurocode 5: Design of timber structures—General—Common rules and rules for buildings (1995).

Chapter 2

Acrylic Poisson ratio: Displacement rate and structural effects

The effects of the loading type, i.e. tension or compression, and displacement rate on the Poisson ratio of a non-linear viscoelastic ductile structural adhesive have been investigated using digital image correlation-based strain fields. The results showed that the Poisson ratio should be based on true strains to take geometry changes into account. In tension, the ratio exhibited a slight dependency on the true strain level below the yield point and on the displacement rate. The rate dependency was confirmed in regions with necking, where the Poisson ratio locally decreased. Subjected to compression, the ratio was affected by out-of-plane deformations of the specimens and thus exhibited values above 0.5. The necking in tension and out-of-plane deformations in compression may be considered as structural effects on the Poisson ratio that may be attributed to changes in the molecular structure of the polymer.¹

Keywords: *adhesives, acrylics, Poisson ratio, displacement rate, necking.*

¹ Angelidi M., Vassilopoulos A. P., Keller T. Displacement rate and structural effects on Poisson ratio of a ductile structural adhesive under tension and compression. *International Journal of Adhesion and Adhesives* (2017).

2.1. Introduction

In civil engineering, new structural materials with promising new physical and mechanical properties are appearing in bridge and building construction, such as fiber-reinforced polymers or structural glass. A common feature of these materials is that they behave in a more or less brittle manner, similar to the generally used timber. In order to overcome this drawback, i.e. compensate for the lacking material ductility, ductility can be incorporated on the structural system level, e.g. by using ductile structural joints [1]. An appropriate type of such joints can be developed using ductile structural adhesives, as has already been proved experimentally [2, 3]. Since the stress state in such adhesive joints is complex, the adhesive is subjected to different types of loading and loading rates, which may vary significantly, even locally, and to which the adhesive response may be very sensitive due to its viscoelastic nature [4]. Furthermore in the numerical modeling of such joints the Poisson ratio is required as an input parameter and the question arises as to what extent this ratio is a constant or depends on loading type and rate.

Originally, the Poisson ratio was defined as a constant value for elastic, isotropic materials, linking the transverse to the longitudinal deformations upon uniaxial loading [5]. The ratio may vary between -1 and 0.5 for linear, isotropic materials and within this range macroscopically homogeneous materials normally exhibit values between 0.2 and 0.5 [6]. However, experimental evidence has also shown values below and above this first interval, mainly due to structural effects in foam-like or porous materials [7, 8, 9] or anisotropic composites [10, 11, 12, 13]. Most of the investigations concerning the Poisson ratio have been based on tensile loading and thus values based on compressive loading are rare, e.g. [14, 15].

In the case of viscoelastic materials, such as adhesives and elastomers, that exhibit time- and temperature-dependent material properties, the Poisson ratio is no longer constant but varies with time and temperature [16, 17, 18]. Mechanisms that soften the polymer, such as viscoelastic flow (i.e. creep or relaxation [18, 19, 20]) or increasing temperature [21], increase the Poisson ratio which then tends towards the 0.5 limit of an incompressible fluid [22]. The ratio is thus particularly loading rate-dependent and increases with decreasing loading rate [23]. Furthermore, in necking regions exhibiting higher strain rates, a corresponding decrease of the Poisson ratio has been observed [23].

In this work, a ductile acrylic structural adhesive used to develop ductile joints in timber structures is investigated. The viscoelastic material is subjected to different loading types (tension and compression) and different displacement rates in the joint. In order to mechanically characterize the adhesive, the quasi-static tensile and compressive behavior under different displacement rates was experimentally investigated, also taking large non-linear strain development into account. It was of primary interest to understand the effect of the loading type, the displacement rate and the associated highly non-linear response on the Poisson ratio, which is required for subsequent numerical modeling of the joint behavior.

2.2. Experimental set-up and instrumentation

2.2.1. Material and specimen fabrication

The investigated material is a two-component, fast-curing commercial acrylic adhesive (SikaFast5221NT), which is based on ADP (Acrylic Double Performance) technology and provided by Sika Schweiz AG. The two components (SikaFast5221NT and SikaFast5200) are mixed at a ratio of 10:1 (by volume), using a suitable mixing gun for the adhesive application. The adhesive is highly deformable and exhibits a ductile behavior [2].

The specimens for tension loading were fabricated according to ASTM D638 [24] using aluminum molds. A dog-bone shape of 165-mm length by 13-mm width and thickness of 3 mm was selected and aluminum tabs covered with sand paper were glued to the specimen ends to prevent grip failure and slippage, see Fig. 2.1. The specimens for compression loading were based on ASTM D695-96 [25], with a square cross section of 12.7 mm and a height of 25.4 mm, see Fig. 2.2. A plate of 12.7-mm thickness was produced and the compressive specimens were cut using a water-jet cutting machine. Furthermore, three rectangular-shaped specimens with dimensions 35x10x3 mm were fabricated for Dynamic Mechanical Analysis (DMA) investigations in a single-cantilever beam configuration according to ASTM E1640 [26]. After fabrication, all specimens were cured for 24 hours under ambient laboratory conditions ($21\pm 3^\circ\text{C}$ and $38\pm 10\%$ relative humidity) and then post-cured at 50°C for seven days to obtain fully cured specimens.

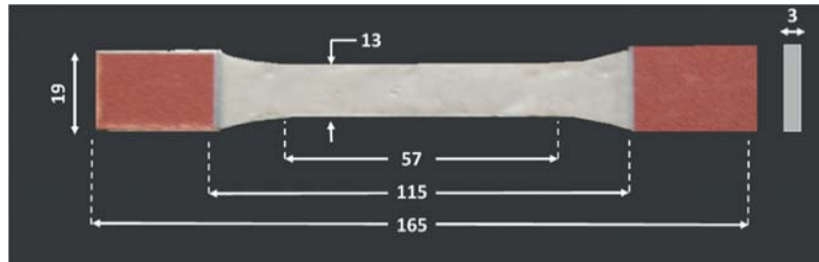


Figure 2.1: Tensile specimen (ASTM D638)

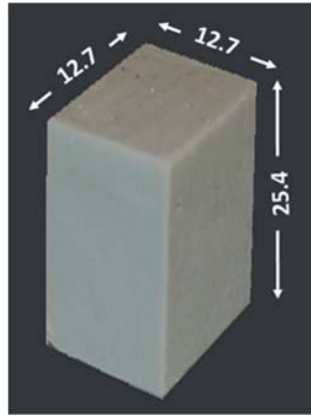


Figure 2.2: Compressive specimen (ASTM D695-96)

2.2.2. Experimental program and instrumentation

Three DMA experiments were performed using a TA Instruments Q800 thermodynamic mechanical analyzer (DMA) to obtain the glass transition temperature, T_g , storage modulus, E' , and loss modulus, E'' . All experiments were run from -100°C to $+100^\circ\text{C}$, at a rate of $1^\circ\text{C}/\text{min}$, an amplitude of $15\mu\text{m}$ and a frequency of 1Hz.

An MTS 810 Landmark testing frame with a 2.5-kN load cell was used for the tensile experiments and a W+B 250-kN capacity testing machine for application of the compressive loading by using two parallel plain steel plates, covered with Teflon sheets to reduce friction. All experiments were conducted under ambient laboratory conditions using displacement-control mode. The tensile specimens were loaded up to failure. Since no failure occurred in compression, all experiments were stopped at a displacement of $d=20$ mm, corresponding to 80% of the initial specimen height.

Five different displacement rates were selected for each type of experiment, ranging around the rates recommended by the standards (5 mm/min \pm 0.25% for tension [24] and 1.3 mm/min \pm 0.25% for compression [25]), so that failure would occur within 0.5 to 5 minutes. In tension 2, 10, 50, 100 and 200 mm/min were applied and in compression 0.2, 2, 5, 10, and 20 mm/min. Three specimens were investigated at each displacement rate; they were labeled according to the material (A for Acrylics), type of loading (T or C for tension or compression), rate of displacement applied (e.g. 10 for 10 mm/min) and designation of the specimen (a, b or c). The complete experimental matrix, which includes 15 tensile and 15 compressive specimens, is shown in Tables 2.1 and 2.2. Also indicated are the engineering strain rates which correspond to the displacement rates.

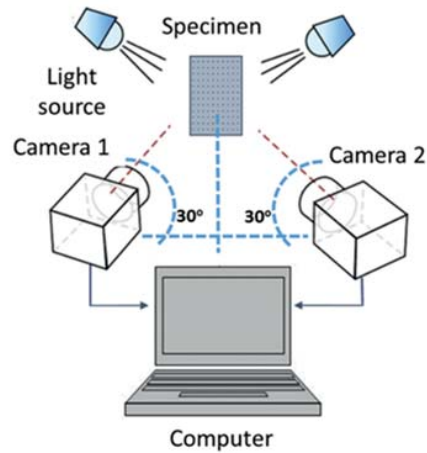


Figure 2.3: Experimental set-up for Digital Image Correlation (DIC)

The load and specimen displacements were obtained from the machine readings. Furthermore, the full 3D strain field was measured on one surface of each specimen using a Digital Image Correlation (DIC) System. As schematically shown in Fig. 2.3, this system includes two digital cameras focused symmetrically on the measurement area at $\pm 30^\circ$. Detailed information about the DIC system is given in [27, 28]. A random pattern of black speckles of similar size was sprayed on all specimens, allowing the DIC to track their relative displacement during the experiment. Different image recording frequencies, between 0.01 Hz and 5 Hz, were selected according to the applied displacement rates. The displacement at a specific point was calculated based on the average displacement of the speckles in a square area (centered on the selected point), which is defined by the filter and step size and approximately corresponds to 12 mm x 12 mm for tension and 3.5 mm x 3.5 mm for compression. Each deformed image was correlated with the initial undeformed image and the resulting displacement fields were smoothed and processed to obtain strain data. The accuracy of the measurements, based on the 68% confidence intervals at the failure load level [28], is ± 0.01 mm for displacements and ± 0.001 for strains and for the strain-based Poisson ratio.

2.3. Experimental results

2.3.1. DMA experiments

The DMA curves shown in Fig. 2.4 indicate that the onset of the glass transition temperature is $T_{g,onset} = 43^\circ\text{C}$, if the storage modulus is considered (defined as the point of interception of the two tangents) or $T_{g,tan\delta} = 68^\circ\text{C}$ according to the peak of the $\tan\delta$ curve. Although the transition zone was broad, the adhesive was considered to be in the glassy state at laboratory temperature ($21 \pm 3^\circ\text{C}$).

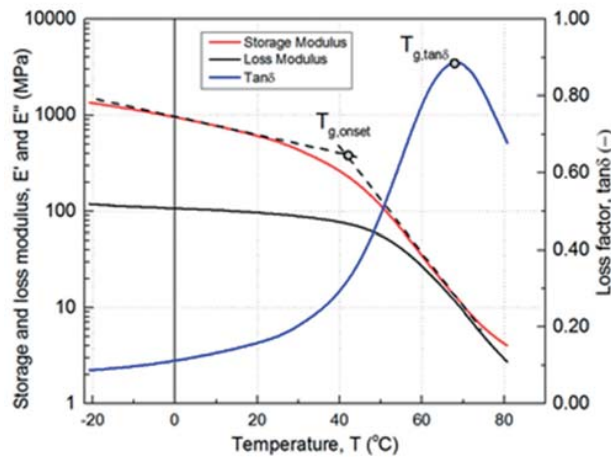


Figure 2.4: DMA results for SikaFast 5221NT

2.3.2. Tension experiments

Typical tensile load vs displacement responses for each displacement rate, obtained from the machine measurements, are shown in Fig. 2.5. Also indicated are the corresponding engineering stresses and strains. The material exhibited a non-linear behavior, with an initial stiffer response up to a local maximum, referred to as yield load. For different loading rates, different yield loads and post-yield behaviors could be observed. The yield load significantly increased with higher displacement rates; however, the corresponding displacement was almost rate-independent, i.e. at around 10 mm. Above the yield point, the stiffness decreased at higher rates until failure occurred. At lower rates, however, the stiffness started increasing again up to a second higher peak before failure. The displacement at failure significantly increased with decreasing displacement rates. All the aforementioned results are summarized in Table 2.1, including the yield load, L_y , the corresponding displacement, d_y , the failure load, L_{fail} and the corresponding maximum displacement, d_{fail} , including the corresponding engineering stresses and strains.

Two different failure modes were observed. At lower displacement rates, large deformations and uniform stretching of the adhesive occurred until failure, while for higher rates, much smaller deformations were observed, accompanied by the formation of necking at one or more locations along the length, inducing failure at one of these locations, as shown in Fig. 2.6.

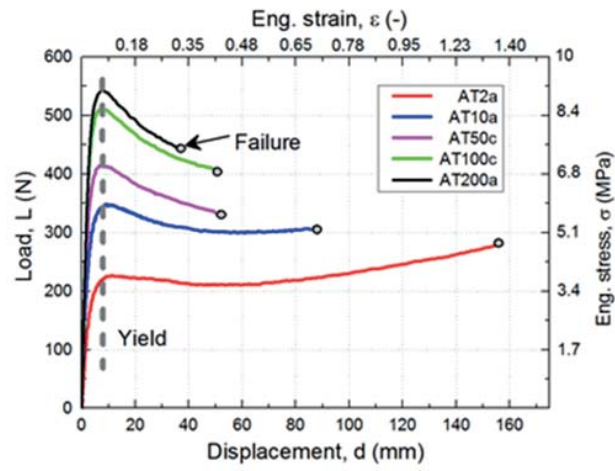


Figure 2.5: Typical load and engineering stress vs (machine) displacement and engineering strain curves in tension for all displacement rates

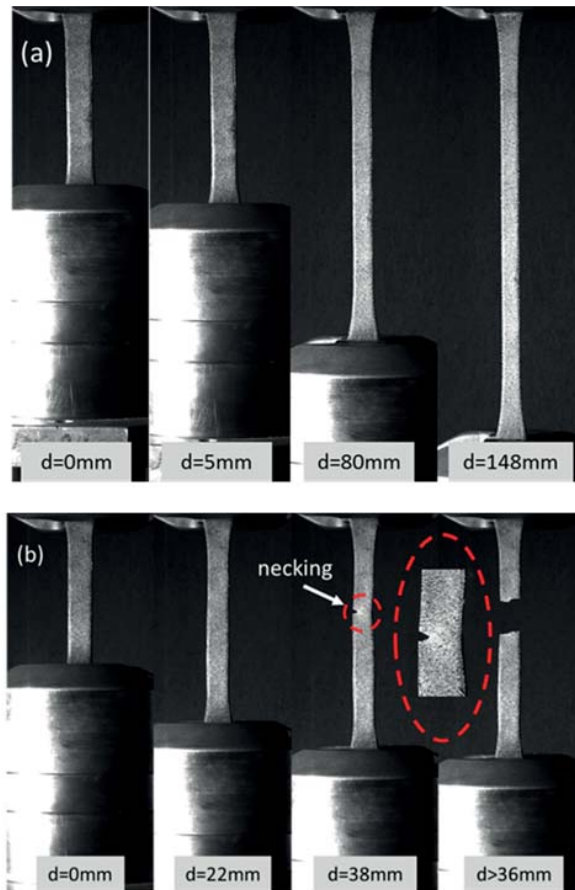


Figure 2.6: Typical deformation and failure modes in tension (a) uniform stretching (AT2a) and (b) necking (AT200a)

Table 2.1: Experimental results in tension

Specimen	Displ. rate r (mm/min)	Eng. strain rate $\dot{\epsilon}$ (min^{-1})	Yield				Failure				
			Load L_y (N)	Eng. stress σ_y (MPa)	Displ. d_y (mm)	Eng. strain ϵ_y (-)	Load L_{fail} (N)	Eng. stress σ_{fail} (MPa)	Displ. d_{fail} (mm)	Strain ϵ_{fail} (-)	
										(eng.)	(true)
AT2a	2	0.017	228	3.63	11.5	0.06	284	4.55	157	1.57	0.95
AT2b			234	3.54	11.3	0.11	285	4.35	156.8	1.56	0.94
AT2c			224	3.17	12.7	0.13	272	4.01	156.5	1.56	0.95
AT10a	10	0.087	350	5.74	11.2	0.07	300	4.88	88.5	0.88	0.63
AT10b			285	4.54	9.2	0.09	289	4.66	122.9	1.23	0.80
AT10c			330	5.03	11.5	0.09	360	5.47	152.0	1.52	0.92
AT50a	50	0.435	432	6.65	8.9	0.08	359	5.57	97.4	0.96	0.67
AT50b			412	6.34	7.2	0.09	353	5.33	98.8	1.02	0.69
AT50c			415	6.54	7.6	0.05	334	5.13	50.7	0.51	0.42
AT100a	100	0.870	487	7.44	8.2	0.08	335	6.86	50.6	1.44	0.90
AT100b			497	7.49	6.1	0.08	402	6.37	89.8	0.92	0.65
AT100c			512	8.36	7.7	0.05	401	6.38	52.3	0.53	0.42
AT200a	200	1.739	545	8.84	7.3	0.05	442	7.14	36.5	0.36	0.31
AT200b			511	7.80	7.6	0.06	402	5.98	59.7	0.60	0.47
AT200c			543	8.14	8.2	0.07	430	6.15	62.2	0.64	0.50

2.3.3. Compression experiments

Representative compressive load vs displacement responses are shown in Fig. 2.7 for all the displacement rates, as derived from the machine. Again indicated are the corresponding engineering stresses and strains. Three different segments could be observed in the curves: an initial stiff part up to the yield point, a second part with reduced stiffness and larger deformations from the yield point up to a point of inflection, above which the third part of the curve exhibited a significant increase in stiffness. The yield point was defined as the vertically projected point of interception of two tangents fitted to the first two segments. The inflection point was defined as the point where the curvature of a 3rd degree polynomial curve, fitted to the second and third segments, changed from negative to positive. Similarly to tension, all the characteristic load levels of the curves (L_y , L_{inf} , $L_{0.5}$) increased with higher displacement rates, while the yield and the inflection displacements, d_y and d_{inf} , remained almost unaffected.

All the results are summarized in Table 2.2, i.e. the yield load, L_y , and displacement, d_y ; the load at the inflection point, L_{inf} , and the displacement, d_{inf} , and the load, $L_{0.5}$, at the level of displacement, $d_{0.5}=12.5\text{mm}$, where the specimen was compressed to half of its initial height (25.2 mm). In addition, corresponding engineering stresses and strains are shown. The latter was used as reference displacement to compare the specimens at large deformations, shortly before the experiments were manually stopped, since no failure occurred. Only non-uniform convex and concave lateral deformations were observed, caused by the specimen crushing, as shown in Fig. 2.8.

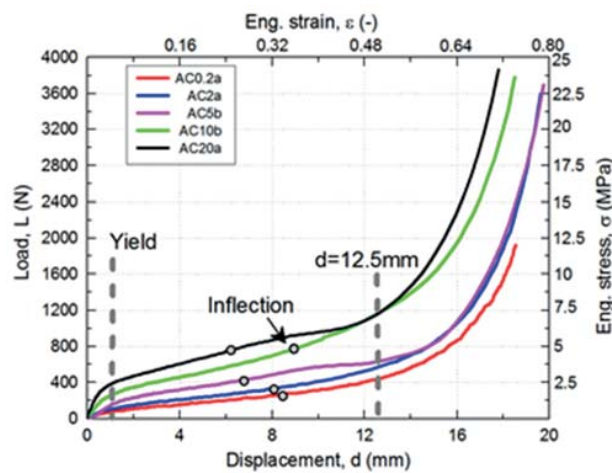


Figure 2.7: Typical load and engineering stress vs (machine) displacement and engineering strain curves in compression for all displacement rates

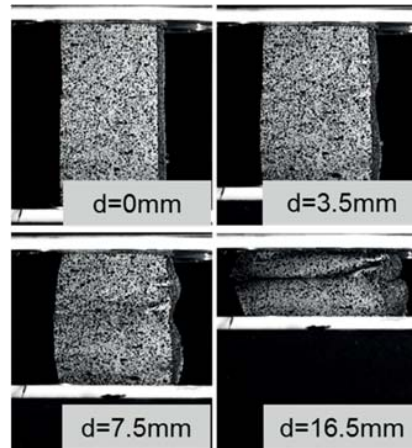


Figure 2.8: Typical non-uniform lateral deformations at high displacements in compression, AC2a ($d_y=0.85$ mm, $d_{inf}=8.00$ mm)

2.4. Discussion

2.4.1. Engineering vs true strains

The acrylic adhesive used in this study was highly deformable. Nominal or engineering strains, which are based on the nominal, i.e. initial, dimensions of the specimen, do not take such geometrical changes into account – in contrast to true strains. In structural design, e.g. in the finite element analysis of the above mentioned adhesively-bonded ductile timber joints, it is important to correctly input the material behavior, i.e. true stress-strain curves in this case. According to Hencky's definition, the true strain at each load step is calculated with respect to the previous specimen length, as follows [29]:

$$\varepsilon_1 = \int_{l_0}^l \frac{dl}{l} \quad (1)$$

where ε_1 is the principal true strain, l_0 is the initial length of the specimen, l is the length at which the strain is calculated and dl is the infinitesimal change in the length during the load step. Figure 2.9 illustrates the resulting differences in the load-strain responses if true or engineering strains are used, in tension and compression, at the same strain rate of 0.08min^{-1} (which corresponds to displacement rates of 10 and 2 mm/min, in tension and compression). It has to be noted that the strains shown here were obtained from the machine displacements and thus represent an average of the effectively non-uniform strain distribution in the specimen. In tension, the true strains were smaller than the engineering strains, because of the continuous increase in the length of the specimen, while in compression the opposite occurred. In both cases, however, the curves only started to diverge after the yield point (- the tension curves overlap -) and the differences increased with increasing load. The point of inflection in the compressive curves thus also shifted to higher values.

Table 2.2: Experimental results in compression

Specimen	Displ. rate r (mm/ min)	Eng. strain rate $\dot{\epsilon}$ (min^{-1})	Yield				Inflection				Load at 12.5mm $L_{0.5}$ (N)	
			Load L_y (N)	Eng. stress σ_y (MPa)	Displ. d_y (mm)	Eng. strain ϵ_y (-)	Load L_{inf} (N)	Eng. stress σ_{inf} (MPa)	Displ. d_{inf} (mm)	Strain ϵ_{inf} (-)		
AC0.2a	0.2	0.008	60	0.37	0.8	0.03	260	1.61	8.5	0.33	0.44	430
AC0.2b			80	0.50	0.8	0.03	300	1.86	7.9	0.31	0.48	535
AC0.2c			60	0.37	0.6	0.03	238	1.48	8.3	0.33	0.59	400
AC2a	2	0.079	100	0.62	0.9	0.03	320	1.98	8.0	0.31	0.39	570
AC2b			80	0.50	0.9	0.03	357	2.21	10.5	0.41	0.55	385
AC2c			110	0.68	0.4	0.02	415	2.57	8.0	0.31	0.45	690
AC5a	5	0.197	200	1.24	1.3	0.05	545	3.38	8.2	0.32	0.51	610
AC5b			200	1.24	0.6	0.02	600	3.72	6.6	0.26	0.54	1150
AC5c			190	1.18	0.6	0.02	630	3.91	7.7	0.26	0.35	1150
AC10a	10	0.394	140	0.87	1.0	0.04	600	3.72	7.5	0.30	0.52	1290
AC10b			200	1.24	0.7	0.03	780	4.84	8.8	0.35	0.55	1125
AC10c			200	1.24	0.6	0.02	670	4.15	8.6	0.34	0.43	820
AC20a	20	0.787	280	1.74	0.5	0.02	990	6.14	6.3	0.42	0.61	1150
AC20b			145	0.90	0.5	0.02	(413)*	(2.56)*	(7.6)*	(0.30)*	(0.45)*	-
AC20c			150	0.93	0.5	0.02	580	3.60	8.0	0.31	0.57	950

Since the differences between engineering and true strains were significant, the load-displacement curves for all displacement rates (Figs. 2.5 and 2.7) were converted to load-true strain curves, as shown in Figs. 2.10 and 2.11, which served as the basis for the subsequent derivations. The curve shapes and rate-dependent sequences did not change in relation to Figs. 2.5 and 2.7. It should be further noted that the true strain rate also decreased when the specimen deformation was taken into account, as shown in Fig. 2.12 for the tension case. The engineering strain rate was independent of the true strain while the true strain rate decreased with increasing true strain, i.e. the higher the rate, the larger the difference between nominal and true strain rate.

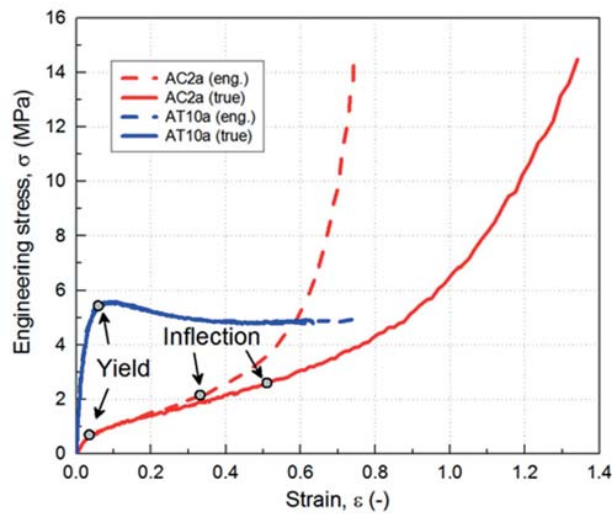


Figure 2.9: Comparison of engineering stress vs engineering and true strains in tension (AT10a) and compression (AC2a), at same strain rate of 0.08 min^{-1} (strains derived from machine displacements)

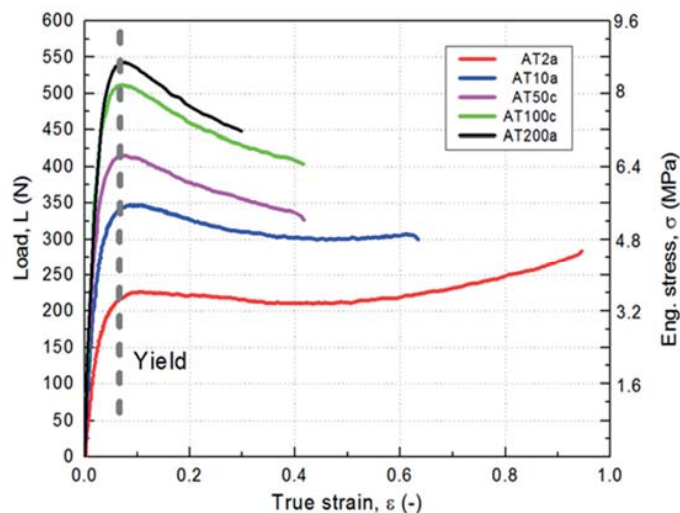


Figure 2.10: Typical load and engineering stress vs true strain curves in tension for all displacement rates (strains derived from machine displacements)

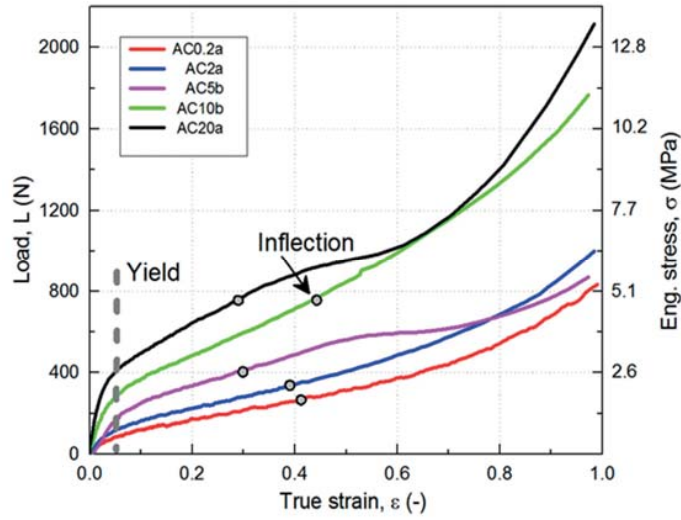


Figure 2.11: Typical load and engineering stress vs true strain curves in compression for all displacement rates, up to 1.0 strain (strains derived from machine displacements)

2.4.2. Poisson ratio based on engineering or true strains

In the following it is investigated, to what extent the Poisson ratio changes if the value is based on engineering or true strains. The complete strain fields measured by the DIC in the local x and y directions (defined in a tangential plane to the deformed surface and thus taking z deformations into account [28]) were transformed by the software into principal strains, ϵ_1 and ϵ_2 (again in a tangential plane to the deformed surface). The Poisson ratio was then calculated as $\nu = \epsilon_2 / \epsilon_1$ and thus excludes the effect of shear deformations (which in this study were anyway small under uniaxial loading).

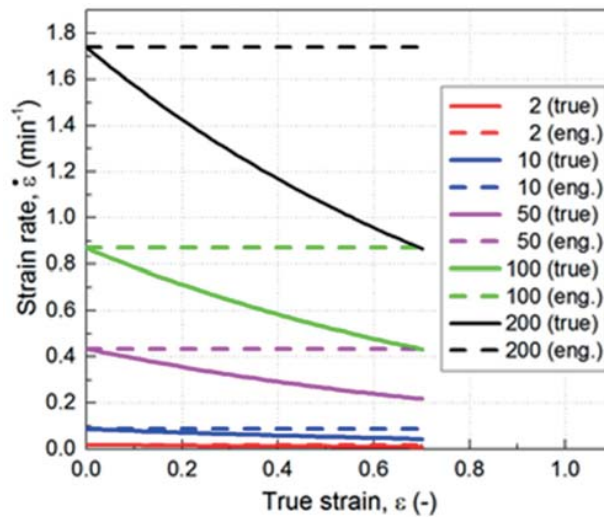


Figure 2.12: Comparison of engineering and true strain rates vs true strain (strains derived from machine displacements)

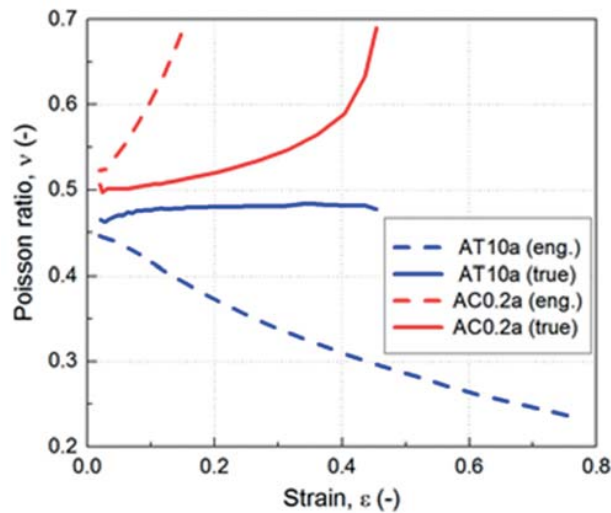


Figure 2.13: Poisson ratio based on engineering and true strains in tension (AT10a) and compression (AC0.2a), in the non-linear part (strains derived from DIC measurements)

The resulting Poisson ratios based on engineering and true strains, in tension and compression, are shown in Fig. 2.13 for two selected nominal strain rates. The ratios are average values calculated by the software taking all data points of the whole measured area of the tension specimens into account, while in the compact compression specimens only 2/3 of the height was considered to exclude the support regions where the values were affected by the support conditions. In tension, the Poisson ratio decreased with increasing engineering strain, while it remained almost constant with increasing true strain. In compression, however, the ratio sharply increased with increasing engineering strain while a moderate increase was obtained after a short plateau with increasing true strain. In both cases, the engineering and true strain curves already started diverging at very low strains and the differences increased with increasing strain.

A full-map illustration of the calculated Poisson ratio along the surface of a selected tensile specimen, based on engineering and true strains, is shown in Fig. 2.14 at different true strain levels (see Fig. 2.10). The figure clearly depicts the decrease of the ratio with increasing strain when engineering strains are considered. The true strain-based values however remain constant, although small fluctuations are visible on the surface, which decrease with increasing strain however. The corresponding principal strains ε_I and ε_{II} for the case of $\varepsilon_{true} = 0.4$ (i.e. engineering strains $\varepsilon_{eng} = 0.49$, load $L = 209.3$ kN) are shown in Fig. 2.15, illustrating the differences between true and engineering strains. Since the effect of the specimen deformation on the Poisson ratio was obviously significant, only true strains are considered in the following discussion.

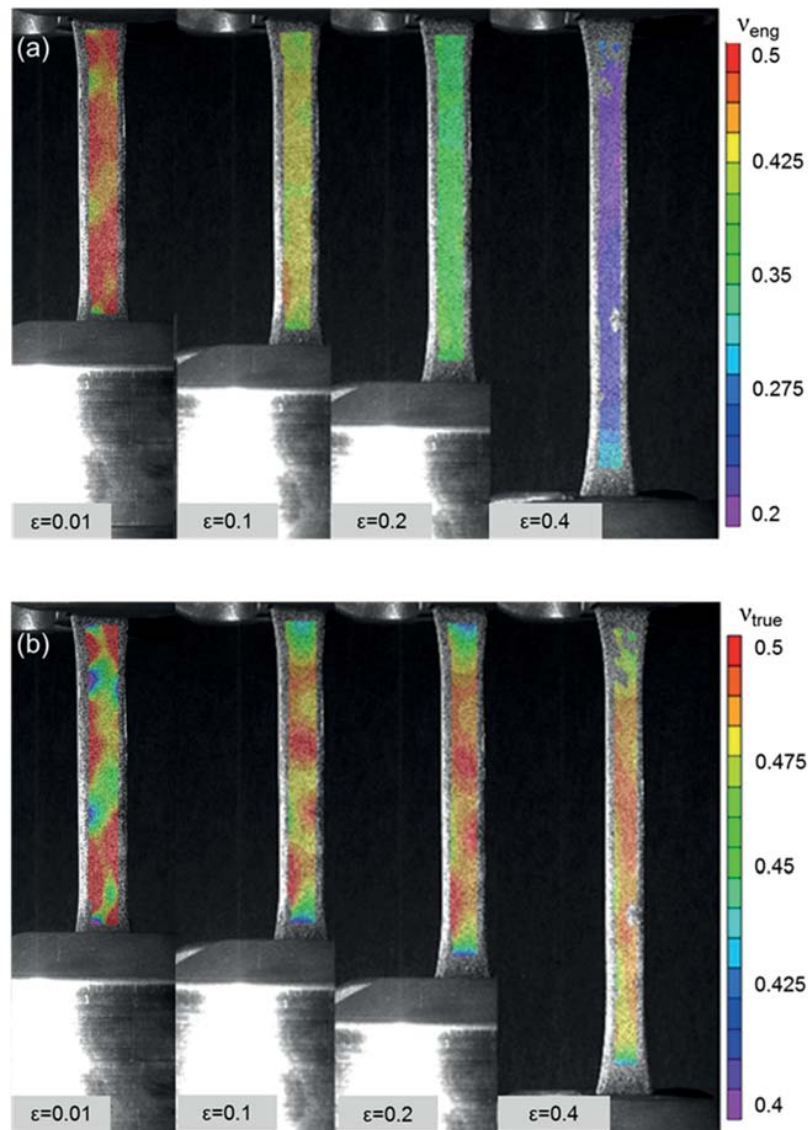


Figure 2.14: Surface distribution of Poisson ratio based on (a) DIC engineering and (b) DIC true strains (AT2a) at different machine true strain levels

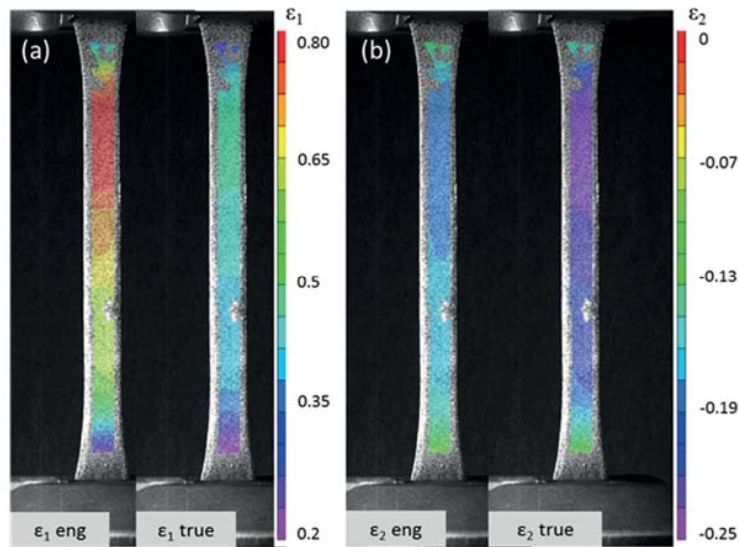


Figure 2.15: Surface distribution of DIC engineering and true principal strains, a) ϵ_1 and b) ϵ_2 , in tension (AT2a), at load = 200.9 N and $\epsilon_{eng} = 0.49$, $\epsilon_{true} = 0.4$ (machine)

2.4.3. True strain Poisson ratio in tension

The average Poisson ratio vs true strain relationships of selected representative specimens in tension are shown in Fig. 2.16 for all displacement rates. The curves exhibited an increasing trend up to strains slightly exceeding the yield point strains and subsequently exhibited a plateau between 0.47 and 0.49, confirming ratios found in literature for other acrylics [22]. Within this plateau, the values were slightly displacement rate-dependent, i.e. a small but consistent increase of 2 to 3% occurred when the rate decreased from 200 to 2 mm/min. This result is in accordance with observations mentioned above that viscoelastic softening increases the ratio. Since the ratio already approached the 0.5 limit however, the effect was small.

The curve at the highest rate (200 mm/min) did not exhibit a plateau as clearly as that seen for the lower rates; the values, which are averages from the whole specimen surface, slightly decreased with increasing true strain. This result could be attributed to the effect of necking on the average values, which was observed at these high rates. In the cross sections exhibiting necking, i.e. a reduction of their area, the strains and thus strain rates increased compared to the unnecked regions [23]. In accordance with the above-observed rate dependency, the ratios thus locally decreased and therefore the average values also decreased at higher strains (when necking occurred). This interpretation was confirmed by a detailed analysis of the Poisson ratio distribution around the necked cross section in Fig. 2.17. The development of the average ratio of four small quadratic areas is shown as a function of the average strain of the whole measured area. Three of the areas (R1-R3) were located outside of the necking region and one of them covered this region. Curves R2 and R3 exhibited a plateau while the curve of the necked region exhibited clearly decreasing values with increasing strain, i.e. propagating necking. Furthermore, the necking effect,

i.e. decrease of strain, already started at strains only slightly above the yield point strain before it could be visually observed. Also shown is the ratio distribution in engineering strains where the ratio differences between necked and unnecked regions are much more significant and thus confirm that the small ratio variations based on true strains were meaningful and not accidental within the scatter of the measurements. Furthermore, also shown is the average curve, which however is calculated from the whole specimen surface and thus does not represent the average of the three quadratic areas.

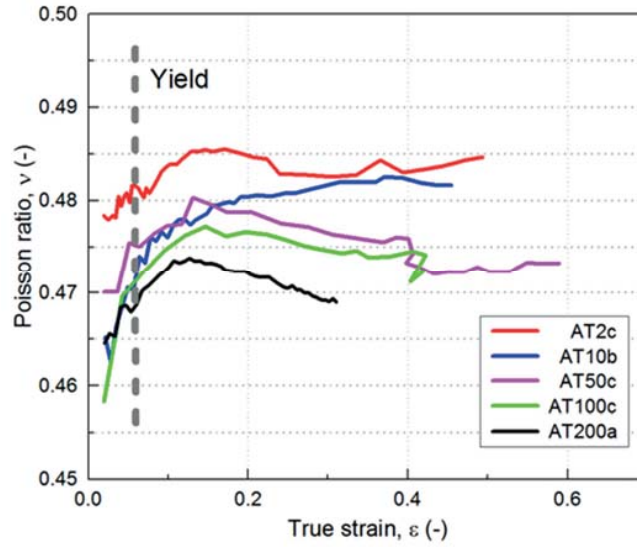


Figure 2.16: Displacement rate effect on Poisson ratio vs (DIC) true strain relationship in tension

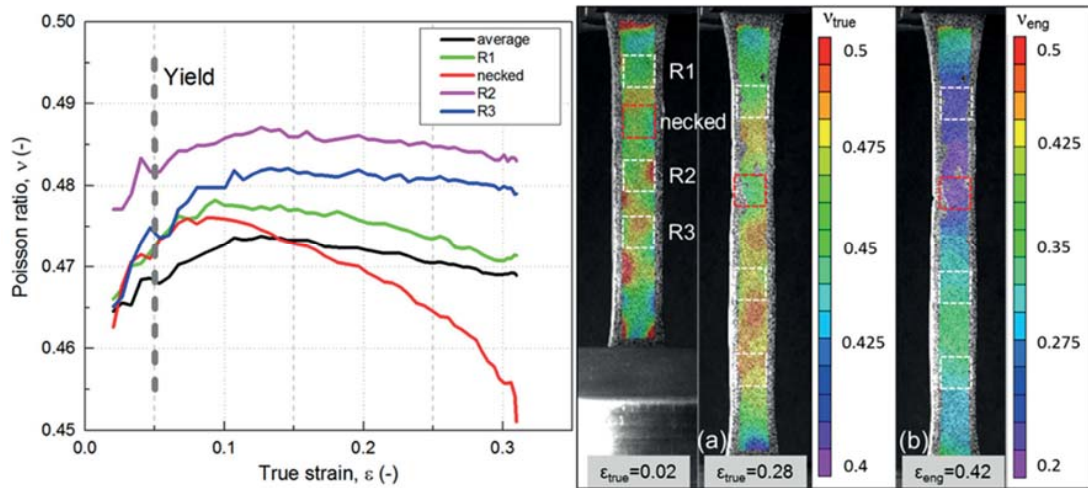


Figure 2.17: Local change in Poisson ratio for DIC true strains, when necking occurs for (a) machine true and (b) machine engineering strain levels (AT200a)

2.4.4. True strain Poisson ratio in compression

The average Poisson ratio vs true strain relationship of selected specimens in compression is shown in Fig. 2.18 for the different displacement rates. The average was calculated over 2/3 of the specimen height as mentioned above. Most of the ratios exceeded the 0.5 value and the curves exhibited a valley, with higher ratios below the yield point strain, a minimum at strains slightly higher than the yield point strain and subsequently exponentially increasing ratios. The compression results showed much higher variations than the tension results; this may have masked a potential rate dependency, which was not identifiable in compression. The larger variations may be attributed to the much more compact specimens and the out-of-plane deformations mentioned above.

A more detailed analysis revealed the effect of the out-of-plane deformations on the Poisson ratio, as shown in Fig. 2.19 for the same specimen as in Fig. 2.8. The average Poisson ratio development of two small square areas, one in a convex and one in a concave surface region, is shown and compared to the average ratio of the whole measured surface. The strain values on the x-axis are the average values of the whole measured surface. The resulting ratios of the convex region were clearly above the 0.5 limit and continuously increased, while the values of the concave region were below 0.5 and steadily decreased, with both trends already starting at the yield point strain. The values in the convex region were higher than the values in the concave region due to the higher strains transverse to the load direction. Furthermore, the rate of increase in the convex regions was much higher than the rate of decrease in the concave regions, as the distribution along the line L_i shows in Fig. 2.20, which is why the average values shown in Fig. 2.18 were above the 0.5 limit. These differences were correlated to the out-of-plane deformations, as shown in Fig. 2.21. The deformations in z direction rapidly increased in the convex regions, but remained quite stable in the concave regions. It should be noted that out-of-plane deformations already existed in the pre-yield-point phase, at $\varepsilon = 0.02$.

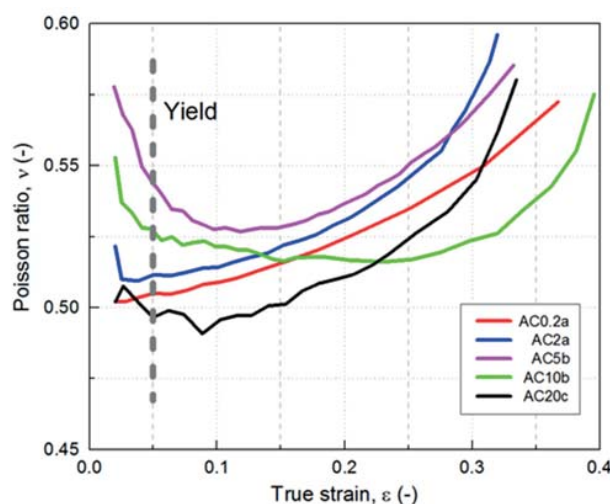


Figure 2.18: Displacement rate effect on Poisson ratio vs (DIC) true strain relationship in compression

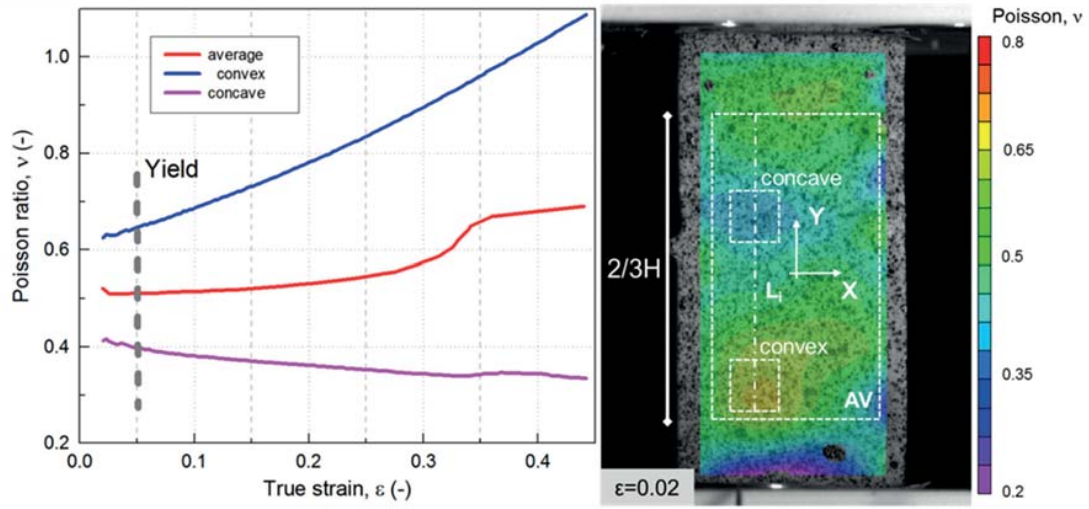


Figure 2.19: Effect of convex or concave curvature on Poisson ratio in compression (AC2a) for DIC true strains

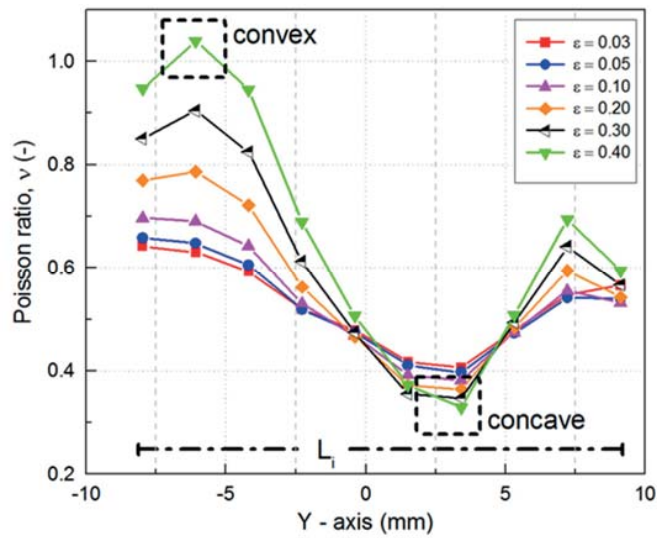


Figure 2.20: Poisson ratio distribution in compression along inspection line L_i of Fig. 2.19 at different machine true strain levels

2.4.5. Comparison between Poisson ratio in tension and compression

The true strain-based Poisson ratios at the different nominal strain rates, in tension and compression, are shown in Fig. 2.22. Based on the above results, average values and standard deviations for all 30 specimens are compared at two distinct true strains in tension, $\epsilon = 0.03$ and 0.20 , and in compression at $\epsilon = 0.03$. The lower strain value is below the yield point strain (0.05 on average) and the higher is clearly above. The values shown are averages of the whole specimen surface in tension and of $2/3$ of the surface in

compression, as explained above. For comparative reasons, all rates have been normalized to the maximum rate applied, 200 mm/min and 20 mm/min respectively for tension and compression.

The tension values exhibited only small variations and therefore two clear observations could be made: 1) the pre-yield-point values were strain level-dependent, i.e. always slightly lower than the post-yield-point values, and 2) the values were rate-dependent, i.e. slightly decreasing with increasing nominal displacement rate. In compression, all values exhibited large variations for the above-mentioned reasons. The pre-yield-point values were much higher than the corresponding tension values and clearly exceeded the 0.5 limit. No rate dependency could be seen due to the large variations.

In both tension and compression, two effects on the Poisson ratio occurred which were visually manifested by changes in the cross section geometry along the specimen length, i.e. necking in tension at higher rates and crushing in compression independent of the rate. Both effects may be attributed to changes in the molecular structure of the polymer, which are facilitated at strains above the yield point due to the loss of the secondary bonds between the molecular chains. In the tension case, an alignment of the chains in the load direction in the reduced necking section is conceivable while in the compression case buckling and kinking of the flexible chains are probable. However, these mechanisms on the molecular level could not be directly observed in this study.

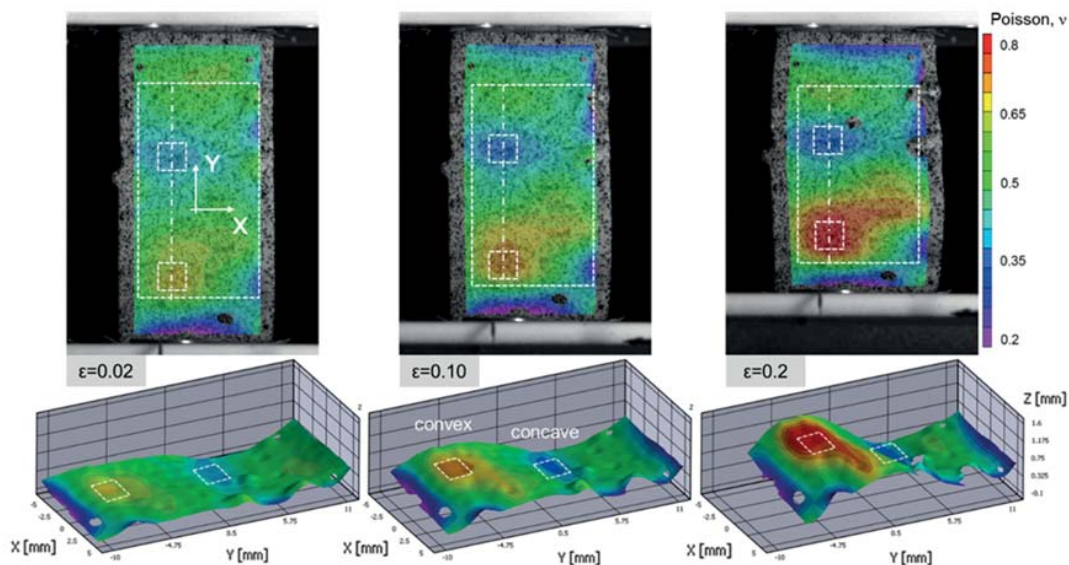


Figure 2.21: Non-uniform distribution of Poisson ratio and out-of-plane deformation in compression (AC2a) at different machine true strain levels

The Poisson ratio may thus have been affected by such structural effects, which also led to the exceeding of the 0.5 value in compression, as observed in other works cited above. In compression in particular, the

out-of-plane deformations already occurred at pre-yield-point strains. The Poisson ratios were thus affected by these structural effects from the beginning.

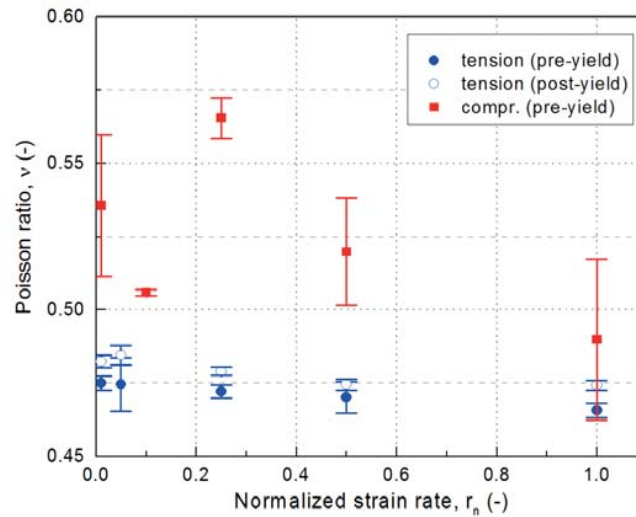


Figure 2.22: Comparison of strain rate effect on Poisson ratio in tension and compression

2.5. Conclusions

An experimental study was conducted on a ductile acrylic structural adhesive to investigate potential effects of the type of loading, i.e. tension or compression, and the displacement rate on the Poisson ratio of this non-linear viscoelastic polymer. The following conclusions were drawn:

- Subjected to tension, the Poisson ratio showed a slight dependency on the true strain level below the yield point strain; above this value, the ratio remained constant and thus independent of the true strain. Furthermore, a slight displacement rate dependency was observed, i.e. slightly increasing ratios with decreasing rate. The rate dependency was confirmed in regions with necking, where the increased rate resulted in a locally decreased Poisson ratio. Since all these effects were small, the Poisson ratio in tension may be approximated by a constant value of 0.48 for this adhesive.
- In compression, the Poisson ratio was affected from the beginning of loading by out-of-plane deformations of the specimens and thus already exhibited values above 0.5 at pre-yield-point strains.
- The observed necking in tension and out-of-plane deformations in compression may be attributed to changes in the molecular structure, i.e. alignment of the chains in tension and buckling or kinking in compression, and thus designated as structural effects on the Poisson ratio.
- In the applications envisaged in this work, i.e. adhesively-bonded lap joints and their numerical modeling, the results of this study can be used as long as they are not affected by these structural effects.

References

- [1] Keller T, De Castro J. System ductility and redundancy of FRP beam structures with ductile adhesive joints. *Composites Part B* 36/8 (2005) 586-596.
- [2] De Castro J, Keller T. Ductile double-lap joints from brittle GFRP laminates and ductile adhesives. Part I: Experimental investigation. *Composites Part B* 39/2 (2008) 271-281.
- [3] De Castro J, Keller T. Design of robust and ductile FRP structures incorporating ductile adhesive joints. *Composites Part B* 41/2 (2010) 148-156.
- [4] Santarsiero, M. (2015). Laminated connections for structural glass applications. Thesis Dissertation No 6828, École Polytechnique Fédérale de Lausanne (EPFL).
- [5] Poisson, Siméon-Denis. (1828). Mémoire sur l'équilibre et mouvement des corps élastiques: L'Académie des sciences.
- [6] Fung, YC, & Drucker, DC. (1966). Foundation of solid mechanics. *Journal of Applied Mechanics*, 33, 238.
- [7] Lakes, R. S. (1987). Foam Structures with a Negative Poisson Ratio. *Science*, 235(4792), 1038-1040.
- [8] Alderson, A, & Evans, KE. (1995). Microstructural modelling of auxetic microporous polymers. *Journal of materials science*, 30(13), 3319-3332.
- [9] Smith, C. W., Wootton, R. J., & Evans, K. E. (1999). Interpretation of experimental data for Poisson's ratio of highly nonlinear materials. *Experimental Mechanics*, 39(4), 356-362.
- [10] Akasaka, T. (1989). Flexible Composites. Chou, TW, Ko, F, Elsevier Science Publishers, 279-330.
- [11] Clark, Samuel Kelly. (1963). The Plane Elastic Characteristics of Cord—Rubber Laminates. *Textile Research Journal*, 33(4), 295-313.
- [12] Chou, T. W. (2005). Microstructural design of fiber composites: Cambridge University Press.
- [13] Peel, Larry D, & Jensen, David W. (2000). Nonlinear Modeling of Fiber-Reinforced Elastomers and the Response of a "Rubber Muscle" Actuator. *Papers - American Chemical Society, Division of Rubber Chemistry* (30).
- [14] Qamar, S. Z., Akhtar, M., Pervez, T., & Al-Kharusi, M. S. (2013). Mechanical and structural behavior of a swelling elastomer under compressive loading. *Materials & Design*, 45, 487-496.
- [15] Zha, C. S., Hemley, R. J., Mao, H. K., Duffy, T. S., & Meade, C. (1994). Acoustic velocities and refractive index of SiO₂ glass to 57.5 GPa by Brillouin scattering. *Physical Review B*, 50(18), 13105.
- [16] Tschoegl, Nicholas W, Knauss, Wolfgang G, & Emri, Igor. (2002). Poisson ratio in linear viscoelasticity—a critical review. *Mechanics of Time-Dependent Materials*, 6(1), 3-51.

- [17] Tscharnuter, D., Jerabek, M., Major, Z., & Lang, R. W. (2011). Time-dependent poisson's ratio of polypropylene compounds for various strain histories. *Mechanics of time-dependent materials*, 15(1), 15-28.
- [18] Pritchard, R. H., Lava, P., Debruyne, D., & Terentjev, E. M. (2013). Precise determination of the Poisson ratio in soft materials with 2D digital image correlation. *Soft Matter*, 9(26), 6037-6045.
- [19] Lakes, R. S. (1992). The time-dependent Poisson's ratio of viscoelastic materials can increase or decrease. *Cell. Polym*, 11, 466-469.
- [20] Lakes, R. S., & Wineman, A. (2006). On Poisson's ratio in linearly viscoelastic solids. *Journal of Elasticity*, 85(1), 45-63.
- [21] McClung, A. J. W., Tandon, G. P., & Baur, J. W. (2012). Strain rate- and temperature-dependent tensile properties of an epoxy-based, thermosetting, shape memory polymer (Veriflex-E). *Mechanics of Time-Dependent Materials*, 16(2), 205-221.
- [22] Greaves, George Neville, Greer, AL, Lakes, RS, & Rouxel, T. (2011). Poisson ratio and modern materials. *Nature materials*, 10(11), 823-837.
- [23] Nitta, Koh-hei, & Yamana, Masahiro. (2012). Poisson ratio and mechanical nonlinearity under tensile deformation in crystalline polymers: INTECH Open Access Publisher.
- [24] American Society for testing and Materials (ASTM) (2010). Standard test method for tensile properties of plastics, D638-94b, Philadelphia, PA, USA.
- [25] American Society for testing and Materials (ASTM) (2010). Standard test method for compressive properties of rigid plastics, D 695-96, Philadelphia, PA. ASTM International.
- [26] American Society for testing and Materials (ASTM) (2013). Standard test method for assignment of the glass transition temperature by dynamic mechanical analysis, E1640-13, Philadelphia, PA. ASTM International.
- [27] Sutton, Michael A, Orteu, Jean Jose, & Schreier, Hubert. (2009). Image correlation for shape, motion and deformation measurements: basic concepts, theory and applications: Springer Science & Business Media.
- [28] Correlated Solutions Inc. (2010). Vic-3D Manual. Columbia, SC.
- [29] Hencky, H. (1928). "Über die Form des Elastizitätsgesetzes bei ideal elastischen Stoffen". *Zeitschrift für technische Physik* 9: 215–220.

Chapter 3

Acrylic ductility, recovery and strain rate-dependency

The ductility and time-dependent recovery of a ductile acrylic adhesive were investigated in this work. The quasi-static true tensile and compressive strain behaviors were examined at different strain rates, taking large deformations into account. Yield stress, elastic modulus, and failure strain exhibited a logarithmic dependency on increasing strain rate, while yield strain and stiffness after yielding were insensitive to strain rate. High energy-based ductility indices were obtained compared to traditional materials. The time-dependent recovery after unloading depended on loading type (tension or compression), the strain rate of loading, and the strain at unloading. The delayed recovered strain development was modeled using an existing Weibull-based model for creep recovery. The strain after unloading almost fully recovered after 48h, indicating that no residual deformation caused by damage or plastic flow occurred.¹

Keywords: *adhesives, acrylics, ductility, recovery, strain rate, viscoelasticity.*

¹ Angelidi M., Vassilopoulos A. P., & Keller T. Ductility, recovery and strain rate-dependency of an acrylic structural adhesive. *Construction and Building Materials*, 140, 184-193 (2017).

3.1. Introduction

In building and bridge construction, the field to which this work applies, an essential requirement for structural systems is ductility, which is the ability of a material or structural system to sustain inelastic deformation prior to collapse, without loss of resistance. Such a behavior increases the robustness and structural safety through load distribution in the case of overloading or local failure if the system is redundant.

The easiest way to provide ductility is through the use of ductile materials such as steel or reinforced concrete. If the materials are brittle however, as is the case with fiber-reinforced polymer (FRP) composites and very often also timber, providing ductility is much more difficult. One approach is to develop ductile joints from brittle components, i.e. by using ductile connectors made of steel for example, or by applying ductile structural adhesives. The feasibility of the latter has already been experimentally proven in [1], where a ductile acrylic adhesive was used to join two FRP beams to a continuous two-span beam which then exhibited load redistribution similar to that occurring in an equivalent steel beam.

In elastoplastic materials such as steel, ductility is characterized by a permanent residual deformation after unloading, while in viscoelastic materials, such as structural adhesives, this remaining deformation after unloading partially or completely recovers. A systematic investigation of the potential level of ductility and the recovery behavior of adhesives has not yet been performed. Furthermore, adhesives have a response that is highly dependent on loading rate, which also differs according to whether they are subjected to tensile or compression loading [2, 3, 4].

On the material level, ductility is normally defined as the ratio between the ultimate and yield deformation [5]. On the structural system level, however, this definition is not always accurate and applicable since mechanisms with effects similar to material ductility, designated pseudo-ductility, can also be achieved in systems composed of only brittle materials or components, if the system is redundant [1, 5]. Instead of expressing ductility in terms of deformations, a characterization based on dissipated energy is more appropriate in such cases, i.e. by comparing the dissipated inelastic energy, E_{inel} , and elastic energy, E_{el} , whereby their sum is the total dissipated energy, $E_{tot}=E_{inel}+E_{el}$.

In a stress-strain curve, the inelastic energy corresponds to the area between the loading and unloading curves, while the elastic energy is characterized by the area below the unloading curve, as shown in Fig. 3.1. In the case of viscoelastic materials, where the onset of the reloading path depends on the recovery after unloading, the inelastic energy is further split into the hysteretic energy, i.e. the area between the unloading and reloading paths and the energy attributed to plasticity or damage, i.e. the area between the loading and reloading path, the latter after full recovery [5, 6]. Based on these energy definitions, different ductility indices are proposed in literature, which all comprise different ratios of these energies, e.g. E_{inel}/E_{tot} [7, 8] or E_{tot}/E_{el} [9].

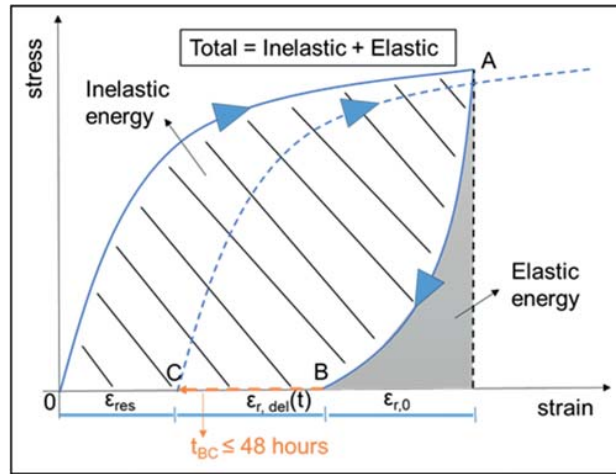


Figure 3.1: Dissipated inelastic and elastic energy and time-dependent recovery (schematic representation)

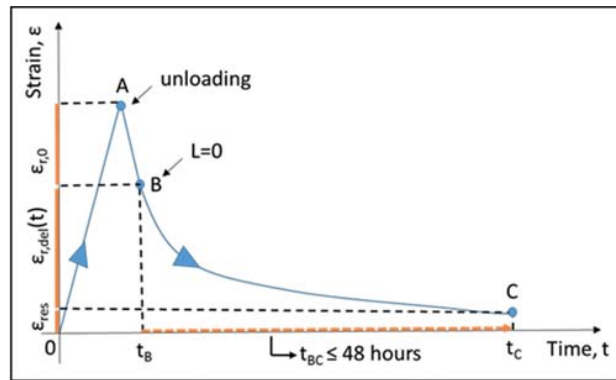


Figure 3.2: Strain recovery after unloading (schematic representation)

Recovery after unloading is a time-dependent process during which the deformed viscoelastic molecular network attempts to recover its initial structure, as shown in Figs. 3.1 and 3.2. In terms of strain, the total recovered strain, $\epsilon_{r,tot}$, is the sum of the instantaneous recovered strain during unloading, $\epsilon_{r,0}$, (path A-B), the delayed recovered strain, $\epsilon_{r,del}(t)$ (path B-C, attaining its maximum level after infinite time, $\epsilon_{r,del}^{\infty}$), and the residual strain, $\epsilon_{r,res}$, if some unrecoverable plastic flow or damage occurred [5].

Concerning the modeling of viscoelastic recovery behavior, an exponentially stretched function was developed by Williams and Watts [10] to represent time-dependent phenomena (mainly relaxation) in amorphous materials, based on the decay function of Kohlrausch [11]. The function has a form similar to that proposed earlier by Weibull [12] for dielectric decay; the latter was then also applied to describe time-dependent creep [13, 14, 15]. Further works focused on the creep-recovery description [16, 17, 18], while [16] was also applied to the model time-dependent recovery of viscoelastic deformations, after unloading, in the web-flange junctions of pultruded FRP bridge decks [5].

This work aims to contribute to a better understanding of the ductile and recovery behaviors of flexible polymers such as acrylic adhesives. Standardized specimens of a commercial acrylic adhesive were subjected to either axial tension or compression loading at different strain rates in order to evaluate the effect of the latter on the true stress-strain behavior, i.e. by also taking large deformations into account. Furthermore, tensile and compressive specimens were subjected to an unloading and reloading cycle, the latter after different periods of recovery. The ductility and recovery behaviors in tension and compression were thus characterized and compared.

3.2. Experimental set-up

3.2.1. Material and specimen fabrication

A commercial structural acrylic adhesive was used in this study. The two-component adhesive (SikaFast 5221NT, from Sika AG) is based on the ADP (Acrylic Double Performance) technology and is fast-curing [19]. The specimens for tension were fabricated according to ASTM D638 [20] in a dog-bone shape and the grip area was reinforced with aluminum tabs. The specimens for compression were manufactured according to ASTM D695-96 [21]; the orthogonal parallelepipeds had a squared cross section of 12.7x12.7 mm² and a height of 25.4 mm.

The specimens were fabricated according to the supplier's specifications, using a suitable mixing gun for application. While aluminum molds were used for the tensile specimens, the compressive specimens were cut using a water jet from plates of 12.7-mm thickness, taking special care to obtain parallel edges for the uniform distribution of the compressive load. The specimen dimensions (total length, width and thickness) were measured using a caliper with an accuracy of 0.01 mm. They were fabricated and cured for 24 hours under ambient laboratory conditions (21±3°C and 38±10% relative humidity) and then post-cured at 50°C for at least four days, after being removed from the molds or cut from the plates, in order to obtain fully cured specimens.

It should be noted that preliminary investigations using dynamic mechanical analysis (DMA), reported in [4], already showed a significant sensitivity of the storage modulus to small temperature variations under laboratory conditions; the onset of the glass transition temperature range occurred at 43°C based on the storage modulus. For this reason, great emphasis was placed on assuring full curing of the specimens and the curing degree was thus validated by preliminary differential scanning calorimetry (DSC) investigations during curing and after post-curing.

3.2.2. Experimental procedure and instrumentation

An MTS 810 Landmark machine equipped with a load cell of 2.5-kN capacity and a W+B 250-kN capacity machine were used for the tensile and compression experiments respectively. All experiments were conducted under ambient laboratory conditions, under displacement-control mode. The ASTM standards for this type of polymer suggest an average rate of 5 mm/min $\pm 0.25\%$ for tension [20] and 1.3 mm/min $\pm 0.25\%$ for compression [21]. In order to investigate the rate dependency, five different displacement rates were selected for each type of experiment, ranging around those recommended by the standards: 0.2, 2, 10, 25 and 50 mm/min. Since the specimen dimensions were different, the displacement rates were converted into engineering strain rates to allow comparisons between tension and compression, see Table 3.1. Tensile and compressive specimens were loaded in one cycle, the former up to failure, the latter, since specimens were crushed and no clear failure occurred, up to a displacement of $d = 20$ mm, corresponding to 80% of the initial specimen height.

The ductility investigation was conducted at one displacement rate, i.e. 2 mm/min. Tensile and compressive specimens were unloaded at the same targeted engineering strain of $\varepsilon = 0.50$ at the same rate of 2 mm/min. They were subsequently reloaded after seven different periods of recovery (1 h, 8 h, 16 h, 24 h, 30 h, 40 h and 48 h) up to failure (tension) or $d = 20$ mm (compression), while their deformation was continuously measured. The targeted unloading strain in tension was more difficult to control than that in compression and varied between 0.40 and 0.70. Since the tensile failure strain varied considerably, unloading could not be performed at a higher strain closer to the failure strain.

Table 3.1: Displacement and strain rates

Displacement rate r (mm/min)	(Eng) strain rate $\dot{\varepsilon}$ (min^{-1})	
	Tension	Compression
0.2	0.002	0.008
2	0.017	0.079
10	0.087	0.394
25	0.217	0.984
50	0.435	1.969

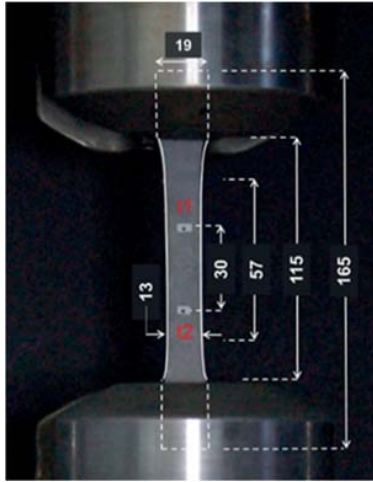


Figure 3.3: Tensile experimental set-up (dimensions in mm)



Figure 3.4: Compressive experimental set-up (dimensions in mm)

In total, 20 specimens each in tension and compression, three per loading rate, were examined, except for the series at a 2 mm/min rate, where all specimens were unloaded and reloaded up to failure. The specimens were labeled accordingly, e.g. AT2b_R1 denotes second specimen (b) in tension (T) at a rate of 2 mm/min and recovery period (R) of 1 hour (if recovery period was applicable).

The tensile load was measured by the load cell of the MTS machine (accuracy $\pm 0.04\%$), while a video-extensometer (accuracy ± 0.1 mm) was used to measure the tensile deformations of a 30-mm distance between two reference dots placed symmetrically with respect to the center of the specimen, see Fig. 3.3. The compressive load was also measured by the machine's load cell (accuracy $\pm 0.5\%$) and a linear variable displacement transducer, (LVDT, accuracy ± 0.02 mm), fixed on the steel plates of the machine, was used to monitor the compressive deformations, see Fig. 3.4. The recovery behavior was continuously measured in tension by the video-extensometer while in compression only periodic measurements with a caliper were possible.

3.3. Experimental results

3.3.1. Differential scanning calorimetry

The results obtained from the DSC investigations are summarized in Table 3.2 and graphically displayed in Fig. 3.5. At laboratory temperature, the adhesive was already 99% cured after the first four hours, as the reaction enthalpy dropped from 174.9 J/g (measured after 3 min) to 2.5 J/g. Nevertheless, it was decided to post-cure the specimens since previous investigations had shown that properties are very sensitive to small changes in the curing degree as full cure is approached [22]. After post-curing, the specimen

exhibited no remaining enthalpy even during the 1st scan. Based on these findings, all specimens were considered to be fully cured before further examination.

Table 3.2: DSC-based curing degree development

Time after preparation (h)	Reaction enthalpy (J/g)		Curing degree (%)
	1 st run	2 nd run	1 st run
0.03	174.9	4.5	0.0
0.50	104.2	3.6	40.4
0.93	71.6	2.6	59.1
4.00	2.5	1.5	98.6
26.0	1.8	1.3	99.0
96.0 (post-cured)	-	-	100.0

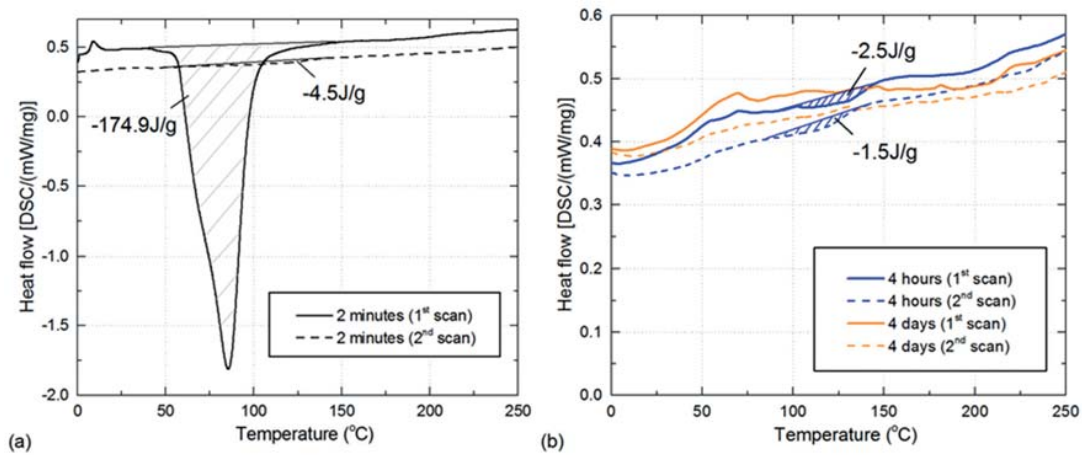


Figure 3.5: DSC scans after a) curing for two minutes, b) four hours and post-curing for four days.

3.3.2. Load-displacement responses

Representative tensile load-displacement curves for all rates are shown in Fig. 3.6. The specimens exhibited an initially almost linear stiff behavior up to a peak load. Subsequently, the load dropped and elongations increased considerably up to failure. Peak and failure loads increased and elongation at failure decreased with increasing strain rate. The specimens were continuously elongating as the load increased, while their cross section became thinner up to failure. At higher rates, i.e. 10 to 50 mm/min, this process was more localized with the development of necking, as shown in the previous work [4].

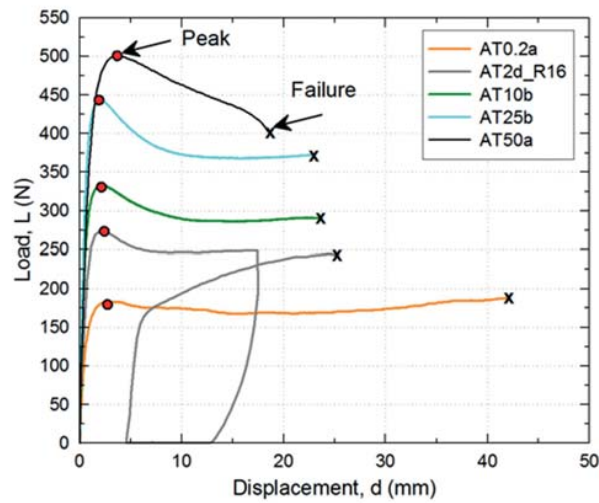


Figure 3.6: Tensile load-displacement responses of selected specimens at all strain rates

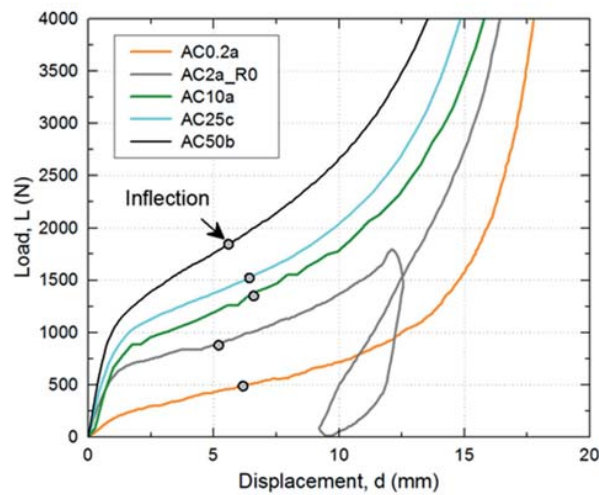


Figure 3.7: Compressive load-displacement responses of selected specimens at all strain rates (curves up to 4-kN load)

Selected load-displacement curves under compression for all rates are shown in Fig. 3.7. After an initially stiff and almost linear response, the stiffness decreased up to a point of inflection and then started increasing again. The curves moved upwards with increasing displacement rate. As mentioned above, the experiments were stopped after 20% of the specimen height was reached, see Fig. 3.8.

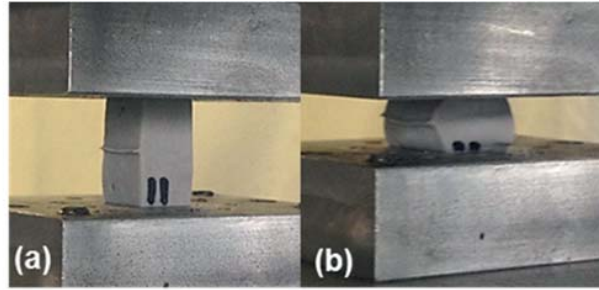


Figure 3.8: Deformation in compression ($d = 12.5$ mm)

3.4. Discussion

3.4.1. True stress-strain relationships

The true stress-strain curves were calculated based on the previous work [4], taking into account the changes in the specimens' dimensions and a constant Poisson ratio of 0.45. A comparison of engineering and true stress-strain curves for the same strain rate of 0.08 min^{-1} (i.e. a displacement rate of 10 mm/min in tension and 2 mm/min in compression) is shown in Fig. 3.9. The responses in compression are only plotted up to $\epsilon_{eng} = 0.5$ ($\epsilon_{true} = 0.95$). In tension, the curve based on the true values exhibited smaller strains and higher stresses compared to the engineering values-based curve, while in compression the opposite was the case. Also, in tension the material exhibited a stiffer response than in compression, although the strain rates were similar. The set-up of the compressive experiments, however, may have caused these differences, i.e. any smallest errors in the parallelism between the specimens' surfaces and the loading plates.

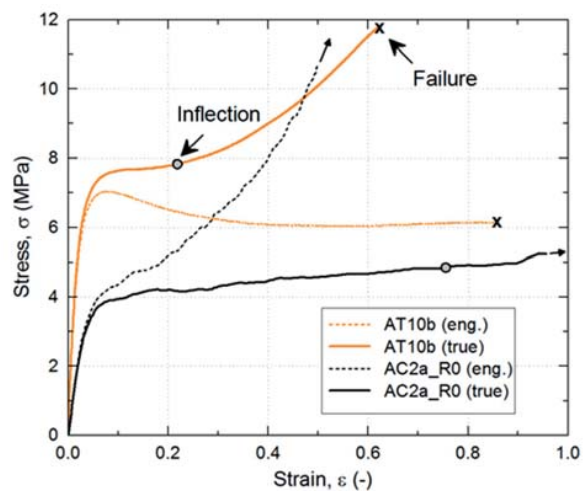


Figure 3.9: Engineering- and true stress-strain curves in tension and compression at same strain rate

Typical true stress-strain curves in tension and compression for all strain rates are shown in Figs. 3.10 and 3.11 respectively. Compared to the tensile load-displacement curves (Fig. 3.6), the true tensile stress-strain curves also exhibited an inflection point, while the inflection point in compression became less obvious. This behavior may be attributed to the molecular chain network, which started losing the secondary bonds as the yield point was approached and the network flexibility thus increased and stiffness decreased. This enabled the chains to rearrange their position and they started aligning to the force direction in tension, which was expressed as an increasing stiffness beyond the inflection point. In compression, the chains started buckling beyond the yield point, which delayed the subsequent increase of stiffness caused by the densification of the network, as confirmed by the much higher strains at the inflection point than in tension.

In order to describe and compare the stress-strain curves, the following mechanical properties were defined, see Fig. 3.12: elastic modulus, E_1 , modulus after yield, E_2 , yield point (σ_y, ϵ_y) and inflection point ($\sigma_{infl}, \epsilon_{infl}$). The elastic modulus, E_1 , was defined in the linear part as the secant modulus between $\epsilon = 0$ and $\epsilon = 0.02$. The inflection point was found by fitting a third order polynomial function to this part of the curve and calculating the zero point of its second derivative. The tangent at this point was then determined and from its slope the modulus after yield, E_2 . Finally, the yield point was defined as the point of interception of the E_1 -secant and E_2 -tangent. The resulting properties in tension and compression are listed in Tables 3.3 and 3.4. The results exhibited some scatter that was mainly attributed to the above- mentioned sensitivity to small temperature changes and small unavoidable geometry differences caused by the material's flexibility.

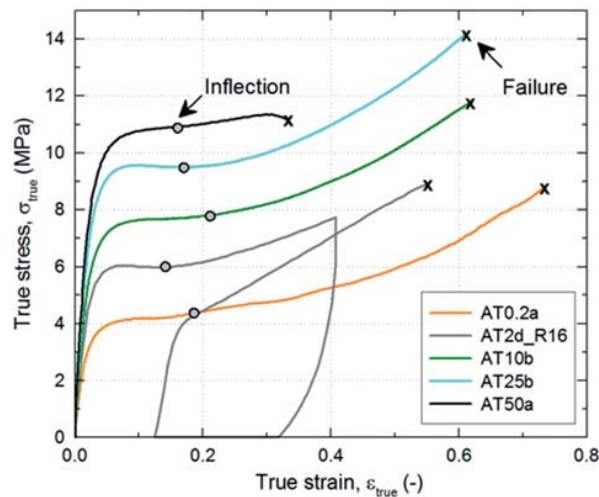


Figure 3.10: True stress-strain curves in tension for all strain rates

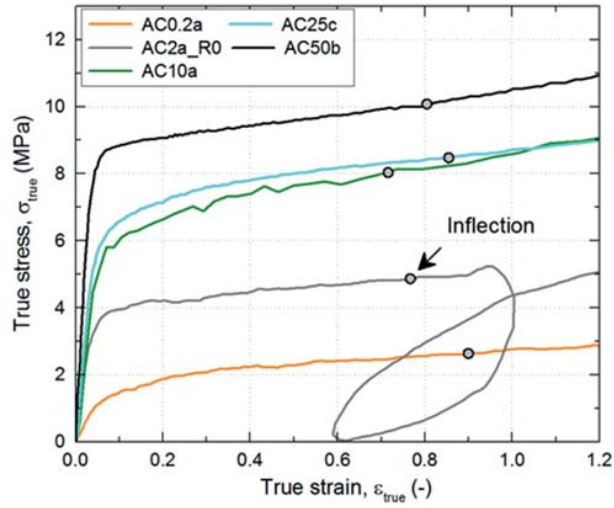


Figure 3.11: True stress-strain curves in compression for all strain rates

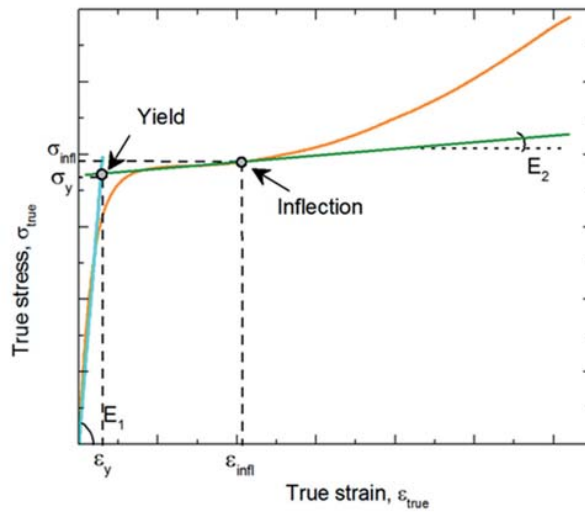


Figure 3.12: Calculation of mechanical properties

Table 3.3: True tensile mechanical properties

Specimen	E-modulus E_1 (MPa)	E-modulus E_2 (MPa)	Yield strain ε_y (-)	Yield stress σ_y (MPa)	Failure strain ε_{fail} (-)	Failure stress σ_{fail} (MPa)	Inflection strain ε_{infl} (-)	Inflection stress σ_{infl} (MPa)
AT0.2a	152.70	3.09	0.025	3.89	0.733	8.76	0.180	4.37
AT0.2b	145.67	3.74	0.026	3.75	0.859	11.28	0.226	4.50
AT0.2c	121.56	3.05	0.029	3.55	0.821	9.51	0.230	4.16
AV $\pm SD$	139.98 ± 16.33	3.30 ± 0.39	0.027 ± 0.002	3.73 ± 0.17	0.804 ± 0.065	9.85 ± 1.30	0.212 ± 0.028	4.34 ± 0.17
AT2a_R0	209.66	1.46	0.026	5.42	0.702	11.80	0.143	5.59
AT2b_R1	233.05	3.25	0.027	6.32	0.629	11.74	0.143	6.70
AT2c_R8	113.93	2.54	0.048	5.45	0.473	6.35	0.114	5.62
AT2d_R16	226.02	1.20	0.027	6.09	0.549	8.87	0.136	6.04
AT2e_R24	280.88	6.72	0.014	5.34	0.360	19.90	0.155	5.99
AT2f_R30	189.77	2.67	0.029	5.56	-	-	0.221	6.07
AT2g_R40	237.51	3.27	0.028	6.62	0.754	14.17	0.222	7.25
AT2h_R48	204.33	2.69	0.027	5.60	0.722	10.92	0.186	6.03
AV $\pm SD$	211.89 ± 48.12	2.97 ± 1.69	0.028 ± 0.009	5.80 ± 0.48	0.598 ± 0.145	11.96 ± 4.28	0.165 ± 0.040	6.16 ± 0.56
AT10a	256.23	2.8223	0.030	7.74	0.862	17.88	0.244	8.35
AT10b	263.72	2.94	0.028	7.37	0.621	11.79	0.215	7.92
AT10c	263.41	3.51	0.029	7.58	0.697	13.19	0.218	8.31
AV $\pm SD$	261.12 ± 4.24	3.09 ± 0.37	0.029 ± 0.001	7.56 ± 0.19	0.727 ± 0.123	14.29 ± 3.19	0.226 ± 0.016	8.19 ± 0.24
AT25a	287.00	2.11	0.031	8.84	0.609	14.16	0.154	8.84
AT25b	325.42	1.51	0.029	9.54	0.609	14.16	0.164	9.54
AT25c	326.90	1.53	0.031	9.98	0.276	10.42	0.155	9.98
AV $\pm SD$	313.11 ± 22.62	1.72 ± 0.34	0.030 ± 0.001	9.45 ± 0.57	0.498 ± 0.192	12.91 ± 2.16	0.158 ± 0.006	9.45 ± 0.57
AT50a	370.83	1.58	0.029	10.66	0.337	11.03	0.153	10.91
AT50b	377.22	0.70	0.029	10.77	0.532	13.77	0.196	11.12
AT50c	356.90	1.76	0.029	10.48	0.350	11.21	0.154	10.79
AV $\pm SD$	368.32 ± 10.39	1.35 ± 0.57	0.029 ± 0.000	10.63 ± 0.14	0.406 ± 0.109	12.00 ± 1.53	0.168 ± 0.025	10.94 ± 0.17

Table 3.4: Compressive mechanical properties

Specimen	E-modulus E_1 (MPa)	E-modulus E_2 (MPa)	Yield strain ε_y (-)	Yield stress σ_y (MPa)	Inflection strain ε_{infl} (-)	Inflection stress σ_{infl} (MPa)
AC0.2a	57.00	0.49	0.081	2.22	0.899	2.65
AC0.2b	65.79	1.80	0.062	4.06	0.754	4.54
AC0.2c	142.32	1.08	0.053	7.53	0.548	8.06
AV $\pm SD$	88.37 ± 46.93	1.13 ± 0.66	0.065 ± 0.014	4.60 ± 2.69	0.734 ± 0.176	5.08 ± 2.75
AC2a_R0	98.97	0.98	0.042	4.16	0.766	4.87
AC2b_R1	66.66	1.02	0.049	3.27	0.514	3.75
AC2c_R8	66.35	0.93	0.050	3.31	0.492	3.72
AC2d_R16	90.07	0.99	0.041	3.68	0.456	4.10
AC2e_R24	62.15	1.26	0.037	2.30	0.472	2.85
AC2f_R30	118.42	1.13	0.047	5.58	0.591	6.20
AC2g_R40	38.11	1.46	0.055	2.11	0.628	2.95
AC2h_R48	58.61	0.48	0.042	2.45	0.577	2.70
AV $\pm SD$	74.92 ± 25.73	1.03 ± 0.28	0.045 ± 0.006	3.36 ± 1.14	0.562 ± 0.102	3.89 ± 1.18
AC10a	194.44	1.48	0.041	7.88	0.730	8.90
AC10b	115.23	1.43	0.062	7.15	0.803	8.21
AC10c	113.57	2.16	0.057	6.50	0.872	8.27
AV $\pm SD$	141.08 ± 46.22	1.69 ± 0.41	0.053 ± 0.011	7.18 ± 0.69	0.802 ± 0.071	8.46 ± 0.38
AC25a	142.32	5.87	0.055	7.85	0.855	8.51
AC25b	126.27	4.46	0.043	5.49	0.684	6.02
AC25c	143.81	4.10	0.050	7.20	0.855	7.67
AV $\pm SD$	137.47 ± 9.73	4.81 ± 0.94	0.050 ± 0.006	6.85 ± 1.22	0.798 ± 0.099	7.40 ± 1.26
AC50a	247.24	3.52	0.036	8.86	0.562	9.69
AC50b	173.79	5.28	0.046	7.98	0.800	8.81
AC50c	162.00	5.67	0.061	6.21	0.983	7.13
AV $\pm SD$	194.34 ± 46.19	4.82 ± 1.15	0.048 ± 0.013	7.68 ± 1.35	0.782 ± 0.211	8.54 ± 1.30

3.4.2. Strain-rate effects

As already observed for the load-displacement curves, the strain rate also significantly influenced the true stress-strain responses. Concerning the yield stress, this had already been observed in [23, 24, 25] and the increasing yield stress with increasing rate was described by the following equation:

$$\sigma_y = \sigma_0 + \sigma_1 \cdot \log(\dot{\epsilon} / \dot{\epsilon}_0) \quad (1)$$

where σ_y is the yield stress at rate $\dot{\epsilon}$, σ_0 is the known yield stress at a given strain rate $\dot{\epsilon}_0$, and σ_1 is a constant. Taking the lowest applied rates for tension and compression according to Table 3.1 as $\dot{\epsilon}_0$, together with the corresponding yield stresses, σ_0 , and fitting Eq. (1) to the experimental results, confirmed the logarithmic trend of the responses [25], i.e. the rate sensitivity decreased with increasing rate, see Fig. 3.13. The stresses at the inflection point followed the same logarithmic trend, as also shown in Fig. 3.13, as did the elastic modulus, E_I , shown in Fig. 3.14. From the molecular point of view, the higher strain rate seemed to hinder the loss of the secondary bonds and the rearrangement of the network; the stress-strain curves thus moved upwards, i.e. yield, inflection and failure stresses and also the elastic modulus increased.

On the other hand, regarding the characteristic strains, the trend of the failure strain, ϵ_{fail} , decreased with increasing rate although also being logarithmic, while the yield and inflection strains, ϵ_y and ϵ_{infl} , seemed to be independent of the strain rate and varied only slightly around a constant value, as shown in Fig. 3.15.

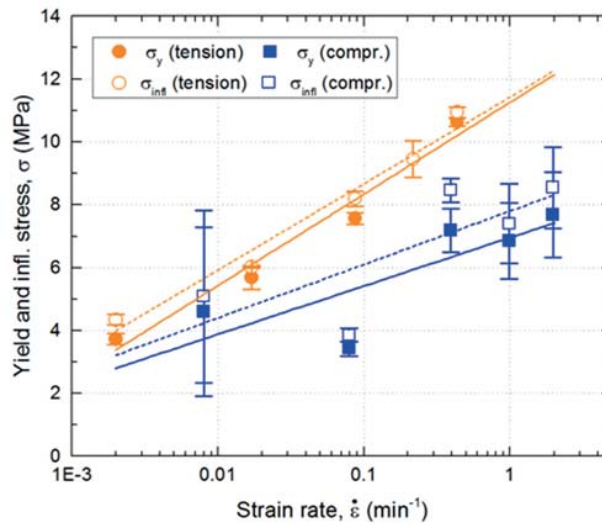


Figure 3.13: Strain rate-dependent yield and inflection stress in tension and compression (strain rate on log scale)

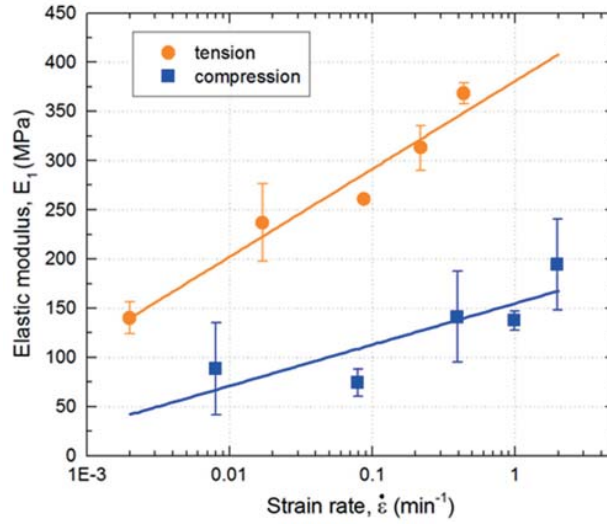


Figure 3.14: Strain rate-dependent elastic modulus (E_1) in tension and compression (strain rate on log scale)

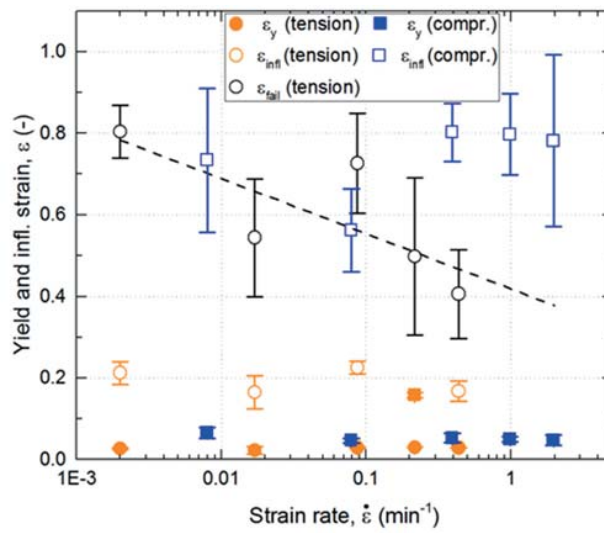


Figure 3.15: Strain rate-dependent yield, inflection and failure true strains in tension and compression (strain rate on log scale)

3.4.3. Ductility

The unloading and reloading curves of selected tensile and compressive specimens are shown in Figs. 3.16 and 3.17 respectively. The energy-based ductility index, μ , was calculated according to Eq. (2) [9]:

$$\mu = 0.5 \cdot (E_{tot} / E_{el} + 1) \quad (2)$$

where E_{tot} is the total energy and E_{el} the elastic energy. The corresponding values and resulting indices are listed in Tables 3.5 and 3.6 for tension and compression respectively.

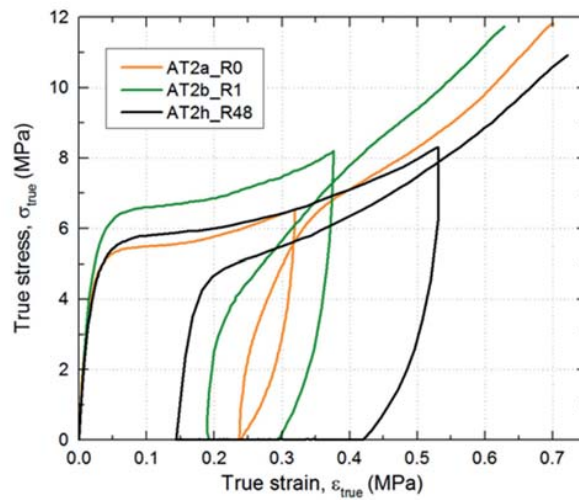


Figure 3.16: Un- and reloading cycles after different recovery periods for tensile specimens

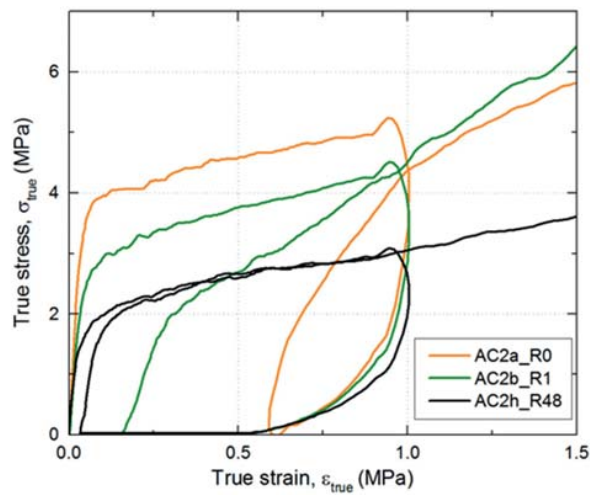


Figure 3.17: Un- and reloading cycles after different recovery periods for compressive specimens

Table 3.5: Ductility index in tension

Specimen	Strain at unloading ϵ_{un} (-)	Stress at unloading σ_{un} (MPa)	Total energy E_{tot} (10^{-3} J/mm ³)	Elastic energy E_{el} (10^{-3} J/mm ³)	Ductility index μ (-)
AT2a_R0	0.319	6.17	1.75	0.14	6.8
AT2b_R1	0.377	7.85	2.51	0.17	7.9
AT2c_R8	0.545	10.90	3.31	0.24	7.4
AT2d_R16	0.408	9.33	2.51	0.14	9.5
AT2e_R24	0.546	9.31	3.62	0.24	8.0
AT2f_R30	0.444	5.67	2.61	0.24	5.9
AT2g_R40	0.457	7.27	3.27	0.25	7.0
AT2h_R48	0.531	8.33	3.37	0.23	7.8
AV\pmSD	0.45\pm0.084	8.10\pm1.74	2.87\pm0.59	0.21\pm0.04	7.5\pm1.0

Table 3.6: Ductility index in compression

Specimen	Strain at unloading ϵ_{un} (-)	Stress at unloading σ_{un} (MPa)	Total energy E_{tot} (10^{-3} J/mm ³)	Elastic energy E_{el} (10^{-3} J/mm ³)	Ductility index μ (-)
AC2a_R0	0.982	5.16	4.40	0.43	5.6
AC2b_R1	0.997	4.48	3.64	0.34	5.9
AC2c_R8	0.965	6.1	4.72	0.34	7.4
AC2d_R16	0.969	9.48	5.96	0.64	5.2
AC2e_R24	0.997	3.63	2.86	0.29	5.4
AC2f_R30	1.121	7.16	6.74	0.48	7.5
AC2g_R40	0.996	3.51	2.63	0.38	4.0
AC2h_R48	0.987	3.07	2.52	0.28	5.0
AV\pmSD	1.00\pm0.05	5.32\pm2.18	4.18\pm1.47	0.40\pm0.11	5.8\pm1.2

The average values of 7.5 in tension and 5.8 in compression seem high if compared with values derived from data published for other materials and systems if metals are excluded. On the material level, concrete and timber in compression exhibit values of 2-3 [26] and 5-6 [27] respectively; much higher, however, are the indices of steel, i.e. 13-19 for S355/500 [28]. Applying Eq. (1) to the web-flange junctions of a pultruded glass-fiber-reinforced polymer (FRP) bridge deck, which were subjected to bending and dissipated inelastic energy through delamination [5], resulted in an index of 1.9. Analyzing the response of the same bridge deck adhesively bonded with a stiff epoxy adhesive onto steel girders and subjected to bending and yielding at failure [29] revealed an index of 2.5. Furthermore, concrete beams prestressed with unbonded FRP tendons subjected to bending [30] exhibited an index of 2-5.

3.4.4. Time-dependent recovery

The specimens of the 2 mm/min series were subjected to different recovery periods, between 1 h and 48 h, before they were reloaded, see Tables 3.7 and 3.8. The measured delayed recovered strains in tension and compression, $\varepsilon_{r,del}(t)$, during the period t_{BC} , are shown in Figs. 3.18 and 3.19 respectively (path B-C), together with the loading and instantaneous recovered strains (path A-B) after unloading. The delayed recovered strains were modeled using Fancey's equation [16]:

$$\varepsilon_{r,del}(t) = \varepsilon_r \cdot \left[\exp \left(- \left(\frac{t}{\eta_r} \right)^{\beta_r} \right) \right] \quad (3)$$

where ε_r , η_r and β_r are parameters obtained from fitting the model to the experimental results. The model considers several latch elements, including sets of elastic springs and dashpots, which are connected in series.

The resulting modeling results are shown in Fig. 3.20 on a logarithmic scale to better differentiate the short-term results. In compression, the unloading started from a higher strain than in tension, compare Figs. 3.18 and 19, and the delayed recovered strains thus started from a higher level in compression than in tension as shown in Fig. 3.20. However, after 48h, both curves approached almost the same value at time t_C . The rate of recovery in compression was thus higher than in tension, similar to the much higher loading rate in compression than in tension, see Table 3.2 (line of 2 mm/min). Whether the higher strain rate at loading or higher strain at unloading or a combination of both was responsible for the higher recovery rate, however, could not be decided based on the available results.

Based on the strains measured at unloading at time t_A , ε_{un} (see Tables 3.7 and 3.8), measured instantaneous recovery strains, $\varepsilon_{r,0}$, and measured and modeled (Eq. (4)) delayed recovery strains, $\varepsilon_{r,del}$, the percentages of instant recovery, R_i , and total recovery, $R_{tot}(t)$, could be calculated according to Eqs. (5) and (6):

$$R_i = \frac{\varepsilon_{r,0}}{\varepsilon_{un}} \quad (4)$$

$$R_{tot}(t) = \frac{\varepsilon_{r,0} + \varepsilon_{r,del}(t)}{\varepsilon_{un}} \quad (5)$$

The percentages of instantaneous and total recovery of each specimen in tension and compression are listed in Tables 3.7 and 3.8 respectively. Similarly to the higher strain rate at loading and higher strain at unloading, the instantaneous recovery in compression ($42.7 \pm 5.3\%$) was higher than in tension ($26.5 \pm 1.1\%$). The measured and modeled total recovery behaviors in tension and compression are also shown in Fig. 3.21. Regarding the measured values, the average values and standard deviations at a specific time for all specimens are shown. The measured and modeling results agree well, as also shown in Tables 3.7 and 3.8 where the average results are listed. As seen in Fig. 3.20, the total recovery in compression was higher than in tension for the same reasons as for the instantaneous recovery. At the end of the maximum experimental recovery period of 48h, the tensile specimens had already recovered 75% and the compression specimens 90% of the unloading strain. The trend of the measurements and the models did not indicate any permanent damage. Full recovery according to the models, however, would take approximately 50 years, which corresponds to the design life of a building structure, see Fig. 3.21.

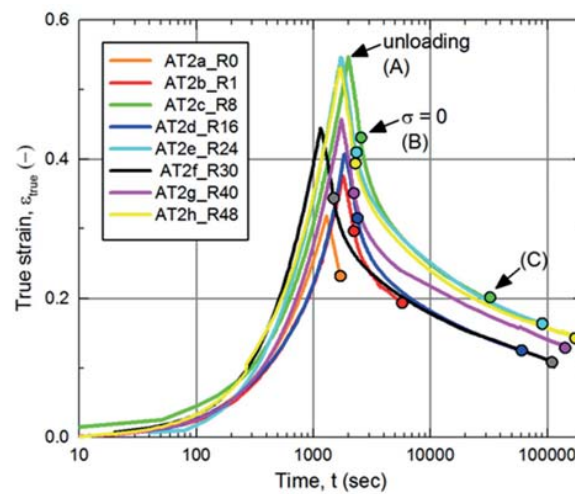


Figure 3.18: Time-dependent recovery strain in tension

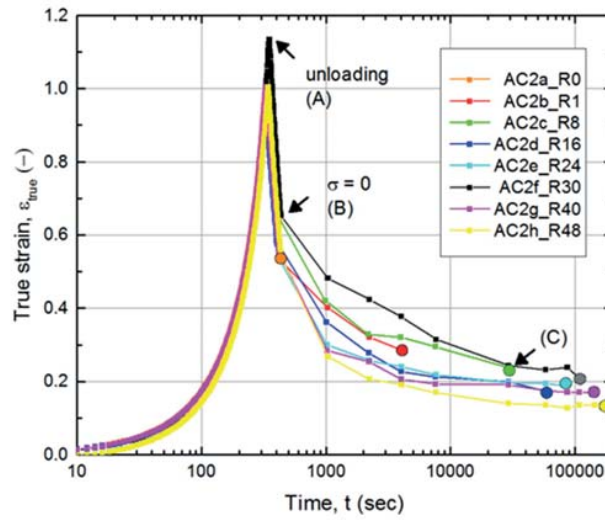


Figure 3.19: Time-dependent recovery strain in compression

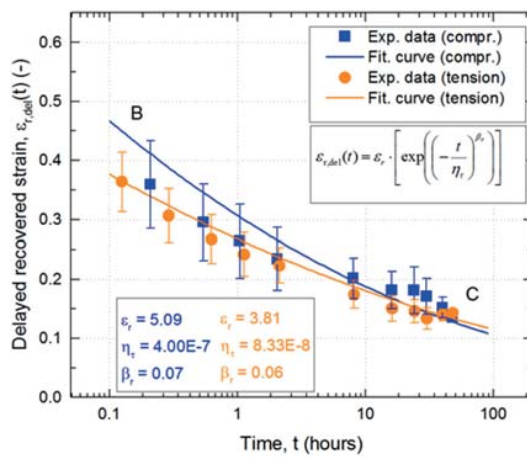


Figure 3.20: Time-dependent delayed recovered strain, $\epsilon_{r,del}$, in tension and compression

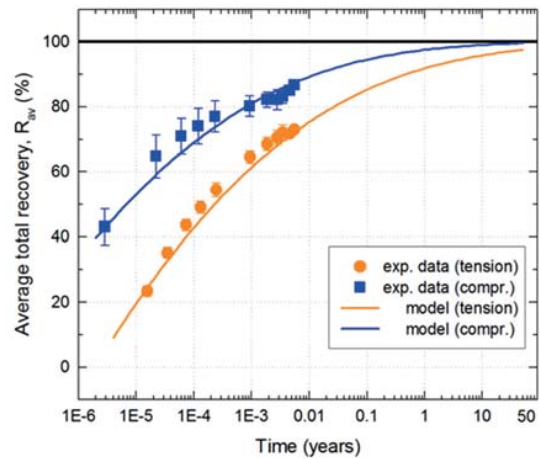


Figure 3.21: Predicted percentage of total recovery, R_{tot} , in tension and compression

Table 3.7: Time-dependent recovery in tension

Specimen	Strain at reloading ε_c (-)	Recovery period t_{BC} (hours)	Instant recovery R_i (%)	Total recovery R_{tot} (%)	Average total recovery R_{av} (%)		Relative error e (%)
					Experimental	Model	
AT2a_R0	0.237	0	25.7	25.7	23.4	23.7	1.0
AT2b_R1	0.193	1	25.3	48.8	35.2	32.5	8.5
AT2c_R8	0.198	8	28.8	63.9	43.6	39.9	9.5
AT2d_R16	0.125	16	27.0	69.4	49.0	45.2	8.5
AT2e_R24	0.164	24	26.0	69.9	54.5	50.6	7.6
AT2f_R30	0.109	30	27.0	75.4	64.5	60.9	5.8
AT2g_R40	0.130	40	25.3	71.6	68.6	65.6	4.6
AT2h_R48	0.143	48	26.9	73.0	70.6	68.1	3.6
<i>AV±SD</i>	<i>0.162±0.041</i>	-	<i>26.5±1.1</i>	-	-	-	-

Table 3.8: Time-dependent recovery in compression

	Strain at reloading, ε_c (-)	Recovery period t_{BC} (hours)	Instant recovery, R_i (%)	Total recovery, R_{tot} (%)	Average total recovery, R_{av} (%)		Relative error, e (%)
					Experimental	Model	
AC2a_R0	0.589	0	40.7	40.7	43.0	39.3	9.6
AC2b_R1	0.285	1	47.2	71.6	64.7	58.0	11.4
AC2c_R8	0.238	8	31.2	75.6	70.9	65.6	8.2
AC2d_R16	0.174	16	40.3	82.0	74.0	69.9	6.0
AC2e_R24	0.187	24	49.3	82.2	77.0	73.8	4.3
AC2f_R30	0.208	30	41.9	81.4	80.2	80.6	0.5
AC2g_R40	0.169	40	44.6	83.0	82.1	83.5	1.7
AC2h_R48	0.135	48	46.1	86.6	82.2	85.1	3.4
<i>AV±SD</i>	<i>0.248±0.136</i>	-	<i>42.7±5.3</i>	-	-	-	-

3.5. Conclusions

The mechanical behavior of a viscoelastic ductile acrylic adhesive in tension and compression and at different strain rates has been investigated. Furthermore, the ductility and recovery behaviors after unloading have been examined. The main conclusions of this study can be summarized as follows:

- Different true stress-strain responses were recorded for the two types of loading, tension and compression, at the same engineering strain rate.
- Increasing the strain rate increased the yield stresses, stresses at the inflection point, and elastic modulus, and decreased the failure strains, all with a logarithmic trend, i.e. the rate sensitivity decreased with increasing rate.
- On the contrary, no effect of the strain rate on the yield strain, strain at the inflection point and stiffness after yielding could be observed.
- The specimens exhibited high energy-based ductility indices compared to traditional materials and structural systems.
- The time-dependent recovery after unloading depended on the loading type, tension or compression, strain rate of loading and strain at unloading. The delayed recovered strain behavior could be modeled using an existing Weibull-based model for creep recovery.
- The deformation of the ductile acrylic adhesive almost fully recovered after 48h, suggesting that no residual deformation caused by any damage or plastic flow occurred.

Further work should take into account the effect of the strain rate during loading and the strain at unloading on the ductility behavior. Furthermore, the separation of the effects of strain rate during loading and strain at unloading on the recovery behavior should be addressed.

References

- [1] Keller T., De Castro J. System ductility and redundancy of FRP beam structures with ductile adhesive joints. *Composites Part B* (2005), 36/8: 586-596
- [2] Boyce M.C., Arruda E.M., Jayachandran R. The large strain compression, tension, and simple shear of polycarbonate. *Polymer Engineering & Science* (1994), 34(9): 716-725.
- [3] Chen W., Lu F., Cheng, M. Tension and compression tests of two polymers under quasi-static and dynamic loading. *Polymer testing* (2002), 21(2): 113-121.
- [4] Angelidi M., Vassilopoulos A. P., Keller T. Displacement rate and structural effects on Poisson ratio of a ductile structural adhesive under tension and compression. *International Journal of Adhesion and Adhesives*, (2017).
- [5] Yanes-Armas S., de Castro J., Keller T. Energy dissipation and recovery in web-flange junctions of pultruded GFRP decks. *Composite Structures* (2016), 148:168-180.
- [6] Widyatmoko I., Ellis C., Read J. M. Energy dissipation and the deformation resistance of bituminous mixtures. *Materials and Structures* (April 1999), 32: 218-223.
- [7] Grace N.F., Soliman A., Abdel-Sayed G., Saleh K. Behavior and ductility of simple and continuous FRP reinforced beams. *J. Compos. Constr.* (1998), 2(4):186-94.
- [8] De Lorenzis L., Galati D., La Tegola A. Stiffness and ductility of fibre-reinforced polymer-strengthened reinforced concrete members. *Proc. ICE-Struct. Build.* (2004), 157(1):31-51.
- [9] Naaman A.E., Jeong S.M. Structural ductility of concrete beams prestressed with FRP tendons, Nonmetallic (FRP) reinforcement for concrete structures, *Proc. of the second international RILEM symposium (FRPRCS-2)* (1995): 379-386.
- [10] Williams G., Watts D. C. Non-symmetrical dielectric relaxation behaviour arising from a simple empirical decay function. *Transactions of the Faraday Society* (1970), 66: 80-85.
- [11] Anderssen R. S., Husain S. A., Loy R. J. The Kohlrausch function: properties and applications. *Anziam Journal* (2004), 45: 800-816.
- [12] Weibull W. A statistical distribution function of wide applicability. *Journal of applied mechanics* (1951), 103: 293-297.
- [13] Wimberger P. H. Plasticity of jaw and skull morphology in the neotropical cichlids *Geophagus brasiliensis* and *G. steindachneri*. *Evolution* (1991): 1545-1563.
- [14] Cherièrè J. M., Belec L., Gacougnolle J. L. The three successive stages of creep of PMMA between 55 C and 90 C. *Polymer Engineering & Science* (1997), 37(10): 1664-1671.
- [15] Marais C., Villoutreix G. Analysis and modeling of the creep behavior of the thermostable PMR-15 polyimide. *Journal of applied polymer science* (1998), 69(10): 1983-1991.
- [16] Fancey K. S. A Latch-Based Weibull Model for Polymeric Creep and Recovery. *Journal of polymer engineering* (2001), 21(6): 489-510.

-
- [17] Schapery R. A. On the characterization of nonlinear viscoelastic materials. *Polymer Engineering & Science* (1969), 9(4): 295-310.
- [18] Zaoutos S. P., Papanicolaou G. C., Cardon A. H. On the non-linear viscoelastic behaviour of polymer-matrix composites. *Composites science and technology* (1998), 58(6): 883-889.
- [19] Sika AG. SikaFast5221 NT: Fast-curing 2-component structural adhesive. Zurich (2013).
- [20] ASTM D 638-96, Standard test method for tensile properties of plastics, *Annual Book of ASTM Standards* (1996), 8(1), United States of America.
- [21] ASTM D 695M-96, Standard test method for compressive properties of rigid plastics [metric], *Annual Book of ASTM Standards* (1996), 8(1), United States of America.
- [22] Moussa O., Vassilopoulos A. P., Keller T. Effects of low-temperature curing on physical behavior of cold-curing epoxy adhesives in bridge construction, *International Journal of Adhesion and Adhesives* (January 2012), 32: 15-2
- [23] Ludwig P. Ober den Einfluss der Deformationsgeschwindigkeit bei bleibenden Deformationen mit besonderer Berücksichtigung der Nachwirkungserscheinungen'. *Physikal. Zeits* (1909), 10: 411.
- [24] Prandtl L. A conceptual model to the kinetic theory of solid bodies. *Z. Angew. Math. Mech.* (1928), 8: 85-106.
- [25] Avendaño R., Carbas R. J. C., Marques E. A. S., da Silva L. F. M., Fernandes A. A. Effect of temperature and strain rate on single lap joints with dissimilar lightweight adherends bonded with an acrylic adhesive. *Composite Structures* (2016), 152: 34-44.
- [26] British Standards Institution. CP 110: Part 1. The Structural Use of Concrete: Design, Materials and Workmanship. BSI (1972), London.
- [27] Natterer J., Sandoz J. L., Rey M. *Construction en Bois, Traité de Génie Civil* (2004), Lausanne, 13.
- [28] Gardner L. The use of stainless steel in structures. *Progress in Structural Engineering and Materials* (2005), 7(2): 45-55.
- [29] Keller T., Gürtler H. Composite action and adhesive bond between FRP bridge decks and main girders. *Journal of Composites for Construction* (2005), 9(4): 360-368.
- [30] Jo B. W., Tae G. H., Kwon B. Y. Ductility evaluation of prestressed concrete beams with CFRP tendons. *Journal of reinforced plastics and composites* (2004), 23(8): 843-859.

Chapter 4

Ductile adhesively-bonded timber joints: Experimental investigation

In the field of timber load-bearing structures, adhesive bonding is a promising, though poorly developed, joining technique that may increase the structural stiffness and capacity of timber joints and structures. The use of ductile adhesives may furthermore allow the designing ductile joints, which can compensate for the material ductility that timber lacks. To demonstrate the potential of this approach, adhesively-bonded double-lap timber joints were manufactured using a ductile acrylic adhesive and then subjected to axial tension and compression loading. The load-displacement responses were measured and compared to those of the same joint configuration for which a brittle epoxy adhesive was used. The effect of the different adhesives on the joint capacity and ductility has been studied and quantified. Strain field measurements using the Digital Image Correlation (DIC) technique and a strain-based Norris failure criterion provided a better understanding of the mechanical behavior of the two different joint types. ¹

Keywords: *acrylics, adhesive, ductility, epoxy, joint, spruce, timber*

¹ Angelidi M., Vassilopoulos A. P., & Keller T. Ductile adhesively-bonded timber joints – Experimental investigation (under review).

4.1. Introduction

Joints are the most critical elements in the majority of timber structures; basically they can be designed as mechanical or adhesively-bonded joints. Bonded joints can exhibit higher efficiency than bolted joints due to a more uniform stress distribution [1, 2]; in the latter, high stress concentrations occur around the bolts and the cross section is reduced [3]. In addition to this higher capacity of bonded joints, the stiffness is increased, the weight-to-strength ratio reduced, and fatigue strength and durability are improved, the latter due to the sealing by the adhesive [4]. Many different types of adhesives can be used, depending on the targeted application [5].

One of the most important requirements for load-bearing structures is ductility, i.e. the ability of a material or structure to sustain inelastic deformation prior to failure, without loss of resistance. Furthermore, the energy generated by any impact or seismic actions is dissipated and large deformations prior to failure provide sufficient warning [6]. In redundant systems, the internal forces are redistributed and the structural safety thus increased. The provision of ductility is however made difficult when using brittle materials, such as fiber-reinforced polymers (FRPs) or wood. To overcome this difficulty in the field of FRP materials, ductile adhesives were proposed [7] and used [2] for developing ductile joints, thus compensating for the lacking material ductility [2].

The basic definition of ductility is expressed as the ratio between the total and yield deformations of a material or structural component [8]. However, ductile behavior cannot be derived based only on an observed non-linear load-displacement response. In an elastically buckling component, for example, the ascending non-linear loading and descending unloading paths overlap and no yield deformation (permanent) or related ductility are developed. Therefore, extended energy-based definitions of ductility, taking into account the inelastic energy dissipated during loading, were developed. The total energy, E_{tot} , corresponds to the total area under the load-displacement curve and is composed of the elastic energy, E_{el} , which is released while unloading and the dissipated inelastic energy, E_{inel} , represented by the area between the loading and unloading paths respectively [9, 10]. Such energy-based definitions usually consider different ratios of these energies: i.e. E_{inel}/E_{tot} [11, 12] or E_{tot}/E_{el} [13].

Ductile adhesive joints to implement ductility in FRP composite structures have already been developed, as mentioned above. A systematic and comprehensive investigation of the application of such ductile adhesives for timber joints, however, has not yet been performed; only a basic study concerning their load capacity has been carried out [14]. The aim of this work is thus to design such ductile adhesive timber joints and compare their performance, if subjected to axial tension and compression loading, with similar joints comprising a brittle adhesive. Stiffness, capacity, failure modes and load transfer mechanisms based on strain field measurements are compared and ductility is quantified. The comparison is based on experimental results obtained from full-scale joint investigations.

4.2. Experimental set-up

4.2.1. Materials and specimens

The experimental program included 19 full-scale, adhesively-bonded dog-bone-shaped double-lap timber joint specimens, in order to facilitate their clamping in the machine, as shown in Fig. 4.1. The wood used was Norway spruce, belonging to the species of *Picea abies*, as it is one of the most widely used types of wood for structural applications in the timber industry. The wooden adherends were cut from spruce wood logs, avoiding any obvious defects such as notches or cracks. For the assembling of these adherends, two kinds of structural adhesives were used and two series of joints were manufactured: a reference series using a brittle epoxy adhesive, SikaDur330, and a series using a ductile acrylic adhesive, SikaFast5221NT; both adhesives were obtained from Sika AG, Switzerland [15, 16]. The ductile behavior of this acrylic adhesive has already been investigated and quantified in a preceding work [17]. The basic mechanical properties of the materials used for the joints are summarized in Table 4.1. It has to be noted that the properties of the acrylic adhesive were highly strain rate-dependent, as shown in a preceding work [18].

The detailed specimen geometry is shown in Fig. 4.1; the total length and width were 970 and 50mm and the thickness of the adhesive layer was 2 and 3mm, for epoxy- and acrylic-adhesive joints ('epoxy joints' and 'acrylic joints' in the following) respectively. In the latter case, subsequently to preliminary experiments exhibiting interface failure, a 0.5-mm layer of epoxy was added between the wood and acrylic adhesive to improve adhesion. The joints were fabricated under ambient laboratory conditions ($21 \pm 3^\circ\text{C}$ and $38 \pm 10\%$ relative humidity) and stored in a conditioning room ($20 \pm 2^\circ\text{C}$ and $60 \pm 3\%$ relative humidity) for at least one week to obtain a) a uniform moisture content (12%), and b) full cure of the adhesives (according to [17]).

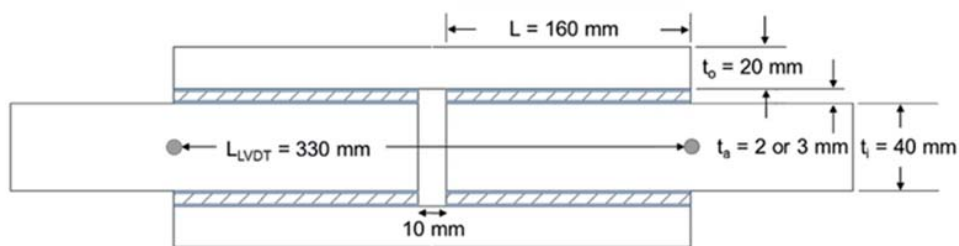


Figure 4.1: Geometry of double-lap joint

Table 4.1: Basic material mechanical properties [¹3, ²18, ³19, ⁴20, ⁵15, ⁶16, ⁷measured]

Material	Mechanical properties			
	Tensile E-modulus (MPa)	Compressive E-modulus (MPa)	Poisson ratio (-)	Density (kg/m ³)
Epoxy	¹ 4500	¹ 3000	¹ 0.37	⁵ 1300
Acrylics*	² 105	² 21	² 0.48	⁶ 1200
Spruce (// fibers)	³ 11600	⁴ 11330	³ 0.4	⁷ 440

4.2.2. Experimental procedure and instrumentation

The experimental program included both axial tensile and compressive experiments. The joint specimens were loaded up to failure at a displacement rate of 2 mm/min. In the acrylic joint specimens an unloading-reloading cycle, at the same displacement rates, was implemented in the plateau region of the load-displacement response.

A universal Schenk machine of 600-kN capacity was used. Teeth-shaped steel plates were installed to prevent grip failure and specimen slip. The machine's load-cell and two linear variable displacement transducers (LVDTs), symmetrically placed on both sides of the specimens at a distance of 330 mm, were used to measure the load and displacements applied to the joints respectively, see Fig. 4.2. In the following, half of the average values of the two LVDT measurements are reported, corresponding to the displacements of one of the two joints per specimen. The accuracy of the LVDT measurements was ± 0.02 mm.

In four epoxy and three acrylic joints in tension, the full 3D displacement fields were measured on one specimen side, using a Digital Image Correlation (DIC) system provided by Correlated Solutions Inc. [21, 22], and the corresponding strain fields were derived. One LVDT was left in place on the opposite side. The DIC surface was sanded and painted white and a random pattern of black speckles of similar size was then sprayed onto it, allowing the DIC to track their relative displacements during the experiment, see Fig. 4.2. The accuracy of these measurements was ± 0.01 mm for displacements and correspondingly ± 0.001 for strains.

In total, 11 specimens (five epoxy and six acrylic) were examined in tension and eight in compression (four and four for each adhesive). The specimens were labeled according to the adhesive (E for epoxy or A for acrylic), type of loading (T for tension or C for compression) and specimen number, e.g. A_T2 denotes the second (2) acrylic (A) joint in tension (T).

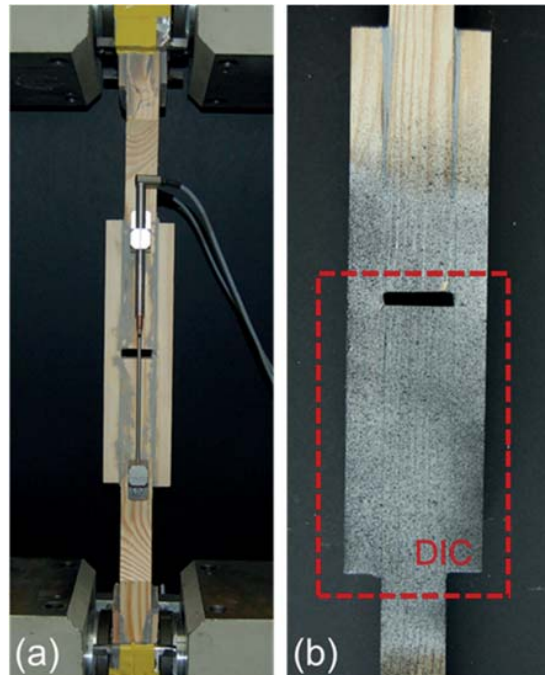


Figure 4.2: Experimental set-up for tension and compression using (a) LVDTs and (b) DIC system

4.3. Results and discussion

4.3.1. Failure modes and load-displacement responses

Different failure modes were observed in tension and compression for the two types of joints, as summarized in Tables 4.2 and 4.3 and shown in Figs. 4.3 and 4.4. All epoxy joints failed in the wood of the inner adherend (adherend failure), except for two of them in compression, which buckled during loading. The initiation of failure in tension occurred just below the adhesive layer at one overlap end, while in compression initiation was at mid-height at the edge of the inner adherend. A mixed failure mode was observed in the acrylic joints in tension; failure occurred partially in the wood and partially in the epoxy-acrylic adhesive interface on one joint side while on the other side failure occurred in the wood. In compression, failure occurred completely in the adhesive interface on one side and in the wood on the other side.

Typical load-displacement curves are shown in Fig. 4.5. The responses were linear for the epoxy joints up to failure but highly non-linear for the acrylic joints. The unloading-reloading cycle of the acrylic joints was performed between 50 and 55 kN.

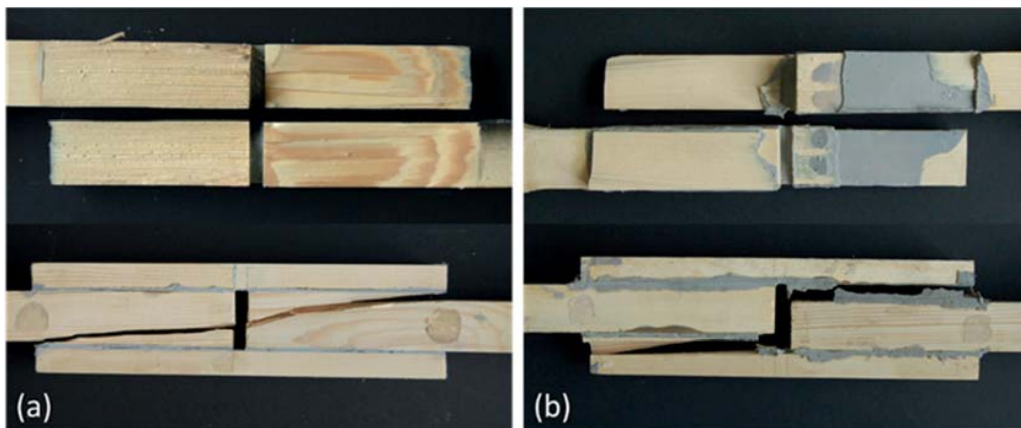


Figure 4.3: Failure modes in tension: (a) adherend failure for epoxy joints (E_T3) and (b) mixed failure for acrylic joints (A_T1), plan and side views

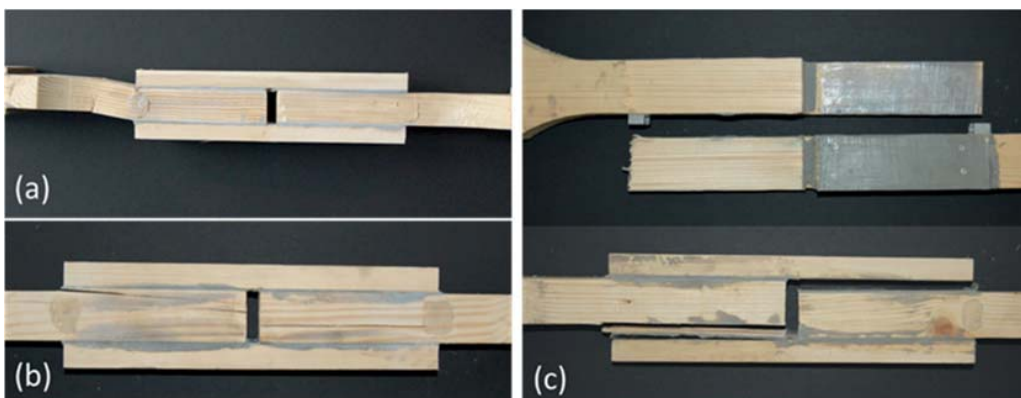


Figure 4.4: Failure modes in compression: (a) buckling (E_C4) and (b) adherend failure for epoxy joints (E_C1) and (c) interface failure for acrylic joints (A_C2)

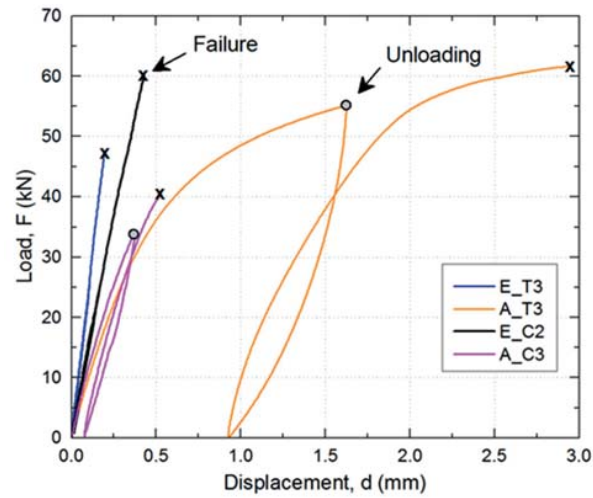


Figure 4.5: Typical load-displacement responses of epoxy and acrylic joints in tension and compression

Table 4.2: Experimental results for joints in tension (*specimens monitored with the DIC)

Specimen	Initial stiffness K_I (kN/mm)	Yield load F_y (kN)	Yield displacement d_y (mm)	Ultimate load F_u (kN)	Ultimate displacement d_u (mm)	Failure mode
E_T1	131.34	-	-	32.21	0.24	adherend
E_T2*	172.00	-	-	29.16	0.17	adherend
E_T3*	231.99	-	-	47.07	0.19	adherend
E_T4*	187.07	-	-	43.50	0.24	adherend
E_T5*	197.61	-	-	33.68	0.17	adherend
AV	184.00	-	-	37.12	0.20	
$\pm SD$	± 32.91	-	-	± 6.91	± 0.03	
A_T1	126.03	39.00	0.33	56.58	3.04	mixed
A_T2	119.54	45.57	0.44	65.11	2.96	mixed
A_T3	99.42	41.00	0.47	61.64	2.95	mixed
A_T4*	129.74	37.72	0.34	53.63	1.86	mixed
A_T5*	139.38	40.76	0.32	65.80	3.47	adherend
A_T6*	98.59	40.00	0.42	55.64	2.46	mixed
AV	118.78	40.68	0.39	59.73	2.79	
$\pm SD$	± 15.17	± 2.45	± 0.06	± 4.71	± 0.51	

Table 4.3: Experimental results for joints in compression

Specimen	Initial stiffness K_l (kN/mm)	Yield load F_y (kN)	Yield displacement d_y (mm)	Ultimate load F_u (kN)	Ultimate displacement d_u (mm)	Failure mode
E_C1	118.75	-	-	53.93	0.49	adherend
E_C2	149.25	-	-	60.25	0.43	adherend
E_C3	128.30	-	-	64.89	0.55	buckling
E_C4	138.63	-	-	63.20	0.54	buckling
<i>AV</i>	<i>133.73</i>	-	-	<i>60.57</i>	<i>0.50</i>	
$\pm SD$	± 28.75			± 4.18	± 0.05	
A_C1	99.27	28.79	0.29	32.23	0.50	interface
A_C2	92.64	32.42	0.35	34.73	0.57	interface
A_C3	111.21	37.00	0.34	40.55	0.53	interface
A_C4	128.25	40.40	0.32	44.55	0.54	interface
<i>AV</i>	<i>107.84</i>	<i>34.65</i>	<i>0.33</i>	<i>38.02</i>	<i>0.54</i>	
$\pm SD$	± 13.53	± 4.41	± 0.02	± 4.83	± 0.03	

4.3.2. Displacement and strain fields

The different joint behaviors could be further analyzed through the DIC mapping of the surfaces. The full-field displacements and strains were extracted for both types of joints at the same load level of 40 kN, which approximately corresponded to the average ultimate load of the epoxy joints (see Table 4.2). The acrylic joints already entered the non-linear range at this load, as shown in Fig. 4.5. The axial displacement behavior of both joint types is compared in Fig. 4.6. The acrylic joints exhibited much larger displacements (e.g. A_T5, 0.60 mm) compared to the epoxy joints (e.g. E_T3, 0.20 mm). In the latter, the displacements were almost uniformly distributed across the joint. In the former, however, most of the displacements (within 70-80%) occurred in the adhesive layer, and the elongation of the wood was comparably small.

The shear strains, ε_{xy} , and two extracted paths in the adhesive mid-plane are shown in Fig. 4.7. The strains in the wood were similar in both joint types. In the adhesive layer, the strains in the epoxy were much lower than those in the acrylic layer due to the higher E-modulus. However, their distribution along the overlap length was not uniform and exhibited high peaks at the edges. The distribution in the acrylic layer, in contrast, was uniform along the length. These differences were much less obvious in the through-thickness or peeling strains, ε_{yy} , as shown in Fig. 4.8. These strains resulted from the joint eccentricity, which was the same in both joint types. Accordingly, the strain distributions were similar, exhibiting on one side a tensile and on the other side a compressive peak.

The differences in the two joint behaviors were also clearly represented in the two principal strain distributions, ε_1 (tension, Fig. 4.9) and ε_2 (compression, Fig. 4.10) and their angles, α , the latter shown for α_1 at two different load levels, 10 kN and 40 kN (Figs. 4.11 and 4.12). Along the adhesive layers, both principal strains varied in the epoxy joints, while they were almost uniformly distributed in the acrylic joints with the exception of small peaks at the edges. The angle of the principal strain ε_1 , α_1 , in the epoxy layer varied between 15 and 40° (20° on average) with respect to the loading axis (which is 0°) and independent of the load level. The angle α_1 in the acrylic joints was almost identical along the length (45° on average) and also independent of the load level.

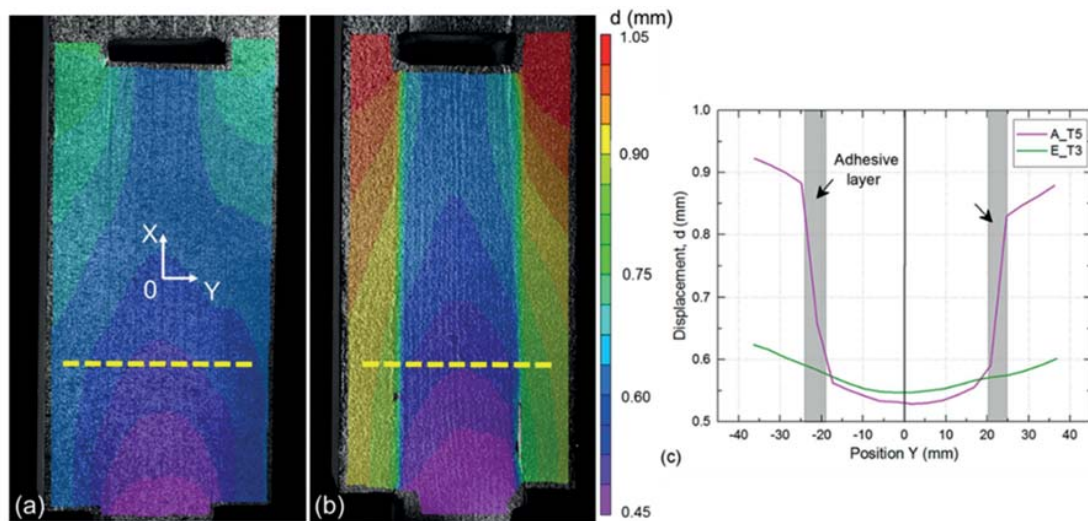


Figure 4.6: Axial displacement distribution at 40 kN of (a) epoxy (E_T3) and (b) acrylic joint (E_T3) and (c) comparison at selected path ($X = -33$ mm)

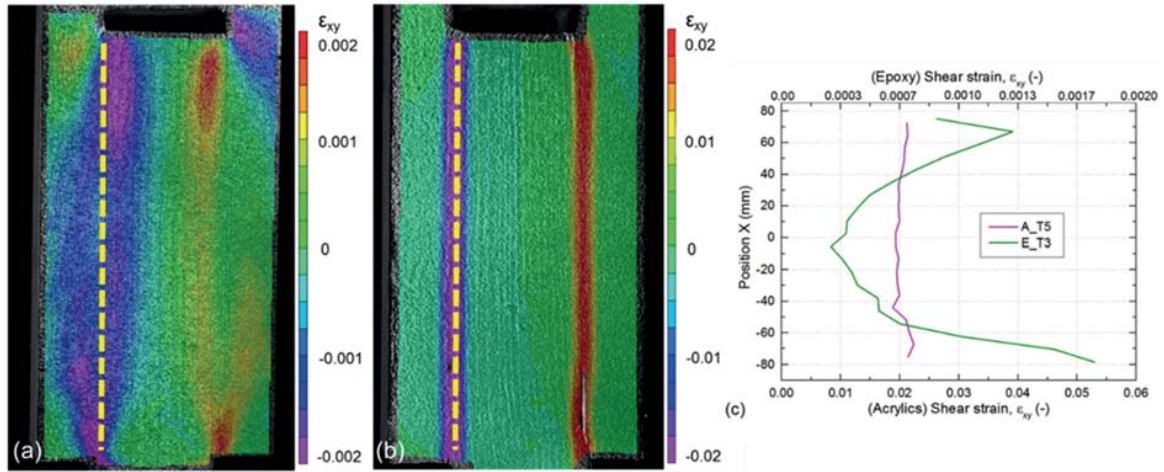


Figure 4.7: Shear strain distribution at 40 kN for (a) epoxy (EP5) and (b) acrylic joint (E_T3) and (c) comparison at selected path (adhesive mid-plane)

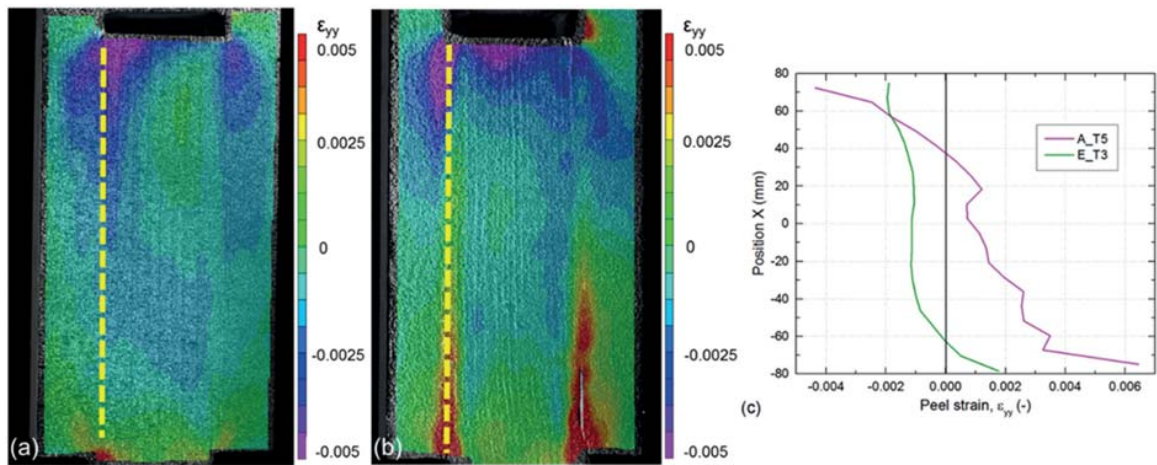


Figure 4.8: Peel strain distribution at 40 kN for (a) epoxy (E_T3) and (b) acrylic joint (A-T5) and (c) comparison at selected path (adhesive mid-plane)

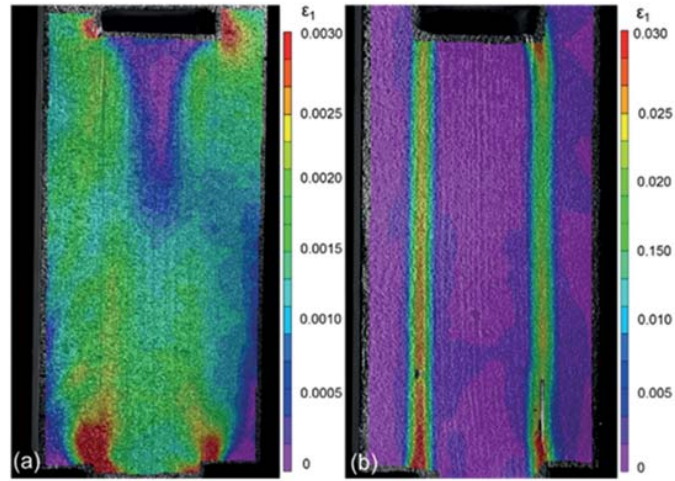


Figure 4.9: Principal strain distribution (ϵ_1) at 40 kN for (a) epoxy (E_T3) and (b) acrylic joint (A_T5)

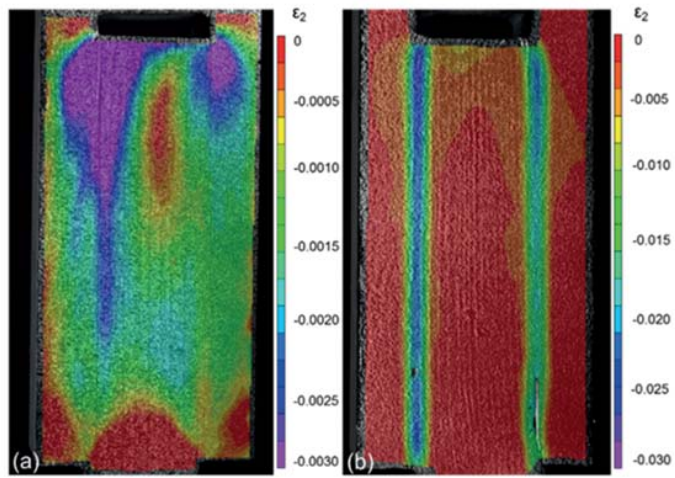


Figure 4.10: Principal strain distribution (ϵ_2) at 40 kN for (a) epoxy (E_T3) and (b) acrylic joint (A_T5)

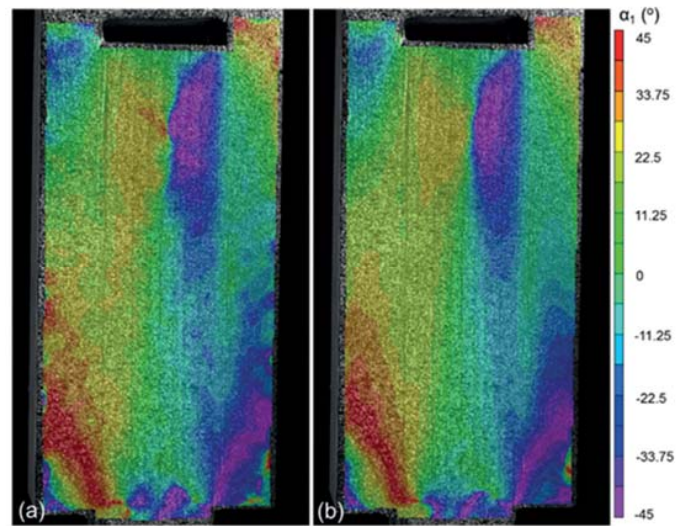


Figure 4.11: Principal strain angle distribution (α_1) (a) for epoxy (E_T3) at 10kN and (b) at 40kN (0° =parallel to loading axis)

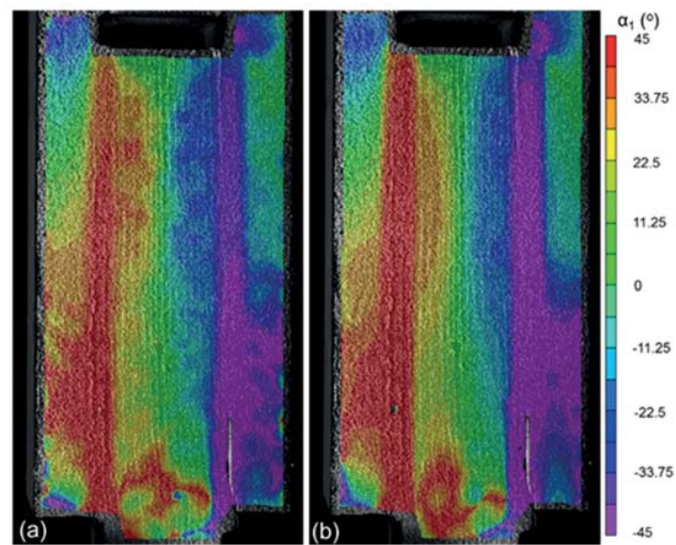


Figure 4.12: Principal strain angle (α_1) (a) for acrylic joint (A_T5) at 10kN and (d) at 40kN (0° =parallel to loading axis)

4.3.3. Mechanical characterization

Based on the Swiss code for timber structures [23] and the load-displacement curves shown in Fig. 4.5, the joints were characterized as described in Fig. 4.13. The main mechanical properties included the initial stiffness, K_I , the yield load and displacement, F_y and d_y , and the ultimate load and displacement, F_u and d_u , where failure occurred. The full set of the calculated properties is included in Tables 4.2 and 4.3.

The results showed that the epoxy joints exhibited a significantly stiffer initial behavior in tension and compression than the acrylic joints, while the latter exhibited a much higher displacement at failure in tension. In compression, the full displacement capacity could not be developed due to the premature failure in the interface, as mentioned in Section 3.1. The acrylic joints in tension exhibited much higher ultimate loads (+ 59% on average) than the epoxy joints in tension, although the former exhibited a mixed and not an adherend failure mode as the latter did. This result could be clearly attributed to the much more uniform strain distributions in the acrylic joints caused by the non-linear behavior. The epoxy joints, in contrast, exhibited much higher strain peaks, as shown above, which limited the ultimate loads. Improving the bond of the acrylic joints to also produce a pure adherend failure would further increase their ultimate loads. In compression, the epoxy joints reached similarly high ultimate loads to the acrylic joints in tension. This result could be attributed to the different location of failure initiation than in tension, as described above, which was mainly caused by the change of sign of the peeling strains from compression to tension at the inner adherend edge. If premature interface failure could have been prevented, the acrylic joints in compression, which exhibited much lower ultimate loads, would certainly have exhibited at least the same values as the epoxy joints since the strain distributions were again more uniform.

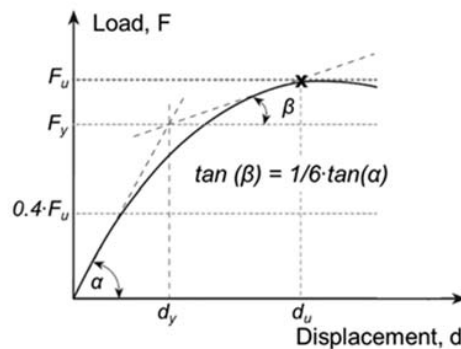


Figure 4.13: Definition of stiffness and ductility properties according to [23]

4.3.4. Joint ductility

The deformation- and energy-based ductility indexes, μ_d and μ_e , as mentioned above, were calculated for the acrylic joints, as follows:

$$\mu_d = \frac{d_u}{d_y} \quad (1)$$

$$\mu_e = \frac{1}{2} \cdot \left(\frac{E_{tot}}{E_{el}} + 1 \right) \quad (2)$$

The energy-based index was selected according to [13] and the corresponding total energy, E_{tot} , and elastic energy, E_{el} , were determined as shown in Fig. 4.14. A difficulty in calculating this index was that the required unloading path just before failure could not be experimentally captured due to the scatter of the ultimate loads, see Tables 4.2 and 4.3. Unloading was thus performed earlier, as described above, and the unloading stiffness, K_2 , as defined in Fig. 4.14, was calculated. A logarithmic relationship between the stiffness ratio K_2/K_1 and the displacement at unloading, d_{un} , could then be established, see Fig. 4.15. Based on this relationship, the stiffnesses of the unloading paths just before failure, K_2' , i.e. at $d_{un} = d_u$, were estimated and μ_e was calculated based on these values, as shown in Tables 4.4 and 4.5. This procedure also allowed the indexes of the joints for which no cycles were performed to be estimated.

The relationship between the displacement- and energy-based ductility indexes was linear, as shown in Fig. 4.16. The much lower values of the prematurely failed specimens in compression also fitted into this result. The two indexes were further exponentially related to the ultimate displacement, as shown for the energy-based index in Fig. 4.17.

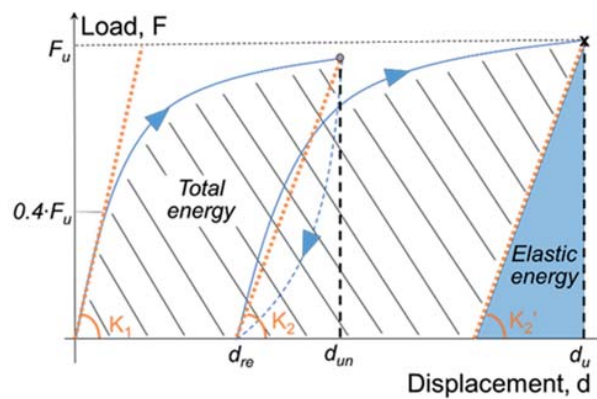


Figure 4.14: Definition of total and elastic energy

The displacement-based indexes in tension, 7.30 on average, were much higher than values given in timber codes for high ductility, e.g. [23], where high ductility is assigned to values of $\mu_d > 3.0$. Considering the energy-based definition, the tension values, 3.49 on average, are also high compared to other materials

(excluding metals), e.g. compared to 2.5 for glass-fiber-reinforced polymer (GFRP) bridge decks, adhesively bonded onto steel girders [24], or prestressed concrete beams with unbonded FRP tendons subjected to bending, whose calculated ductility index was in the range of 2-5 [25].

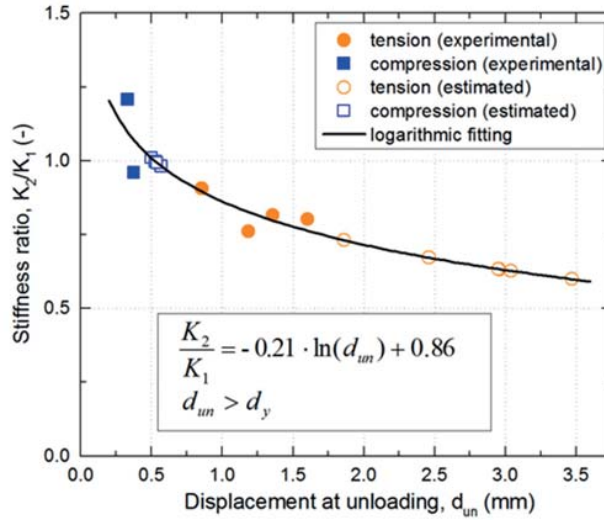


Figure 4.15: Relationship between stiffness ratio K_2/K_1 and displacement at unloading, d_{un}

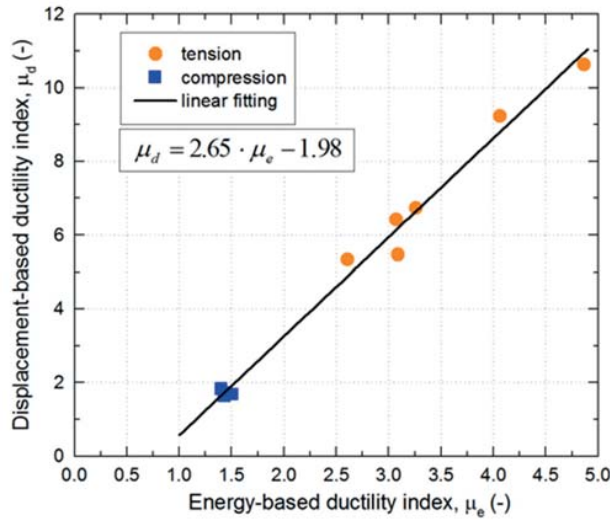


Figure 4.16: Relationship between energy- and displacement-based ductility index

Table 4.4: Displacement- and energy-based ductility indexes of acrylic joints in tension

Specimen	Load at unloading	Displacement at unloading	Unloading stiffness (kN/mm)		Total energy	Elastic energy	Displacement -based ductility	Energy-based ductility
			Experimental	Estimated				
	F_{un} (kN)	d_{un} (mm)	K_2	K_2'	E_{tot} (J)	E_{el} (J)	μ_d (-)	μ_e (-)
A_T1	50.05	1.19	95.88	79.04	144.24	20.25	9.24	4.06
A_T2	-	-	-	75.65	154.61	28.02	6.73	3.26
A_T3	55.11	1.60	79.75	62.99	155.18	30.16	6.41	3.07
A_T4	-	-	-	94.88	78.46	15.16	5.47	3.09
A_T5	52.06	0.86	126.36	83.51	226.43	25.92	10.63	4.87
A_T6	49.74	1.36	80.49	66.26	98.40	23.36	5.33	2.61
AV	51.74	1.25	95.62	77.06	142.89	23.81	7.30	3.49
$\pm SD$	± 2.14	± 0.27	± 18.88	± 10.64	± 47.26	± 5.00	± 1.97	± 0.75

Table 4.5: Displacement- and energy-based ductility indexes of acrylic joints in compression

Specimen	Load at unloading	Displacement at unloading	Unloading stiffness (kN/mm)		Total energy	Elastic energy	Displacement -based ductility	Energy-based ductility
			Experimental	Estimated				
	F_{un} (kN)	d_{un} (mm)	K_2	K_2'	E_{tot} (J)	E_{el} (J)	μ_d (-)	μ_e (-)
A_C1	-	-	-	100.25	9.90	5.18	1.72	1.46
A_C2	-	-	-	90.98	12.36	6.63	1.64	1.43
A_C3	34.07	0.33	134.13	110.93	13.40	7.41	1.83	1.40
A_C4	35.28	0.38	122.93	127.42	15.70	7.79	1.68	1.51
AV	34.68	0.35	128.53	107.39	12.84	6.75	1.72	1.45
$\pm SD$	± 0.61	± 0.02	± 5.60	± 13.55	± 2.08	± 1.00	± 0.07	± 0.04

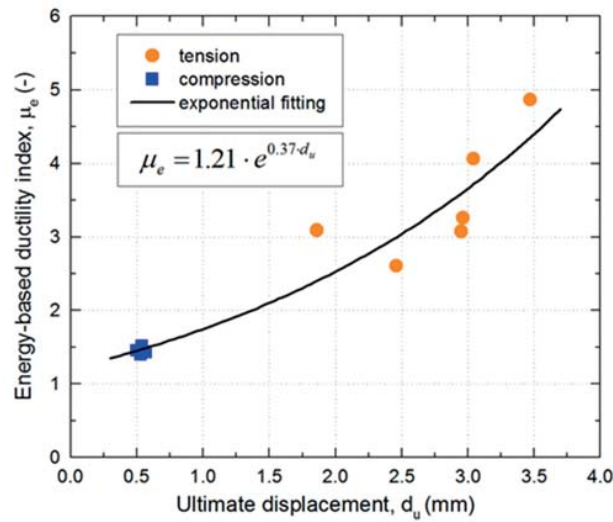


Figure 4.17: Relationship between energy-based ductility index and ultimate displacement

4.3.5. Ultimate load prediction

The Norris failure criterion for wood [26] was applied to predict the ultimate loads of those joints that failed in the wood (epoxy joints in tension) or exhibited mixed failure mode (acrylic joints). Since the strain fields were measured, a strain-based formulation was selected as follows:

$$\frac{\varepsilon_{xx}^2}{X^2} + \frac{\varepsilon_{yy}^2}{Y^2} + \frac{\varepsilon_{xy}^2}{S^2} - \frac{|\varepsilon_{xx} \cdot \varepsilon_{yy}|}{X \cdot Y} \leq 1 \quad (3)$$

where the numerators of the fractions represent the measured tensile, ε_{xx} , peel, ε_{yy} , and shear strains, ε_{xy} , while the denominators indicate the corresponding failure strains, which were obtained from literature (see Table 4.6). In compression, they were assumed to be the elastic strain limits [20], as no ultimate failure occurred. The shear failure strain was derived from the corresponding elastic strength limit (10 MPa) and the G-modulus for the xy-plane (690 MPa) [19], since no other data on shear was available.

Table 4.6: Failure strains for spruce [¹27, ²20, ³19]

Failure strain // fibers, X (-)		Failure strain \perp fibers, Y (-)		Shear, S (-)
Tension	Compression	Tension	Compression	
0.010 ¹	0.070 ²	0.010 ¹	0.040 ²	0.014 ³

The criterion was applied to the measured full strain fields, as shown in Figs 4.18 and 4.19 for an epoxy and an acrylic joint, in each case just before and after the peak load. In the epoxy case (specimen E_T3), values reaching or exceeding 1.0 were obtained just before the peak load at the location where failure initiation in the wood was observed, i.e. at the overlap end in the inner adherend just below the adhesive. Since the joint only partially failed at the peak load, extended areas developed along the crack zone where the criterion also reached or exceeded the 1.0-value. In the case of the acrylic joint (A_T5), the DIC targets on the outer adherends were lost before the peak load. Again, values ≥ 1.0 were obtained at the location where failure initiated at the overlap end below the adhesive. Several further zones of values ≥ 1.0 developed – however, they were located on the adhesive layers, which exhibited much higher strains than the wood (see above) – these zones are thus not indicative. After the peak load and complete separation of the joint, the targets on the left side of the crack were also lost. The remaining specimens showed similar results, i.e. locations of crack initiation and ultimate load levels were well predicted in most cases.

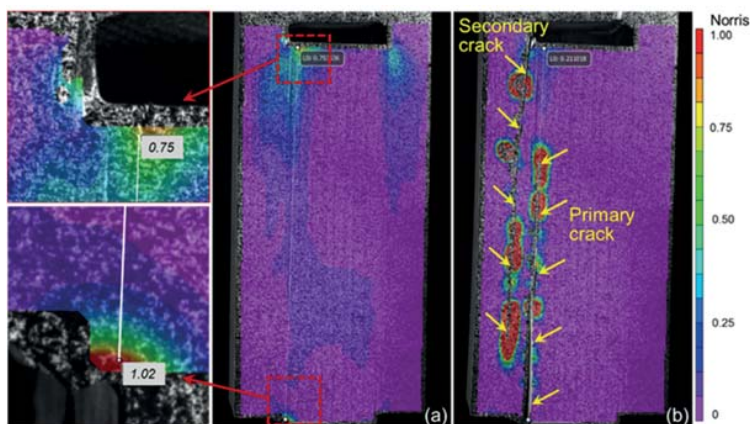


Figure 4.18: Norris criterion
(a) just before and
(b) after peak load
(joint partially failed),
for epoxy joint (E_T3)

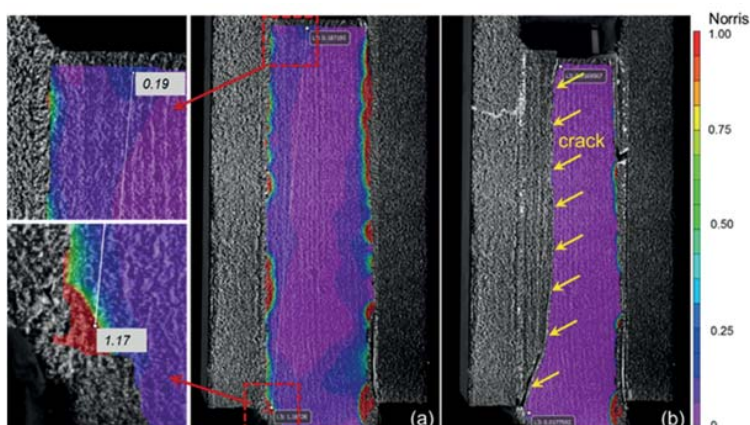


Figure 4.19: Norris criterion
(a) just before and
(b) after peak load
(joint completely failed),
for acrylic joint (A_T5)

4.4. Conclusions

Bonded double-lap timber joints have been experimentally studied in tension and compression, using two different structural adhesives; a brittle epoxy and a ductile acrylic adhesive. The main conclusions of this study can be summarized as follows:

- Epoxy-bonded joints exhibited a stiff linear load-displacement response up to brittle failure. Failure occurred in the inner adherend while the location of failure initiation in tension and compression was different and significantly influenced the ultimate load, i.e. ultimate loads in compression were much higher than in tension.
- Acrylic-bonded joints showed a highly non-linear and ductile load-displacement response in tension. The ultimate loads were much higher than those of the epoxy joints. In compression, they exhibited a premature interface failure.
- The much higher ultimate loads of the acrylic joints could be attributed to the much more uniform strain distributions along the overlap length caused by the nonlinearity and concentration of the deformations in the adhesive layers.
- The angles of principal strains along the adhesive layers were independent of the load level in both joint types. The angles were however much less uniform and smaller in the epoxy joints (20° on average, with respect to the loading axis) than in the acrylic joints (45° on average).
- Displacement- and energy-based ductility indexes were derived for the ductile acrylic joints in tension. The joints exhibited high ductility compared to other materials and structural components.

In a next step, numerical models will be developed to describe the different behaviors of the two joint types. In the modelling of the acrylic joints, in particular, the high strain rate dependency of the adhesive properties will be taken into account.

References

- [1] Tannert, T., Vallée, T., & Hehl, S. Temperature dependent strength of adhesively bonded timber joints. In Proceedings of the International Conference on Wood Adhesives (pp. 76-80), (2009, September).
- [2] De Castro J.: “System ductility and redundancy of FRP structures with ductile adhesively-bonded joints”, EPFL PhD Thesis no 3214, Lausanne (2005).
- [3] Lehmann M., Vallée T., Tannert T., Brunner M. “Adhesively bonded joints composed of wooden load-bearing elements”, 12th International Conference on Fracture (2009), ICF-12, p: 2741-2749, Ottawa, ON.
- [4] Tannert T., Vallée T., Hehl S. “ Experimental and numerical investigations on adhesively bonded hardwood joints”, International Journal of Adhesion and Adhesives (2012), Vol. 37, p: 65-69
- [5] Banea M. D., da Silva L. F. M. “Mechanical characterization of flexible adhesives”, Journal of Adhesion, Vol.85, Issue: 4-5, p: 261-285 (2009).
- [6] Keller T, De Castro, J. “System ductility and redundancy of FRP beam structures with ductile adhesive joints”, Composites Part B: Engineering, Vol. 36, Issue 8, p: 586-596 (2005).
- [7] Hart-Smith, L. J. Adhesive-bonded double-lap joints. National Aeronautics and Space Administration (NASA), (1973).
- [8] Park R., Pauley T. “Reinforced Concrete Structures”, John Wiley and Sons, New York, United States of America (1975).
- [9] Baker JF, Horne MR., Heyman J. “Plastic behavior and design, the steel skeleton”, vol.2, UK: Cambridge University Press (1956).
- [10] Yanes-Armas S., de Castro J., Keller T. Energy dissipation and recovery in web-flange junctions of pultruded GFRP decks. Composite Structures, (148) p: 168-180 (2016).
- [11] Grace NF., Soliman A., Abdel-Sayed G., Saleh K. Behavior and ductility of simple and continuous FRP reinforced beams. J Compos Constr, 2(4) p: 186–94 (1998).
- [12] De Lorenzis L., Galati D., La Tegola A. Stiffness and ductility of fibre-reinforced polymer-strengthened reinforced concrete members. Proc. ICE-Struct. Build, 157(1) p: 31–51 (2004).
- [13] Naaman A.E., Jeong S.M. Structural ductility of concrete beams prestressed with FRP tendons, Nonmetallic (FRP) reinforcement for concrete structures, Proc. of the second international RILEM symposium (FRPRCS-2) p: 379-386 (1995).
- [14] Vallée T, Tannert T, Hehl S. “Ductile adhesively bonded timber joints”, Wood Adhesives, Session 4B, p: 315-318 (2009).
- [15] Sika AG. SikaDur-330: 2-part epoxy impregnation resin (2006).
- [16] Sika AG. SikaFast5221 NT: Fast-curing 2-component structural adhesive. Zurich (2013).

- [17] Angelidi M., Vassilopoulos A. P., Keller T. Ductility, recovery and strain rate dependency of an acrylic structural adhesive. *Construction and Building Materials*, (140) p: 184-193 (2017).
- [18] Angelidi M., Vassilopoulos A. P., Keller T. Displacement rate and structural effects on Poisson ratio of a ductile structural adhesive under tension and compression. *International Journal of Adhesion and Adhesives*, (2017).
- [19] Dinwoodie J. M. Timber - a review of the structure-mechanical property relationship. *Journal of Microscopy*, 104(1), 3-32. (1975).
- [20] Zhong W., Rusinek A., Jankowiak T., Huang X., & Farid A. B. E. D. Experimental and Numerical Investigation on Compression Orthotropic Properties of Spruce Wood in Axial and Transverse Loading Directions. *Engineering Transactions*, 62(4), p: 381-401 (2015).
- [21] Correlated Solutions Inc. (2010). *Vic-3D Manual*. Columbia, SC.,
- [22] Sutton Michael A, Orteu Jean Jose, & Schreier Hubert. (2009). *Image correlation for shape, motion and deformation measurements: basic concepts, theory and applications*: Springer Science & Business Media.
- [23] SIA. "265–Timber structures." Swiss Standards Association (2003).
- [24] Keller T., Gürtler H. Composite action and adhesive bond between FRP bridge decks and main girders. *Journal of Composites for Construction*, 9(4) p: 360-368 (2005).
- [25] Jo B. W., Tae G. H., Kwon B. Y. Ductility evaluation of prestressed concrete beams with CFRP tendons. *Journal of reinforced plastics and composites*, 23(8) p: 843-859 (2004).
- [26] Norris C. B. *Strength of orthotropic materials subjected to combined stresses*, Madison: U.S. Department of Agriculture (1962).
- [27] Farajzadeh Moshtaghin A., Franke S., Vassilopoulos A. P., & Keller T. Spatial variability in longitudinal elastic modulus of clear timber. *Euromech Colloquium 556*, Dresden, Germany (2015).

Chapter 5

Ductile adhesively-bonded timber joints: Strain rate effect

The mechanical behavior of adhesively-bonded timber joints, composed of a ductile acrylic or a brittle epoxy adhesive, was numerically modeled. The models took the strain rate sensitivity of the ductile adhesive into account. They were validated by experimental results and the effect of a varying joint displacement rate on the responses of the ductile joints was subsequently numerically studied. At the same joint displacement rate, the true strain rates in the acrylic adhesive layer varied significantly throughout the loading process and along the adhesive layer. Increasing the joint displacement rate shifted the load-displacement curve upwards, i.e. the yield load and displacement increased, the ultimate load and displacement however decreased, while the joint stiffness was not affected. A logarithmic relationship between these loads and displacements and the displacement rate was observed. The energy- and displacement-based ductility indexes of the acrylic joints decreased with increasing displacement rate, changing the joint behavior from ductile to brittle at higher rates.¹

Keywords: *acrylics, adhesive, ductility, epoxy, joint, spruce, timber, finite element*

¹ Angelidi M. & Keller T. Ductile adhesively-bonded timber joints – Strain rate effect (under review).

5.1. Introduction

Joints between structural components represent one of the most critical elements in timber structures regarding structural safety and deformability. Adhesively-bonded joints, though still rarely used, may offer many advantages over mechanical joints (e.g. made using steel bolts), since they can offer higher efficiency due to more uniform stress distribution in the timber adherends [1, 2], higher stiffness due to the absence of hole tolerances [3], which also leads to better fatigue strength [4] and improved durability due to complete sealing [5]. In addition, since adhesive bonding requires only simple tooling and consumes small amounts of energy, it can represent a cost-effective alternative to other joining methods [6].

Furthermore, ductile adhesives, such as commercial acrylics, may compensate for the lack of inherent ductility of timber materials [7]. If used in joints they can provide ductility at the system level. Ductility is understood as the ability to sustain inelastic deformations prior to failure without loss of resistance. If adequately provided, ductility can thus substantially increase structural safety [8, 9]. Ductility can be evaluated and quantified based on two main approaches; the displacement-based ductility index, which is the ratio between the ultimate and yield displacements, and the energy-based index, which considers the ratio of the total energy (equal to the total area under the load-displacement curve) and the elastic energy (released during unloading) [7 and 10].

There are however few studies that investigate the mechanical and structural behavior of ductile adhesively-bonded joints [11, 12, 13, 14, 15, 16], and even fewer in the field of timber engineering [17]. In the latter case, works are limited to parametrical studies on the effects of geometry and material properties on the load capacity [18]. They do not specifically consider the adhesive's non-linear and viscoelastic nature; i.e. the high strain rate dependency in particular of the adhesive's structural response and ductility are not addressed. In the field of adhesively-bonded joints with fiber-reinforced polymer (FRP) adherends it has been shown that the strain rate can significantly affect the load-displacement behavior and joint strength [15, 16, 19], while the initial stiffness may be less influenced [15]. If the rate-dependency can affect the behavior of FRP composite joints, which are generally much stiffer than timber joints, rate dependency can be expected to have exert more influence in timber joints. Furthermore, in timber applications, the applied rates may vary significantly depending on the load and structure type; much higher rates may apply for bridges or buildings in the case of vehicular or wind loads than in the case of pedestrian or snow loads.

In the current research, experiments on full-scale ductile acrylic-bonded timber joints have already been conducted and their performance has been compared with that of brittle epoxy-bonded joints; a non-linear response, higher ultimate loads due to the more uniform strain distributions along the adhesive layer [9] and considerable ductility were observed in the ductile adhesive joints [8, 9]. Furthermore, concerning the ductile acrylic adhesive, strain rate-dependent true stress-strain relationships were experimentally

established [7], including the rate effect on the Poisson ratio [20]. The experimental basis for the modeling of rate-dependent ductile adhesively-bonded timber joints has already been established.

The objective of this work is thus to 1) numerically model the experimentally observed load- displacement and strain responses and ultimate loads of the brittle (epoxy) and ductile (acrylic) joints. In the latter case, the highly non-linear and strain rate-dependent responses of the ductile adhesive are taken into account. The established and experimentally validated models will then be used to 2) study and quantify the displacement rate effect on the load-displacement responses, ultimate loads and joint ductility.

5.2. Summary of experimental set-up

Since the numerical models developed in the following will be validated with experimental results from the above-mentioned previous work [8, 9], the information concerning the experimental set-up required to retrace this validation process is briefly summarized. The experimental program included 19 full-scale, adhesively-bonded double-lap joint specimens subjected to axial tension and compression. However, the modeling presented here was limited to the 11 joints loaded in tension. Norway spruce wood and two different commercial adhesives were used: a brittle epoxy adhesive, SikaDur330, in five joints, and a ductile acrylic adhesive, SikaFast5221NT, in six joints; both adhesives were obtained from Sika AG, Switzerland [21, 22]. In contrast to the stiff epoxy adhesive, the flexible acrylic adhesive exhibited a high strain rate sensitivity as mentioned above. The true stress-strain responses from five different displacement (or engineering strain) rates, shown in Fig. 5.1, were obtained in the previous work [20]. The tensile stiffness properties of all materials are summarized in Tables 5.1 and 5.2.

The joint geometry is shown in Fig. 5.2; the total joint specimen length and width were 970 and 50 mm and the thickness of the adhesive layer was 2 or 3 mm for epoxy and acrylic joints respectively. An extra layer of 0.5 mm was added in the acrylic joints to improve adhesion. The specimens were axially loaded in tension up to failure at a displacement rate of 1 mm/min, see Fig. 5.3. For the acrylic specimens one unloading-reloading cycle, at the same displacement rates, was performed after the specimen had already entered the post-yield region.

The machine's load cell and two linear variable displacement transducers (LVDTs), symmetrically placed on both sides of the specimens, were used to measure the load and displacement (elongation) of the joints. Half of the averaged joint displacements, i.e. those of one overlap (distance between points 1 and 2 in Fig. 5.2) are compared in the following. In addition, full-field 3D displacements were measured using a Digital Image Correlation (DIC) system. The joint specimens were labeled according to the adhesive (E for epoxy and A for acrylic), type of loading (T for tension) and number of the specimen, e.g. A_T2 denotes the second (2) acrylic (A) joint in tension (T).

Table 5.1: Orthotropic tensile properties of spruce wood [23]

E_x (MPa)	E_y (MPa)	E_z (MPa)	ν_{xy} (-)	ν_{yz} (-)	ν_{xz} (-)	G_{xy} (MPa)	G_{yz} (MPa)	G_{xz} (MPa)
11600	896	496	0.4	0.04	0.4	690	758	390

Table 5.2: Tensile properties of acrylic (rate-dependent) [20] and epoxy adhesive [2]

Adhesive	Displacement rate, \dot{d} (mm/min)	Eng. strain rate, $\dot{\epsilon}$ (min^{-1})	E-modulus, E_I (MPa)	Poisson ratio, ν (-)
Acrylics	2	0.0174	105	0.48
	10	0.0870	181	
	50	0.4348	251	
	100	0.8696	307	
	200	1.7391	309	
Epoxy	5	0.0625	4500	0.37

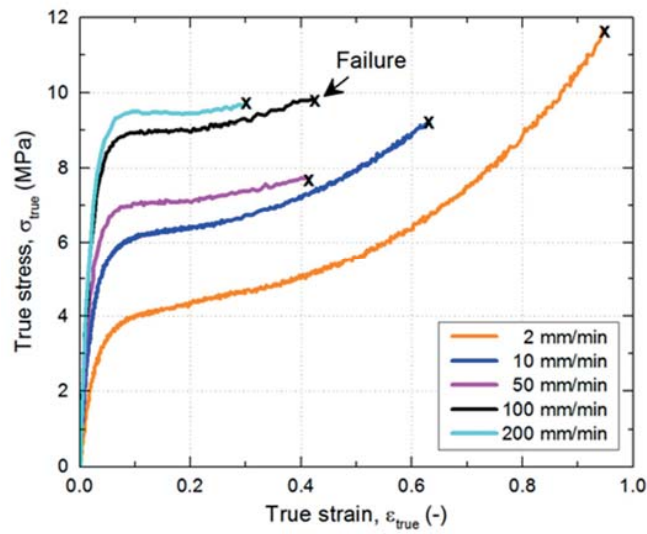


Figure 5.1: Displacement rate-dependent true stress-strain curves of acrylic adhesive [20]

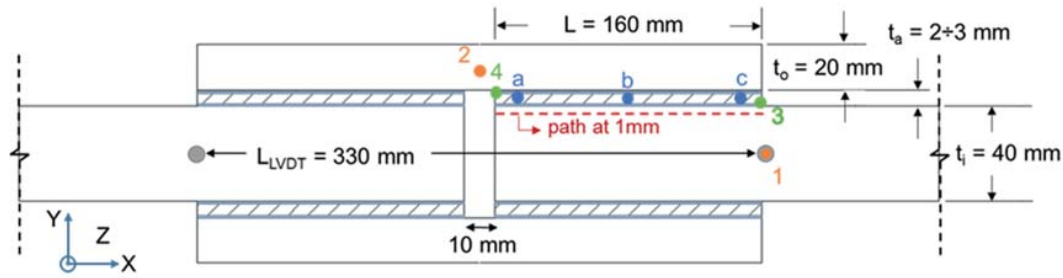


Figure 5.2: Schematic joint representation and points selected for comparisons

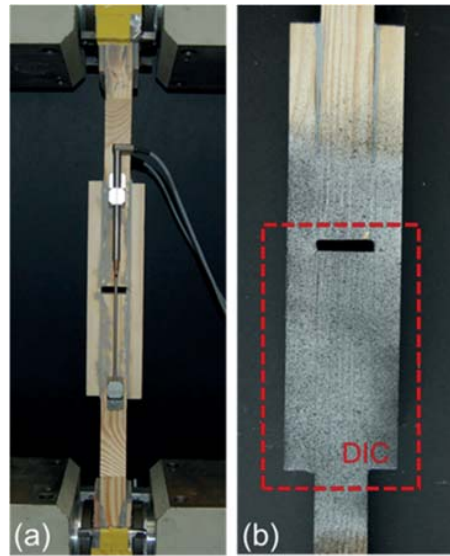


Figure 5.3: Experimental set-up using (a) LVDTs and (b) Speckle pattern of DIC system [9]

5.3. Numerical models

Finite element (FE) models for both joint types were developed in the commercial Finite Element Analysis software Abaqus 6.14. Quadratic, 2D plane-strain solid 4-node elements with reduced integration (CPE4R) were used. The general element size was selected as 0.5 mm (equal to the minimum epoxy layer in the case of acrylic joints), but was increased to 5 mm further away from the interfaces or edges, see Fig. 5.4. These sizes were selected after conducting mesh size sensitivity checks.

Elastic orthotropic material properties, according to Table 5.1 [23], were selected for the timber adherends. The epoxy adhesive was modeled as being elastic isotropic, using the properties shown in Table 5.2. For the acrylic adhesive, a non-linear elastoplastic model was adopted, allowing different strain rates to be taken into account. For each of the above-mentioned five experimental (engineering) strain rates, the complete true stress-strain curve, as shown in Fig. 5.1, was provided as input in the form of a table. Based on an iterative process, the software selected the material properties for each displacement added, based

on the previously attained strain rate. The model assumed similar behaviors in tension and compression and calculated shear properties based on the Poisson ratio.

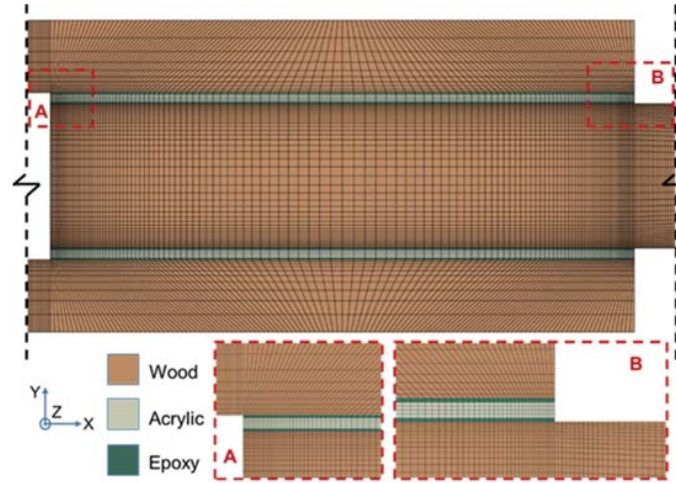


Figure 5.4: Detail (one overlap) of FE model for acrylic joint specimens

Table 5.3: Rate effect on joint properties

Specimen	Displ. rate, \dot{d} (mm/min)	Yield		Ultimate		Adhesive 1 st principal true strain rate (point <i>b</i>)	
		Load, F_y (kN)	Displ., d_y (mm)	Load, F_u (kN)	Displ., d_u (mm)	(pre-yield) $\dot{\epsilon}_A$ (min-1)	(post-yield) $\dot{\epsilon}_B$ (min-1)
AT_0.1x	0.05	35	0.35	65	2.7	0.002	0.012
AT_1x	0.5 (exp.)	45	0.42	60	1.6	0.040	0.119
AT_10x	5	60	0.56	57	0.7	0.304	1.186
AT_1000x	500	86	0.75	40	0.4	19.6	159.4

Similarly to the experiments, the model was loaded in displacement mode, using ramp amplitude, which signifies a uniform rate of loading. The displacement was applied on one end of the joint, while the other end remained fixed. The total defined time of the applied displacement varied for the acrylic joints in order to achieve different displacement rates. The displacement rate corresponding to the experimental investigation on half of the joint (one overlap) was 0.5 mm/min. In addition to this case (designated AT_1x), three more models were run at different rates designated accordingly: at 10 times lower (AT_0.1x), and 10 (AT_10x), and 1000 (AT_1000x) times higher rates, see Table 5.3. The lower bound was limited to avoid interfering with creep effects and the upper bound was limited by the available experimental rate-dependent results. Subsequently, for each case, a suitable number of substeps (displacement increments) was defined in order to minimize the total analysis time without any convergence problems.

5.4. Numerical model validation

5.4.1. Load-displacement responses

The numerically and experimentally obtained load-displacement responses are shown in Figs. 5.5 and 5.6 for the epoxy and acrylic joints respectively. Concerning the epoxy joints, the numerical result lay within the (large) scatter band of the experimental responses. There was good agreement between the numerical and experimental results of the acrylic joints. The model was able to trace the stiffness changes after yielding.

The ratio of the adhesive layer displacement (elongation) over the total joint displacement (i.e. ratio between points (3-4)/(1-2) elongations in Fig. 5.2) is shown in Fig. 5.7 (A/ET_{1x} curves). At low displacements, 78% of the total displacements occurred in the adhesive layers, independent of adhesive type, i.e. although the adhesive elastic modulus, E_I , was very different, see Table 5.2. The adhesive layer contribution of the epoxy joint did not change with increasing load, in contrast to the acrylic joint, where the contribution started increasing as yielding was approached and further increased to 96% at high displacements.

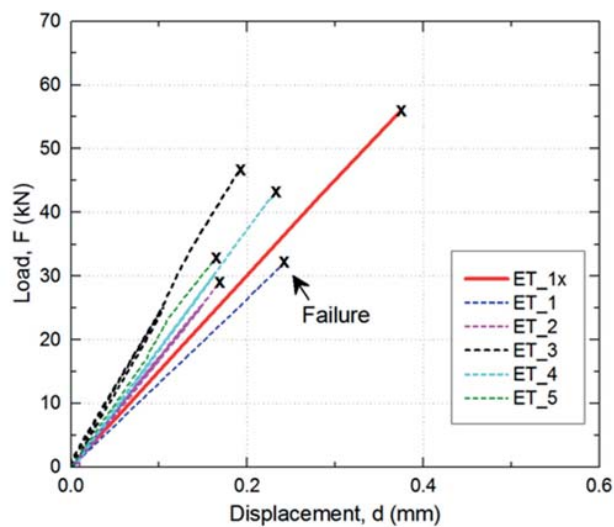


Figure 5.5: FE model validation: numerical and experimental load-displacement responses of epoxy joints

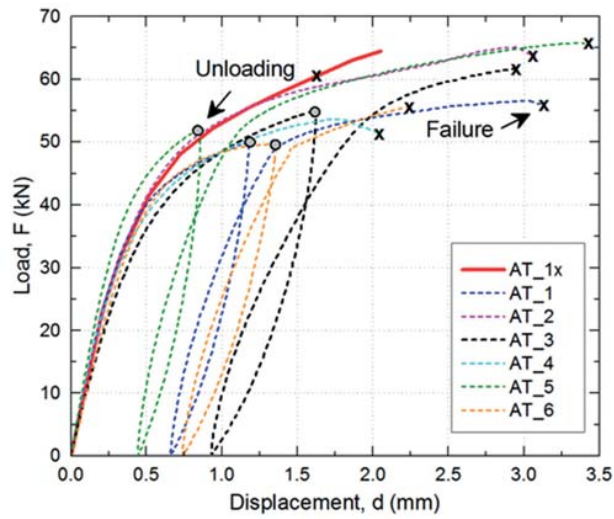


Figure 5.6: FE model validation: numerical and experimental load-displacement responses of acrylic joints

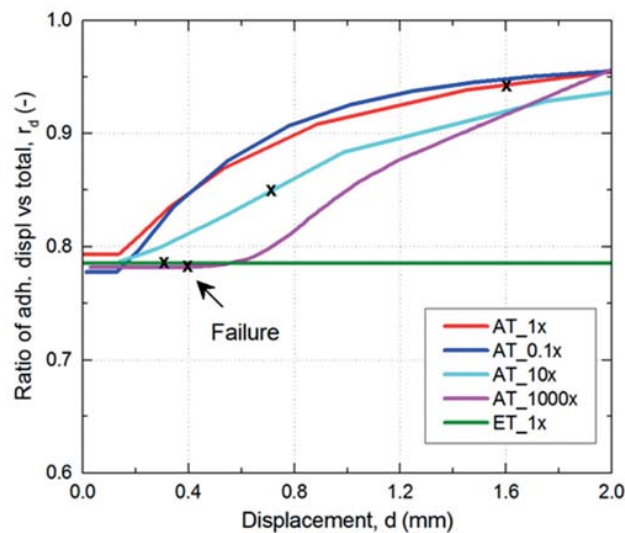


Figure 5.7: Percentage of displacement resulting from adhesive layer

5.4.2. Stress and strain distributions

In order to further validate the numerical models, experimental and numerical strain distributions (tensile, shear and peel strains) are compared in Fig. 5.8. They were derived along the adhesive overlap, in the inner timber adherend at 1-mm depth below the adhesive (where failure occurred in the acrylic joints, see Fig. 5.2), at the same load of 40 kN. The experimental values were obtained from the DIC measurement on the lateral specimen surfaces. Taking into account the significant local variability in the timber stiffness properties [24], an acceptable agreement was observed. This agreement in the linear epoxy system was

slightly better than in the non-linear acrylic system, where the high sensitivity to the strain rate was also taken into account.

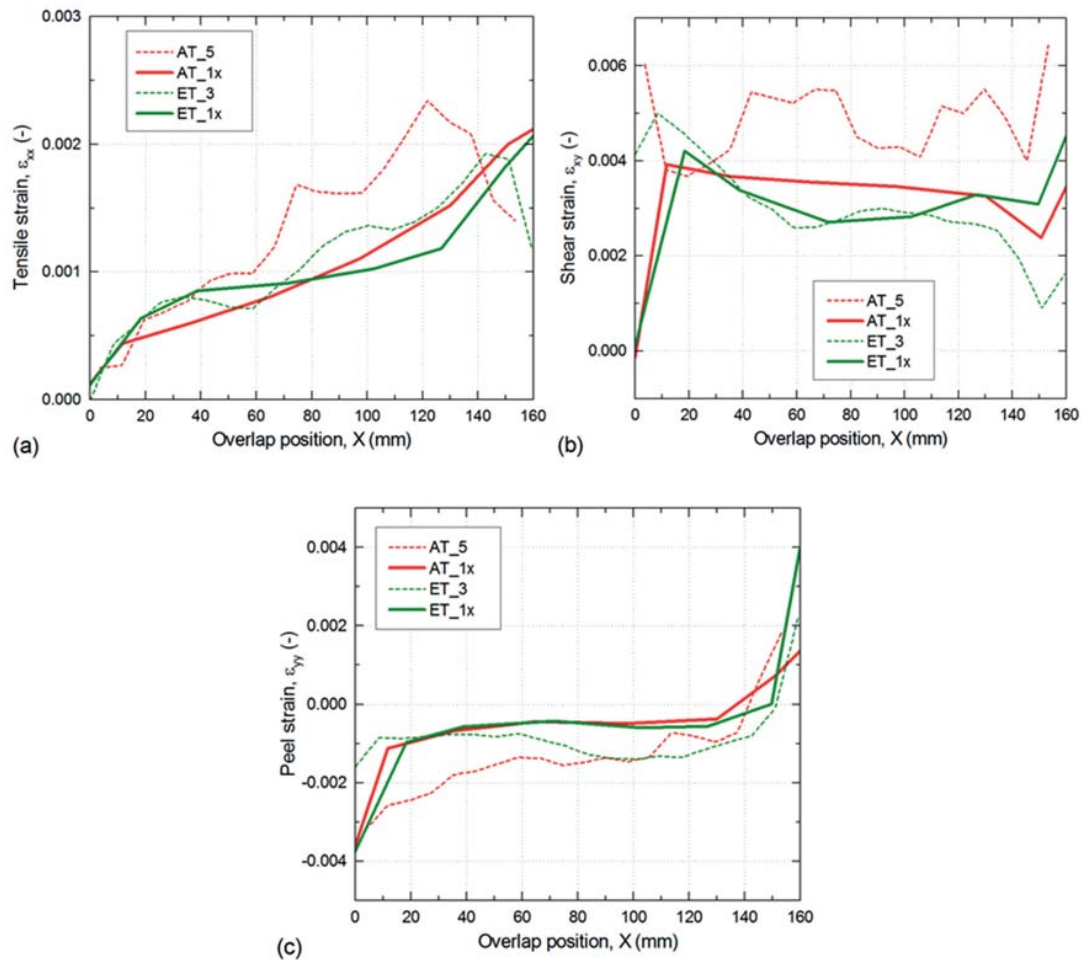


Figure 5.8: FE model validation: numerical and experimental strain distributions along overlap, at 1-mm depth below adhesive and 40 kN load, a) tensile, b) shear, c) peel (through-thickness) true strains

Corresponding to the above strain distributions, the numerically obtained stress distributions (tensile, shear and peel stresses) are shown in Fig. 5.9, along the same path, but at the predicted ultimate loads (see below), i.e. at 51 kN for the epoxy (Fig. 5.3) and 60 kN (Fig. 5.4) for the acrylic joints at the experimental displacement rate. The conclusions drawn in [19] were confirmed, i.e. the shear stress distribution in the acrylic joint was much more uniform than in the epoxy joint. During loading, stresses were redistributed due to the non-linear behavior from the peaks at the edges to the middle part, which contributed to a greater extent than in the epoxy joints, explaining the higher ultimate load.

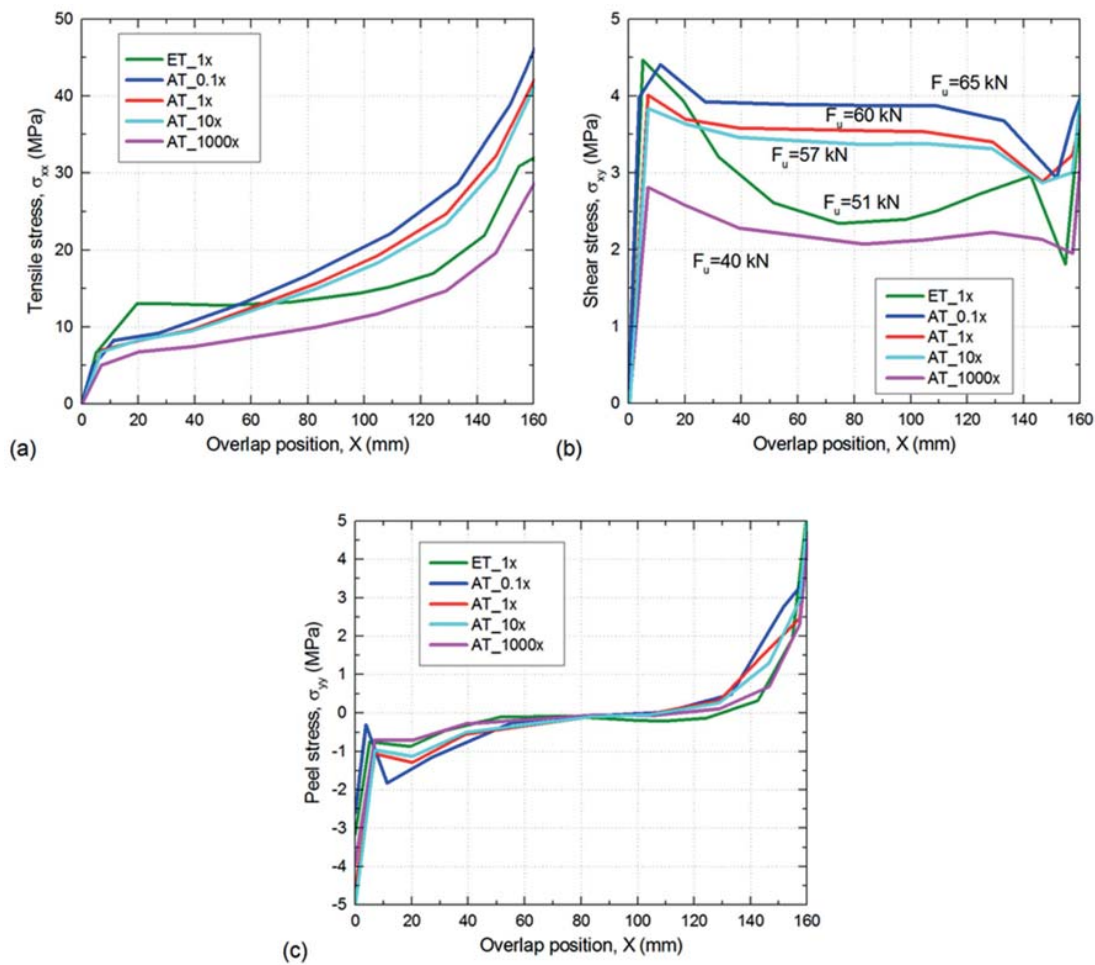


Figure 5.9: Stress distributions along overlap, at 1-mm depth below adhesive and (rate-dependent) ultimate load, a) tensile, b) shear, c) peel (through-thickness) stresses

A further model validation was possible by comparing experimental (DIC) and numerical principal strains and their orientation (angle), see Figs. 5.10 and 5.11. The experimental results were confirmed - the differences in the strain magnitudes between the timber and adhesives were much smaller in the epoxy than in the acrylic joint. Furthermore, in the case of the epoxy joint, the angle of the first principal strains along the adhesive layer increased significantly from 20° to 38° , as the loaded edge of the joint (point c in Fig. 5.2) was approached, while the much larger angle of the acrylic joint did not significantly change and varied between 40 and 45° , exhibiting a slightly decreasing trend with increasing displacement however. The experimental and numerical results for both joint types agreed well.

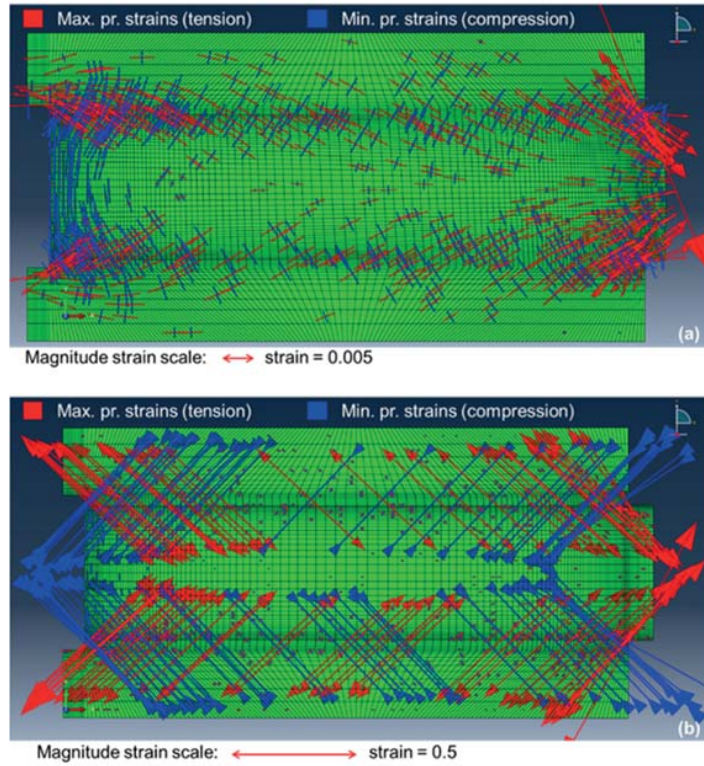


Figure 5.10: Numerical principal strain distributions at 40 kN for a) epoxy and b) acrylic joints

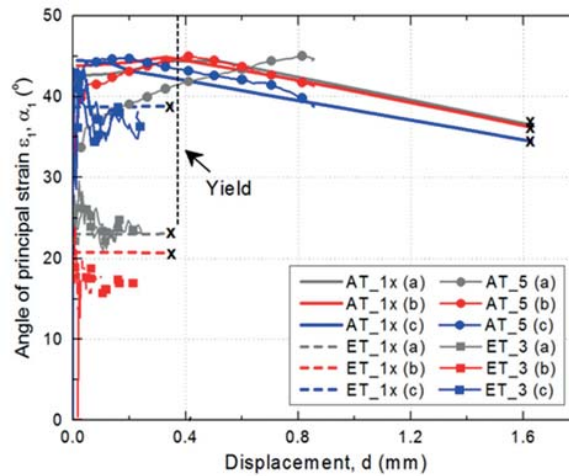


Figure 5.11: FE model validation: numerical and experimental 1st principal strain angle in adhesive layers at three different locations (a, b, c, see Fig. 5.2)

5.4.3. Ultimate load prediction

In the previous experimental work [9], a strain-based version of the typical Norris failure criterion [25] used for wood was applied to predict the joint ultimate loads based on the DIC measurements. In the following, the criterion will be applied stress-based using the numerically obtained stresses, σ , and the corresponding timber strength for all three directions as follows:

$$\frac{\sigma_{xx}^2}{X^2} + \frac{\sigma_{yy}^2}{Y^2} + \frac{\sigma_{xy}^2}{S^2} - \frac{|\sigma_{xx} \cdot \sigma_{yy}|}{X \cdot Y} \leq 1 \quad (1)$$

The directions are shown in Figure 5.4; tensile (xx) - parallel to the applied displacement and grain direction of the timber, peel (yy) and shear (xy). The corresponding timber strength values (considering the elastic limits of timber deformation, before any fiber crushing) are shown in Table 5.4 (tensile X, peel Y and shear S) and were assumed as being rate-independent. The stress values were again extracted along the overlap at 1-mm depth below the adhesive (where experimental failure occurred). The resulting Norris value distribution for different loads of the acrylic joint is shown in Fig. 5.12. The critical 1.0 value was slightly exceeded at 60 kN, at the right edge, where the through-thickness tensile (peel) stresses reached their maximum, as shown in Fig. 5.9. This value agreed well with the experimental values, however, the corresponding displacement was smaller, see Fig. 5.6. Similarly, the ultimate load was predicted for the epoxy joint, i.e. 51 kN, which slightly exceeded the experimental values shown in Fig. 5.5. Again it should be noted that the timber properties can locally vary significantly [24], which was confirmed by the large scatter in the experimental results.

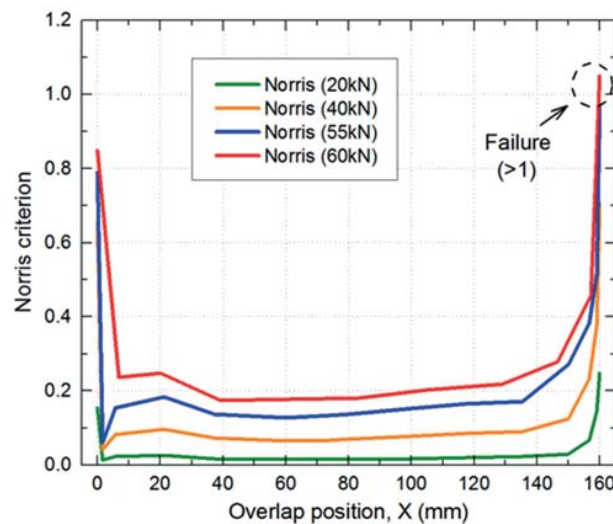


Figure 5.12: Norris ultimate load prediction for acrylic joint based on FE model stresses along overlap at 1-mm depth below adhesive layer

Table 5.4: Strength properties of spruce wood [26]

Strength // fibers, X (MPa)		Strength \perp fibers, Y (MPa)		Shear, S (MPa)
Tension	Compression	Tension	Compression	
70	45	4	5	10

5.4.4. Ductility indexes

Displacement- and energy-based ductility indexes were defined and quantified based on the experimental results in [8, 9], see Fig. 5.13. The displacement-based index, μ_d , corresponded to the ultimate/yield displacement ratio, d_u/d_y , while the energy-based value, μ_e , was obtained from $\mu_e=0.5 \cdot (E_{tot}/E_{el}+1)$, with E_{tot} being the total and E_{el} the elastic energy. The elastic energy depended on the stiffness indicated by the unloading branch of the load-displacement curve, K_2 . The numerical value of K_2 was obtained i) from the K_2/K_1 stiffness ratio relationship derived in [8, 9] and shown in Fig. 5.14, where K_1 is the initial joint stiffness, and ii) assuming the displacement at unloading as equal to the ultimate displacement, $d_{un}=d_u$. The resulting numerically-based index values are also shown in Table 5.5. Both experimentally derived ductility indexes were slightly underestimated but remained on the indicated experimental fitting line. The underestimation could be attributed to the above-mentioned underestimation of the ultimate displacement.

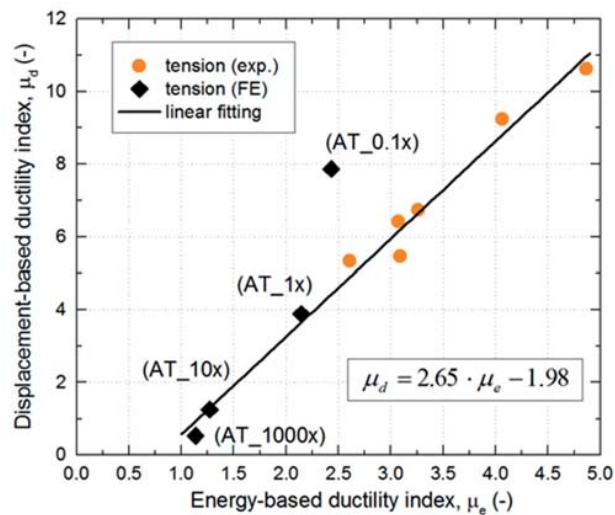


Figure 5.13: FE model validation: numerical and experimental displacement- and energy-based ductility indexes of acrylic joints

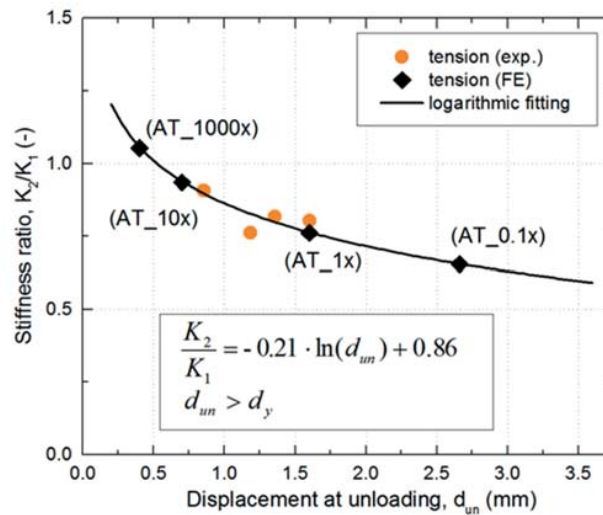


Figure 5.14: Relationship between stiffness ratio K_2/K_1 and displacement at unloading of acrylic joints [8]

Table 5.5: Rate effect on joint ductility

Specimen	Initial stiffness K_1 (kN/mm)	Stiffness ratio, K_2/K_1 (-)	Unloading stiffness, K_2 (kN/mm)	Displacement-based ductility index μ_d (-)	Energy-based ductility index μ_e (-)
AT_0.1x	100.0	0.65	65.5	7.60	2.38
AT_1x	107.1	0.76	81.2	3.88	2.15
AT_10x	107.1	0.93	100.2	1.25	1.28
AT_1000x	114.7	1.05	120.7	brittle	brittle

5.5. Rate effect on acrylic joints – parametric study

Based on the satisfactory agreement between experimental and numerical results, the models were considered sufficiently validated to perform a parametric study to evaluate the effect of slower or faster displacement rates on the acrylic joint behavior. The three additional displacement rates, as mentioned above and shown in Table 5.3, were applied to the acrylic joint model.

5.5.1. Rate effect on load-displacement responses and ultimate loads

The effect of different displacement rates on the load-displacement responses is shown in Fig. 5.15; the curve simulating the experimental rate is denominated AT_1x. The varying rates did not affect the initial stiffness of the joint, which thus remained clearly below that of the epoxy joint. The yield point and the subsequent lower stiffness branch moved upwards however for higher and downwards for lower rates. A clear rate effect on the post-yield stiffness could not be observed, which is in agreement with corresponding results from the bulk adhesive experiments performed previously [7]. Furthermore, the ultimate load (based

on the Norris criterion) and displacement clearly decreased with increasing rate and increased with decreasing rate. In the case of AT_1000x, failure even occurred before the yield point was approached.

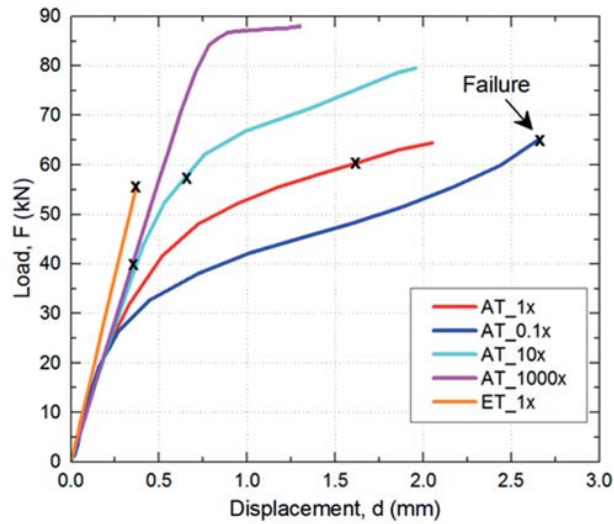


Figure 5.15: Displacement rate effect on load-displacement responses and predicted ultimate loads

The joint stiffness was thus not affected by the rate, unlike the yield displacement and load, d_y and F_y , and ultimate displacement and load, d_u and F_u . All these values are quantified in Table 5.3 and also shown in Fig. 5.16, as a function of the displacement rate. Displaying the displacement rate on a logarithmic scale resulted in a linear relationship between the latter and d_y , F_y , d_u and F_u , as was already observed in the bulk adhesive experiments [7] and similar works [27, 28]. The same relationship as used in [7] was thus applied, shown here for F_y :

$$F_y = F_0 + c \cdot \log\left(\frac{\dot{d}}{\dot{d}_0}\right) \quad (2)$$

where F_y is the yield load at any displacement rate, \dot{d} , F_0 is the yield load for a known displacement rate, \dot{d}_0 , and c is a constant defined by fitting. The resulting fitting lines agreed well with the experimental results, as shown in Fig. 5.16.

The varying displacement rate also influenced the displacement distribution between the timber adherends and adhesive layers, as shown in Fig. 5.7. The higher the imposed rate, the more the distribution in the acrylic joint approached that of the epoxy joint. In the case of AT_1000x, the distribution remained constant, and had the same value as in the epoxy joint up to failure, since the yield point was not reached. The rate dependency was not linear, the experimental and 10x lower rate (AT_0.1x) exhibited a similar distribution, while a 10x higher rate (AT_10x) had a significant influence on the distribution.

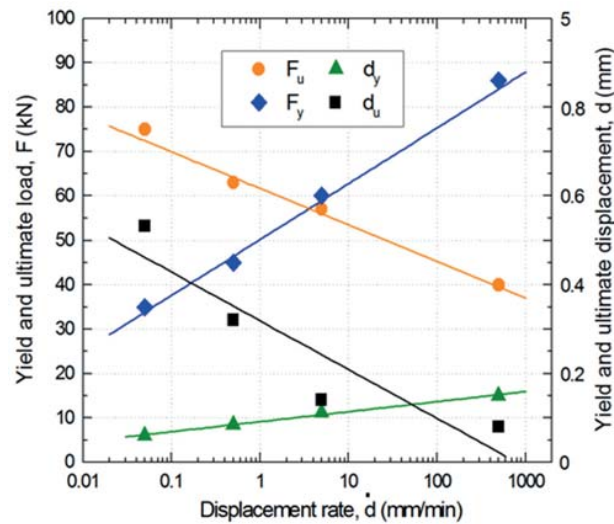


Figure 5.16: Displacement rate effect on yield and ultimate loads and displacements of acrylic joints

5.5.2. Rate effect on stress-strain responses and true strain rates

The displacement rate effect on the stress responses along the overlap length is shown in Fig. 5.9. The axial tensile stresses, σ_{xx} , and shear stresses, σ_{xy} , decreased with increasing rate, in accordance with the decreasing ultimate load, and vice versa. The effect of the displacement rate on the through-thickness (peel) stresses, σ_{yy} , however, was much smaller.

The effect of the displacement rate on the first principal true strain vs displacement and time relationship in the middle of the adhesive layer (point b in Fig. 5.2) is shown in Fig. 5.17. Both sets of curves could be approximated by a bilinear behavior and it could thus be concluded that the true strain rates were almost constant in the pre- and post-yield phases, while the true strain rate in the latter case was significantly higher, as also shown in Table 5.3 and Fig. 5.18. The relationships between the displacement and true strain rates were linear on double-logarithmic scales (corresponding to power-law relationships), and furthermore parallel, with lower values in the pre- than in the post-yielding phase.

The distribution of the first principal true strain rate along the overlap length is further also shown in Fig. 5.19, at the experimental displacement rate (AT_1x). The results show that the strain rate was non-uniformly distributed in the pre-yield phase with much higher rates at the edges than in the middle. In the post-yield phase, however, the rates were much higher (around 10x) than in the pre-yield phase, but almost constant along the length. This highlights the importance of taking the effect of the true strain rate on the mechanical properties into account.

The changes in the pre- and post-yield principal strain rates in the middle of the overlap (point b in Fig. 5.2) with changing displacement rate are shown in Fig. 5.19 and Table 5.3. On the double-logarithmic

scale, linear relationships resulted (corresponding to power-law equations); the line curves obtained for the pre- and post-yield phase were parallel.

The effect of the displacement rate on the angle of the first principal strain in the middle of the adhesive layer (point *b* in Fig. 5.2) is shown in Fig. 5.20. The angle remained at around 45° up to the yield point, which however shifted to higher displacements at higher rates, as shown in Fig. 5.15. Subsequently, the angle started decreasing as already shown in Fig. 5.11. The effect of the displacement rate was noticeable but small; at slower rates the angle remained slightly smaller, since the adhesive yielding occurred earlier and thus the angle decrease initiated in advance compared to the case with higher rates.

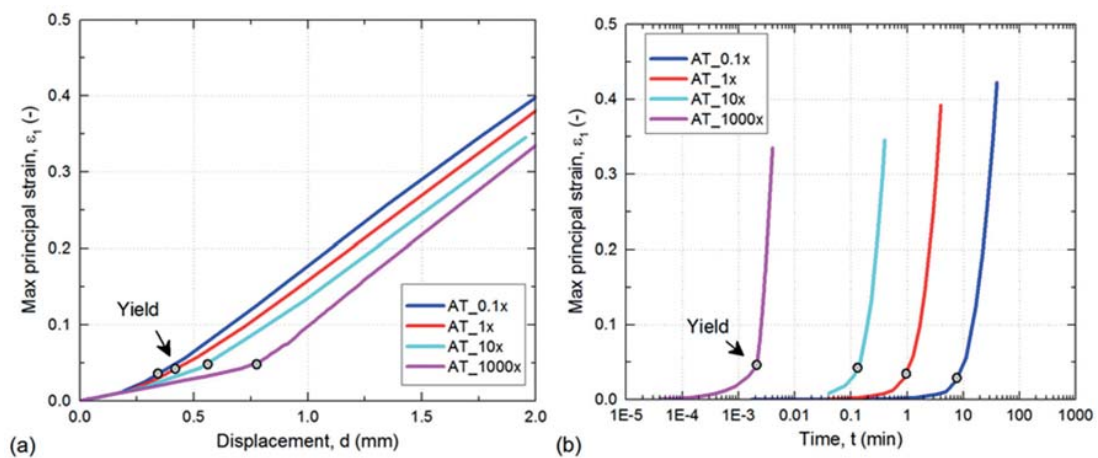


Figure 5.17: First principal true strain versus a) displacement and b) time (point *b* in Fig. 5.2)

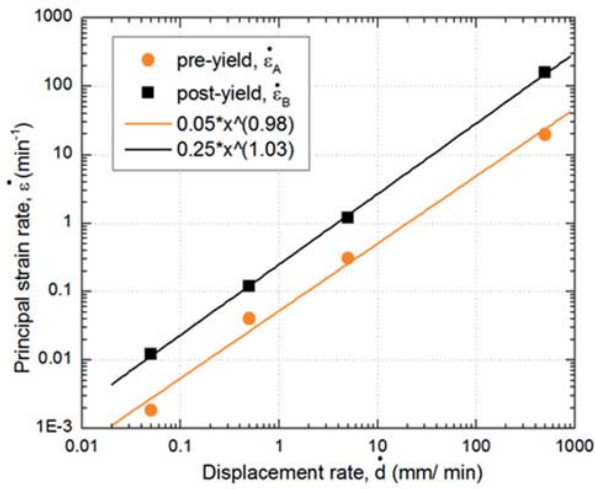


Figure 5.18: Displacement rate effect on first principal true strain rate in acrylic adhesive layer (pre- and post-yield, point b in Fig. 5.2)

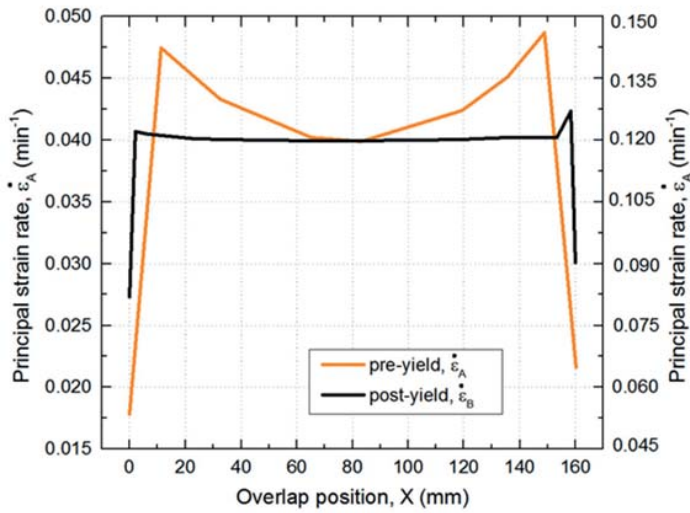


Figure 5.19: First principal true strain rate along acrylic adhesive layer (pre- and post-yield, AT_1x)

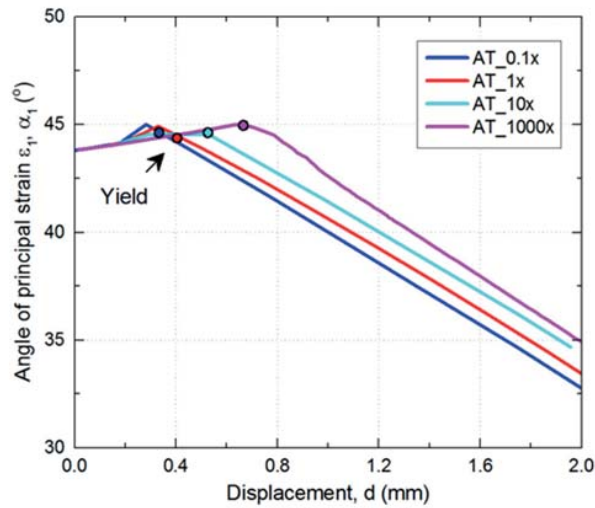


Figure 5.20: Displacement rate effect on first principal strain angle in acrylic adhesive layer (point b in Fig. 5.2)

5.5.3. Rate effect on ductility

The displacement- and energy-based ductility indexes were calculated for the different displacement rates, the latter index again using the K_2/K_1 -relationship, shown in Fig. 5.14. The resulting values are shown in Table 5.5 and Fig. 5.21, where the displacement rate is again displayed on a logarithmic scale. In this representation, both indexes exhibited a linear dependence on the displacement rate with decreasing values for increasing rates. At the 10x higher rate (than the experimental rate), almost no ductility remained, which is confirmed in Fig. 5.15, where failure occurred in the yield point region. On the other hand, ductility significantly improved at the 10x lower rate.

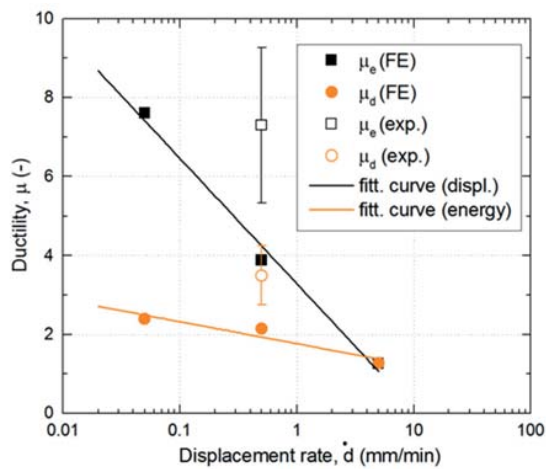


Figure 5.21: Displacement rate effect on displacement- and energy-based ductility indexes of acrylic joints

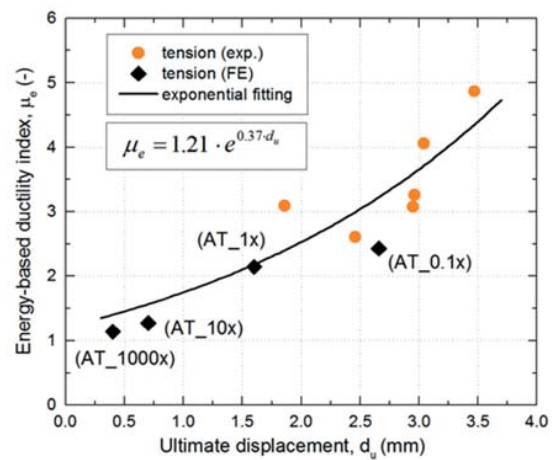


Figure 5.22: Relationship between energy-based ductility index and ultimate displacement [8]

Furthermore, a relationship between the energy-based index, μ_e , and the ultimate displacement, d_u , was established in the preceding experimental work, as shown in Fig. 5.22 [8, 9]. The numerically derived indexes at the different rates fitted well into this graph, confirming that ductility is significantly increased when the displacement rate is decreased.

5.6. Conclusions

The experimentally observed mechanical responses of adhesively-bonded timber joints were numerically modeled. The joints were composed of two types of adhesives, either a highly strain- rate-sensitive ductile acrylic or a brittle epoxy adhesive. The numerical models were validated by experimental results and the effect of varying joint displacement rates on the responses of the ductile joints was then studied. The following conclusions were drawn:

- The numerical models were successfully validated. In particular, the non-linear load-displacement and true strain responses, angles of principal strains, ultimate loads and ductility indexes were effectively simulated by taking the high strain rate sensitivity of the acrylic adhesive into account.
- The numerical results showed that, at the same joint displacement rate, the true strain rates in the acrylic adhesive layer varied significantly throughout the loading process and along the adhesive layer. This underlined the importance of taking into account these varying strain rates and associated different true stress-strain relationships of the adhesive in the modeling.
- Increasing the joint displacement rate shifted the load-displacement curve upwards, i.e. yield load and displacement increased, ultimate load and displacement however decreased, while the joint stiffness was not affected. A logarithmic dependence of these loads and displacements on the displacement rate was observed.
- The energy- and displacement-based ductility indexes decreased with increasing displacement rate; at higher rates the joint behavior changed from ductile to brittle.

References

- [1] Tannert T., Vallee T., & Hehl S. Temperature dependent strength of adhesively bonded timber joints. In Proceedings of the International Conference on Wood Adhesives, p: 76-80 (2009, September).
- [2] De Castro J.: “System ductility and redundancy of FRP structures with ductile adhesively-bonded joints”, EPFL Thesis No 3214, Lausanne (2005).
- [3] Natterer J., Sandoz J.L., Rey M., Construction en Bois, Traité de Génie Civil 13, Lausanne (2004).
- [4] Banea M. D., da Silva L. F. M. “Mechanical characterization of flexible adhesives”, Journal of Adhesion, Vol.85, Issue: 4-5, p: 261-285 (2009).
- [5] Tannert T., Vallée T., Hehl S. “ Experimental and numerical investigations on adhesively bonded hardwood joints”, International Journal of Adhesion and Adhesives, Vol. 37, p: 65-69 (2012)
- [6] Korta J., Młyniec A., Zdziebko P., & Uhl, T. Finite element analysis of adhesive bonds using the cohesive zone modeling method. Mechanics and Control, 33(2), p: 51 (2016).
- [7] Angelidi M., Vassilopoulos A. P., & Keller T. Ductility, recovery and strain rate dependency of an acrylic structural adhesive. Construction and Building Materials, 140, p: 184-193 (2017).
- [8] Angelidi M., Vassilopoulos A. P., & Keller T. Ductility of adhesively bonded timber joints. International Journal of Computational Methods and Experimental Measurements. (1st International Conference On Timber Structures and Engineering, New Forest, UK, June 2017).
- [9] Angelidi M., Vassilopoulos A. P., & Keller T. Ductile adhesively-bonded timber joints: Experimental investigation. (under review).
- [10] Naaman A.E., Jeong S.M. Structural ductility of concrete beams prestressed with FRP tendons, Nonmetallic (FRP) reinforcement for concrete structures, Proc. of the second international RILEM symposium (FRPRCS-2), p: 379-386 (1995).
- [11] Da Silva L. F., & Campilho R. D. Advances in numerical modelling of adhesive joints, p: 1-93, Springer Berlin Heidelberg (2012).
- [12] Campilho R. D. S. G., & Fernandes T. A. B. Comparative evaluation of single-lap joints bonded with different adhesives by cohesive zone modelling. Procedia Engineering, 114, p: 102-109 (2015).
- [13] Hoang-Ngoc C. T., & Paroissien E. Simulation of single-lap bonded and hybrid (bolted/bonded) joints with flexible adhesive. International Journal of Adhesion and Adhesives, 30(3), p: 117-129 (2010).
- [14] Cognard J. Y., Créac’hdec R., Sohier L., & Davies, P. Analysis of the nonlinear behavior of adhesives in bonded assemblies—Comparison of TAST and Arcan tests. International Journal of Adhesion and Adhesives, 28(8), p: 393-404 (2008).

-
- [15] Zgoul M., & Crocombe A. D. Numerical modelling of lap joints bonded with a rate-dependent adhesive. *International journal of adhesion and adhesives*, 24(4), p: 355-366 (2004).
- [16] Karac A., Blackman B. R. K., Cooper V., Kinloch A. J., Sanchez S. R., Teo W. S., & Ivankovic A. Modelling the fracture behaviour of adhesively-bonded joints as a function of test rate. *Engineering Fracture Mechanics*, 78(6), p: 973-989 (2011).
- [17] Vallée T., Tannert T., Murcia-Delso J., & Quinn D. J. Influence of stress-reduction methods on the strength of adhesively bonded joints composed of orthotropic brittle adherends. *International Journal of Adhesion and Adhesives*, 30(7), p: 583-594 (2010).
- [18] Vallée T., Tannert T., & Fecht S. Adhesively bonded connections in the context of timber engineering—A Review. *The Journal of Adhesion*, 93(4), p: 257-287 (2017).
- [19] Yu X. X., Crocombe A. D., & Richardson, G. Material modelling for rate-dependent adhesives. *International journal of adhesion and adhesives*, 21(3), p: 197-210 (2001).
- [20] Angelidi M., Vassilopoulos A. P., Keller T. Displacement rate and structural effects on Poisson ratio of a ductile structural adhesive under tension and compression. *International Journal of Adhesion and Adhesives* (accepted, 2017).
- [21] Sika AG. SikaDur-330: 2-part epoxy impregnation resin (2006).
- [22] Sika AG. SikaFast5221 NT: Fast-curing 2-component structural adhesive. Zurich (2013).
- [23] Dinwoodie J. M. Timber - a review of the structure-mechanical property relationship. *Journal of Microscopy*, 104(1), p: 3-32 (1975).
- [24] Farajzadeh Moshtaghin A. Stochastic analysis of clear timber as a structural material. EPFL Thesis No 6944, Lausanne (2016).
- [25] Norris GB. Strength of orthotropic materials subjected to combined stress, Report No. 1816. US Department of Agriculture, Forest Research Laboratory. Madison, WI, p: 40 (1950).
- [26] Kretschmann D. E, Ross R. J. Wood handbook: wood as an engineering material, USDA Forest Service General Technical Report FPL-GTR-113, (5): 29, Madison (2010).
- [27] Ludwig P. Ober den Einfluss der Deformationsgeschwindigkeit bei bleibenden Deformationen mit besonderer Berücksichtigung der Nachwirkungserscheinungen'. *Physikal. Zeits*, 10: 411 (1909)
- [28] Prandtl L. A conceptual model to the kinetic theory of solid bodies. *Z. Angew. Math. Mech.*, 8, p: 85-106 (1928).

Chapter 6

Comparative study on structural efficiency of adhesively-bonded and mechanical timber joints

In this study, ductile adhesively-bonded and mechanical timber joints were compared in terms of resistance. All joints were double-lap joints with identical geometry. In total, two bonded joints using epoxy and acrylic adhesives and two mechanical joints using nails and bolts were examined. For the bonded joints, the characteristic response to loading was obtained from experiments and was then transformed into design values, using Eurocode 0. On the other hand, the design values for the mechanical joints were directly derived from analytical calculations, based on guidelines provided by Eurocode 5. In the second part, a parametric study was performed, considering increased overlap lengths and widths. The results revealed that ductile adhesively-bonded joints may offer significantly higher capacities than comparable mechanical joints.¹

Keywords: *adhesively-bonded joints, timber joints, mechanical joints, Eurocode, resistance, design, nails, bolts, epoxy, acrylic*

¹Angelidi M. & Keller T. Comparative study on structural efficiency of adhesively-bonded and mechanical timber joints (under review)

6.1. Introduction

Joints are one of the most critical components in timber structures since they define the dimensions of components and the total resistance. There are many different types of timber joints, the most common being either mechanical or adhesively-bonded. Typical examples of mechanical fasteners, which are widely used in timber engineering and carpentry, are nails, bolts, dowels, screws or staples and they can be used to assemble timber to timber (glued, laminated or solid) or timber to steel plates. The most common mechanical fasteners are presented in Fig. 6.1. Existing standards, e.g. European Eurocode 5 [4], contain guidelines for the design of mechanical joints, based on knowledge acquired mainly from practice.

Adhesive bonding on the other hand is poorly addressed in the aforementioned standards for timber structures, despite the benefits associated with its application for other materials, such as fiber-reinforced polymer composites. It has been proved that adhesive bonding results in a more uniform stress distribution along the overlap area, stress concentrations close to the fastener hole are avoided and the component section is not reduced, nor are the fibers interrupted [5]. Furthermore, in terms of fatigue and durability, adhesive bonding limits the slip displacements that occur in the case of mechanical joints upon force application [6]. It has also been proved that with suitable adhesives it is possible to create ductile timber joints, despite the fact that timber is a brittle material by nature [7]. For all these reasons, adhesive bonding seems a promising option for increasing joint efficiency.

Within the framework of this work, in order to further evaluate whether the use of ductile adhesives may result in increased joint resistance compared to traditional, mechanical fasteners, mechanical joints of the same geometry and materials were investigated. For the mechanical joints, two different dowel-type fasteners were considered: nails and bolts, since these are some of the most widely applied fasteners in timber engineering. The aim of this study was thus to compare the design resistance of the two joint types resulting from the characteristic values obtained experimentally and numerically for the bonded joints and analytically (based on the Eurocode 5 for timber [4]) for the mechanical joints.



Figure 6.1: Typical mechanical fasteners used for timber joints:
a) nails [1], b) screw [2] and c) bolt [2]

6.2. Adhesively-bonded joint design values of resistance

6.2.1. Summary of experimental setup

Since the characteristic joint resistance was already obtained from previous experimental work [7], only a brief summary of the developed experimental setup is presented here for reference. For the formation of the adhesively-bonded timber joints, a very common type of structural softwood, spruce, was used, which is abundant in central Europe. For the adhesive bonding of the joints, the ductile acrylic adhesive SikaFast 5221 NT [8] and, for comparison, the stiff epoxy adhesive SikaDur 330 [9] were used.

The geometry of the joints is shown in Fig. 6.2; they are double-lap joints with double symmetry, horizontal and vertical. They consist of two identical double-lap parts to facilitate the experimental procedure (gripping is easier in the case of symmetric ends). As can be also seen from the figure, the bonded area in one double-lap part (half-joint) is equivalent to $2 \times (160 \times 50 \times t)$, where bond line thickness, t , is 3 or 2 mm in the case of the acrylic or epoxy adhesive respectively. Two 0.5 mm epoxy extra layers were added in the acrylic joints to improve adhesion between timber and the acrylic adhesive.

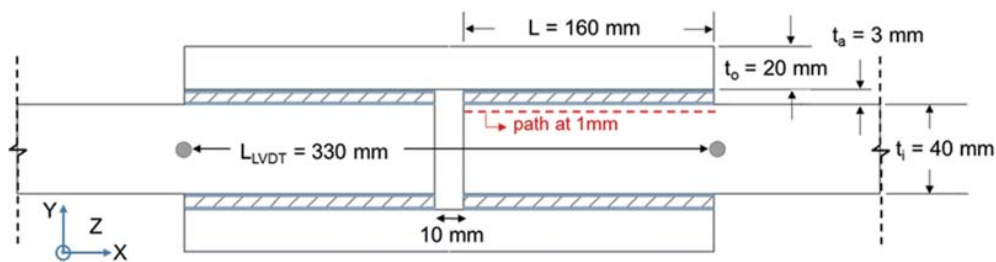


Figure 6.2: Geometry of the double-lap acrylic joint (total specimen length = 970 mm and width = 50 mm)

Table 6.1: Experimental results for epoxy and acrylic joints

Epoxy joints	Ultimate load, F_u (kN)	Acrylic joints	Ultimate load, F_u (kN)
E_T1	32.2	A_T1	56.6
E_T2*	29.2	A_T2	65.1
E_T3*	47.1	A_T3	61.6
E_T4*	43.5	A_T4*	53.6
E_T5*	33.7	A_T5*	65.8
-	-	A_T6*	55.6
<i>AV ± SD</i>	<i>37.1 ± 6.9</i>	<i>AV ± SD</i>	<i>59.7 ± 4.7</i>

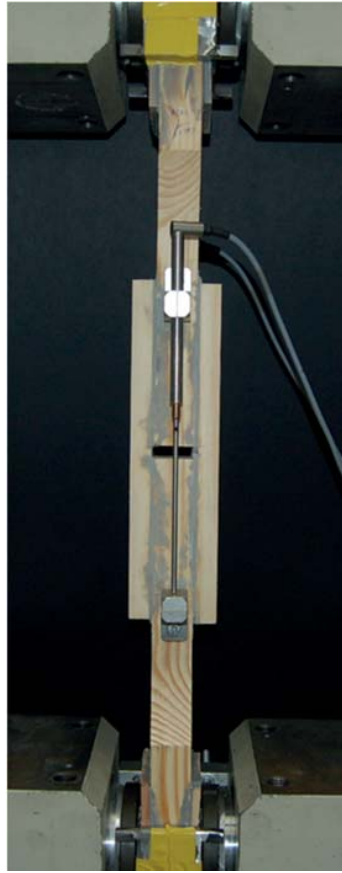


Figure 6.3: Experimental setup for the acrylic-bonded joints [7]

In total, 11 specimens (6 acrylic and 5 epoxy ones) were investigated in tension. The specimens were axially loaded up to failure at a displacement rate of 1 mm/min, as shown in Fig. 6.3. The machine's load cell and two linear variable displacement transducers (LVDTs), symmetrically placed on both sides of the specimens, were used to measure the load and displacement (elongation) of the joints. All results are summarized in Table 6.1, including average values, *AV* and standard deviation, *SD*.

6.2.2. Characteristic and design values of joint resistance

The standards provide information for converting the characteristic values of resistance into design values using suitable material or resistance factors. In the case of adhesive joints, it was necessary to convert the characteristic resistance, X_k , obtained from the average experimental results and the coefficient of variation into design resistances, X_d , which can be used for comparison with any other type of mechanical joint, based on existing standards. For this purpose, the following equation from Eurocode 0 [10] was used:

$$X_d = k_{mod} \cdot X_{k(n)} / \gamma_M \quad (1)$$

where $k_{mod} = 0.8$ and $\gamma_M = 1.3$ for class of service 1 (medium load duration) and timber joints [4]. The characteristic value, X_k , for n experiments can be found using the following equation:

$$X_k = m_x \cdot \{1 - k_n \cdot V_x\} \quad (2)$$

where

- m_x is the average value obtained from the experiments (see Table 6.1)
- $k_n = 2.33$ for five epoxy joints and 2.18 for six acrylic joints (EC0: Table D1 [10])
- and V_x the coefficient of variation, estimated from the experimental set as 0.186 and 0.086 for epoxy and acrylic joints respectively.

As a result, the design resistances, $F_{v,Ed}$, attained for acrylic and epoxy joints were found to be 29.9 kN and 13.0 kN respectively. These values will be used later for comparison with the design resistances of the mechanical joints.

6.3. Design value of resistance of dowel-type joints using nails

Double-lap joints of the same adherend geometry and timber type as used for the adhesive joints were chosen for the application of mechanical fasteners. Spruce wood corresponding to the quality C30 defined in Eurocode 5 [11] was assumed, based on its characteristic density, ρ_k of 380 kg/m³ (average measured density 440 kg/m³ and standard deviation 39 kg/m³) and E -modulus close to 12000 MPa [7, 12]. For the formation of this joint, smooth, round nails with diameter $d = 3$ mm and tensile strength, $f_u = 600$ N/mm² were selected. No pre-drilled holes were used, as this would require a minimum diameter of 8 mm, which is not possible for this joint geometry.

To determine the characteristic resistance value of the mechanical joint, $F_{v,Rk}$, the characteristic resistance of each plane and fastener must be considered separately [4]. This resistance is equal to the minimum of the following group of equations (3), for the case of simple, 1-plane shear (EC5: Eq. 8.6):

$$F_{v,Rk} = \min \left\{ \begin{array}{l} f_{h,1,k} t_1 d \quad (a) \\ f_{h,2,k} t_2 d \quad (b) \\ \frac{f_{h,1,k} t_1 d}{1 + \beta} \left[\sqrt{\beta + 2\beta^2 \left[1 + \frac{t_2}{t_1} + \left(\frac{t_2}{t_1} \right)^2 \right]} + \beta^3 \left(\frac{t_2}{t_1} \right)^2 - \beta \left(1 + \frac{t_2}{t_1} \right) \right] + \frac{F_{ax,Rk}}{4} \quad (c) \\ 1,05 \frac{f_{h,1,k} t_1 d}{2 + \beta} \left[\sqrt{2\beta(1 + \beta) + \frac{4\beta(2 + \beta)M_{y,Rk}}{f_{h,1,k} d t_1^2}} - \beta \right] + \frac{F_{ax,Rk}}{4} \quad (d) \\ 1,05 \frac{f_{h,1,k} t_2 d}{1 + 2\beta} \left[\sqrt{2\beta^2(1 + \beta) + \frac{4\beta(1 + 2\beta)M_{y,Rk}}{f_{h,1,k} d t_2^2}} - \beta \right] + \frac{F_{ax,Rk}}{4} \quad (e) \\ 1,15 \sqrt{\frac{2\beta}{1 + \beta}} \sqrt{2M_{y,Rk} f_{h,1,k} d} + \frac{F_{ax,Rk}}{4} \quad (f) \end{array} \right. \quad (3)$$

where:

- $F_{v,Rk}$: characteristic resistance value per plane and assembling tool /fastener (e.g. nail) (in N)
- t_i : thickness of the assembled timber piece or fastener penetration (in mm)
- $f_{h,i,k}$: characteristic embedment strength of assembled timber piece i (N/mm²)
- d : diameter of fastener used (in mm)
- $M_{y,Rk}$: characteristic moment of resistance to plastic flow of fastener (in N·mm)
- $\beta = f_{h,2,k} / f_{h,1,k}$: ratio between the two characteristic strengths of the two timber pieces ($\beta=1$ for same timber used)
- $F_{ax,Rk}$: characteristic withdrawal resistance of fastener used (in N)

The failure mode corresponding to each of these equations is explained in Fig. 6.4. In order to calculate the load-bearing resistance of the shear plane, the following variables must be defined first.

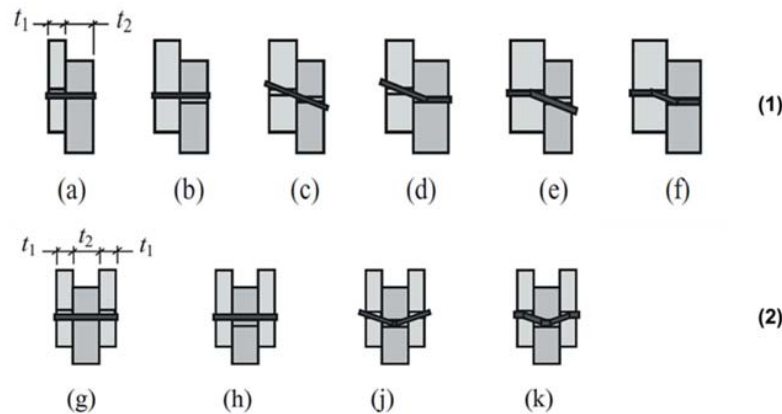


Figure 6.4: Failure modes in (1) single and (2) double shear (timber-to-timber) [4]

Plastic moment flow

The plastic moment flow (yield moment), $M_{y,Rk}$, of the nail was obtained based on the following equation (EC5: Eq. 8.14) for a circular section of the nails used:

$$M_{y,Rk} = 0.30 \cdot f_u \cdot d^{2.6} = 0.30 \cdot 600 \cdot 3^{2.6} = 3132 \text{ N}\cdot\text{mm} \quad (4)$$

Characteristic timber strength value:

The characteristic embedment strength of timber parallel to the grain is the average compressive strength of timber under the action of a stiff dowel. This depends on the timber quality (density, ρ_k) and diameter of nail, d , and is calculated separately for each timber part (headside and pointside). In this case, the two

assembled parts are composed of the same timber quality and thus the characteristic embedment strength is the following for both parts (EC5: Eq. 8.15):

$$f_{h,k} = 0.082 \cdot \rho_k \cdot d^{0.3} = 22.4 \text{ N/mm}^2 \quad (5)$$

Withdrawal capacity

The nail withdrawal resistance was calculated based on the penetration length, t_{pen} , and the characteristic withdrawal strength, $F_{ax,k}$, (for pointside and headside) as the minimum of the following equation (EC5: Eq. 8.24):

$$F_{ax,Rk} = \min \left\{ \begin{array}{l} f_{ax,k} \cdot d \cdot t_{pen} \\ f_{head,k} \cdot d_h^2 \end{array} \right. \quad (6)$$

where :

- $t_{pen} = 28 \text{ mm} \geq 8 \cdot d = 24 \text{ mm}$,
- $f_{ax,k} = 20 \cdot 10^{-6} \cdot \rho_k^2 = 2.89 \text{ N/mm}^2$ (for the pointside) and
- $f_{head,k} = 70 \cdot 10^{-6} \cdot \rho_k^2 = 10.11 \text{ N/mm}^2$ (for the headside).

As a result, from Equation (6): $F_{ax,Rk} = \min \{2.89 \cdot 3 \cdot 24; 10.11 \cdot 6^2\} \text{ N} = \{208.1; 364\} \text{ N} = 208.1 \text{ N}$ (for head diameter, $d_h = 6 \text{ mm}$ as in [10]). The overlapping of the nails was also verified: as long as $(t - t_2) = 40 - 28 = 12 \text{ mm} \geq 4d = 12 \text{ mm}$, the nails may overlap, as shown in Fig. 6.5. For smooth nails, when t_{pen} is lower than $12d$, a reduction factor equal to $(t_{pen}/4d - 2)$ (EC5: 8.3.2.7) should be applied in the $F_{ax,Rk}$. In this case, t_{pen} is equal to $8d$ and this factor is zero, so, there is no withdrawal resistance for this joint configuration.

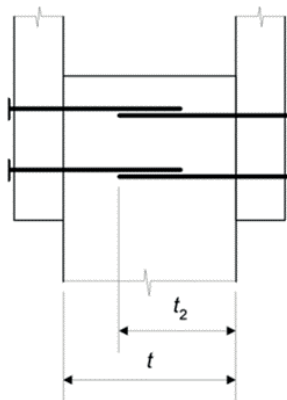


Figure 6.5: Overlapping nails (EC5: Fig. 8.5)

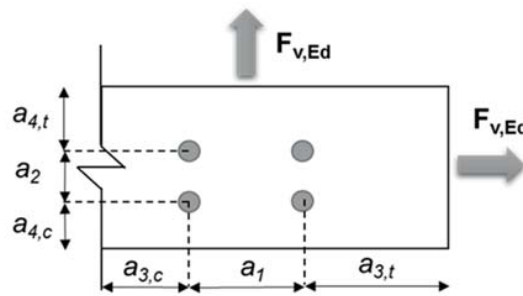


Figure 6.6: Schematic description of end and edge distances

Minimum spacings and edge and end distances for nails (see Fig. 6.6)

- a_1 : spacing of nails within one row parallel to grain;
- a_2 : spacing of rows of nails perpendicular to grain;
- $a_{3,c}$: distance between nail and unloaded end;
- $a_{3,t}$: distance between nail and loaded end;
- $a_{4,c}$: distance between nail and unloaded edge;
- $a_{4,t}$: distance between nail and loaded edge;
- α : angle between force and grain direction, 0° in this study.

The following design is therefore proposed in Fig. 6.7 in order to satisfy the distances criteria, which are summarized in Table 6.2 (EC5: Table 8.2).

Table 6.2: Minimum distance requirements for nails ($d=3$ mm) and bolts ($d=8$ mm)

(in mm)	Nails (for $\rho_k \leq 420$ kg/m ³)	Bolts
a_1	$10d = 30$ mm	($\alpha=0^\circ$) $5d = 40$ mm
a_2	$5d = 15$ mm	$4d = 32$ mm
$a_{3,t}$	$15d = 45$ mm	($\alpha=0^\circ$) max { $7d=56, 80$ mm}
$a_{3,c}$	$10d = 30$ mm	($\alpha=180^\circ$) $4d = 40$ mm
$a_{4,c}$	$5d = 15$ mm	$3d = 24$ mm

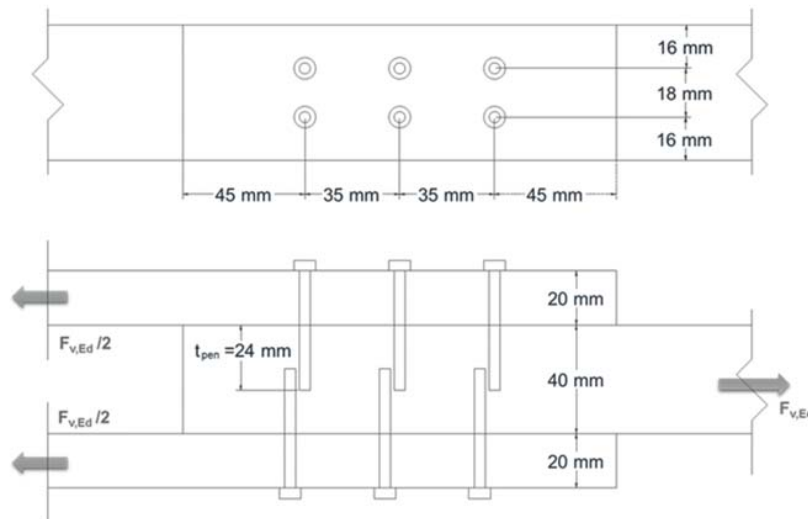


Figure 6.7: Mechanical double-lap joint using nails

From the group of equations (3) (a to f), the results are included in Table 6.3. For equations (d), (e) and (f), the second term, $F_{ax,Rk} / 4 = 0$ N, is commonly referred to as the rope effect force, while the first term is related to the Johansen yield load. It is specified in the Eurocode [4] that the second term should be limited to 15% of the first one in the case of round nails. As a result, in this case, this criterion is satisfied. The characteristic resistance should be the minimum of all examined cases, which are included in Table 6.3: $F_{v,Rk} = \min \{a, b, \dots, f\} = 622.7$ N.

Table 6.3: Characteristic load-bearing capacity of nails (simple shear)

Nails		Bolts	
(a)	1344.6	(g)	4587.2
(b)	2689.2	(h)	4587.2
(c)	913.6	(j)	3800.1
(d)	622.7	(k)	5629.1
(e)	1021.7		
(f)	746.3		
$F_{v,Rk} (= \min)$	622.7	$F_{v,Rk} (= \min)$	3800.1

Effective load-bearing resistance parallel to grain

For one row of n nails parallel to the grain, the load-bearing resistance parallel to the grain should be calculated using the effective number of fasteners, n_{ef} :

$$F_{v,ef,Rk} = n_{ef} \cdot F_{v,Rk} \quad (7)$$

where:

- $n_{ef} = n^{k_{ef}}$, is the effective number of nails in the row (EC5: Eq. 8.17);
- n the number of nails in a row and
- k_{ef} is given in Table 8.1 Eurocode 5 [4].

According to Fig. 6.7, there are two rows of three nails, and $a_l = 35$ mm = $11.7d$, so, $k_{ef} = 0.91$, after interpolating between 0.85 and 1.0. Then, $n_{ef} = 2 \cdot 3^{0.91} = 2 \cdot 2.7 = 5.4$. Thus, for the double-lap joint: $F_{v,ef,Rk} = 2 \cdot (5.4 \cdot 622.7) = 6725$ N, which is then transformed into the design value: $F_{v,Ed} = F_{v,ef,Rk} \cdot k_{mod} / \gamma_M = 4139$ N or 4.1 kN, where $k_{mod} = 0.8$ and $\gamma_M = 1.3$, as explained in Section 2.

6.4. Design value of resistance of dowel-type joints using bolts

Bolts of steel class 5.6 ($f_u = 500 \text{ N/mm}^2$) and diameter $d=8\text{mm}$ were selected for the design of this joint type. A design approach similar to that of the nail joint was adopted for the bolt type. In contrast to Equations (3), the following group of equations (10) should be applied for fasteners in double shear for calculating the load-bearing joint resistance per plane (EC5: Eq. 8.7):

$$F_{v,Rk} = \min \begin{cases} f_{h,1,k} t_1 d & \text{(g)} \\ 0,5 f_{h,2,k} t_2 d & \text{(h)} \\ 1,05 \frac{f_{h,1,k} t_1 d}{2 + \beta} \left[\sqrt{2\beta(1 + \beta) + \frac{4\beta(2 + \beta)M_{y,Rk}}{f_{h,1,k} d t_1^2}} - \beta \right] + \frac{F_{ax,Rk}}{4} & \text{(j)} \\ 1,15 \sqrt{\frac{2\beta}{1 + \beta}} \sqrt{2M_{y,Rk} f_{h,1,k} d} + \frac{F_{ax,Rk}}{4} & \text{(k)} \end{cases} \quad (8)$$

Minimum distances for the bolts are also defined in Table 6.2 and Fig. 6.8. Based on the overlapping area geometry, $d = 8 \text{ mm}$ is the maximum bolt diameter that can satisfy these minimum distance requirements ($a_{4,c} \geq 24 \text{ mm}$). The following characteristic value for the yield moment was calculated (EC5: Eq. 8.30):

$$M_{y,Rk} = 0.3 \cdot f_{u,k} \cdot d^{2.6} = 0.3 \cdot 500 \cdot 8^{2.6} = 33429 \text{ N}\cdot\text{mm} \quad (9)$$

For bolts up to 30-mm diameter, the following characteristic embedment strength values for timber, $f_{h,a,k}$, should be used (EC5: Eq. 8.31), at an angle α to the grain (in this case $\alpha = 0^\circ$):

$$f_{h,a,k} = \frac{f_{h,0,k}}{k_{90} \sin^2 \alpha + \cos^2 \alpha} \quad (10)$$

where:

- $f_{h,0,k} = 0.082 \cdot (1 - 0.01d) \cdot \rho_k$ (EC5: Eq. 8.32) and
- $k_{90} = 1.35 + 0.015 \cdot d$ (EC5: Eq. 8.33).

Consequently: $k_{90} = 1.47$, $f_{h,0,k} = 28.7 \text{ N/mm}^2$ and (9) $f_{h,a,k} = 28.7 \text{ N/mm}^2$. For calculating the axial bolt resistance to tension, $F_{ax,Rk}$, the following equations are applied [13]:

$$F_{ax,Rk} = \min \{ F_{t,Rk}; 3 \cdot f_{c,90,d(\text{timber})} \cdot \pi \cdot (D_{ext}^2 - d_{int}^2) / 4 \}, \quad (11)$$

where:

- $F_{t,Rk}$ (=tensile strength of the bolt) $= f_{u,k} \cdot A_s = 500 \cdot 37.2 = 18600 \text{ N}$ [14] and
- Bearing resistance of the timber: $3 \cdot f_{c,90,k(\text{timber})} \cdot \pi \cdot (D_{ext}^2 - d_{int}^2) / 4$, in which:
 - $f_{c,90,k}$ (softwoods) $= 0.007 \cdot \rho_k = 2.66 \text{ N/mm}^2$ [11],
 - $D_{ext} = 30 \text{ mm}$, $d_{int} = 10 \text{ mm}$ and $A_s = 37.2 \text{ mm}^2$ for $d=8\text{-mm}$ bolt [15].

Applying all the values in Equation (8), the obtained resistance is:

$$F_{ax,Rk} = \min \{18600; 5014\} \text{ N} = 5014 \text{ N}.$$

Then, according to Eurocode [4], one quarter or the axial resistance, $F_{ax,Rk}/4$, has to be limited to the 25% of the Johansen yield equation, which corresponds to the left part of the equations (j) and (k). In other words (EC5: 8.2.2.2):

$$\frac{\frac{F_{ax,Rk}}{4}}{F_{v,Rk}(j \text{ or } k) - \frac{F_{ax,Rk}}{4}} 100 \leq 25\% \quad (12)$$

which results into: $\frac{1253}{4293-1253} 100 = 41\%$ for (j) and $\frac{1253}{5756-1253} 100 = 28\%$ for (k). Thus, equations (j) and (k) have to be transformed as follows:

$$F_{ax,Rk} (j) = 1.25 \cdot 3040.1 = 3800.1 \text{ N} \text{ and } F_{ax,Rk} (k) = 1.25 \cdot 4503.3 = 5629.1 \text{ N}.$$

The results are also summarized in Table 6.3 for all four cases and the minimum is again selected from (j) as $F_{v,Rk} (j) = \min \{g, h, j, k\} = 3800.1 \text{ N}$.

For n bolts in a row parallel to the grain direction, the effective load-bearing resistance should be calculated using the following effective number of bolts, n_{ef} (EC5: Eq. 8.34):

$$n_{ef} = \min \left\{ n, n^{0.9} \sqrt{\frac{a_1}{13d}} \right\}, \quad (13)$$

which in this case results in $n_{ef} = \min \{1, 0.79\} = 0.79$. Consequently, the effective load-bearing resistance is calculated as 3002 N per plane and 6004 N in total. Finally, the equivalent design value $F_{v,Rd} = 3695 \text{ N}$ or 3.7 kN, for assumed $k_{mod} = 0.8$ and $\gamma_M = 1.3$, as before.

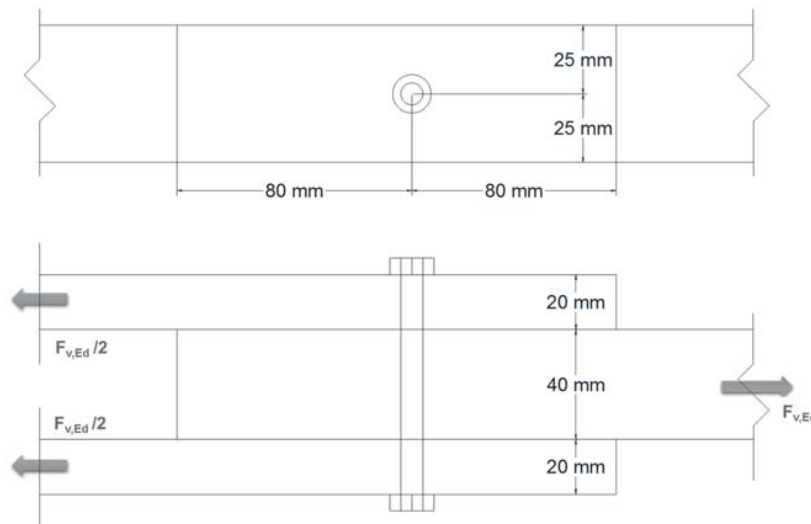


Figure 6.8: Bolted double-lap joint

6.5. Comparison between adhesively-bonded and mechanical joints

The design resistance for each of the studied joints is summarized here:

- Epoxy-bonded: 13.0 kN
- Acrylic-bonded: 29.9 kN
- Nail-fastened: 4.1 kN and
- Bolted: 3.7 kN.

Comparing these values, the design resistance for the acrylic (ductile) adhesively-bonded joint is significantly higher than that of the epoxy and mechanical joints for this specific geometry; two and seven times higher respectively. It is expected that for larger overlap areas, an increased number of the mechanical fasteners would improve the joint resistance, while it has been previously shown that it is not always the case for stiff adhesives for example. For epoxy joints exists an optimum overlap length, after which no further increase can improve the joint resistance [6, AnnexF]. On the other hand it is also expected that the resistance increases for ductile adhesive joints. For this reason, the study was extended for additional joint overlap geometries, considering 2 more overlap lengths, L ($2L = 320$ mm and $3L = 480$ mm) and widths, w ($2w = 100$ mm and $3w = 150$ mm).

For the case of the acrylic-bonded joints, a previously developed finite element model [16] was used for the estimation of the new-geometry-joints resistance (see Fig. 6.9). The model takes into account the strain-rate sensitivity of the used acrylic and has already been experimentally validated in previous work [16]. The joint resistance resulted from the following stress-based Norris criterion, which is widely applied for orthotropic materials and timber in particular [17]:

$$\frac{\sigma_{xx}^2}{X^2} + \frac{\sigma_{yy}^2}{Y^2} + \frac{\sigma_{xy}^2}{S^2} - \frac{|\sigma_{xx}\sigma_{yy}|}{X \cdot Y} \leq 1 \quad (13)$$

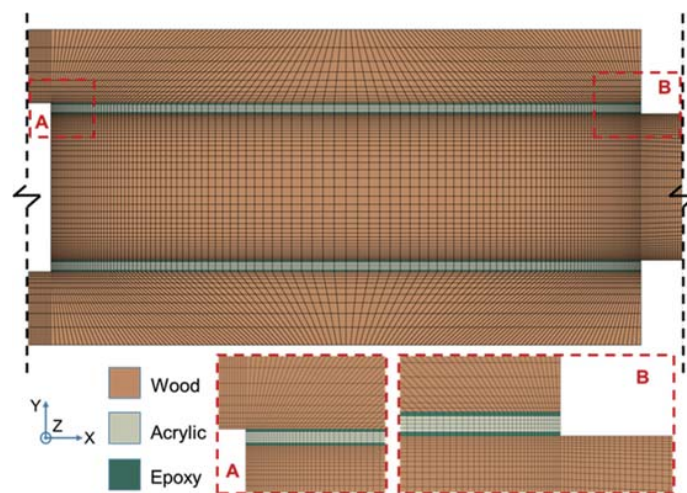


Figure 6.9: Detail (one overlap) of FE model for acrylic joint specimens

Table 6.4: Average strength properties of spruce wood [18]

Strength // fibers, X (MPa)		Strength ⊥ fibers, Y (MPa)		Shear, S (MPa)
Tension	Compression	Tension	Compression	
70	45	4	5	10

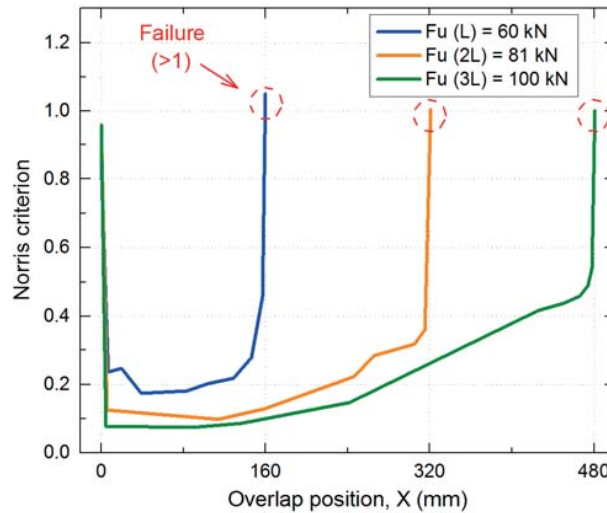


Figure 6.10: Norris criterion at failure load for different joint overlap lengths

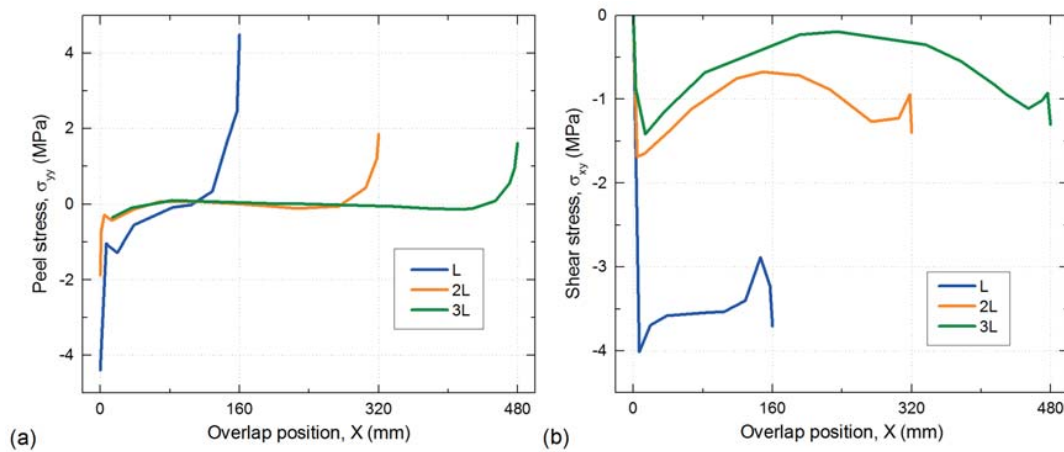


Figure 6.11: Effect of overlap length on (a) peel and (b) shear stress distributions (at $F_u(L) = 60$ kN)

In the model, the average timber resistance parallel (X), perpendicular to the grain (Y) and in shear (S), included in Table 6.4, are compared with the corresponding obtained values of stress (σ_{xx} , σ_{yy} , σ_{xy}), as they appear on a selected path of inspection. In the case of these joints, this path is selected parallel to the

adhesive interface, at 1-mm depth on the inner timber adherend (see Fig. 6.2), as all failures had experimentally occurred along this path. The average joint resistance, F_u , is reached when the Norris criterion along the selected path reaches 1.0; it is displayed for the three different overlap lengths in Fig. 6.10, resulting from different stress distributions, as shown for each geometry for the ultimate load of the L-joint ($F_{u(L)} = 60$ kN) in Fig. 6.11. It is shown that by increasing the overlap length the edge peaks are reduced for the same loads applied and consequently, the joint can sustain larger loads before failure.

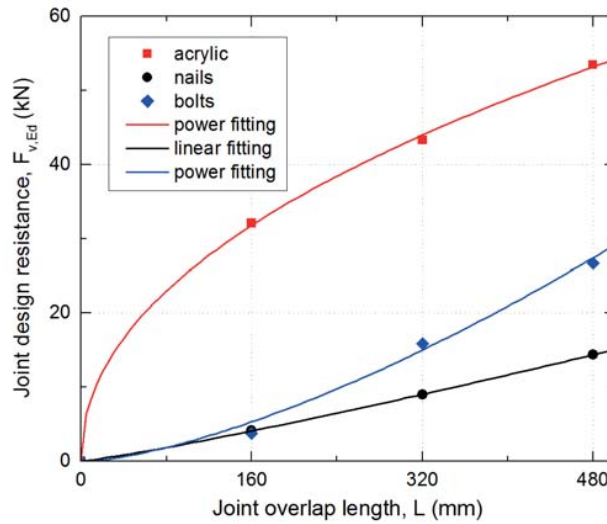


Figure 6.12: Effect of overlap length on joint resistance

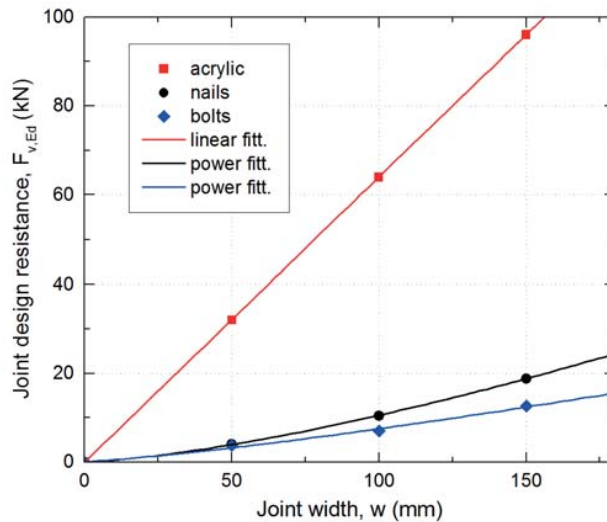


Figure 6.13: Effect of width on joint ultimate load

The estimated joint resistance for all adhesively-bonded cases were then converted to joint design resistance, $F_{v,Ed}$, assuming similar, known standard deviation as in the experiments ($V_x = 0.086$) and infinite number of specimens ($k_n = 1.64$). For the estimation of the design resistance, the loading conditions and material factor, k_{mod} and γ_M were then, also applied. All results were plotted in Figs. 6.12 and 6.13, including suitable fitting curves (i.e. coefficient of determination, $R^2 = 0.99 \div 1$ in all cases).

On the other hand, concerning the mechanical joints, the calculations were done similarly to the procedures developed in the previous sections, considering the minimum spacings (see Table 6.2) and the effective number of nails or bolts, assuming similar characteristic resistances, $F_{v,Rk}$. The resulting joint geometries are presented in Figs. 6.14, 6.15 and 6.16, revealing the total, maximum number of fasteners per case. The latter together with the corresponding effective numbers of nails and bolts, n_{ef} , are summarized in Table 6.5 for each case. The characteristic resistance per connector and per shear plane, $F_{v,Rk}$ from sections 3 and 4, for nails and bolts respectively, was multiplied by this effective number of fasteners per case to obtain the total joint resistance. Each calculated, total resistance was then converted into the design value, using the same factors for the materials and loading conditions, γ_M and k_{mod} and all results were also included in Table 6.5 and Figs. 6.12 and 6.13, to allow further comparisons with the bonded joints.

Table 6.5: Total and effective number of fasteners and joint design resistance

Geometry	Nails (x2 laps)			Bolts		
	Total number, n (-)	Effective number, n_{ef} (-)	Joint design resistance, $F_{v,Ed}$ (kN)	Total number, n (-)	Effective number, n_{ef} (-)	Joint design resistance, $F_{v,Ed}$ (kN)
L	6	5.4	4.1	1	0.8	3.7
2L	16	11.7	9.0	5	3.4	15.9
3L	28	18.8	14.4	9	5.7	26.7
w	6	5.4	4.1	1	0.8	3.7
2w	15	13.6	10.4	2	1.5	7.0
3w	27	24.5	18.8	4	2.7	12.6

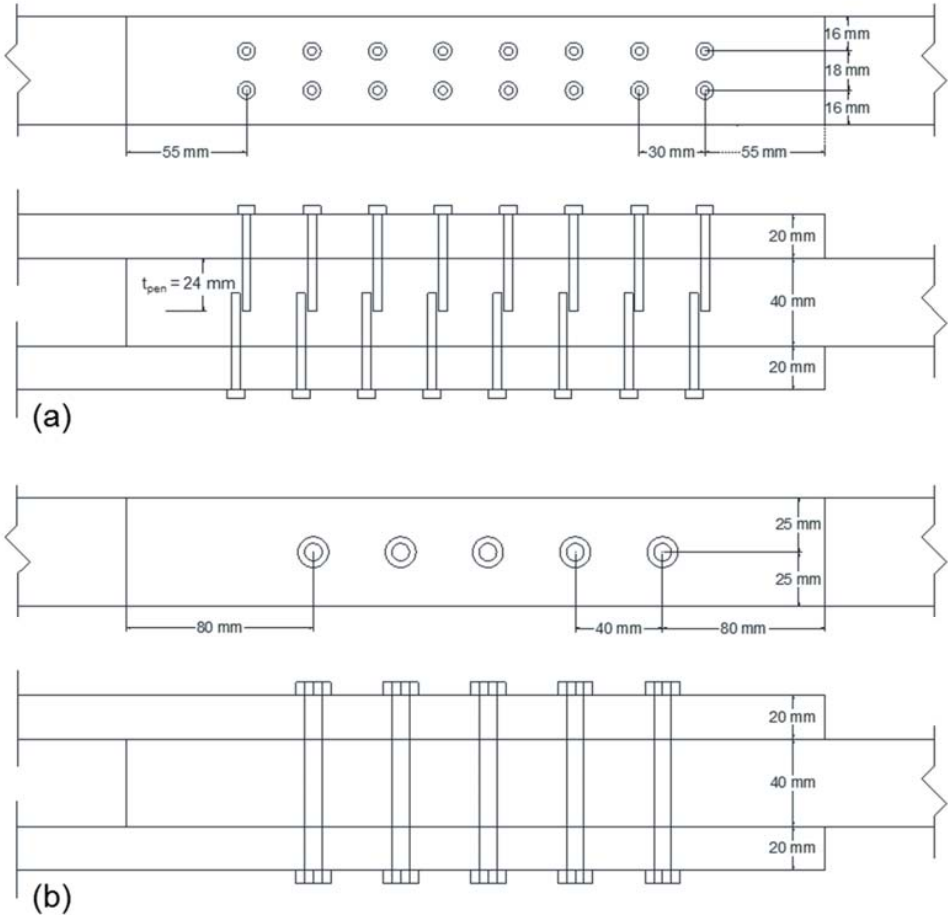


Figure 6.14: Joint configuration for double overlap length for (a) nails and (b) bolts

Based on these graphs, any change in the joint geometry within commonly used overlap dimensions in practice still proved the advantageous behavior of the ductile adhesively-bonded joints, despite the fact that for both changes performed, the acrylic joint presented more limited increase, compared to the other assembling methods: in both cases, the acrylic joint exhibited either a power-law trend with decreasing tendency either a linear trend, while the mechanical methods both increased faster with an ascending power-law trend.

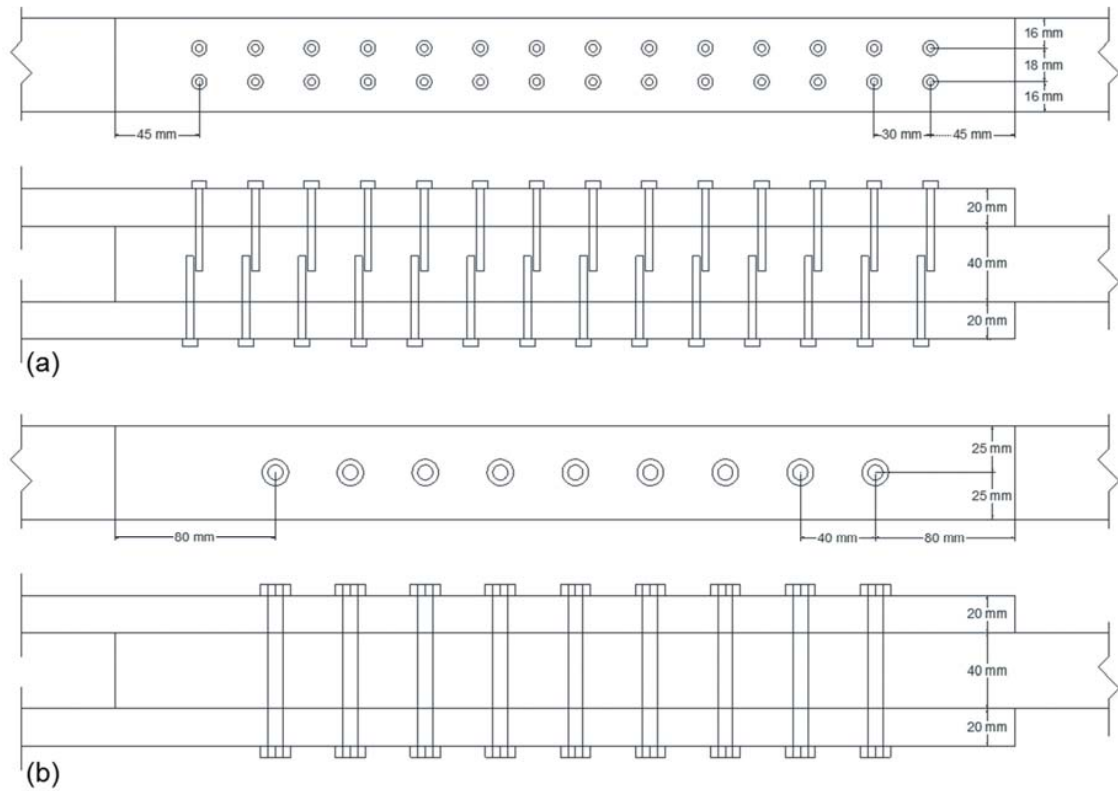


Figure 6.15: Joint configuration for triple overlap length for (a) nails and (b) bolts

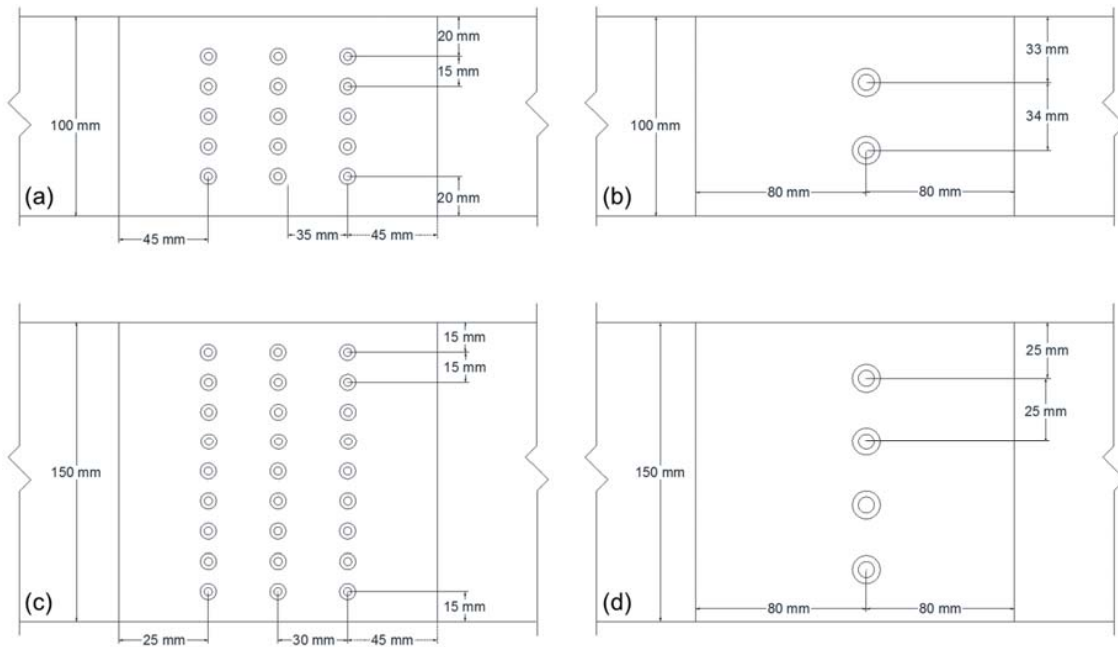


Figure 6.16: Joint configuration for double and triple overlap width for (a), (c) nails and (b), (d) bolts

6.6. Conclusions

In this study, the design value of resistance of two timber joint types (adhesively-bonded and mechanical) has been compared. In the case of the bonded joints, developed with epoxy and acrylic adhesives, the design load was found based on an estimation of the characteristic values of resistance obtained from previous experimental [7] and numerical work [16]. In the case of the mechanical joints, nails and bolts were used and the analytical relationships contained in Eurocode 5 [4] lead directly to an estimation of the characteristic and design capacities. For both cases, similar safety (load and material) factors were considered and variable geometries for the joint overlap area. The following two conclusions were drawn:

- The adhesively-bonded joints proved to be more efficient since they presented higher design resistance than the two mechanical types; the ductile acrylic-bonded joints were almost twice as resistant as the epoxy joints and seven times more resistant compared to the mechanical ones, for similar assumed joint overlap area.
- For a given, limited bonded area, adhesives performed better than mechanical fasteners. However, should the overlap area not be restricted, the resistance of the latter could increase with an increasing number of fasteners. The same also applied for ductile adhesives, such as acrylics, but not rigid ones, such as epoxy.
- Although this increase was more noticeable in the case of mechanical joints, the acrylic joints still exhibited higher resistance compared to all other examined types.

References

- [1] http://faridabad.all.biz/threaded-nails-g398216#.WPy_g2clGUI
- [2] <http://www.shallcrossbolt.com/product-catalog-bolts-nuts-screws-and-fasteners-online-shall-cross-bolt-linden-nj.html>
- [3] <https://adxdepot.com.au/fasteners-258/rivets>
- [4] EN 1995-1-1:2004, Eurocode 5: Design of timber structures - Part 1-1: General - Common rules and rules for buildings (CEN: Brussels).
- [5] De Castro J.: “System ductility and redundancy of FRP structures with ductile adhesively-bonded joints”, EPFL PhD Thesis no 3214, Lausanne (2005).
- [6] Tannert T., Vallée T., Hehl S. “ Experimental and numerical investigations on adhesively bonded hardwood joints”, *International Journal of Adhesion and Adhesives* (2012), Vol. 37, p: 65-69
- [7] Angelidi M., Vassilopoulos A. P., & Keller T. Ductility of adhesively bonded timber joints. *International Journal of Computational Methods and Experimental Measurements*. 1st International conference on timber structures and engineering, New Forest, UK (June 2017).
- [8] Sika AG. SikaDur-330: 2-part epoxy impregnation resin (2006).
- [9] Sika AG. SikaFast5221 NT: Fast-curing 2-component structural adhesive. Zurich (2013).
- [10] EN 1990:2002, Eurocode — Basis of structural design.
- [11] EN, B. (2013). 338 Structural timber. Strength classes. British Standards Institute, London (2003).
- [12] Farajzadeh Moshtaghin A. Stochastic analysis of clear timber as a structural material. EPFL Thesis No 6944 (2016).
- [13] Porteous J., & Kermani A. (2013). *Structural timber design to Eurocode 5*. John Wiley & Sons.
- [14] Code, P. (2007). Eurocode 3: Design of Steel Structures-Part 1-2: General Rules-Structural Fire Design.
- [15] Benoit Y., Legrand B., & Tastet V. (2009). *Calcul des structures en bois*. Editions Eyrolles.
- [16] Angelidi M, Keller T. Ductile adhesively-bonded timber joints – strain rate effect (under review)
- [17] Norris GB. Strength of orthotropic materials subjected to combined stress, Report No. 1816. US Department of Agriculture, Forest Research Laboratory. Madison, WI, p: 40 (1950).
- [18] Kretschmann D. E, Ross R. J. Wood handbook: wood as an engineering material, USDA Forest Service General Technical Report FPL-GTR-113, (5): 29, Madison (2010).

Chapter 7

Conclusions and future work

7.1. Main conclusions

Ductile adhesively-bonded timber joints were studied in this thesis, using acrylic adhesives. First the mechanical properties of the acrylics were defined at different loading rates, including the Poisson ratio, true and engineering stress-strain curves, E-modulus, yield and failure stress, ductility and time-dependent recovery. The acrylic joints were then experimentally and numerically investigated to prove the concept of ductility, compared to stiffer, epoxy joints. For the finite element modeling of the acrylic joints, the rate-dependent properties from the first part of the study were used. All comparisons mainly focused on the joint's stiffness, capacity and failure mode, strain and stress distribution and ductility. Finally, the study was extended to include the different possible rates that may also occur in real applications. The main conclusions of the current work are also summarized in the following paragraphs separately for each chapter.

Chapter 2

In this chapter the Poisson ratio of the studied acrylic was evaluated for engineering and true strains, in tension and compression, with the help of the Digital Image Correlation (DIC) technique. It was proved that in the case of highly deformable polymers, such as acrylics, true strains, which take into account the geometry changes, should be used for calculating the **Poisson ratio**. True strains in tension predicted a constant average value close to 0.48, independent of the strain level attained, confirming what is reported in literature for acrylics, while after yield, the engineering strains under- and overestimated the ratio in tension and compression respectively. On the contrary, the ratio in tension was slightly dependent on the displacement rate applied and presented a slight decrease at higher rates or at necking regions, where the rate also locally increased. On the other hand, in compression the structural effects and out-of-plane deformations of the specimens did not allow an accurate estimation of the Poisson ratio, which already exceeded the acceptable limit of 0.5 for polymers at low strains (pre-yield part). However, in the applications envisaged in this work, i.e. the bonded timber joints, the attained results can be used as long as these structural effects are not significant.

Chapter 3

With the help of the previously established Poisson ratio value (equal to 0.48), the **true stress-strain curves** were calculated for this type of acrylic for both types of loading, tension and compression. The obtained true stress-strain responses differed for the two loading types, despite the similar engineering strain rates applied. Based on these true curves, the main mechanical properties of this adhesive were evaluated at **different rates** and the results proved that increasing the strain rate led to a general upward shift of the curves in all cases - increased yield and inflection stresses and elastic modulus, but decreased failure strains. All these trends were accurately modeled with logarithmic formulas, which were previously reported in literature for other rate-dependent polymers as well, proving that the rate sensitivity was more

limited at higher rates. On the other hand, yield and inflection strains and post-yield elastic modulus exhibited almost no change with the various displacement rates applied.

The second part of this study included unloading and reloading cycles, which served to estimate displacement- and energy-based **ductility** indexes and **time-dependent recovery** of this acrylic adhesive. All specimens attained high ductility indices compared to other, traditional materials, such as steel and concrete, and structural systems. The loading type influenced the speed of the recorded recovery, which increased with the increased time during which the specimens remained unloaded. This time-dependency was analytically modeled with an existing exponential, Weibull-based formula for creep recovery; the acrylic adhesive almost fully recovered under both types of loading after 48 hours, indicating that no damage or plastic flow, which would cause residual deformations, took place.

Chapter 4

Acrylic-bonded double-lap joints were experimentally investigated and compared with epoxy joints of similar geometry, in terms of response to loading, stiffness, failure mode and load, ductility and strain distribution. The joints' behavior reflected the properties of the adhesive used. As a result, the epoxy joints exhibited a stiffer, linear behavior up to brittle failure, which was mainly caused by the tensile peel peaks and thus occurred in the inner adherend, close to the adhesive bond line below the outer adherend end in tension, but close to the middle of the inner adherend end in compression. The ultimate loads attained in compression were also much higher than in tension. On the other hand, the acrylic joints exhibited a less stiff, highly non-linear and ductile load-displacement curve in tension. The ultimate loads were also higher than those of the epoxy joints, with mixed-mode failure in most cases, resulting from debonding and crushing of the wood, while in compression, premature failure caused by adhesion problems prevented any conclusions from being drawn. It was noted that, if these problems could have been avoided, a similar non-linear response and higher ultimate loads would have been expected.

The DIC technique was also applied to map the surface of the specimens concerning the displacement and strain fields developed during loading. The displacement applied was mainly borne by the deformation of the acrylic adhesive, while in the case of the epoxy joints, the timber also participated, limiting the epoxy layer's deformation. The reason was the much higher E-modulus of the epoxy, close to that of the timber used, while the E-modulus of the acrylic was 30 times lower on average and thus the acrylic much more deformable. Regarding the **strains** along the overlap length, more uniform distributions and **angles of principal strains** close to 45° on average with respect to the loading axis were recorded in the case of the acrylic joints, linked to the non-linearity of the acrylics and the greater participation of the adhesive in transmitting the applied displacements, as previously discussed. The epoxy joints, however, presented less uniform strains, with significant edge peaks and smaller principal strain angles (20° on average). All these observed differences explained the different ultimate loads attained in each case.

The experimental study of the joints also included a calculation of the **ductility** index, as the main objective was to develop ductile adhesively-bonded joints. Similarly to what was done for the adhesive, the index was calculated using a displacement- and energy-based approach. For the energy-based index, a model for evaluating the degradation of the unloading stiffness in relation to the displacement of unloading was established and this allowed the index to be estimated close to the ultimate displacement, where unloading would have been impossible to achieve in practice. The two kind of indices obtained were proportionally related and increased exponentially for bigger ultimate displacements (i.e. in cases where joints were more deformable). In addition, the estimated ductility (from both applied methods) proved to be higher than those of other structural systems and those recommended by the European timber standards, making the developed joints suitable for application in real timber structures.

Finally, an estimation of the failure load was attempted, based on a strain-based version of the **Norris failure criterion**, which was developed for orthotropic materials and has thus been widely used in timber engineering. The criterion allowed an identification of the areas with high strain concentrations, based on the DIC results, and thus, confirmed the observed points of failure initiation for both types of joints. The criterion was applied for cases where failure was either in the wood or mixed, since it can only be used for timber.

Chapter 5

Finite element models were developed to confirm and complete the experimentally obtained results for the joints. The material types used in the models were the following: orthotropic for the wood, linear elastic for the epoxy and **rate-dependent** elastoplastic for the acrylics, according to the previous findings of this work. First the models were **validated** by the experimental results; the load-displacement response was stiffer and linear for the epoxy joints and less stiff and non-linear for the acrylic joints. All strain distributions and principal strain angles were also validated and similar conclusions were drawn for stresses close to failure.

After the acrylic model had been validated, it was **extended for other applied rates** as well, in order to assess their effect on the joint response. The increased rate resulted in a stiffer response to loading for the acrylic joints, approaching that of epoxy joints; an increasing logarithmic trend was established for the yield load and displacement, while the ultimate load and displacement decreased likewise. The percentage of total displacement borne by the adhesive layer then also increased at a later point for the higher rates, since yield occurred later. Similarly, the angle of the maximum principal strains, which started decreasing from 45° in all cases after yielding, decreased with a certain delay for the higher examined rates.

For all cases, the **stress-based Norris failure criterion** was applied to predict failure; the results matched the experimental values well despite the scatter and the model's sensitivity to the path selection. At higher rates, the edge peaks appeared earlier causing failure at lower loads, while at lower rates the stress

distribution was more uniform, leading to increased joint capacity. Finally, **ductility** was also calculated at all the studied rates, with the help of the previously established relationship between unloading displacement and stiffness. Generally, the previous conclusion linking increased ductility indices with larger ultimate displacements was confirmed by the numerical results and a greater ductility potential was shown at lower rates.

Chapter 6

The developed double-lap joints were finally compared with two different types of mechanical joints of similar geometry, assembled using nails and bolts. After converting all design values into characteristic values, using the safety and material factors from the relevant Eurocodes the two methods of assembling - bonding and mechanical fastening - were compared in terms of joint stiffness and capacity and adhesive bonding proved to be much more efficient for this geometry.

7.2. Original contribution

This thesis contributed from an experimental, numerical and analytical point of view to the following main topics:

Regarding the acrylic adhesive (SikaFast 5221 NT)

- The **Poisson ratio** was evaluated under different displacement rates for a highly deformable acrylic in tension and compression. The ratio was measured based on the two different strain types, true and engineering, and the differences were discussed. The changes in the measured ratio were then associated with changes of the applied rate and the molecular structure during loading.
- The **ductility** (energy- and displacement-based) of acrylics was quantified and compared with that of other existing, more conventional materials and structural systems. The energy-based definition, also taking into account the unloading path, confirmed that a significant amount of energy could be dissipated and stored during loading through displacement.
- An analytical model for predicting the acrylic's **time-dependent recovery** after unloading was conceived based on existing models for recovery after creep loading.

Regarding the adhesively-bonded timber joints

- **Ductile joints** were successfully developed using acrylic adhesives; they were non-linear, less stiff and more deformable compared with traditional, epoxy joints. Their ductility was predicted and quantified based on both existing methods (energy and displacement) through the degradation of the unloading stiffness of the joints.
- The effective use of the **DIC technique** as supplementary experimental tool for investigation of the strain distribution along the specimen surface was established. The obtained results helped to interpret the mechanical response to loading for the two different types of adhesive joints.

- A **strain-failure prediction** was achieved based on the DIC results and a modified stress-based failure criterion for timber. Despite the significant scatter related to the timber's modulus of elasticity and failure strain, if the calibration is well done, it is possible to identify areas of large strain concentrations, where failure is likely to occur.
- A **rate-dependent FE model** (validated by the DIC), suitable for describing the viscoelastic nature of the acrylic used, was adopted, based on the rate-dependent true stress-strain curves obtained from the first part of the thesis. An **FE parametric study** for various theoretical displacement rates was consequently conducted for the acrylic joint, based on this model. The effect of the applied rate was mainly evaluated with regard to the following mechanical properties of the joint:
 - Stiffness
 - Yield and ultimate displacements and loads
 - Ductility (energy- and displacement-based)
 - Strain and stress distributions and angles of principal strains

7.3. Future research

Several recommendations are presented in the following paragraphs as a potential extension of the current study on adhesively-bonded timber joints.

7.3.1. Extend the adhesive investigation for compression

The rate effect on the Poisson ratio of the investigated acrylic was limited in compression, due to the structural effects that occurred from the beginning of the experiments. Large out-of-plane deformations and concentrated friction close to the edges, where displacement was applied, did not allow a safe estimation of the true stress-strain curves, or of the two strains developed (longitudinal and transverse), which were then used for the Poisson ratio estimation. If a different experimental set-up were used, these problems would be addressed and the accurate adhesive properties would also be acquired for compression.

7.3.2. Extend the parametric study for higher rates

The parametric study of the acrylic joint, conducted with the help of the finite element model, was limited at higher rates because the input properties of the acrylics were only given for a limited range of five different rates. If this set of adhesive properties were broadened, the case studies could also be extended for higher loading rates. This inevitably also requires an expansion of the experimental investigation of the acrylic true stress-strain curves at higher rates, which could be the topic of a future work.

7.3.3. Extend these experiments on the joints to a larger number of rates

Although the FE can accurately simulate the adhesively-bonded joints and the parametric study has already predicted the effect of the displacement rate on the mechanical response of the joint, supplementary

experimental data for the acrylic joints should be collected for various applied rates. This could further validate the developed model and allow the safe estimation of the low limits below which creep occurs.

7.3.4. Extend the parametrical study for compression

In addition to the current study in tension, the parametrical study should equally be extended to include compression, since both types of loading may occur in real applications and the acrylic properties proved to differ significantly between these two types. A necessary step to achieve this would be to solve on an experimental level the adhesion problems that lead to premature failure of the acrylic joints in compression and obtain the full load-displacement curve, with failure initiating in the timber and not in the adhesive interface. This would provide the researcher with the essential input for validation of the finite element model, before further changes in the applied displacement rate are attempted.

7.3.5. Develop a ductile timber structure

A ductile timber structure, composed only of adhesively-bonded joints, could be the main topic of future research in the field of adhesive bonding in timber engineering because it could prove in practice all the aforementioned advantages of the ductile adhesively-bonded joints. The current literature does not contain information related to adhesively-bonded timber structures although ductility is a key issue related to timber. The developed bonded structure (an acrylic timber truss for example) could be compared with a similar mechanical structure composed only of mechanical joints in terms of mechanical behavior, as was done in this thesis for the adhesively-bonded timber joints.

In addition to the comparison of the mechanical response (e.g. stiffness, ultimate loads, failure mode, yield and nonlinearity, ductility, strain distribution), the study could be extended for several loading rates that may occur in a real timber structure (e.g. a timber roof or bridge). The result would be a proved ductile concept for timber structures, which could be applied by timber engineers to compensate for timber's absence of ductility.

7.3.6. Search for alternative ductile adhesives

In this work, it has been seen that there have been two sources of limitation for the studied adhesive, the acrylic SikaFast 5221 NT;

- The first one is related to the low glass transition temperature, T_g (close to 45°) and
- The second one is linked to the adhesion problems that caused the premature failure in compression.

Consequently, research in the adhesive industry could be oriented towards developing ductile adhesives with a higher T_g and better adhesion with timber. These are necessary for developing ductile timber joints, the benefits of which, when used in timber structures, have already been analyzed.

Annex A

Tensile and compressive properties of the acrylic (Poisson ratio)

This Annex contains all the experimental load-displacement and stress-strain (true and engineering) curves related to **Chapter 2**. The measurements derived from the machine readings. In addition, it contains the average Poisson ratio for each specimen, as it has been extracted from the Digital Image Correlator (DIC) software. They can be used to retrace all the mechanical properties of the specimens, which were already summarized in the tables of that chapter.

A.1. Tension

Load-displacement and stress-strain curves

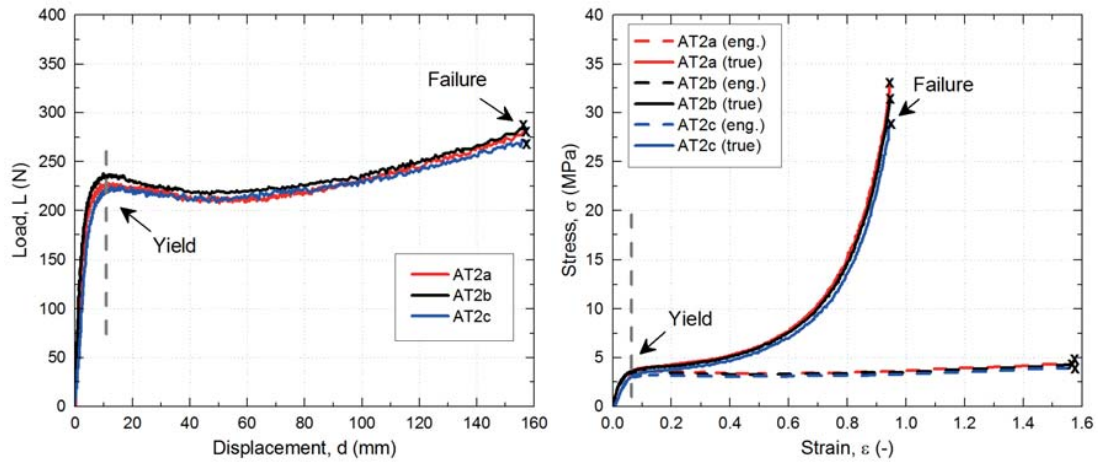


Figure A.1: Tensile specimens at 2 mm/min

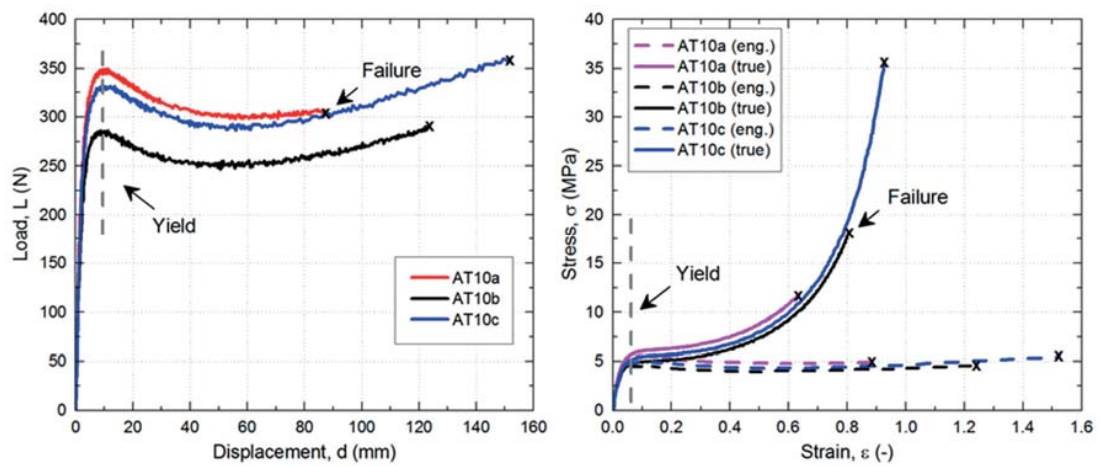


Figure A.2: Tensile specimens at 10 mm/min

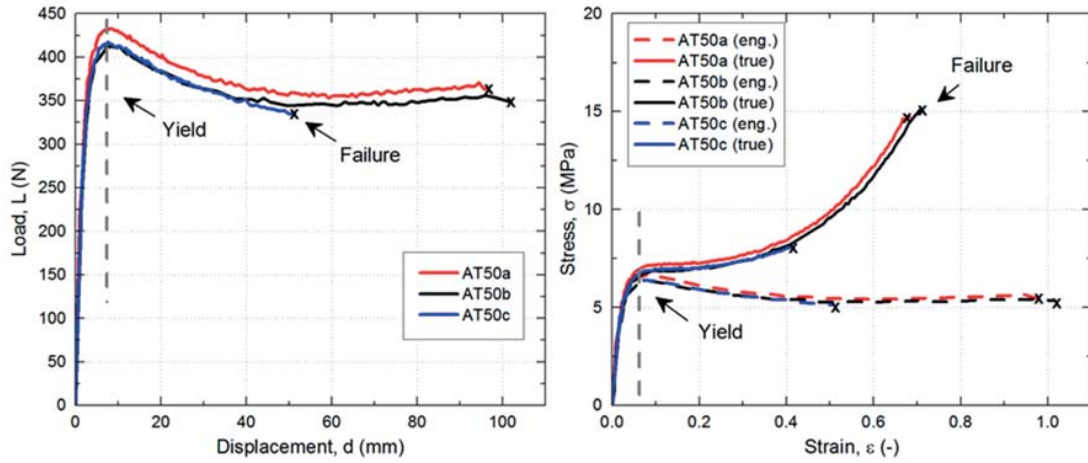


Figure A.3: Tensile specimens tested at 50 mm/min

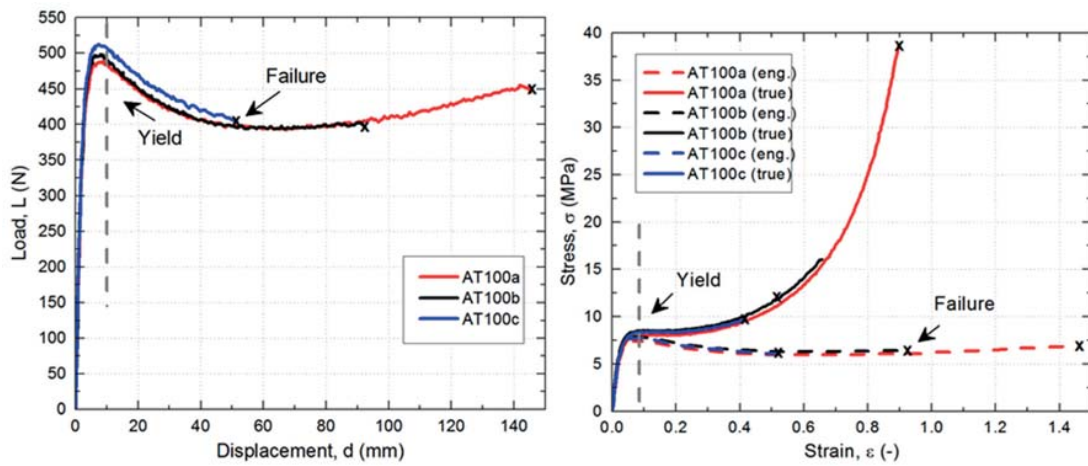


Figure A.4: Tensile specimens at 100 mm/min

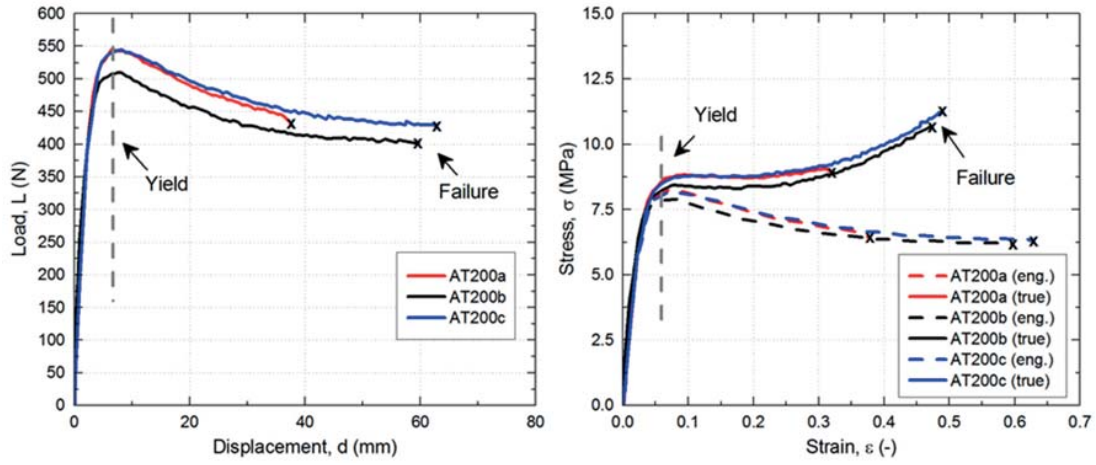


Figure A.5: Tensile specimens at 200mm/min

A.2. Compression

A.2.1. Load-displacement and stress-strain curves

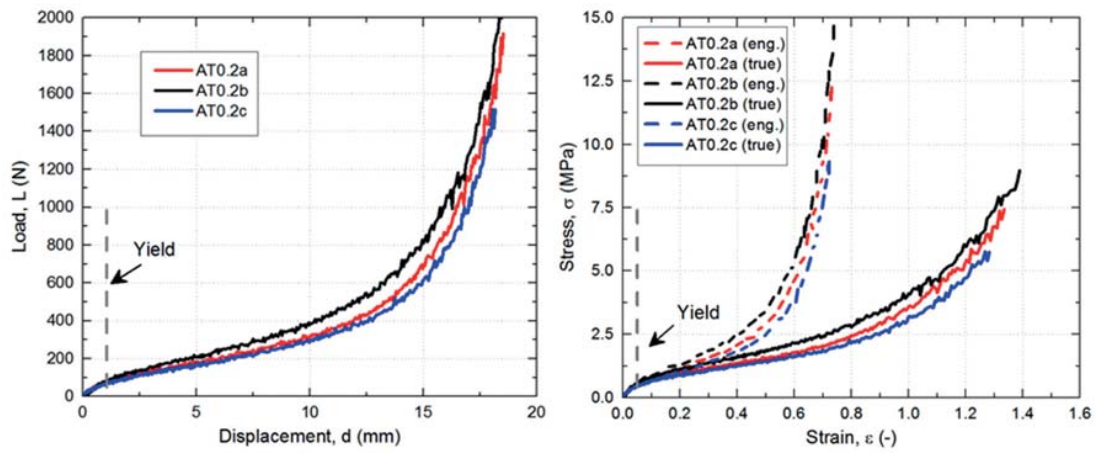


Figure A.6: Compressive specimens at 0.2 mm/min

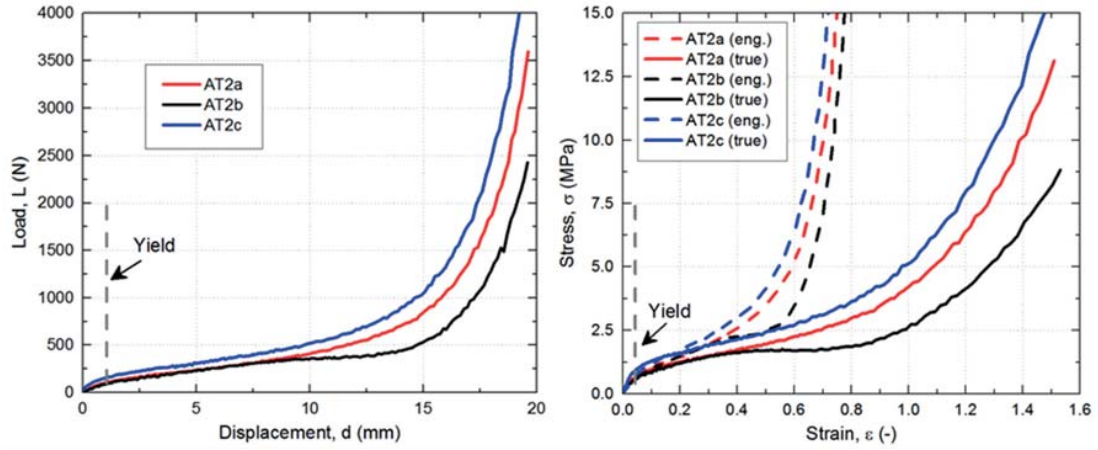


Figure A.7: Compressive specimens tested at 2 mm/min

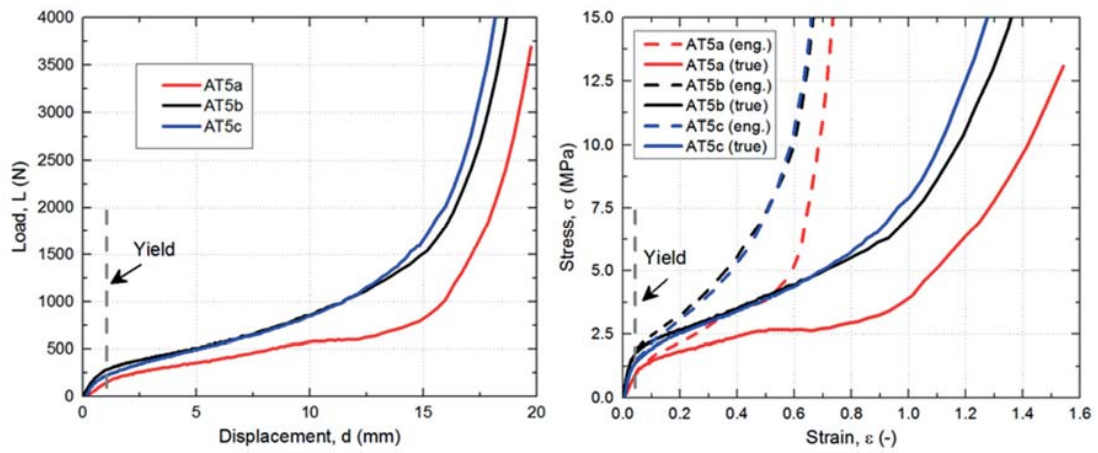


Figure A.8: Compressive specimens at 5 mm/min

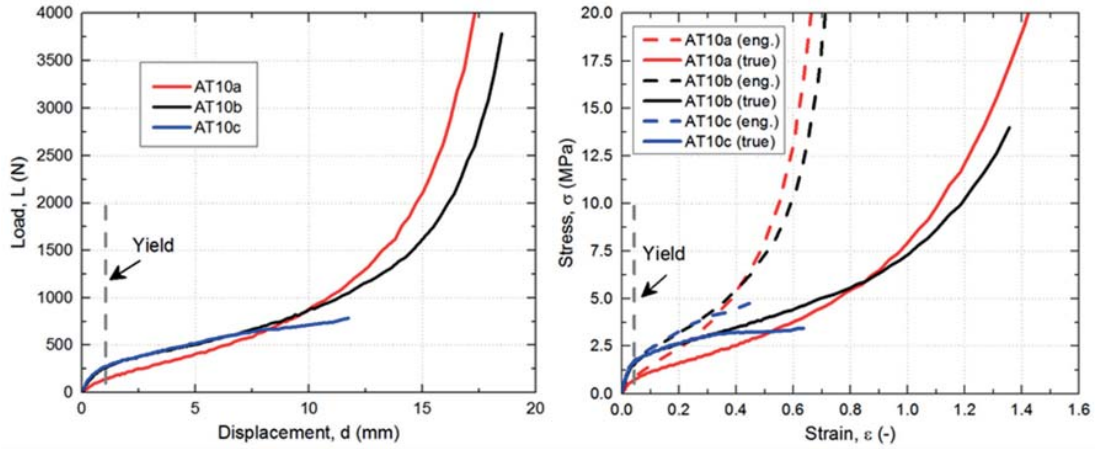


Figure A.9: Compressive specimens tested at 10 mm/min

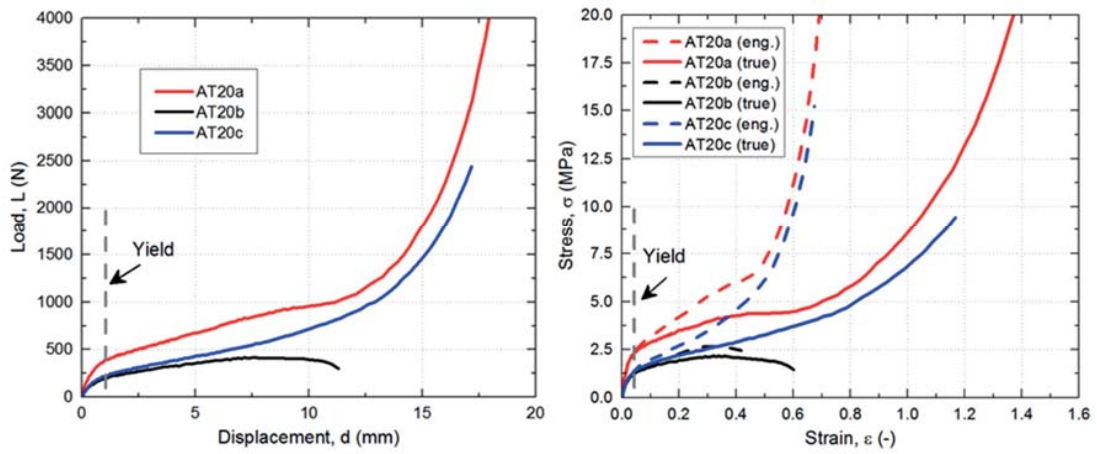


Figure A.10: Compressive specimens at 20 mm/min

A.2.2. True Poisson ratio

0.2 mm/min

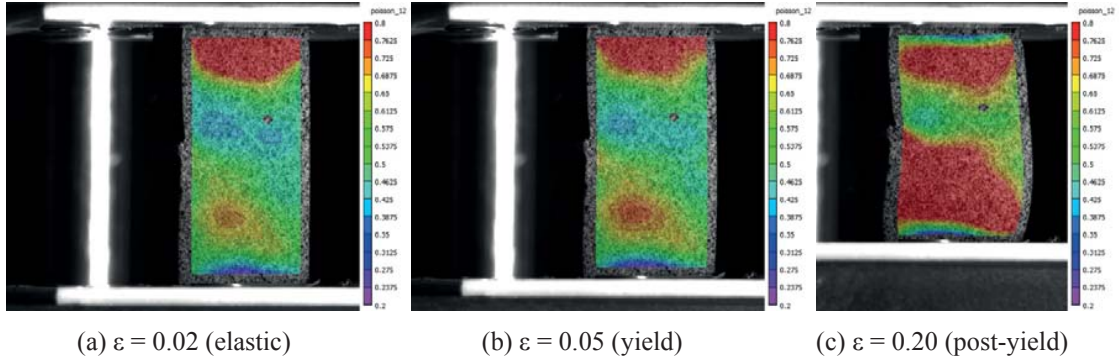


Figure A.11: Specimen AC0.2a

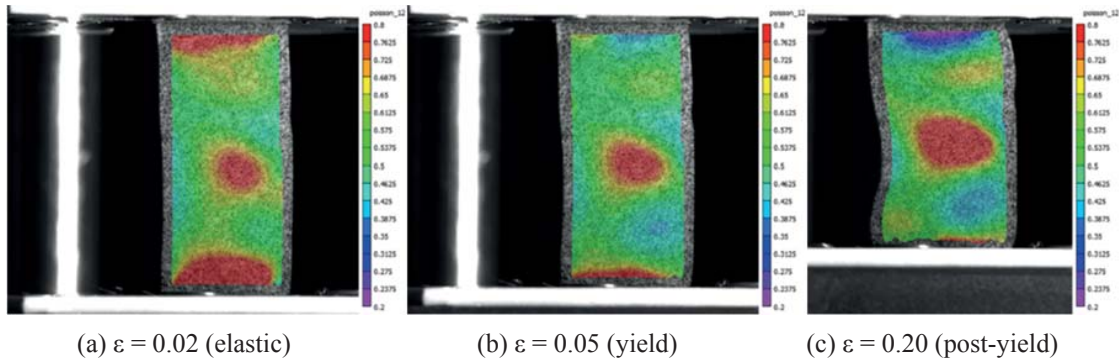


Figure A.12: Specimen AC0.2b

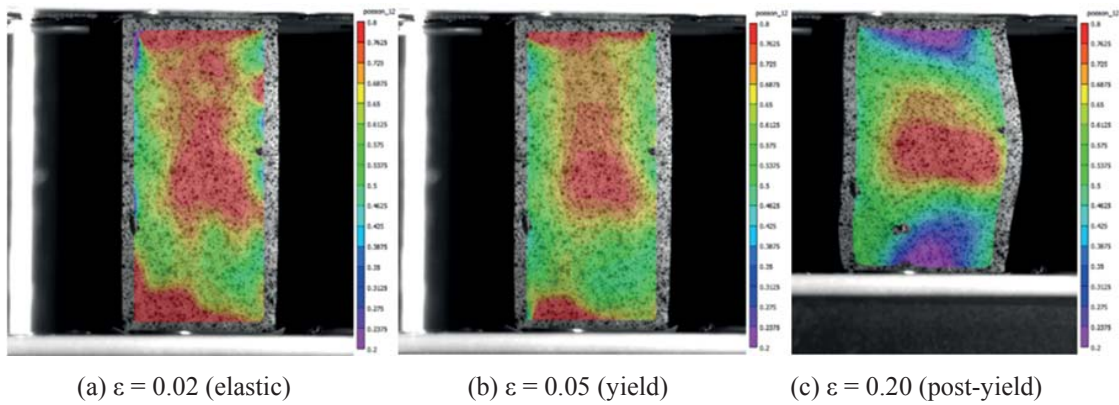


Figure A.13: Specimen AC0.2c

2 mm/min

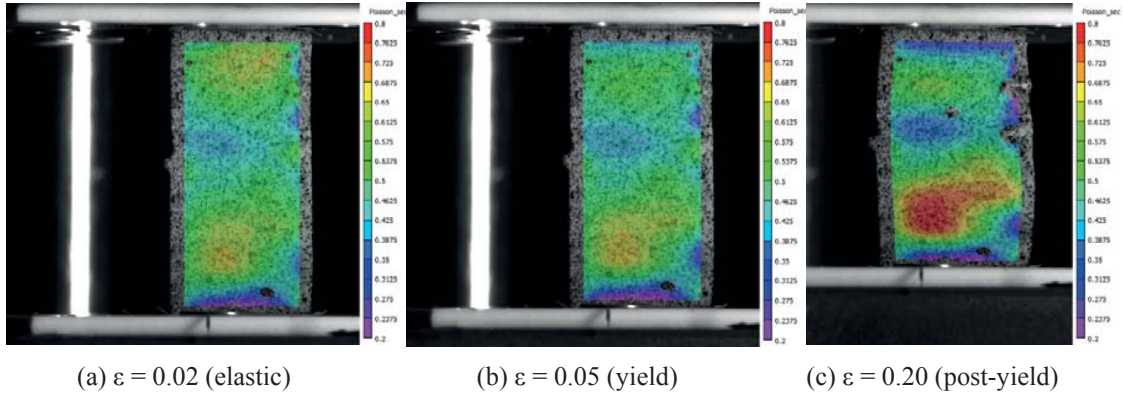


Figure A.14: Specimen AC0.2a

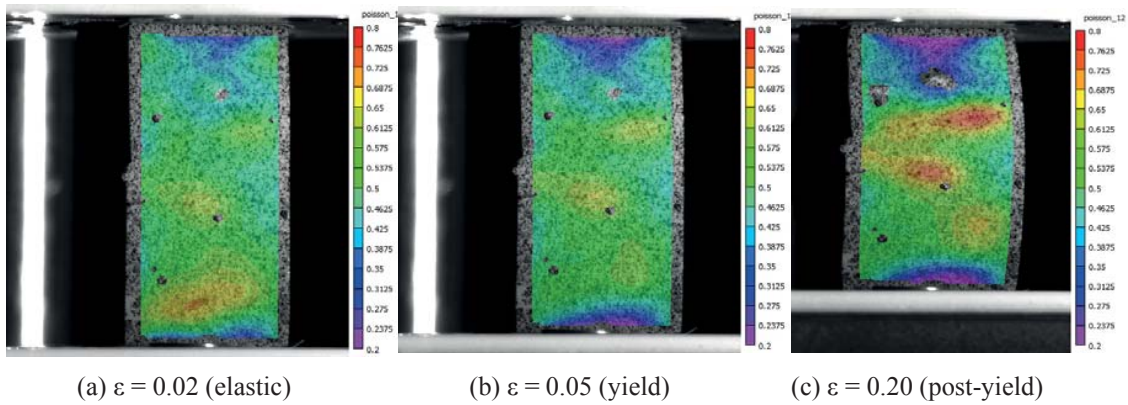


Figure A.15: Specimen AC0.2a

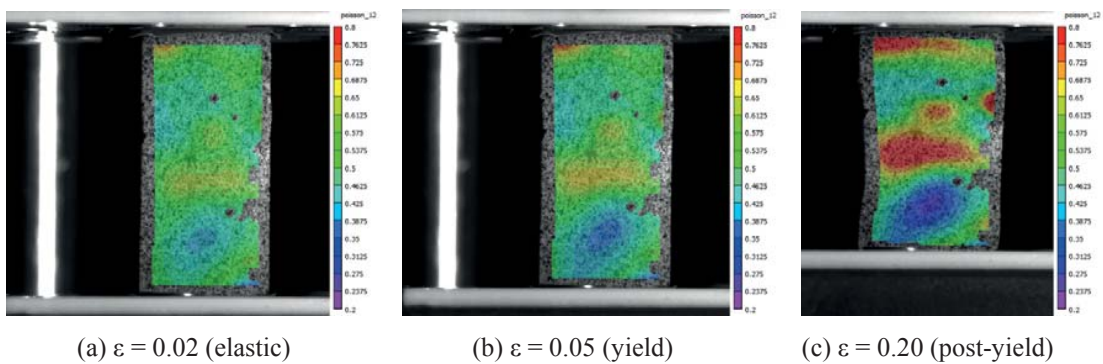


Figure A.16: Specimen AC0.2a

5 mm/min

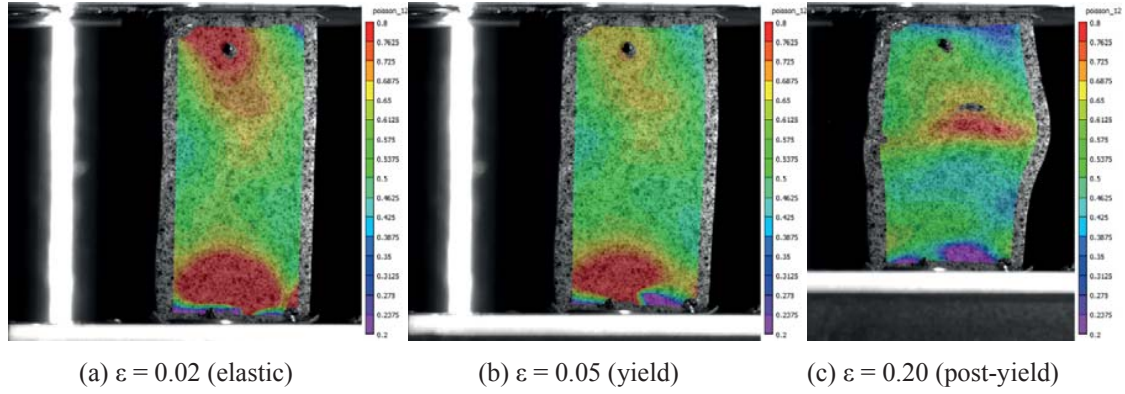


Figure A.17: Specimen AC0.2a

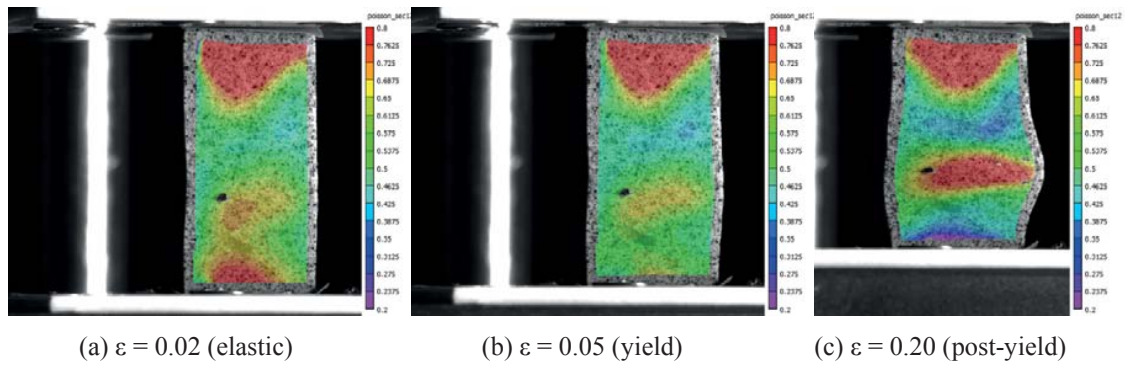


Figure A.18: Specimen AC0.2a

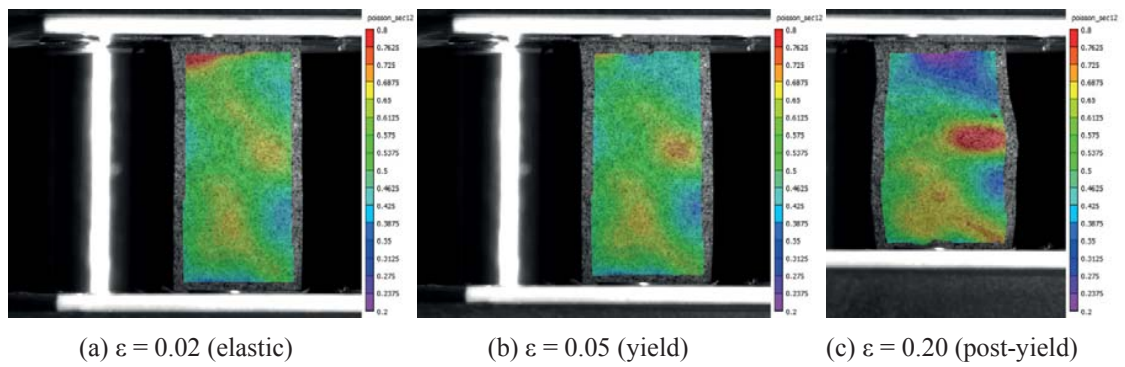


Figure A.19: Specimen AC0.2a

10 mm/min

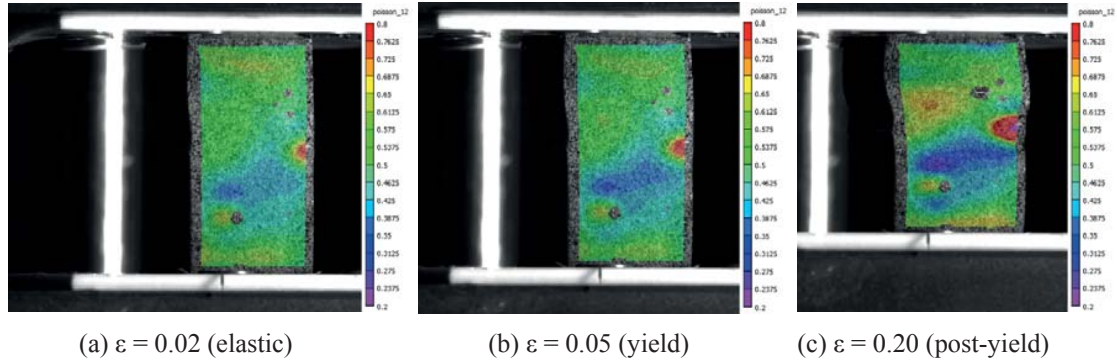


Figure A.20: Specimen AC0.2a

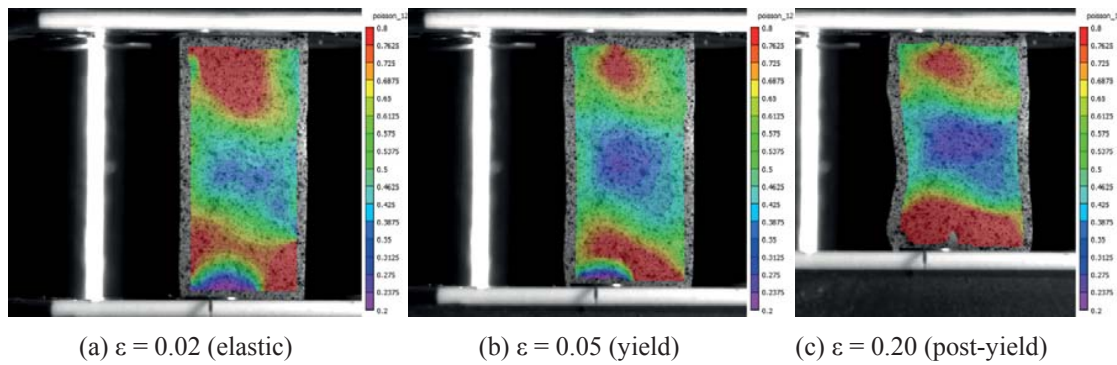


Figure A.21: Specimen AC0.2a

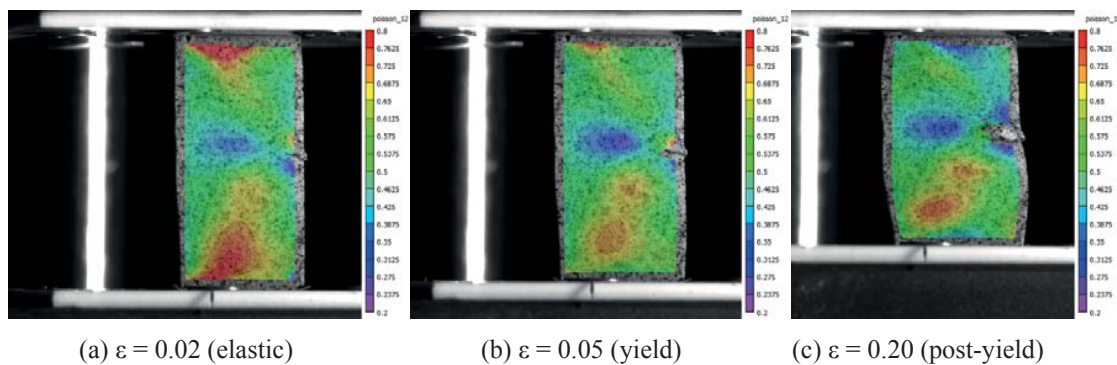


Figure A.22: Specimen AC0.2a

20 mm/min

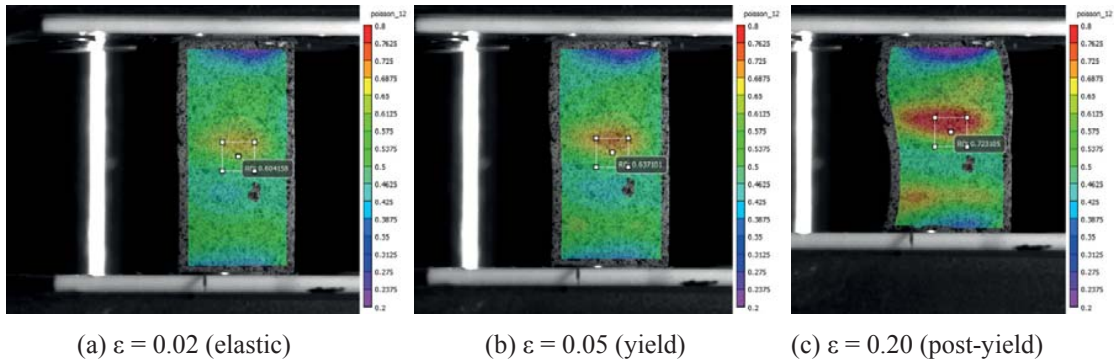


Figure A.23: Specimen AC0.2a

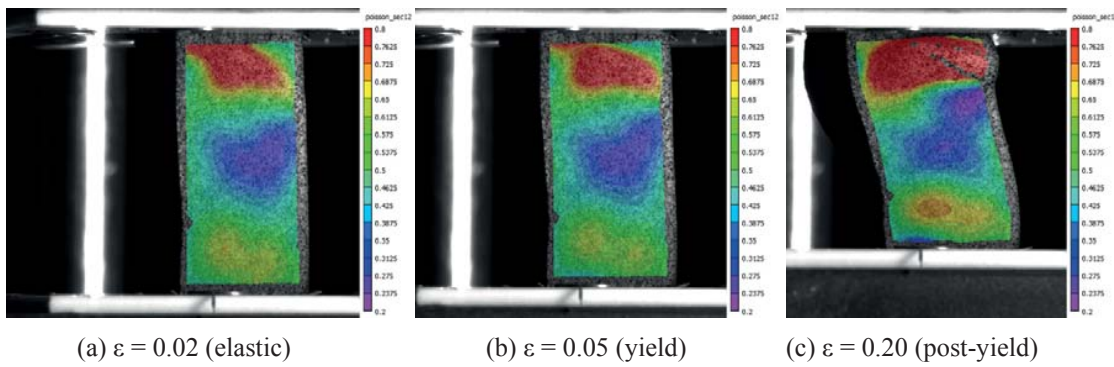


Figure A.24: Specimen AC0.2a

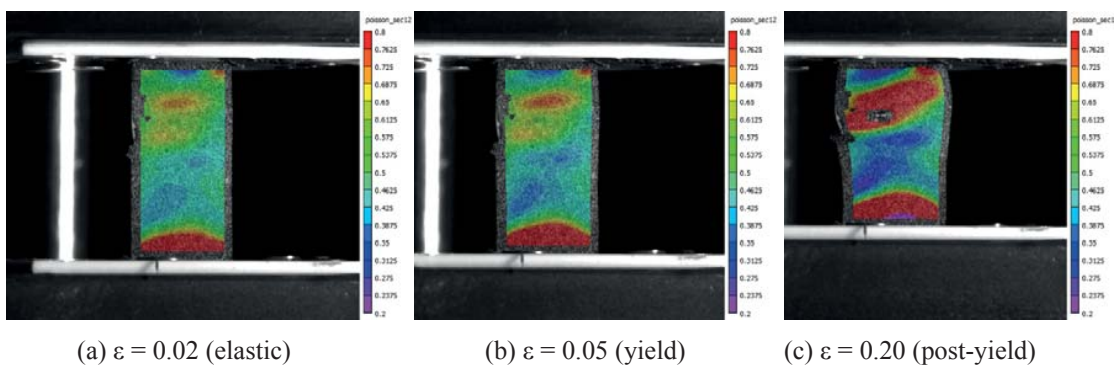


Figure A.25: Specimen AC0.2a

Annex B

Tensile and compressive properties of the acrylic (Ductility and recovery)

This Annex contains all the experimental load-displacement and stress-strain (true and engineering) curves related to **Chapter 3**. The measurements derived from the machine readings and the linear variable displacement transducer (LVDT). They can be used to retrace all the mechanical properties of the specimens, which were already summarized in the tables of that chapter.

B.1. Tension

Load-displacement and stress-strain curves (true and engineering)

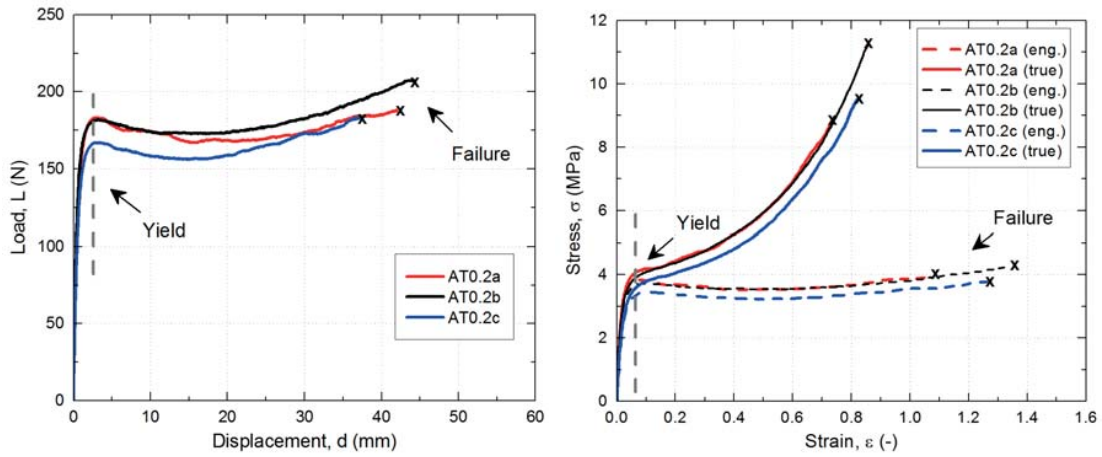


Figure B.1: Tensile specimens at 0.2 mm/min

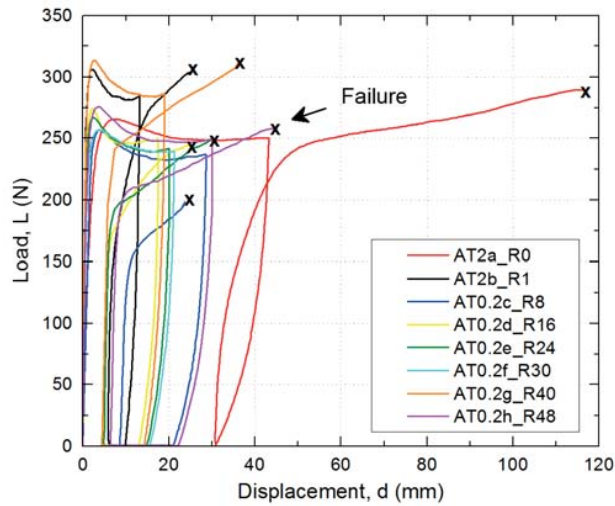


Figure B.2: Tensile specimens at 2 mm/min (reloading curves)

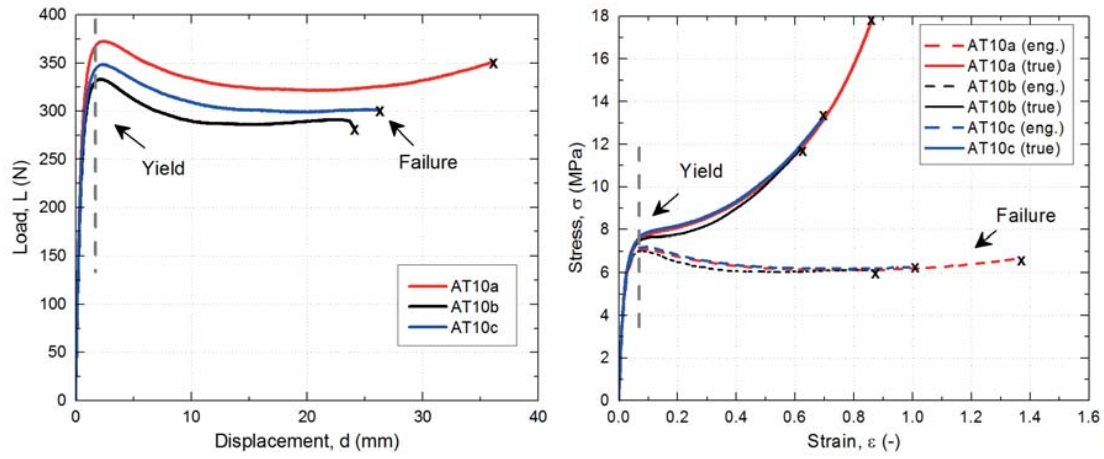


Figure B.3: Tensile specimens tested at 10 mm/min

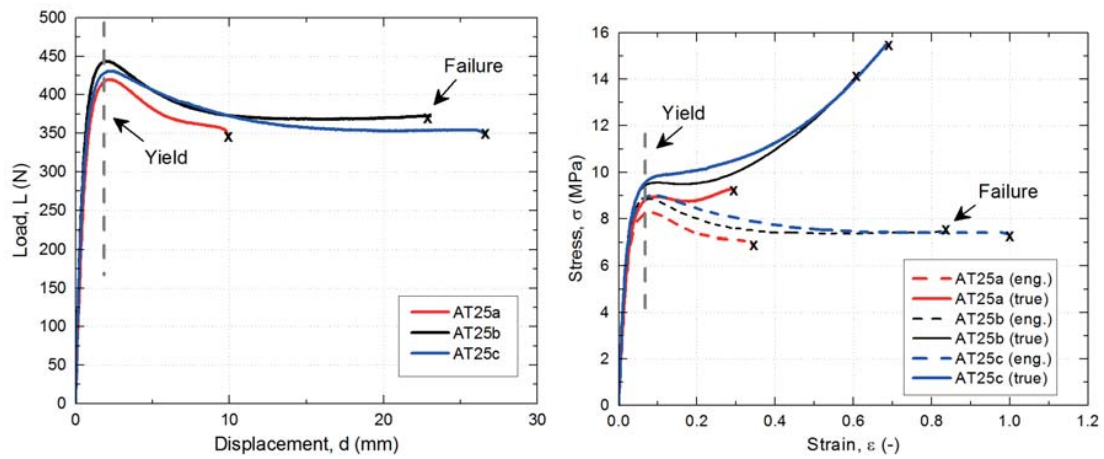


Figure B.4: Tensile specimens at 25 mm/min

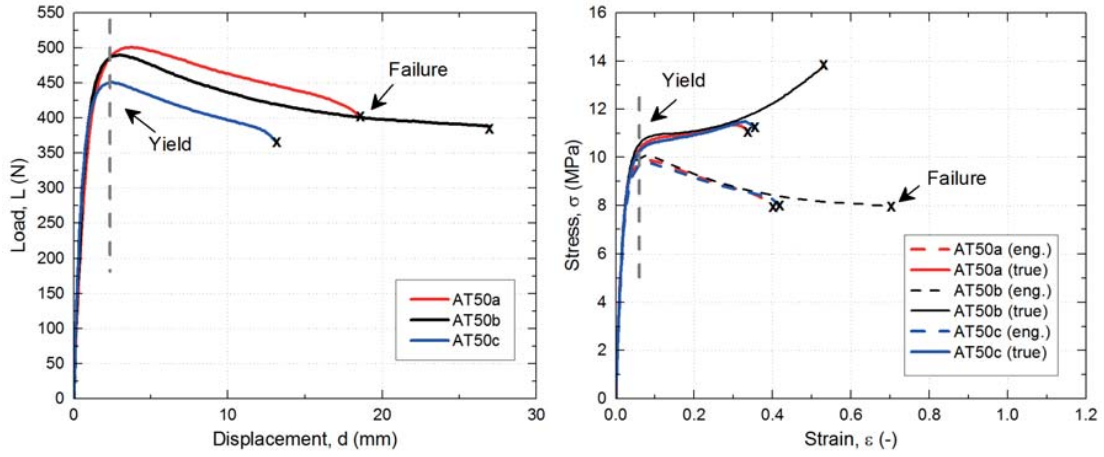


Figure B.5: Tensile specimens at 50 mm/min

B.2. Compression

A.2.1. Load-displacement and stress-strain curves

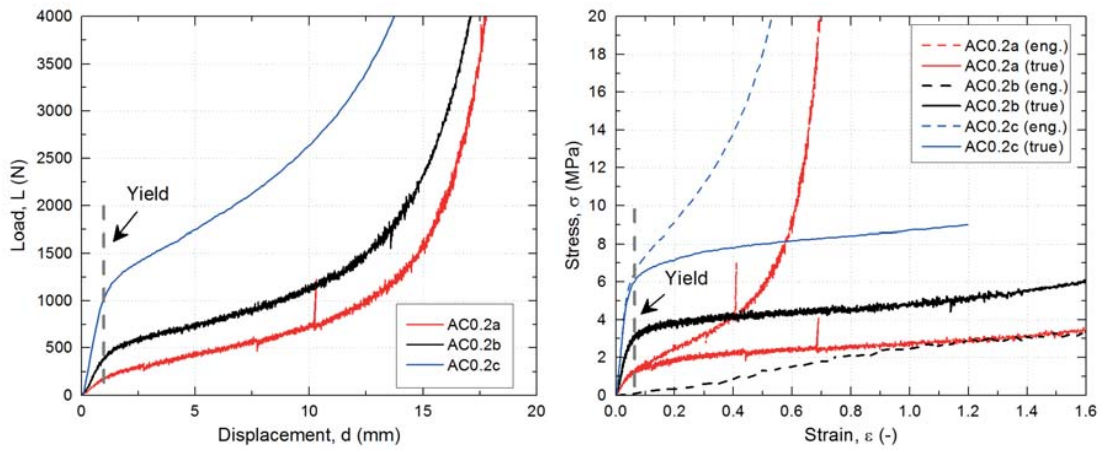


Figure B.6: Compressive specimens at 0.2 mm/min

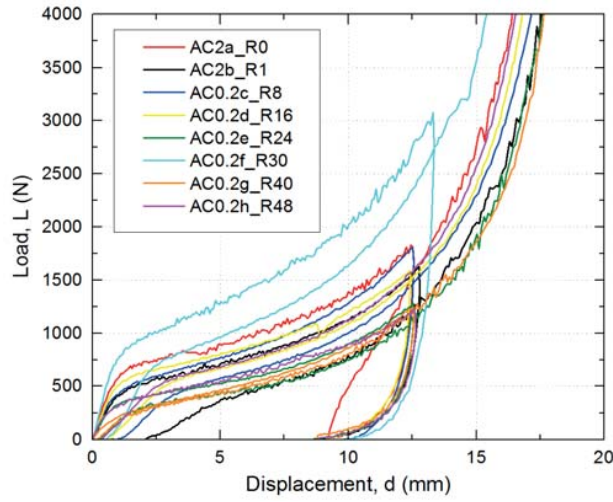


Figure B.7: Compressive specimens tested at 2 mm/min (reloading curves)

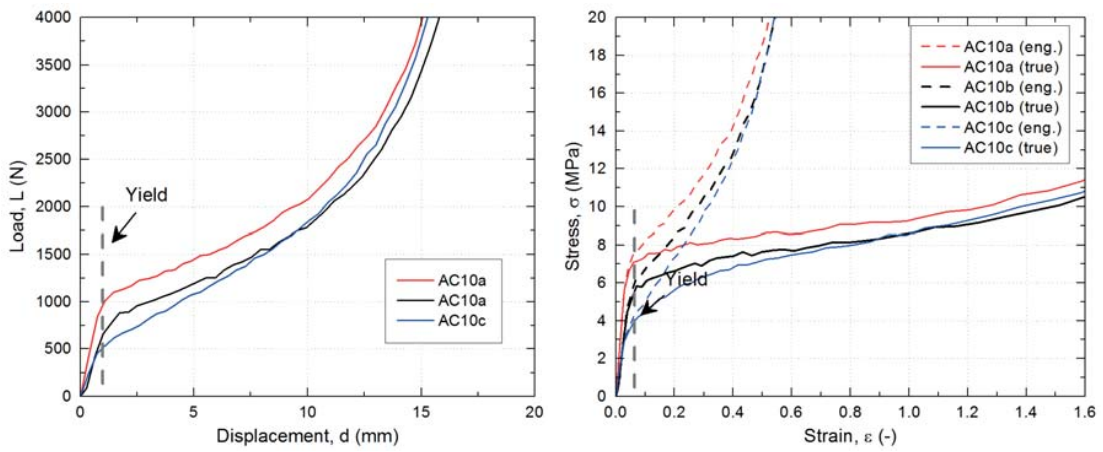


Figure B.8: Compressive specimens at 10 mm/min

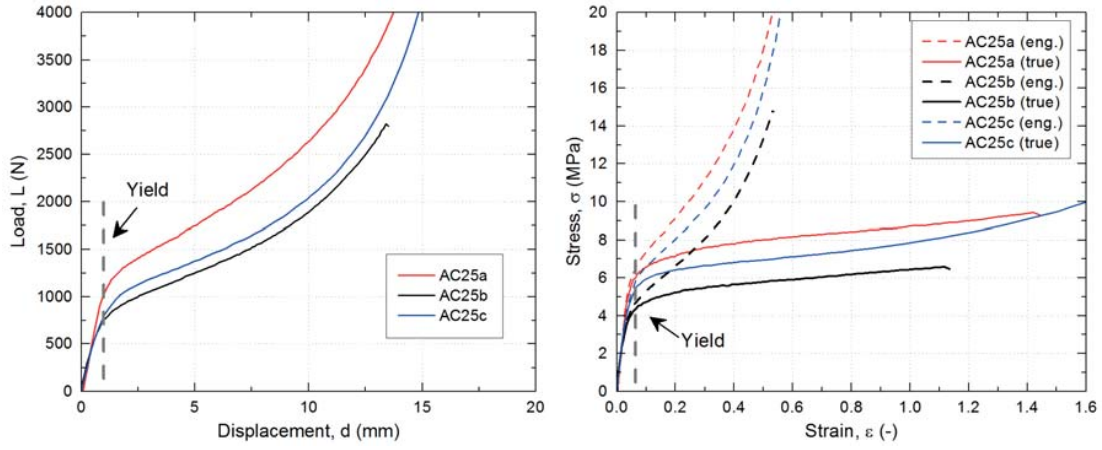


Figure B.9: Compressive specimens tested at 25 mm/min

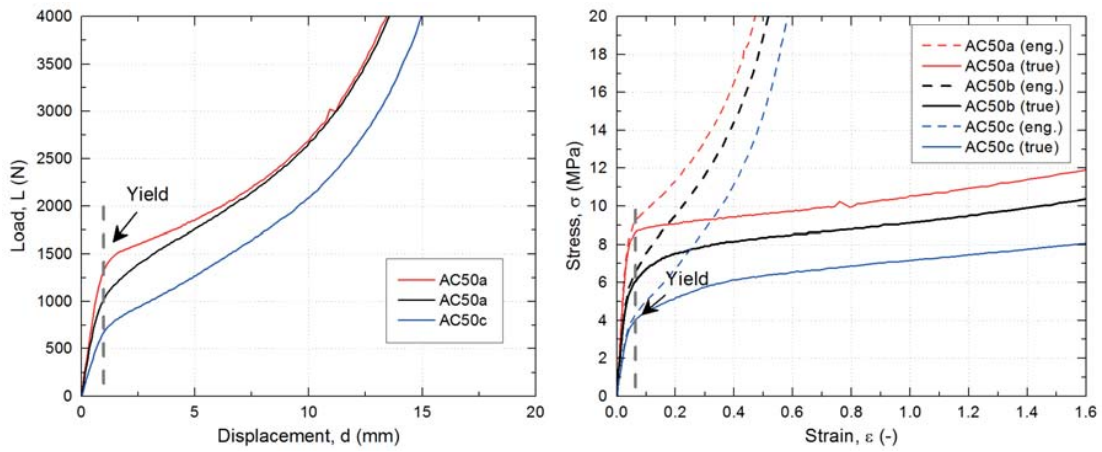


Figure B.10: Compressive specimens at 50 mm/min

Annex C

Experiments on double-lap joints: Failure modes

This Annex contains supplementary failure photos from the experiments on the two types of adhesively-bonded double-lap timber joints: epoxy- and acrylic-bonded. The results are shown for tension and compression and they can be used to retrace all the failure modes of the specimens, which were already summarized in the tables of **Chapter 4**.

C.1. Tensile experiments

C.2.1 Epoxy-bonded joints



Figure C.1: Joint E_T1

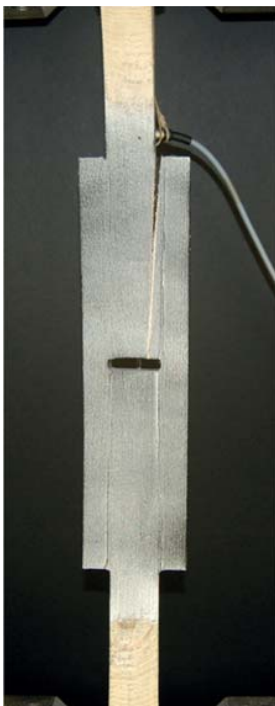


Figure C.2: Joint E_T2

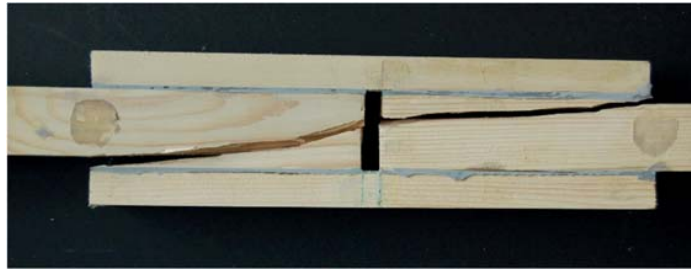
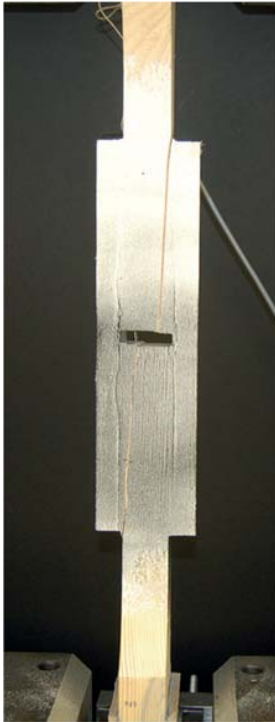


Figure C.3: Joint E_T3

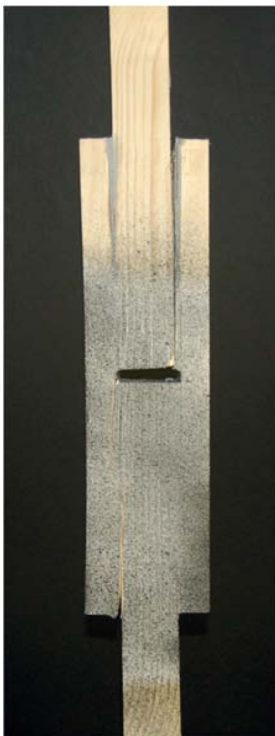


Figure C.4: Joint E_T4

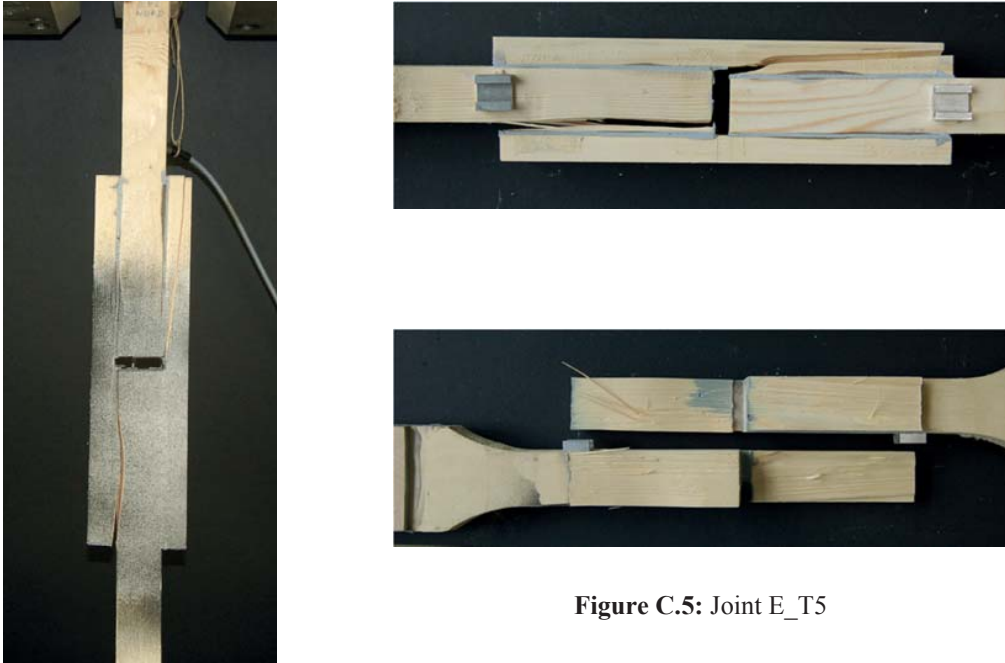


Figure C.5: Joint E_T5

C.2.2 Acrylic-bonded joints

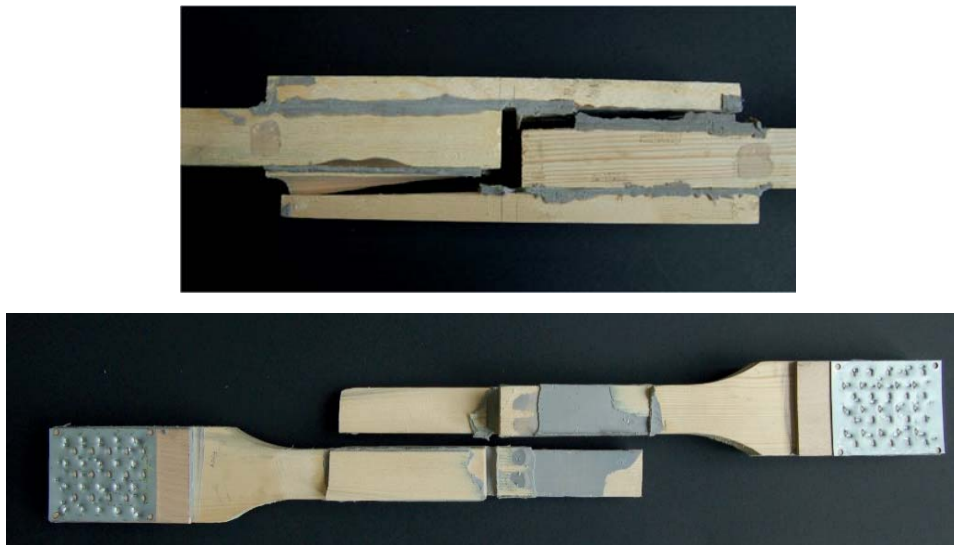


Figure C.6: Joint A_T1



Figure C.7: Joint A_T2



Figure C.8: Joint A_T3

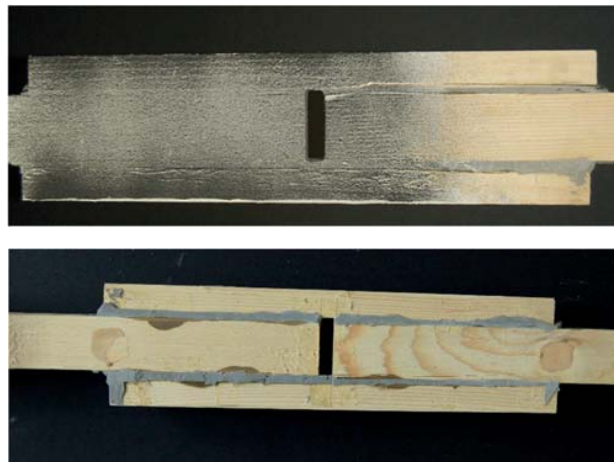


Figure C.9: Joint A_T4

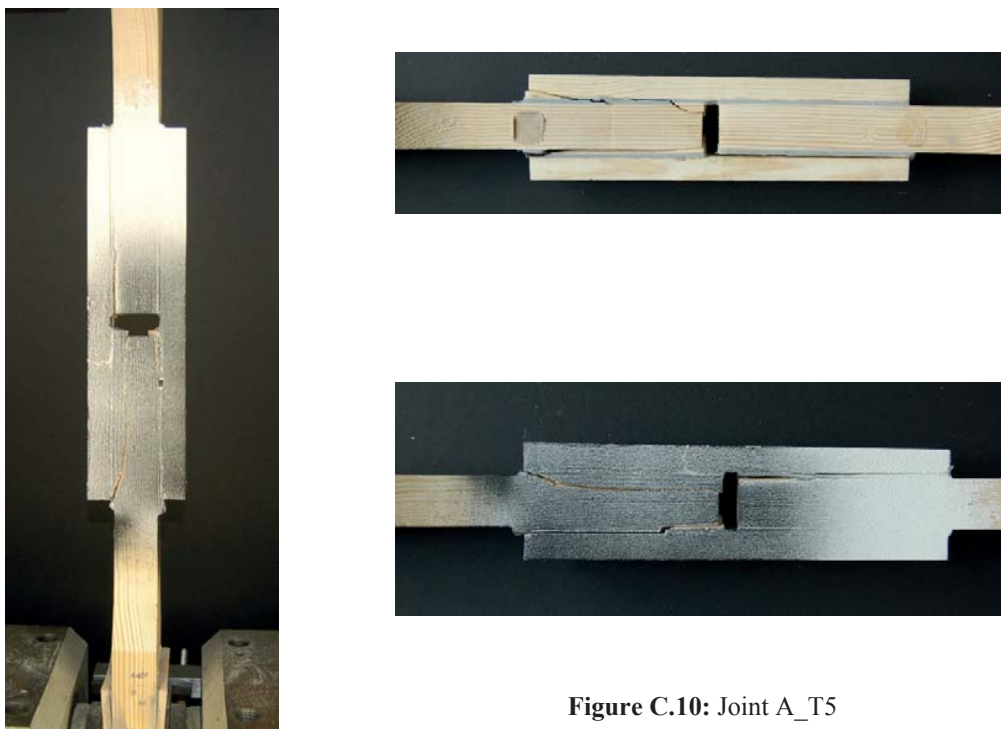


Figure C.10: Joint A_T5

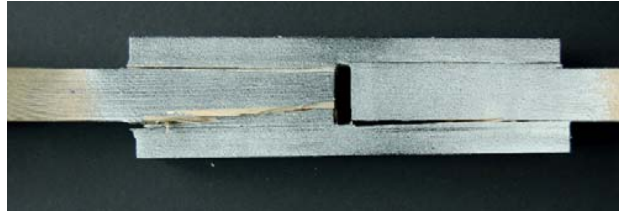
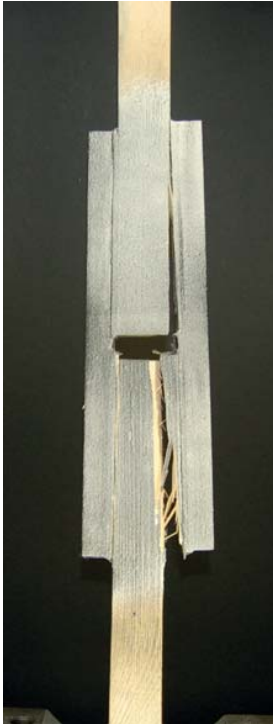


Figure C.11: Joint A_T6

C.2. Compressive experiments

C.2.1 Epoxy-bonded joints



Figure C.12: Joint E_C1

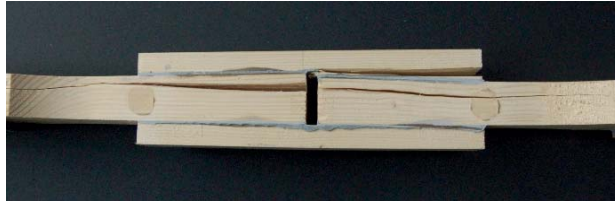


Figure 13: Joint E_C2



Figure 14: Joint E_C3



Figure 15: Joint E_C4



C.2.2 Acrylic-bonded joints



Figure C.16: Joint A_C1



Figure C.17: Joint A_C2

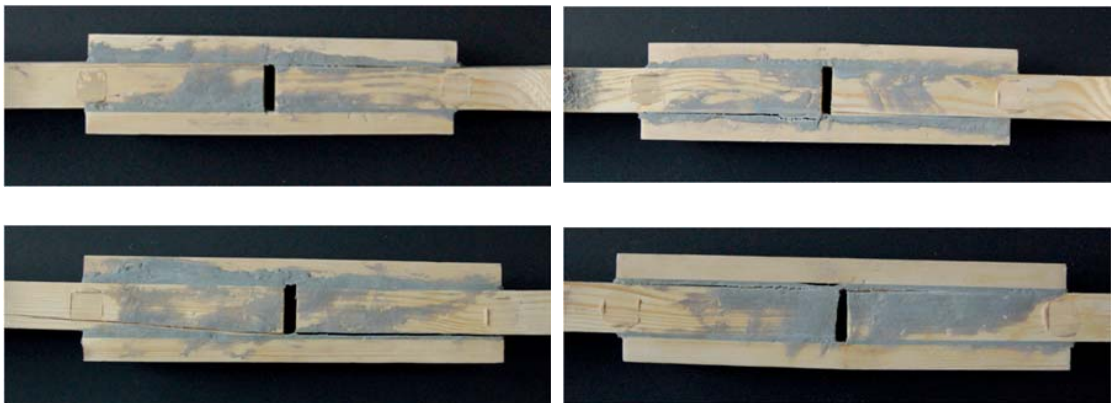


Figure C.18: Joint A_C3

Figure C.19: Joint A_C4

Annex D

Numerical modeling of double-lap joints: Compression

All experimental results regarding the epoxy- and acrylic-bonded timber joints were presented for both types of loading, tension and compression, in **Chapter 4**. Later, in **Chapter 5**, the validation of the finite element (FE) models developed as well as the different case studies for several applied displacement rates were conducted for the case of tension. In this annex, the two FE models (for the epoxy and acrylic joints) are also presented for compression, in order to complete the current study.

Finite element models for compression

Both FE models were developed as described in [chapter 4](#), using the same materials, element type and meshing. The only difference was the applied displacement, which was applied under the same rate but opposite direction, as in the compressive experiments. The obtained load-displacement curves are included in Figures D.1 and D.2. As it can be seen, the FE curves matched very well with the experimental ones. They present similar initial (pre-yield) stiffness, despite the fact that acrylic joints failed prematurely, due to adhesion problems, as discussed in [chapter 5](#) as well.

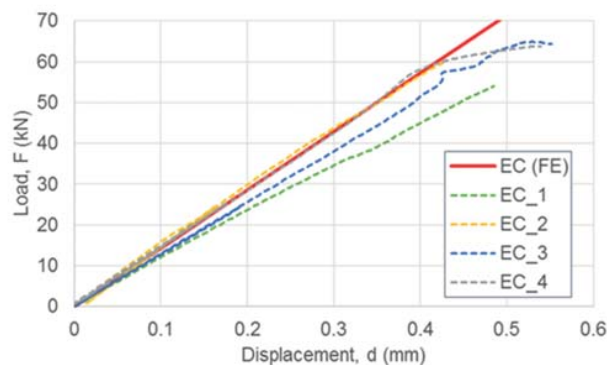


Figure D.1: Load-displacement curves for epoxy-joints in compression

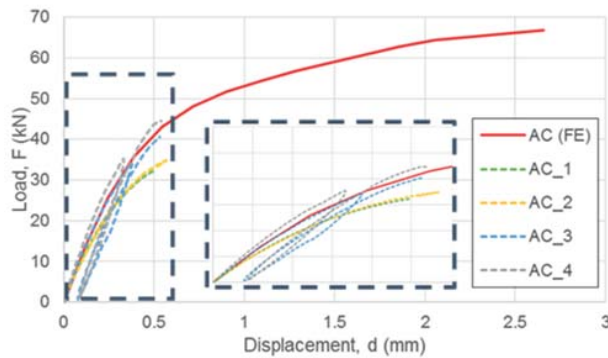


Figure D.2: Load-displacement curves for acrylic-joints in compression

Annex E

Geometrical and material parameters on the double-lap timber joint capacity

As the advantages of using adhesively-bonded joints in modern construction are gradually becoming obvious, they are being used in an increasing number of applications. In this work, using statistical analyses, the relative importance of factors affecting the capacity of a double-lap joint are evaluated. For this purpose, input data required for statistical analysis are extracted from experiments and numerical simulations. Then, using full and fractional factorial designs, the factors with the highest influence are determined. The results show that the material parameters of timber and adhesive are more important than geometrical parameters in determining joint capacity. Moreover, the comparison of the output obtained from fractional factorial design with that from full factorial design shows that the former is also sufficiently accurate.¹

Keywords: *double-lap joint, timber, adhesive, joint capacity, factorial design*

¹ This study was conducted partly in collaboration with Francesco Cavagnis and Alireza Farajzadeh Moshtaghin (EPFL).

E.1. Introduction

During recent years, the need for sustainable structures composed of environmentally friendly materials has become more and more apparent. New structures are continuously being built to meet the different needs of the human population worldwide, but at the same time the environmental crisis emphasizes the necessity of using new materials, different from conventional ones such as concrete and steel, in order to produce structures with low CO₂ emissions and reduce the carbon footprint.

One of the most renewable and recyclable materials is wood, as its origin is completely natural and trees can be replenished. Wood is one of the most ancient construction materials, but its mass production and the extensive use of concrete and steel have gradually led to wood being used in only a limited number of structural applications, although it has many advantages to offer, such as strength, long-term endurance, appearance and abundance [1].

Joining techniques

There are many ways to join two or more pieces of wood together, forming a safe and durable connection that guarantees the safe transfer of all loads. The most common are mechanical joints (using rivets, dowels, bolts, steel plates), welded joints (where joining is achieved through coalescence) and finally, bonded joints, using a suitable adhesive.

This study focuses on adhesively-bonded timber joints, which offer many advantages compared to mechanical joints. Bonded joints usually exhibit higher capacities than connections using dowel-type mechanical fasteners, but also higher stiffness, the latter being of great importance when the governing factor is serviceability limit state (SLS), as is often the case with timber structures. In addition, adhesive joints can be less expensive in general and provide better fire resistance. Moreover, their application is easier and faster and allows much greater variety in structural design, offering architects wider scope for inspiration and new forms of structures [2, 3].

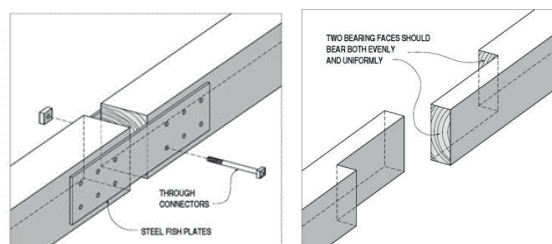


Figure E.1: Mechanical and bonded timber joints

Another benefit of adhesively-bonded joints is that the adhesive can also serve as a good sealant and provide the joint and consequently the structure with effective insulation properties.

Finally, it is important to obtain homogenized properties and standard design dimensions and bonded joints allow both of these, because the load is more uniformly distributed and there is much better stress distribution along, with fewer and lower stress peaks on, the areas of connection, especially when more ductile adhesives are used. Fig. E.1 illustrates examples of mechanical and bonded joints.

Parameters of bonded joints

There are many parameters that affect the capacity and resistance of a bonded joint and it is really important to investigate the effect of all of them before designing a structural joint.

One important parameter is the geometry of the joint. Determining the type of joint is not enough, because other details such as overlap length, thickness of the adhesive layer, thickness of the bonded timber members, height of the specimen, and dimensions of the part used for the grips also have to be defined at the very beginning when designing a timber joint. In addition, the type of wood used for such joints plays a major role. The wood industry separates wood into two main categories, hardwood and softwood, according to the tree of origin and its structure. Furthermore, wood is the product of many years of natural processes and it is therefore only to be expected that there is a great variety of wood quality depending on many factors such as age and local environmental conditions. As a result, different types of wood can be expected to behave differently under the same loading conditions. Moreover, in the case of wood, an essential consideration is its natural conditioning. Not only is wood a highly anisotropic material but, since it is a natural composite, it is also highly influenced by environmental conditions, mostly temperature and moisture (content and surrounding). Therefore, before experiments on such joints are conducted, it has to be ensured that the same environmental conditions are maintained.

Moreover, the capacity of the bonded joint depends extensively on the quality of the adhesive used. There are many different types of adhesives, from more brittle ones like epoxy adhesives to more ductile ones like polyurethane and acrylics, but which have lower ultimate strength. In other words, once again, the correct adhesive must be selected and correctly applied, according to the manufacturer's guidelines. And last but not least, the loading conditions on such joints determine the expected results. More precisely, besides applying tensile, compressive, shear forces or bending moments, the rate of application of the load also plays a major role as well as the mode of application (load-control or displacement-control).

E.2. Materials and methods

The bonded joint chosen for this study was a double-lap joint, as shown in Fig. E.2. It was designated ‘double-lap’ because the timber parts are bonded through two surfaces, and it was thus considered to provide greater strength and credibility at a structural level. Double-lap joints are also widely used for bonding composite materials, such as FRPs, because of their proven efficiency after many years of application.

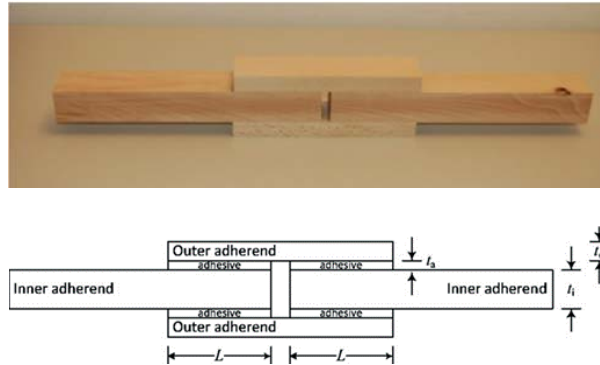


Figure E.2: Double-lap timber joint

In order to provide sufficient data for the statistical analysis of the joint capacity, both experiments and finite element (FE) models can be used. For this project, some experiments (Fig. E.3) were performed but the results required for the statistical analysis were mainly derived from the numerical model, developed in Ansys 15.0 (Fig. E.4), due to the lack of an adequate number of experiments.



Figure E.3: Typical failure of the double-lap timber joint

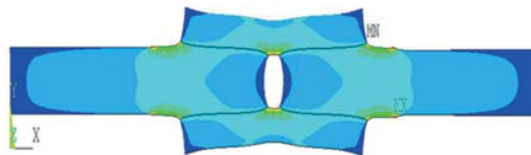


Figure E.4: FE model used to provide input data for statistical analysis

In the case of the experiments, the joint capacity can be derived directly from the load-displacement curve, created during the test, while, in the case of the numerical model, it is more complex. The critical path

where failure occurs has to be defined and the stresses along this path have to be plotted. After successfully acquiring these values, with the aid of one credible failure criterion, joint capacity can be predicted. In this case, the critical path was selected at 2.5 mm inside the inner timber adherend and the failure criterion used was the Norris criterion [4].

$$\frac{\varepsilon_{xx}^2}{X^2} + \frac{\varepsilon_{yy}^2}{Y^2} + \frac{\varepsilon_{xy}^2}{S^2} - \frac{|\varepsilon_{xx} \cdot \varepsilon_{yy}|}{X \cdot Y} \leq 1 \quad (1)$$

When the value of the equation is higher than 1, failure occurs in the path where the stresses are calculated. The purpose of the following calculations is to optimize the joint capacity by determining which parameters influence it most in order to subsequently save both material and time in acquiring the desired joint strength.

Investigated parameters

Among all the parameters mentioned, this study focuses on the influence of the four main ones, two geometrical and two concerning the material, on the joint's capacity. Thus the overlap length, L , thickness of the adhesive layer, t , mechanical properties of the wood and mechanical properties of the adhesive are the parameters investigated as shown in Table E.1. The different materials used in each case result in different input properties for the FE model and different strength properties for the failure criterion. The main properties of the spruce and beech used are shown in Tables E.2a and b and the elastic properties of the two different types of adhesive used, SikaFast5221 (acrylics or ADP) and SikaForce7851 (polyurethane or PU), are given in Table E.3.

Table E.1: Investigated parameters

Overlap length, L (mm)	100, 110, 120, 130, 140, 150, 160
Thickness, t (mm)	2, 5
Type of wood	spruce, beech
Adhesives	ADP, PU

Table E.2a: Elastic properties of the two types of wood [5]

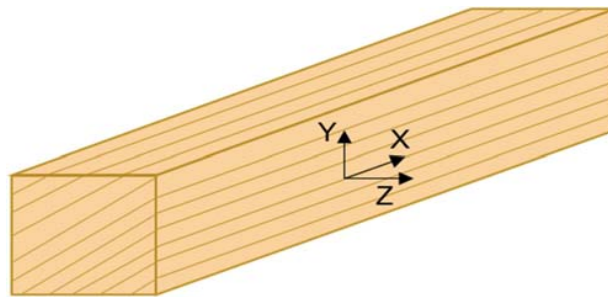
wood	E_x (GPa)	E_y (GPa)	E_z (GPa)	ν_{xy} (-)	ν_{yz} (-)	ν_{xz} (-)	G_{xy} (MPa)	G_{yz} (MPa)	G_{xz} (MPa)
beech	13.9	1.1	2.2	0.09	0.64	0.07	860	490	1280
spruce	11.6	0.896	0.496	0.4	0.04	0.4	690	758	39

Table E.2b: Strength parameters of the two types of wood [6]

wood	X (MPa)	X' (MPa)	Y (MPa)	Y' (MPa)	S (MPa)
beech	86.2	50.3	7	7	13.9
spruce	75	45	4	5	10

Table E.3: Elastic properties of the adhesives [7]

Adhesive	E -modulus, E (MPa)	Poisson ratio, ν (-)
PU	600	0.42
ADP	100	0.4


Figure E.5: Schematic description of timber axes

E.3. Statistical analysis

E.3.1. Factorial desings

In this study, both full and fractional factorial designs are used. First, a full factorial model is used to determine the relative importance of the main factors and their interactions. A linear model including two by two interactions has been considered:

$$y = a_0 + \sum a_i x_i + \sum a_{ij} x_i x_j$$

$$y = X\beta \quad (2)$$

where a_0 are the constant effects, a_i are the main half effects and a_{ij} are the first order interaction half effects and x_i are the factors. The matrix of the model is constructed from the matrix of the experiments. The matrix of experiments is built up by attributing a value between -1 (minimum value of the factors) to 1 (maximum value of the factors) in order to normalize the input values. The matrix of the model X has the same number of columns as the number of coefficients of the model. The column that is used to

calculate the coefficients a_{ij} and that corresponds to the interaction $X_i X_j$ is the product of columns i and j of the matrix of the experiments. The first column contains elements equal to 1 and corresponds to the coefficients a_0 . The number of rows is equal to the number of experiments. In order to determine the value of each coefficient, the least square method is used as follows:

$$\beta = (X^T X)^{-1} X^T y \quad (3)$$

The vector β is the vector $m \times 1$ of the coefficients, and y is the vector $n \times 1$ of the test results. In the first phase of the analysis, the whole set of experimental results is considered. The matrix of the experiments is a 56×4 matrix. In the second phase, a partial set of the experiments is analyzed using the same method. According to the fractional factorial design model, only the maximum and minimum values of the experimental results are considered. The dimensions of the matrix of experiments are thus reduced to 16×4 .

For both the full and partial experimental sets, the relative effects are calculated for each coefficient. All coefficients with a relative effect below a threshold value defined by the designer are not considered in the subsequent analysis because their effect can be neglected.

E.3.2. ANOVA

Once the significant coefficients are known, an analysis of variance (ANOVA) can be performed on the model. “The analysis of variance is not a mathematical theorem but a simple method of arranging arithmetical facts, so as to isolate and display the essential features of a body of data with the utmost simplicity” (Fisher, 1934). As illustrated in Fig. E.6, the experimental results are represented by vector Y , which is decomposed into two perpendicular vectors: the model and the residual. Moreover, the model is also decomposed into two vectors: the mean (constant) and the effect.

According to the Pythagoras theorem, the sum of the square of the test results should be equal to the sum of the square of the effects, the constant and the residual. The ANOVA analysis consists of comparing the sum of the squares of the effects with the sum of the squares of the residual.

The sum of squares (SS) of the constant, the effect and the residual must be standardized by its degree of freedom (DF) to obtain the mean squares. The mean square is calculated by dividing the sums of the square of the constant, the effects and the residual by their respective degree of freedom. The degree of freedom is 1 for the constant and for each effect. Concerning the residual, the degree of freedom is equal to the number of experiments minus the degree of freedom of the constant and the effects.

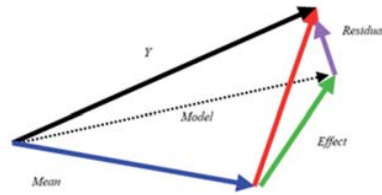


Figure E.6: Graphical qualitative description of relationship between model, constant, effect, test results and residual [8]

The mean square of the effects and of the residual errors are then compared. The mean square of a significant effect is expected to be significantly greater than the mean square of the residual errors.

To complete the verification of the significance of each parameter, the probability of a random effect is calculated according to a Fisher distribution. An effect with a high Fisher probability has a higher probability of being a random effect and being related to noise effects.

E.3.3. Full experimental set

The objective of this study is to understand the relationship between the chosen factors in order to provide the best parametric model. Fifty-six experiments have been performed and considered in the full fractional design method. The standardized variables for the four factors of the experiments have been calculated by means of the formula:

$$x_i = \frac{u_i - u_i(0)}{\Delta u} \quad (4)$$

where u is the natural variable, $u(0)$ is the center of the natural variable interval and Δu is half of the interval. For example, 100 mm of overlap length corresponds to -1 and 160 mm to 1 in standardized factors (see Table E.4).

Table E.4: Normalized values for the four factors in full experimental set

x_1	x_2	x_3	x_4
Overlap length, L	Thickness, t	E (wood)	E (adhesive)
-1, -0.66, -0.33, 0, 0.33, 0.66, 1	-1, 1	-1, 1	-1, 1

Annex E

In order to represent the response, the data have been analyzed with a linear model with interactions described by:

$$y = a_0 + a_1x_1 + a_2x_2 + a_3x_3 + a_4x_4 + a_{12}x_{12} + a_{13}x_{13} + a_{14}x_{14} + a_{23}x_{23} + a_{24}x_{24} + a_{34}x_{34} + \varepsilon \quad (5)$$

Where:

- y is the response
- a_0 is the constant term
- a_1 is the coefficient overlap length
- a_2 is the coefficient thickness
- a_3 is the coefficient type of wood
- a_4 is the coefficient type of adhesive
- a_{ij} is the interaction coefficients
- ε is the experimental error

The model matrix is:

$$X = \begin{pmatrix} 1 & x_{11} & x_{12} & x_{13} & x_{14} & x_{11}x_{12} & x_{11}x_{13} & x_{11}x_{14} & x_{12}x_{13} & x_{12}x_{14} & x_{13}x_{14} \\ 1 & x_{21} & x_{22} & x_{23} & x_{24} & x_{21}x_{22} & x_{21}x_{23} & x_{21}x_{24} & x_{22}x_{23} & x_{22}x_{24} & x_{23}x_{24} \\ \dots & & & & & & & & & & \\ 1 & x_{N1} & x_{N2} & x_{N3} & x_{N4} & x_{N1}x_{N2} & x_{N1}x_{N3} & x_{N1}x_{N4} & x_{N2}x_{N3} & x_{N2}x_{N4} & x_{N3}x_{N4} \end{pmatrix} \quad (6)$$

where N is the number of experiments.

The full model matrix is a 56×11 , where 11 is the number of coefficients for a linear model with a constant and interactions. The equation coefficients can be calculated with Eq. 3. The resulting responses, Y , for all cases examined (56×4) are included in Table E.5 for reference.

Table E.5: Model response for all examined parameters

x_1	x_2	x_3	x_4	<i>Response, Y</i>
Overlap length, L (mm)	Thickness, t (mm)	Type of wood	Type of adhesive	Joint capacity (kN)
100	2	spruce	ADP	30
100	2	spruce	PU	39
100	5	spruce	ADP	22
100	5	spruce	PU	30
100	2	beech	ADP	50
100	2	beech	PU	83
100	5	beech	ADP	30
100	5	beech	PU	50
110	2	spruce	ADP	33
110	2	spruce	PU	42
110	5	spruce	ADP	26
110	5	spruce	PU	33
110	2	beech	ADP	54
110	2	beech	PU	89
110	5	beech	ADP	35
110	5	beech	PU	59
120	2	spruce	ADP	36
120	2	spruce	PU	46
120	5	spruce	ADP	29
120	5	spruce	PU	36
120	2	beech	ADP	57
120	2	beech	PU	95
120	5	beech	ADP	40
120	5	beech	PU	67
130	2	spruce	ADP	40
130	2	spruce	PU	48
130	5	spruce	ADP	33
130	5	spruce	PU	39
130	2	beech	ADP	60

Annex E

130	2	beech	PU	102
130	5	beech	ADP	44
130	5	beech	PU	75
140	2	spruce	ADP	43
140	2	spruce	PU	51
140	5	spruce	ADP	37
140	5	spruce	PU	42
140	2	beech	ADP	64
140	2	beech	PU	108
140	5	beech	ADP	50
140	5	beech	PU	83
150	2	spruce	ADP	46
150	2	spruce	PU	52.8
150	5	spruce	ADP	41
150	5	spruce	PU	45
150	2	beech	ADP	67
150	2	beech	PU	114
150	5	beech	ADP	55
150	5	beech	PU	92
160	2	spruce	ADP	50
160	2	spruce	PU	56
160	5	spruce	ADP	44
160	5	spruce	PU	48
160	2	beech	ADP	70
160	2	beech	PU	120
160	5	beech	ADP	60
160	5	beech	PU	100

E.3.4. Partial experimental set

The full factorial method is then applied to a smaller number of experiments, 16. The idea behind this reduction is to determine whether, with a lower number of runs, it is still possible to obtain reasonable and similar estimations for the half-effects.

In order to do so, the experiments with intermediate points in the interval are eliminated. In this case, the partial model matrix is a 16×11 . Since each factor has two levels, the dispersion matrix is diagonal and the equation coefficients can be calculated with the formula:

$$a = \frac{1}{N} \cdot X^T \cdot y \tag{7}$$

The aim is to demonstrate whether with a factorial design, which takes into account only the extreme of the experimental factors, it is possible to obtain a model which is sufficiently accurate to describe the response of the whole experimental set.

E.3.5. Fractional factorial design

The fractional factorial method is applied when fewer experiments are available. The fractional factorial design has been constructed by choosing a generator $j=1 \cdot k \cdot m$. The number of experiments has been reduced from $2k$ to $2k-1$, where k is the number of factors. In this case, the model matrix is 8×8 . The dispersion matrix is diagonal and the equation coefficients can be calculated with Eq. 7. The aim is to demonstrate whether with a fractional factorial design it is possible to obtain a model that is sufficiently accurate to describe the response.

E.4. Analytical results

E.4.1. Full experimental set

In order to evaluate which coefficients have a greater influence on the response, the relative effects of each factor have been obtained by dividing the coefficients a_i and a_{ij} by a_0 .

Table E.6: Model coefficients

	a_0	a_1	a_2	a_3	a_4	a_{12}	a_{13}	a_{14}	a_{23}	a_{24}	a_{34}
effects	55.2	13.4	-7.1	15.3	10.7	1.6	3.8	1.9	-3.3	-1.6	7.3
relative effects (%)		24.3	-12.9	27.7	19.3	3	6.9	3.4	-6.0	-3.0	13.1

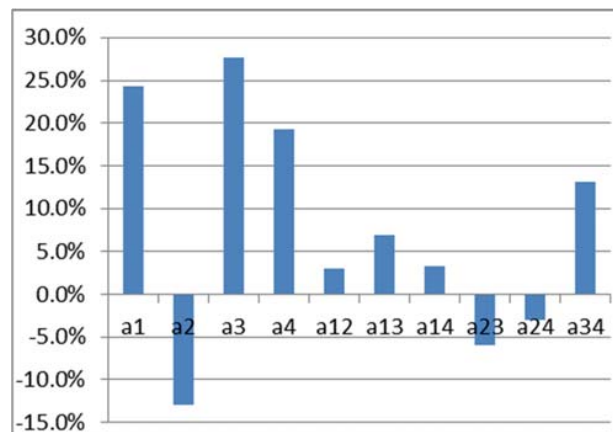


Figure E.7: Graphical qualitative description of relationship between model, constant, effect, test results and residual

As can be seen from Table E.6 and Fig. E.7, the most dominant factors are the mechanical properties of the wood (27.7%) and the overlap length (24.3%).

ANOVA

In order to obtain a more precise evaluation of the coefficients, an analysis of variance (ANOVA) is carried out. The sum of the squares (SS), the degrees of freedom (DF), the mean squares (MS), the Fisher distribution (T) and the Fisher probability (p) are summarized in Table E.7.

Table E.7: The ANOVA table of factors (56 experiments)

Source	SS	DF	MS	F	p (%)
constant	170590	1	170590	25296	0.000
a₂₄	150	1	150	22	0.002
a₁₂	153	1	153	23	0.002
a₁₄	194	1	194	29	0.000
a₂₃	616	1	616	91	0.000
a₁₃	808	1	808	120	0.000
a₂	2831	1	2831	420	0.000
a₃₄	2949	1	2949	437	0.000
a₄	6369	1	6369	944	0.000
a₁	10106	1	10106	1499	0.000
a₃	13060	1	13060	1937	0.000
residual	303	45	7	1	-
Total	208131	56	-	-	-

The last column, p, represents the level of significance of randomness of a measurement. Very low p values indicate that the effect computed for a factor appears statistically significant. On the other hand, where the

probability p is large, the effect of the factor is random. The ANOVA table was computed first for each factor [8, 9].

According to the probability values, the effects that are significant are those with $p < 0.0001\%$. According to the results presented in Table E.7, only the significant values should be considered in the final model: the overlap length, the thickness, the mechanical properties of the wood, the mechanical properties of the adhesive and the interaction between the mechanical properties of the wood and of the adhesive. The final model is:

$$y = 55.2 + 13.4 \cdot x_1 - 7.1 \cdot x_2 + 15.3 \cdot x_3 + 10.7 \cdot x_4 + 7.3 \cdot x_{34} + 3.8 \cdot x_{13} - 3.3 \cdot x_{23} \quad (8)$$

The ANOVA table of the new model shows that all the coefficients with $p < 0.0001\%$ are significant (see Table E.8). The sum of the square of the residual has increased from 0.15% to 0.29%.

Table E.8: ANOVA table of final model

Source	SS	DF	MS	F	p (%)
constant	170590	1	170590	13490	0.00
a23	616	1	616	49	0.00
a13	808	1	808	64	0.00
a2	2831	1	2831	224	0.00
a34	2949	1	2949	233	0.00
a4	6369	1	6369	504	0.00
a1	10106	1	10106	799	0.00
a3	13060	1	13060	1033	0.00
residual	607	48	13		
Total	207938	56			

The half-normal plot in Fig. E.8 illustrates which effects are not aligned with the rest and is widely used instead of the normal plot because the difference is much clearer. A comparison between the values estimated using the model and the measured values has been plotted in Fig. E.9. A graphic representation of the half-effects with the confidence intervals is shown in Fig E.10.

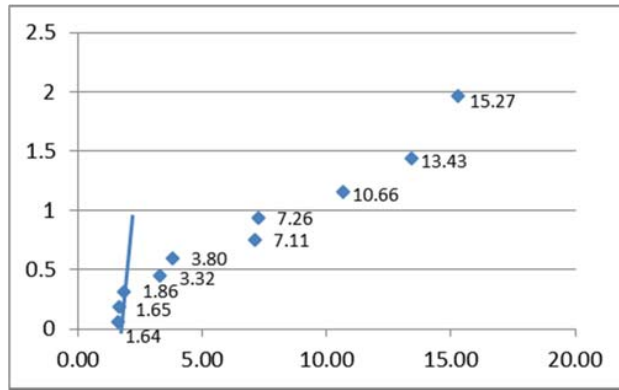


Figure E.8: Half-normal plot (56 experiments):

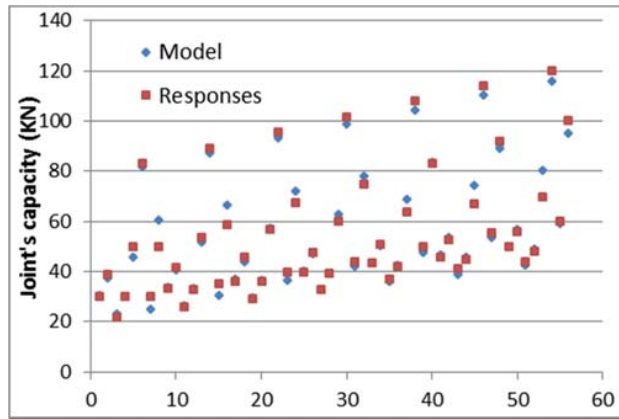


Figure E.9: Comparison between response and model values

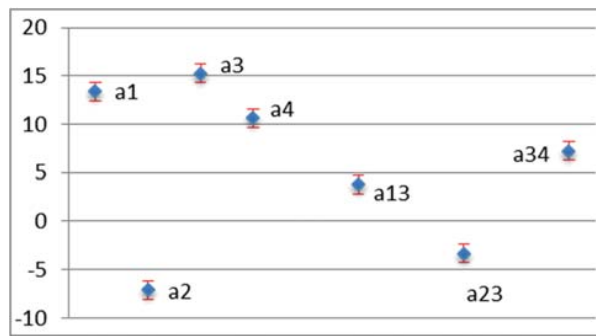


Figure E.10: Confidence intervals of coefficient selected in new model

E.4.2. Partial experimental set

Similarly to the previous method, the effect of each factor has been estimated calculating the relative coefficients. As it can be seen from Table E.9 and Figure E.11, the most dominant factors are the E-modulus of the wood (27.7%) and the overlap length (24.3%).

Table E.9: Model coefficients (partial set)

	a_0	a_1	a_2	a_3	a_4	a_{12}	a_{13}	a_{14}	a_{23}	a_{24}	a_{34}
effects	55.1	13.4	-7.1	15.2	10.6	1.6	3.8	1.9	-3.3	-1.6	7.2
relative effects (%)		24.3	-12.9	27.7	19.3	2.9	6.8	3.4	-6.0	-3.0	13.1

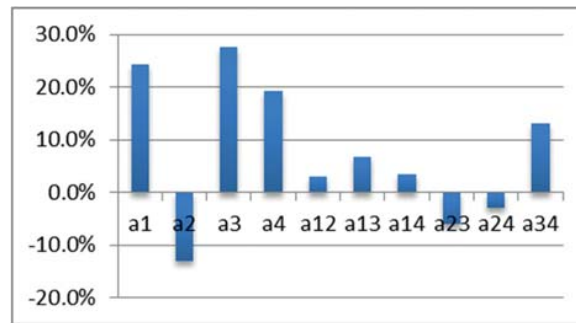


Figure E.11: Graphical qualitative description of relationship between model, constant, effect, test results and residual

ANOVA

The ANOVA table was computed first for each factor (see Table E.10). According to the probability values, the effects that are significant are the smaller ones. In this analysis the effects with $p < 1\%$ have been considered. According to the results presented in Table E.9, the final model is:

$$y = 55.13 + 13.38 \cdot x_1 - 7.13 \cdot x_2 + 15.25 \cdot x_3 + 10.63 \cdot x_4 + 7.25 \cdot x_{34} \tag{9}$$

The ANOVA table of the new model shows that all the coefficients with $p < 1\%$ are significant (see Table E.11). The sum of the square of the residual has increased from 0.29% to 1.19%.

A comparison between the model and the responses is shown in Fig. E.12. The misaligned points can also be seen from the half-normal plot in Fig. E.11. A comparison between the values estimated using the model and the measured values has been plotted in Fig. E.13. A graphic representation of the half-effects with the confidence intervals is shown in Fig. E.14.

Table E.10: ANOVA table of factors

Source	SS	DF	MS	F	p (%)
constant	170590	1	170590	25296	0.000
a₂₄	150	1	150	22	0.002
a₁₂	153	1	153	23	0.002
a₁₄	194	1	194	29	0.000
a₂₃	616	1	616	91	0.000
a₁₃	808	1	808	120	0.000
a₂	2831	1	2831	420	0.000
a₃₄	2949	1	2949	437	0.000
a₄	6369	1	6369	944	0.000
a₁	10106	1	10106	1499	0.000
a₃	13060	1	13060	1937	0.000
residual	303	45	7	1	-
Total	208131	56	-	-	-

Table E.11: ANOVA table of final model

Source	SS	DF	MS	F	p (%)
const	48'620	1	48'620	687.70	0.00
a₂	812	1	812	11.49	0.69
a₃₄	41	1	841	11.90	0.62
a₄	1'806	1	1'806	25.55	0.05
a₁	2'862	1	2'862	40.48	0.01
a₃	3'721	1	3'721	52.63	0.00
residual	707	10	71		
Total	59'370	16			

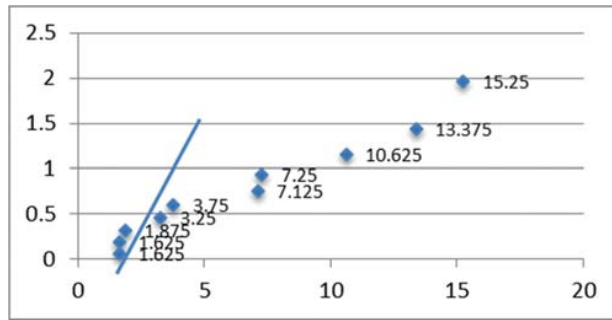


Figure E.12: Half-normal plot (16 experiments)

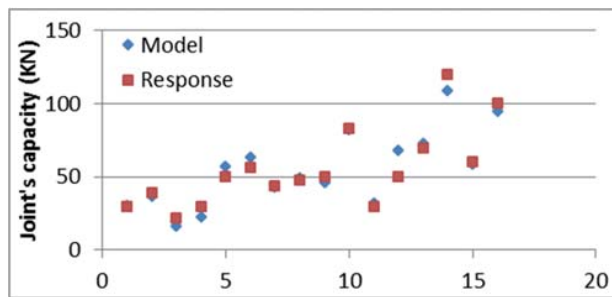


Figure E.13: Comparison between response and model values

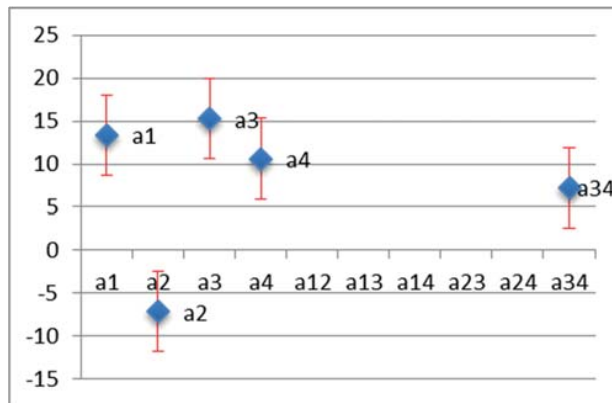


Figure E.14: Confidence intervals of coefficient selected in new model

E.4.3. Fractional factorial design

To apply the fractional factorial design a generator is needed. In this case, from the previous results, x_2 has been selected as the least important factor; therefore the generator $2 = 134$ has been chosen. The number of experiments has been reduced from 24 to 24-1. As it can be seen from Table E.13 and Fig. E.15, The most dominant factors, as shown in Fig. E.14, are the E-modulus of the wood (27.8%), the overlap length (21.9%) and the E-modulus of the adhesive (21.4%).

Table E.12: Model coefficients (fractional factorial design)

	a_0	a_1	a_{134}	a_3	a_4	a_{13}	a_{14}	a_{34}
effects	55.4	12.13	-4.375	15.38	11.88	2.13	-1.38	8.88
relative effects (%)		21.9	-7.9	27.8	21.44	3.8	2.5	16.03

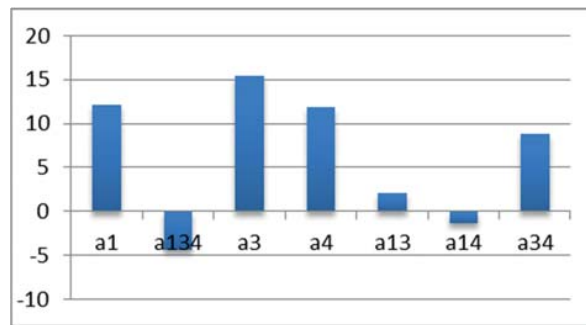


Figure E.15: Graphical qualitative description of relationship between model, constant, effect, test results and residual

ANOVA

In this case none of the parameters gives a probability $p < 1\%$, which means that this analysis is not very representative because of the small number of experiments. A graphic representation of the half-effects with the confidence intervals is shown in Fig. E.16. As expected the range increases to 9.29, compared to the range calculated in the full experimental set (0.96) and the partial experimental set (4.48).

Table E.13: ANOVA table of final model (fractional factorial design)

Source	SS	DF	MS	F	p (%)
constant	24531.13	1	24531.13	360.09	0.03
a_{34}	630.125	1	630.125	9.25	5.58
a_4	1128.125	1	1128.125	16.56	2.68
a_1	1176.125	1	1176.125	17.26	2.53
a_3	1891.125	1	1891.125	27.76	1.33
residual	204.375	3	68.125		
total	29561	8			

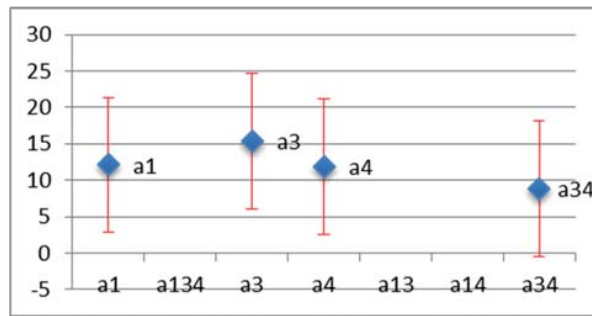


Figure E.16: Confidence intervals of coefficient selected in new model

E.5. Discussion

In order to compare the three methods applied, two comparative plots, showing relative effects from all methods, are presented in Figs. E.17 and E.18. In the first figure, the full experimental set of 56 experiments is compared to the partial one of 16 experiments and then the partial set is compared to the fractional factorial design of the eight experiments.

As can be seen from Fig.E.17, when one variable has more than two levels, if instead of taking all of them into account, the designer considers only the two extreme values, it makes little difference to the estimation of the relative effects of each parameter on the design of the experiments. This means that, as shown in this case, time can be saved by taking into account fewer experiments to reach the same results.

Furthermore, as can be seen from Fig. E.18, the relative effects lose a lot of their accuracy when the number of experiments is halved, even though it is still obvious which parameters influence the joint's capacity most. Besides, it is expected that when the number of experiments is already low, it is not possible to reduce it even more.

Also, comparing the confidence intervals between the methods used (Fig. E.10 and Fig. E.14), it can be observed that in the case of the factorial method, they are much bigger. This is reasonable because when the number of experiments is reduced, the accuracy also decreases.

As a result, a partial experimental set can be used to save time if the extreme values of the parameters are used and fractional factorial analysis can be used theoretically to reduce the time and cost of the analysis, but it provides the designer with less accurate results. The extent to which this can be applied depends on each project and the needs of the designer in each case.

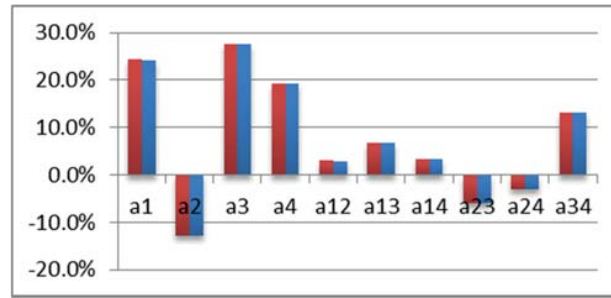


Figure E.17: Comparison between relative effects of both full methods used (56 and 16 experiments)

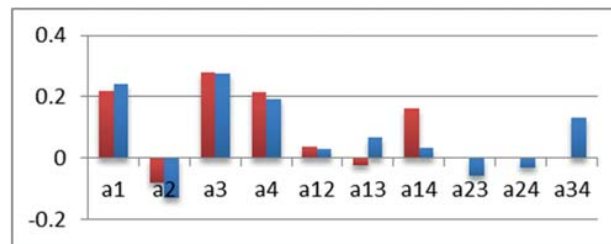


Figure E.18: Comparison between relative effects of both methods used (full and fractional, 16 and 8 experiments)

E.6. Conclusions

The partial experimental set with two levels for the parameter of the overlap length instead of the initial seven has been successfully selected, providing accurate results. On the other hand, the factorial design has been useful to establish a simple relationship between the factors studied and gives an idea of the main influences on the joint capacity, but in practice it showed that it is not reliable and more experiments should be done.

It has been possible to deduce that the overlap length, type of wood and type of adhesive have some influence and that the only interaction that is significant is the interaction between the type of wood and type of adhesive used. In addition, it has been observed that the material properties have much more influence on the joint capacity than the geometrical properties. Furthermore, the comparison between the three design methods applied showed that the results are in agreement and this proves the accuracy of the partial experimental set but not of the fractional one. As a result, partial factorial design can be successfully used to reduce the time and cost of the analysis, but in the case of fractional factorial design, it is clearly insufficient for this study and more experiments are needed.

References

- [1]. Wood Handbook: Wood as an engineering material, edited by Robert J. Ross, USDA Forest Service, April 2010
- [2]. Tannert T, Vallée T, Hehl S. Experimental and numerical investigations on adhesively bonded hardwood joints. *International journal of Adhesion and Adhesives*, 37, 2012
- [3]. Tannert T, Vallée T, Hehl S. Probabilistic strength prediction of adhesively bonded timber joints. *Wood Science Technology*, 2012
- [4]. Norris CB. 1950. Strength of orthotropic materials subjected to combined stress, U.S. Forest Products Laboratory Report #1816
- [5]. Dinwoodie J. M. Timber - a review of the structure-mechanical property relationship. *Journal of Microscopy*, 104(1), 3-32. (1975).
- [6]. Kretschmann D. E, Ross R. J. Wood handbook: wood as an engineering material, USDA Forest Service General Technical Report FPL-GTR-113, (5): 29, Madison (2010).
- [7]. De Castro J.: "System ductility and redundancy of FRP structures with ductile adhesively-bonded joints", EPFL PhD Thesis no 3214, Lausanne (2005).
- [8]. Fürbringer J. 2005, Lecture notes: Design of experiments (on <http://moodle.epfl.ch/>)
- [9]. Box G, Hunter W, Hunter J. 2005, *Statistics for Experimenters: Design, Innovation, and Discovery*, 2nd Edition (Wiley)

Annex F

Preliminary numerical investigations Parametric study

Preliminary investigations were conducted (first numerically and then experimentally) on the stress state in a double-lap timber joint; the objective was to assess the possibility of creating ductile joints, mainly by changing the geometry and the adhesives used. For all calculations concerning the joint's failure, the Norris failure criterion was used.

Keywords: *double-lap joint, timber, adhesive, joint capacity, ductility, stress peaks*

F.1. Effect of different parameters on joint capacity

F.1.1. Optimization of overlap length

Several investigations on the effect of the overlap length on single- and double-lap joints have already been carried out. It has been proved analytically and experimentally that for each joint, there is one specific overlap length for which the joint presents the highest capacity and after which any increase does not affect the strength of the joint. For the timber joints with the dimensions used in these calculations, this length has been found to be $L = 160$ mm. [1, 2] As can be seen in figure F.1, as the overlap length is increased, the stresses in the middle part are continuously tending to zero and the stress peaks on the edges also decrease. However, after a certain overlap length (the optimum one - in this case 160 mm), the stress peaks no longer significantly decrease and there is therefore no point in further increasing the length of the joint.

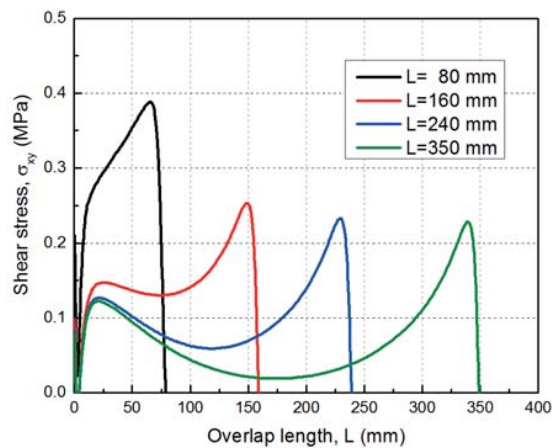


Figure F.1: The effect of overlap length on shear stresses (epoxy adhesive)

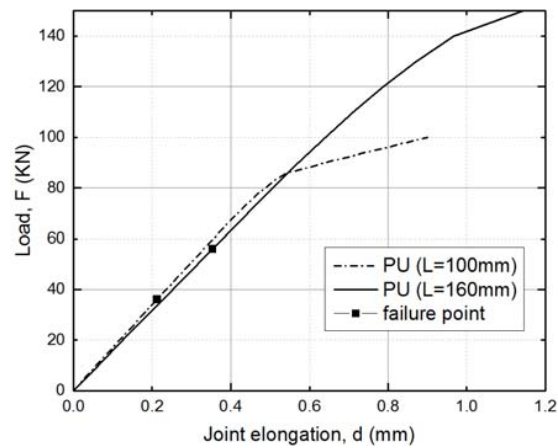


Figure F.2: The joint's L-d curve and capacity for two different overlap lengths (100 mm, 160 mm)

If the load-elongation curve is then compared for two different overlap lengths (see Fig. F.2), 100 mm and 160 mm, it can easily be seen that in the case of the longer joint, the capacity is increased from 38 kN to 58 kN and the yield point is also increased from 85 kN to 140 kN. Thus, in both cases, from the ductility point of view, merely changing the overlap length of the joint is not a solution.

For the FE simulation, bilinear modeling was applied when needed for adhesives whose stress-strain curve in tension is also bilinear, such as polyurethane and acrylics.

F.1.2. Effect of different adhesives

Theoretically, when designing a joint using the FE programs, the desired properties for the adhesive used can be easily defined, depending on the requirements of the application. In this case, great emphasis was placed not only on increasing joint capacity but mainly on achieving ductility.

For this study, three adhesives were chosen with significant differences in their properties: epoxy, polyurethane and acrylic (see Fig. 2.7), the latter two with bilinear, ductile behavior. The comparative results between the three cases regarding stress distribution are presented here (two more linearly elastic adhesives, one stiffer and one softer were included purely for the comparison).

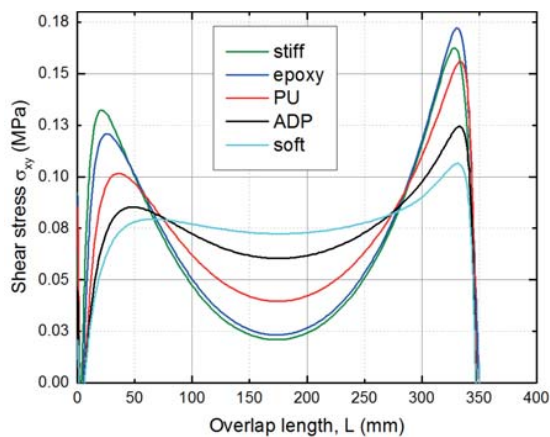


Figure F.3: Effect of adhesive on shear stress of a double-lap joint with $L=350$ mm

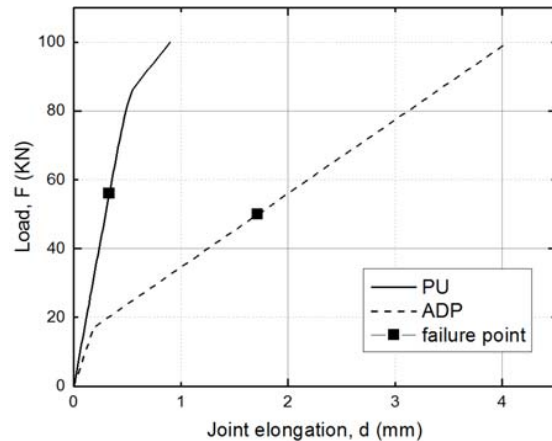


Figure F.4: Effect of different adhesives on L-d curve and joint capacity

Based on Figures F.3 and F.4 the following observations can be made:

- ✓ decreasing the yield point of the adhesive results in decreasing the yield point of the joint
- ✓ the capacity was not greatly influenced by the change of adhesive
- ✓ the acrylic creates a ductile joint, but the results may not be very satisfactory due to creep problems even at very low loads. However, this depends on the design requirements.

Ideally, an adhesive can be defined as having properties in between those of the other two adhesives, so that failure will occur in the second part of the graph, after yielding, without comprising the initial high stiffness (see Fig. 3.1).

F.1.3. Effect of adhesive thickness

Similarly to changing the type of adhesive to reduce stresses and obtain a more uniform stress distribution, increasing the thickness of the adhesive layer can have the same result (see Fig. F.5). This is because the addition of more adhesive makes the adhesive layer more deformable and therefore stresses are reduced. However, there is a limit to how much the thickness of the adhesive used to bond two timber parts together can be increased before problems of creep occur and also as from a certain value, there are no big differences in the joint capacity.

From Fig. F.6 it can be seen that the yield point for the two adhesive thicknesses (2 mm and 5 mm) remains the same, but the second part of the curve, the post-yield deformation until failure is larger in the case of the thicker adhesive layer.

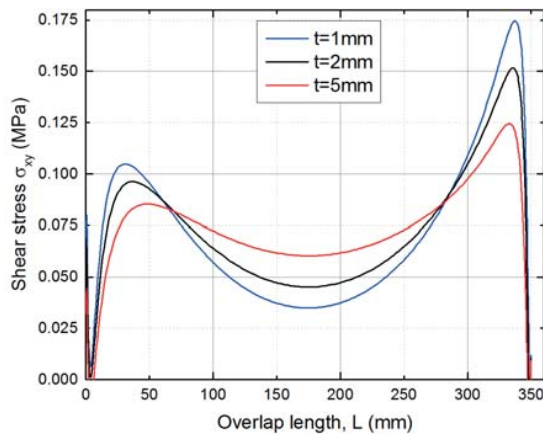


Figure F.5: Effect of adhesive thickness on shear stresses

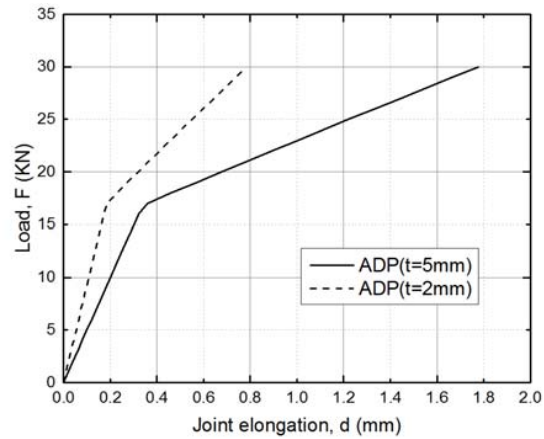


Figure F.6: Effect of adhesive thickness on joint F-d curve

All the effects of the possible changes in geometry and materials are summarized in Table 1.

Table F.1: Geometric and material effects

change	Yield load, P_y	Yield deformation, d_y	Joint capacity, P_u
increase t	same	20-30% increase	decrease
decrease E (wood)	same	increase (proportionally)	increase
increase L	increase (proportionally)	20% increase	(optimum \approx 160 mm)
decrease E (adhesive)	decrease (large)	50% decrease	slight decrease
decrease width ($w/2$)	$P_y/2$	same	$P_u/2$

F.2. Stress reduction methods

In reality, joint capacity very often needs to be further increased. Therefore a study of possible ways to reduce the peak stresses near the edge of the joint and consequently increase joint capacity is presented in the next paragraphs. Several techniques, most of which were previously applied on composite joints, were investigated and conclusions were drawn as to what can effectively be used on wood.

Some of the techniques proposed in the literature for other materials were not suitable for timber joints or were very difficult to apply in real timber structures and, they were thus not investigated. The idea of shaping a spew fillet in the end part of the adhesive, covering the plate end, as a way to prevent high stress concentrations at the edges has been mainly investigated on composite and metal joints [3, 4]. However, in timber joints, because of the greater thickness of the timber adherends, it is quite pointless and time-consuming to spew the adhesive ends, as it would have little effect on stress distribution since the wood itself is what determines the joint's capacity. Another technique is the counter-taper technique (see Fig. F.7), which is very difficult to apply in practice because it involves changing the thickness of the adhesive while applying it.

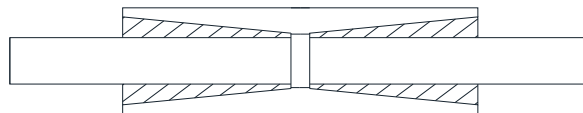


Figure F.7: Counter-taper technique

F.2.1. Tapered ends

One of the most commonly employed techniques to reduce the edge stress peaks is the use of tapered plates. This idea is very old, and was even discussed in 1974 by Hart-Smith [5, 6] in a case study for optimizing a titanium-to-graphite/epoxy stepped-lap and tapered-lap joint. The concept is that by gradually reducing the thickness of the outer adherends towards the ends, the joints become more deformable, strains are higher and stresses lower.

Several possible geometrical variations for the tapered timber joints were examined, as shown in Fig. F.8. The two main parameters changed were the percentage, $\phi\%$, of the total overlap length L , along which the thickness of the wood was reduced and the final tapering thickness, t_f . Four possible configurations were studied: with $\phi = 50\% L$ or $100\% L$ and $t_f = 0$ or 5 mm, and the results are presented in Fig. F.9. The change in the load-displacement curve is not big but the change in joint capacity is more significant. As expected, the greater the tapering area, the more resistant the joint. It then depends on the user to define the desired level of tapering that meets the needs of each application.

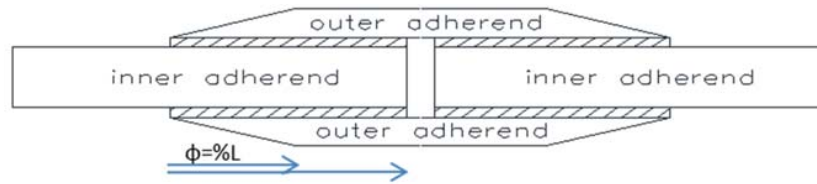


Figure F.8: Tapered double-lap joint

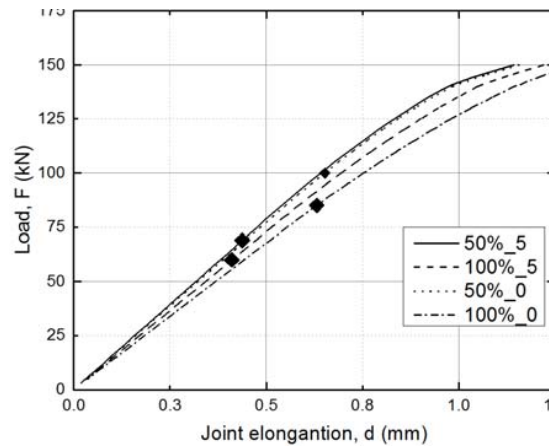


Figure F.9: Load-displacement response for different tapered joints Bi-adhesive joints

F.2.2. Bi-adhesive joints

The first to introduce the use of multiple adhesives in a single-lap joint was Raphael C. in 1961 [7]. This was an attempt to reduce the stress peaks at the edges, where failure begins. Indeed, a stiffer adhesive was used in the middle of the overlap part, while a more flexible one was applied at the edges (see Fig. F.10). This technique was later adopted by several investigators, in metal, composite and only briefly in timber joints [8, 9]. In this study, the two adhesives used were SikaForce7851 and SikaFast5221, a polyurethane and acrylic adhesive respectively, while the grading level was varied from 33% to 50% for two adhesive thicknesses, $t=1$ mm and $t=2$ mm. More precisely, the ratio $\phi\%$ defines the percentage of the total overlap length L that is covered by the softer acrylics. The numerical analysis, combined with the failure criterion applied by Norris, showed that compared to using only the polyurethane or the acrylic, the joints present higher failure loads and most importantly, they enter the post-yield phase of the adhesive used, meaning the plastic region, where there are larger deformations for little increase in the loads applied. This is very interesting, because it is the key to achieving ductile timber joints, which is the original purpose of this study.

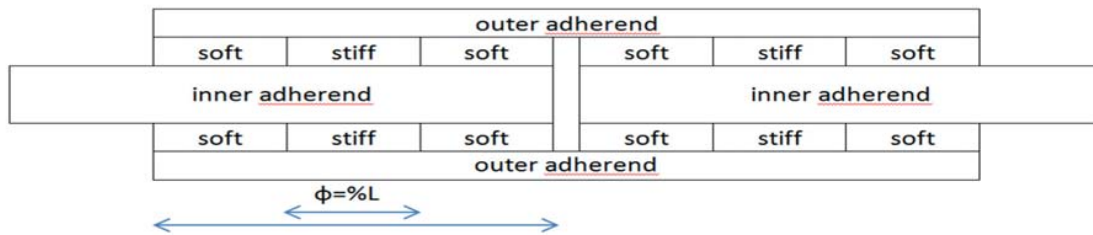


Figure F.10: Bi-adhesive double-lap joint

From Fig. F.11, it is clear that when the percentage of the softer adhesive is increased, the joint capacity also increases. In Fig. F.12, the change in the distribution of the shear stresses along the joint is clearly demonstrated for two different joints, leading to the conclusion that after the yield load, the distribution changes and becomes more even.

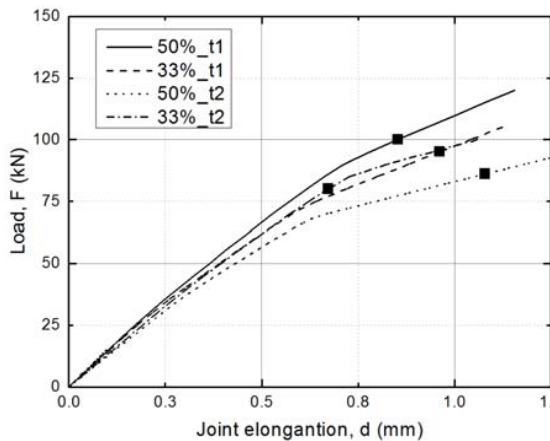


Figure F.11: Load-displacement curve for bi-adhesive joints

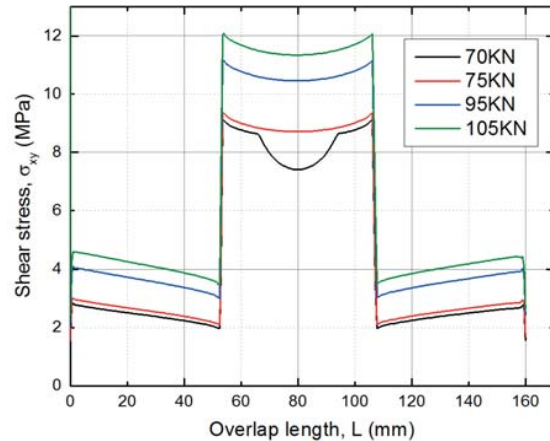


Figure F.12: Shear stresses for bi-adhesive joint (adp-pu-adp-50%-t1mm; yield load=85 kN)

F.2.3. Pre-stressed joints

This technique originates from concrete and metal applications and was inspired by an attempt to reduce the high tensile through-thickness (peel) stresses σ_y near the edge of the interface. Very simply, since failure is caused by the high tensile peak on the peel stresses close to this point, if this peak can somehow be reduced, theoretically the joint should sustain higher loads. As indicated in the following figures (see Figs. F.13-15), by adding an opposing pre-stress at the edges, lower stress peaks can finally be achieved. This technique seems quite promising but there are certain limitations. Firstly, it is not easily applicable due to the time-consuming preparation required for each joint and it is doubtful how long it can be sustained due to possible creep deformations. However, even if the problem of peel stresses is solved, that of axial tensile and shear stress peaks still remains. Finally, this technique is not very easily applied on timber because timber has a very low compressive strength perpendicular to the grains. For all these reasons, no further investigations were conducted concerning this solution.

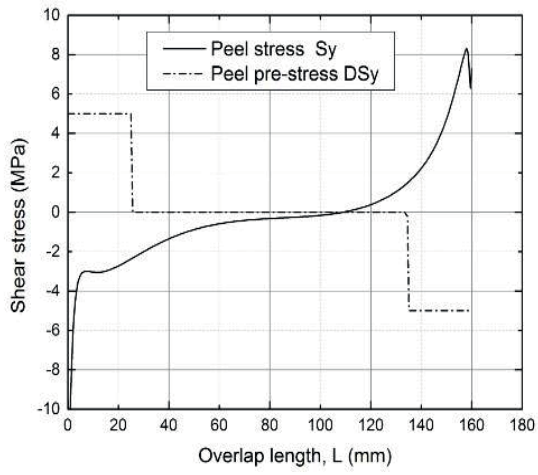


Figure F.13: Adding peel stresses for PU double-lap joint

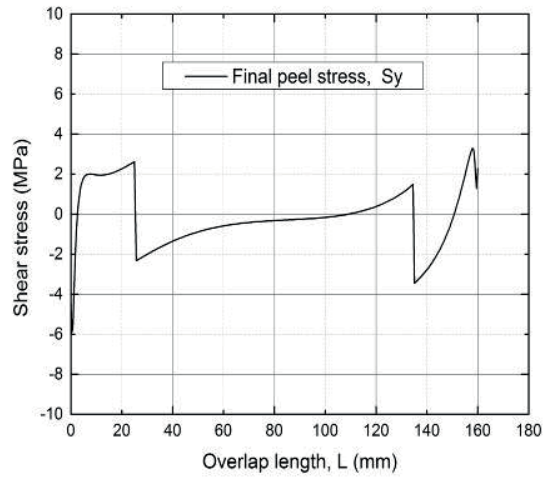


Figure F.14: Pre-stressed PU double-lap joint

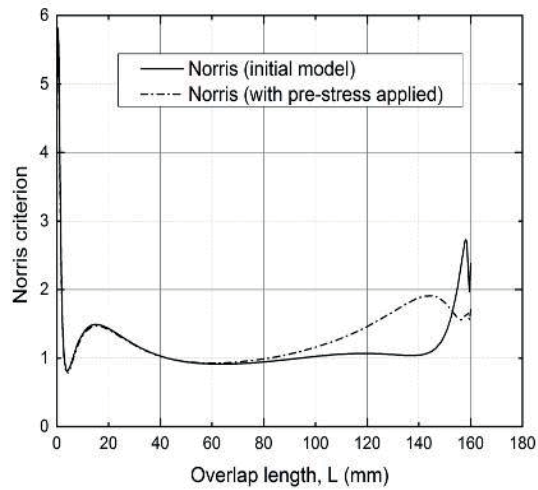


Figure F.15: Comparison between initial and pre-stressed joint

F.3. Conclusions

Based on this study, the following concluding remarks can be made:

- For each joint and stiff adhesives, there is a maximum length after which no further improvement in the joint capacity can be observed.
- Ductile adhesives can lead to ductile load-displacement joint response, provided that the joint does not fail before yield.
- Increasing the bondline thickness results in more deformable joints but similar yield loads.
- Tapered adherends, bi-adhesive bondline and pre-stressing the joints can all help reduce the stress peaks and improve joint capacity.

References

- [1]. Tannert T, Vallée T, Hehl S. Experimental and numerical investigations on adhesively bonded hardwood joints. *International journal of Adhesion and Adhesives*, 37, 2012.
- [2]. Tannert T, Vallée T, Hehl S. Experimental and numerical investigations on adhesively bonded timber joints. *Wood Science Technology*, 2012.
- [3]. Fitton M.D, Brouton J.G. Variable modulus adhesives: an approach to optimized joint performance. *Int. J. of Adhes. Adhes*, 25, 329-336, 2005.
- [4]. Tannert T, Vallée T, Hehl S. Ductile Adhesively Bonded Timber Joints. *Wood Adhesives, Session 4- Engineered Wood*, 2009.
- [5]. Hart-Smith, L.J. Adhesively bonded Single-lap joints, Report NASA CR-112236. Langley Research Center, Hampton, VA, 1973.
- [6]. Hart-Smith, L.J. Analysis and Design of Advanced Composite Bonded Joints. Technical Report-NASA CR-2218, Washington DC, 1974.
- [7]. Raphael, C. (1966). Variable-adhesive bonded joints. In *Appl. Polym. Symp* (Vol. 3, pp. 99-108).
- [8]. Pires I, L. Quintino, J.F. Durodola, and A. Beevers. Performance of bi-adhesive bonded aluminium lap joints. *Int. J. Adhes. Adhes.* 23:215-23, 2003.
- [9]. Bouchikhi A.S, Megueni A, Gouasmi S, Boukoulou F.B, Effect of mixed adhesive joints and tapered plate on stresses in retrofitted beams bonded with a fiber-reinforced polymer plate, *Materials and Design*, 2013.

MYRSINI ANGELIDI

Chemin de l'Eglise 27, 1066 Epalinges, Switzerland

(+41) 789.19.09.97

myr.angel@hotmail.com

www.linkedin.com/angelidi



Education

Ecole Polytechnique Fédérale de Lausanne (EPFL)

2012 (Oct) –
2017 (now)

PhD candidate in Structural Civil Engineering
(Composite Constructions' Laboratory)

Thesis' title: "Ductility and strain rate-dependency in adhesively bonded timber joints"

- Parametrical study of different timber joints & introduction of ductile adhesives
- Extend the benefits of adhesive joints (over mechanical ones) & develop ductile timber structures

National Technical University of Athens, School of Civil Engineering (NTUA)

2011 (Oct) –
2012 (Sep)

Master Diploma in Structural Analysis and Design (Post-Master)

Thesis' title: "Structural analysis of a steel-bearing structure (Karaiskaki Stadium)"

Grade: 8.67/10
(Top 5%)

- Proposal of alternative design method & cost-structural efficiency comparison and evaluation

National Technical University of Athens, School of Civil Engineering (NTUA)

2006 (Oct) –
2011 (July)

Master of Civil Engineer (5-year Diploma)

Thesis' title: "Sustainable Design of a hotel complex in the area of Attiki"

- Architectural design and planning of the facilities
- Evaluation of the CO₂ (carbon footprint) releases & innovative methods for reducing it

Grade: 8.50/10
(Top 5%)

Lycee Leonin, Nea Smyrni (greek-french school) (LLNS)

1994-2006

High School Diploma

Grade: 19.7 /20
(Highest distinction, ranked 1st)

Professional Experience

EPFL - Doctoral Assistant:

2012 (Oct) – 2016 (now)

- **Teaching** assistant: annual course "Structures and Materials"
- **Research** assistant: experimental, analytical and numerical work

Architectural Office (Patra) - Junior Assistant Engineer (Designer)

Aug-Sept (2010, 2011)

National Bank of Greece: Employee in summer camps (Greece and France)

Aug (2006 and 2007)

Piraeus Bank - REDEXPRESS: Courier-delivering services

Dec (2009, 2010, 2011)

Radical Promotions: Advertisement and Promotion

2007-2008

Technical Knowledge	
Programming Languages	MatLab
Productivity Tools	Microsoft Excel, Word, PowerPoint, MS Project, OriginPro
Drawing (2D and 3D) Tools	AutoCAD (ECDL) and Cadware, SolidWorks, SketchUp
FE & Structural analysis software	Sap, Sofistik, Ansys, Statik, Abaqus
Others (used during the PhD)	Vic-3D (3D correlation processing), Endnote
Standards and Codes	Eurocode, SIA

Publications

Journal papers

1. M. Angelidi, A.P. Vassilopoulos, T. Keller. Displacement rate and structural effects on Poisson ratio of a ductile structural adhesive under tension and compression, International Journal of Adhesion and Adhesives (accepted)
2. M. Angelidi, A.P. Vassilopoulos, T. Keller. Ductility, recovery and strain rate dependency of an acrylic structural adhesive, Construction and Building materials (available online)
3. M. Angelidi, A.P. Vassilopoulos, T. Keller. Ductile adhesively-bonded timber joints: experimental investigation (submitted in March 2017, under review)
4. M. Angelidi, T. Keller. Ductile adhesively bonded timber joints: rate effect (submitted in April 2017)
5. M. Angelidi, T. Keller. Comparative study on structural efficiency of adhesively-bonded and mechanical timber joints (submitted in July 2017)

Conference papers

1. M. Angelidi, A. Vassilopoulos, J. de Castro San Roman and T. Keller. Time-dependent mechanical behavior of acrylic adhesives, 3rd International Conference of Structural Adhesives Bonding, Porto, Portugal, 2015.
2. M. Angelidi, A. Vassilopoulos and T. Keller. Ductility of adhesively-bonded timber joints, 1st International Conference on Timber Structures and Engineering, New Forest, UK, 2017.

Other Awards / Distinctions

- Scholarship-awarded for post-graduate studies abroad (Alumni Assoc. of Lycée Léonin, June 2012)
- Mathematical contests of the Greek Mathematical Society → National distinctions (2001, 2002 & 2003)
- A mathematical competition among Greek-French schools, in 2003 → Ranked 3rd (prize-awarded)
- The European Youth Parliament, 19-21 March 2004 → Proposed solutions for the GMOs, ranked 2nd
- The national Microsoft contest (Word and Excel), March 2007 in Athens → Ranked 3rd (prize-awarded)

Languages

- **Greek:** native language
- **English:** C2 (Cambridge Certificate of Proficiency in English, TOEFL iBT 114/120)
- **French:** C2 (Sorbonne 2), French-speaking school (12 years) & work during the PhD (5 years)
- **Italian:** B2 (Celi 3- Università di Perugia per stranieri)
- **German:** B1/B2 (EPFL Attestation, 8 semestrer courses)

